"CHEMICAL SYNTHESIS OF COBALT MANGANESE PHOSPHATE THIN FILMS FOR SUPERCAPACITOR APPLICATION"

A THESIS SUBMITTED TO

D. Y. PATIL EDUCATION SOCIETY (DEEMED TO BE UNIVERSITY), KOLHAPUR

FOR THE DEGREE OF

DOCTOR OF PHILOSOPHY

IN

PHYSICS

UNDER THE FACULTY OF

INTERDISCIPLINARY STUDIES

BY

Mr. PRANAV KALIDAS KATKAR

M.Sc.

UNDER THE SUPERVISION OF

Dr. UMAKANT M. PATIL

M.Sc., Ph.D.

ASSISTANT PROFESSOR, (DST-INSPIRE FACULTY),

CENTRE FOR INTERDISCIPLINARY RESEARCH,

D. Y. PATIL EDUCATION SOCIETY (DEEMED TO BE UNIVERSITY),

KOLHAPUR- 416 006, MAHARASHTRA, (INDIA)

December-2020

DECLEARATION

I hereby declare that the thesis entitled **"Chemical Synthesis of Cobalt Manganese Phosphate Thin Films for Supercapacitor Application"** submitted for the degree of **Doctor of Philosophy (Ph.D.)** in the **Centre for Interdisciplinary Research** faculty of the **D. Y. Patil Education Society (Deemed to be University), Kolhapur** is completed and written by me, has not before made the basis for the award of any degree/diploma/other related heading of this or any other university in india/any other country/examining body to the best of my knowledge. Further, I assert that, I have not dishonored any of the requirements under copyright and piracy/cyber/IPR act amended by UGC from time to time.

Place: Kolhapur **Mr. Pranav K. Katkar**

Date: / /20 **(Research Student)**

D. Y. Patil Education Society (Deemed to be University), Kolhapur

Centre for Interdisciplinary Research

Certificate

This is to certify that the thesis entitled ***"Chemical Synthesis of Cobalt Manganese Phosphate Thin Films for Supercapacitor Application"*** which is being submitted herewith for the award of the Degree of ***Doctor of Philosophy (Ph.D.)*** in ***Physics*** of ***D. Y. Patil Education Society (Deemed to be University), Kolhapur***, is the result of the original research work completed by ***Mr. Pranav Kalidas Katkar*** under my supervision and guidance and to the best of my knowledge and belief the work embodied in this thesis has not formed earlier the basis for the award of any Degree or similar title of this or any other University or examining body.

Place: **Kolhapur** Research Guide

Date: **/ /20**

Dr. Umakant M. Patil
Asist. Professor
(DST-INSPIRE Faculty)

Forwarded through,
Prof. C. D. Lokhande
Head and Research Director,
Centre for Interdisciplinary Research

DEDICATED

TO

MY BELOVED...

FAMILY

(Aai, Pappa & Didi)

ACKNOWLEDGEMENT

A journey is easier when you travel together. Interdependence is certainly more valuable than independence. This thesis is the result of work where I have been accompanied and supported by many peoples.

At the completion of my Ph.D. thesis, I would like to express my sincere gratitude towards my advisor, **Dr. U. M. Patil** [Assist. Professor and DST-INSPIRE Faculty, Centre for Interdisciplinary Research (CIR), D. Y. Patil Education Society (Deemed to be University), Kolhapur] for the continuous support during my Ph.D. study and related research, for his motivation, and immense knowledge. I thank him not only for the guidance he rendered in the field of research but also for enlightening the path of my life with a deep love for science. With his support, I could overcome my personal and scientific problems on writing scientific papers including this Ph.D. thesis and this work could not have been completed without his inspiring guidance and constant encouragement during the course of research tenure.

I sincerely acknowledge the whole hearted help, valuable discussions, guidelines and suggestions focused by **Prof. C. D. Lokhande**, Head and Research Director, Centre for Interdisciplinary Research (CIR). He provided a very fruitful discussion and helpful guidance for time management regarding my Ph.D. progress.

I would like to express my sincere thanks to Vice-Chancellor **Prof. R. K. Mudgal**, Pro-Vice Chancellor **Dr. Shimpa Sharma** and Registrar **Dr. V. V. Bhosale** for the inspiration and support. I thank **Dr. J. L.**

Gunjakar, Dr. Vishwajeet Khot and **Dr. Arvind Gulbake** who helped me to analyze the results with all their empathy and cooperative mind. I also thank **Dr. A. C. Lokhande, Dr. V. G. Parale,** and **Dr. P. R. Deshmukh, Dr. R. N. Bulakhe** for providing me very important sample characterization data, during entire research work.

I would like to express sincere thanks to my seniors **Dr. R. B. Pujari, Dr. A. M. Patil, Dr. A. R. Shelke,** and **Dr. P. A. Shinde** for insightful guidelines, scientific discussions and valuable suggestions on the present work. Good scientific research could not blossom in an alienated desert; it is a result of fruitful discussions and co-operative exercises of many analytical minds. I am thankful to **Dr. V. S. Jamadade**, Head, Department of Physics, D. P. Bhosale College, Koregoan (Satara) for their good wishes and support. I am also thankful non-teaching staff of the CIR Department for their kind co-operation during my research work.

In addition, I acknowledge the funding support from **Chhatrapati Shahu Maharaj Research Training and Human Development Institute (SARTHI), Pune** of the **Government of Maharashtra** State for **Chief Minister Special Research Fellowship (CMSRF)** sanctioned to me.

I own a word of thanks to all my friends and research colleague from CIR department viz. **Supriya Marje, Sachin Pujari, Suraj Khalate, Shivaji Ubale, Navnath Padalkar, Rohini Shinde, Satish Jadhav, Shrikant Sadavar, Trupti Ghogare, Priti Bagawade, Vikas Mane, Dhanaji Malavekar, Shital Kale, Deepak Sawant, Vikas Magdum,**

Yogesh Chitare, Shirin Kulkarni, Vinod Patil, Akash Patil, Sambhaji Kumbhar and Shraddha Bhosale.

I hereby express my deepest appreciation and regards to my beloved parents **(Aai and Pappa),** sister **(Pranali), Pramod** (Daji) and uncle **(Rudreshwar Appa, Krishna Anna)**, all of family members who in spite of their hard times and sufferings, continuously supported and encouraged me to complete my research.

I would like to confess that even though I try my best, it is not possible for me to acknowledge and thank all those known and unknown faces individually for their direct and indirect contribution for the successful completion of this work. I am grateful to all of you for your kind cooperation.

Place- Kolhapur **-Pranav Katkar**

Date: / /20

SUMMARY OF RESEARCH WORK

A) Papers Published/Submitted at International Journals:

1) **Pranav K. Katkar**, Supriya J. Marje, Sachin S. Pujari, Suraj A. Khalate, Prashant R. Deshmukh, Umakant M. Patil, "Single-pot hydrothermal synthesis of manganese phosphate microrods as a cathode material for highly stable flexible solid-state symmetric supercapacitors", Synth. Met., 267, (2020), 116446-116458 **(I.F.- 3.28).**
2) **Pranav K. Katkar**, Supriya J. Marje, Sachin S. Pujari, Suraj A. Khalate, Abhishek C. Lokhande, Umakant M. Patil, "Enhanced energy density of all-solid-state asymmetric supercapacitors based on morphologically tuned hydrous cobalt phosphate electrode as cathode material", ACS Sustain. Chem. Eng., 7, (2019), 11205-11218 **(I.F.- 7.63).**
3) **Pranav K. Katkar**, Supriya J. Marje, Shital B. Kale, Abhishek C. Lokhande, Chandrakant D. Lokhande, Umakant M. Patil, "Synthesis of hydrous cobalt phosphate electrocatalysts by a facile hydrothermal method for enhanced oxygen evolution reaction: effect of urea variation", CrystEngComm, 21, (2019), 884-893 **(I.F.- 3.11).**
4) Suraj A. Khalate, Sujit A. Kadam, Yuan R. Ma, Sachin S. Pujari, Supriya J. Marje, **Pranav K. Katkar**, Abhishek C. Lokhande, Umakant M. Patil, "Hydrothermally synthesized Iron Phosphate Hydroxide thin film electrocatalyst for electrochemical water splitting", Electrochim. Acta, 319, (2019), 118-128 **(I. F. - 6.21).**
5) Supriya J. Marje, **Pranav K. Katkar**, Shital B. Kale, Abhishek C. Lokhande, Chandrakant D. Lokhande, Umakant M. Patil, "Effect of phosphate variation on morphology and electrocatalytic activity (OER) of hydrous nickel pyrophosphate thin films", J. Alloys Compd., 779, (2019), 49-58 **(I. F.- 4.65).**
6) Supriya J. Marje, **Pranav K. Katkar**, Sachin S. Pujari, Suraj A. Khalate, Prashant R. Deshmukh, Umakant M. Patil, "Effect of phosphate (anion) precursor on structural and morphology behavior of nickel phosphate thin films and its supercapacitive performance", Mater. Sci. Eng. B, 261, (2020), 114641-114650 **(I.F.- 4.70).**

7) Supriya J. Marje, **Pranav K. Katkar**, Sachin S. Pujari, Suraj A. Khalate, Abhishek C. Lokhande, Umakant M. Patil, "Regulated micro-leaf like nickel pyrophosphate as a cathode electrode for asymmetric supercapacitor", Synth. Met., 259, (2020), 116224-116234 **(I.F.- 3.28)**

8) Sachin S. Pujari, Sujit A. Kadam, Yuan R. Ma, **Pranav K. Katkar**, Supriya J. Marje, Suraj A. Khalate, Abhishek C. Lokhande, Umakant M. Patil, "Facile synthesis of microstrip-like copper phosphate hydroxide thin films for supercapacitor applications", J. Electron Mater., 49, (2020), 3890-3901 **(I.F.- 1.77).**

9) S. S. Pujari, S. A. Kadam, Y. R. Ma, S. A. Khalate, **P. K. Katkar**, S. J. Marje, U. M. Patil, "Highly sensitive hydrothermally prepared nickel phosphate electrocatalyst as non-enzymatic glucose sensing electrode", J. Porous Mater., (2020), 1-13 **(I. F- 2.18).**

10) Umakant M. Patil, **Pranav K. Katkar**, Supriya J. Marje, Chandrakant D. Lokhande, Seong C. Jun, "Hydrous nickel sulphide nanoparticle decorated 3D graphene foam electrodes for enhanced supercapacitive performance of an asymmetric Device", New J. Chem., 42, (2018), 20123-20130 **(I. F. - 3.28).**

11) **Pranav K. Katkar,** Supriya J. Marje, Vinayak G. Parale, Umakant M. Patil, "Fabrication of High performance asymmetric supercapacitors based on hydrothermally synthesized highly stable cobalt manganese phosphate thin films", New J. Chem, (Submitted).

12) **Pranav K. Katkar**, Supriya J. Marje, Vinayak G. Parale, Umakant M. Patil, "Chemical synthesis of cobalt manganese phosphate thin films via SILAR method for supercapacitor applications", J. Mater. Chem. C, (Submitted).

B) Published (Indian) Patents:

1) Umakant M. Patil, **Pranav K. Katkar**, Supriya J. Marje, Vishwanath V. Bhosale, Chandrakant D. Lokhande, "A chemical synthesis process of cobalt-manganese phosphate thin films on conducting substrates", **(2018),** Application No.- **201821018918**.

2) Umakant M. Patil, **Pranav K. Katkar**, Supriya J. Marje, Chandrakant D. Lokhande, Vishwanath V. Bhosale, "A new chemical method to coat cobalt phosphate onto solid substrates", **(2020),** Application No.- **202021003019**.

C) Papers/Poster Presented at National/International Conferences:

1) **Pranav K. Katkar**, Mayur M. Kulkarni, Yogesh B. Gite, Jitendra S. Kounsalye, Vinayak S. Jamdade, Chandrakant D. Lokhande, Umakant M. Patil, Physical properties of $Li_{0.5}Fe_{2.5}O_4$ and $Li_{0.5}Al_{2.5}O_4$ nanoparticles prepared by sol-gel auto combustion method, IC-NACMBM-2017, D. Y. Patil Education Society (Deemed to be University), Kolhapur.
2) **Pranav K. Katkar**, Supriya J. Marje, Sachin S. Pujari, Suraj A. Khalate, Abhishek C. Lokhande, Chandrakant D. Lokhande, Umakant M. Patil, Single-pot hydrothermal synthesis of manganese phosphate hexagonal microrods as an active material for highly stable flexible solid-state symmetric supercapacitors, AMSCA-2018, Savitribai Phule Pune University, Pune.
3) **Pranav K. Katkar**, Supriya J. Marje, Sachin S. Pujari, Suraj A. Khalate, Abhishek C. Lokhande, Chandrakant D. Lokhande, Umakant M. Patil, Synthesis and characterization of hydrous cobalt phosphate thin films for supercapacitor application, MAS-2019, K. N. Bhise Arts, Commerce and Vinayakrao Patil Science College, Bhosare (Kurduwadi), Solapur (Consolation Prize).
4) **Pranav K. Katkar**, Supriya J. Marje, Sachin S. Pujari, Suraj A. Khalate, Abhishek C. Lokhande, Chandrakant D. Lokhande, Umakant M. Patil, Synthesis of hydrous cobalt phosphate thin films using facile hydrothermal method for supercapacitor application, 4th ICPM-MDF-2019, Shivaji University, Kolhapur.

D) Workshops Attended:

1) Participated in "Biodiversity conservation and biodiversity act 2002" held at D. Y. Patil Education Society (Deemed to be University), Kolhapur at **15th February 2019** organized by Department of Stem Cell and Regenerative Medicine, Centre for Interdisciplinary Research.
2) Participated in "Entrepreneurship and innovation as carrier opportunity" held at D. Y. Patil Education Society (Deemed to be University), Kolhapur during **19th December 2019** organized by Institution Innovation Council (IIC).

CONTENTS

Chapter No.	Title	Page No.
1	General introduction and literature survey	1-58
2	Theoretical background of hydrothermal, SILAR method and thin film characterization techniques	59-98
3	Synthesis, characterization and supercapacitive performance of cobalt manganese phosphate thin film by hydrothermal method	99-132
4	Synthesis, characterization and supercapacitive performance of cobalt manganese phosphate thin film by SILAR method	133-160
5	Asymmetric supercapacitor device fabrication and performance evaluation	161-192
6	Summary and conclusions	193-201

CHAPTER -1

GENERAL INTRODUCTION AND LITERATURE SURVEY

CHAPTER 1

General Introduction and Literature Survey

Sr. No.	Title			Page No.
1.1	**General Introduction**			**1**
	1.1.1	*Need of Supercapacitor*		**1**
	1.1.2	*Historical Background and Current Status of Supercapacitors*		**5**
	1.1.3	*Modern Tendency of Research in Supercapacitors*		**8**
	1.1.4	*Working Principle of Supercapacitor*		**10**
	1.1.5	*Types of Supercapacitor and Electrode Materials*		**12**
		1.1.5.1	*Electric Double Layer Capacitors (EDLCs)*	**13**
		1.1.5.2	*Pseudocapacitors*	**18**
		1.1.5.3	*Hybrid Capacitors*	**21**
	1.1.6	*Basics of Metal Phosphate Materials*		**22**
1.2	**A Review of Literature**			**24**
	1.2.1	*Literature Survey on Cobalt Phosphate*		**25**
	1.2.2	*Literature Survey on Manganese Phosphate*		**30**
	1.2.3	*Literature Survey on Cobalt Manganese Phosphate*		**34**
1.3	**Orientation and Purpose of the Dissertation**			**46**
1.4	**References**			**49**

1.1 General Introduction:

1.1.1 Need of Supercapacitor:

Air-pollution, global warming, diminishing sources of fossil fuel and rising oil prices, limited availability of natural resources in the global ecosystem has been increasingly driving the world towards the progress of eco-friendly high power energy resources **[1]**. To overcome these issues, there is a need to develop safe, clean and green renewable energy resources **[2, 3]**. Nowadays, the alteration of natural energy into sustainable and renewable resources, such as the sun, wind and sea tides, can produce high electric energy. But, humans have been limited control over natural phenomena because renewable sources depend on geographical and environmental factors such as climate, location, or gravitational forces on earth by sun or moon. Utilizing these renewable energy resources like fossil fuel substitution, their implementation for continuous energy production is more important. Moreover, energy storage in different forms is an essential factor, which can solve the problems. The electrical energy storage systems perform a crucial role in a lot of practical application **[4, 5]**. The role of advanced technologies in the area of renewable energy storage and electric vehicles become an important one. To meet future energy demands, the development of lightweight, flexible, high-performance, and low-cost energy storage devices are essential. This situation has inspired researchers to investigate superior energy storage technologies, **[6, 7]** such as sodium-ion batteries, lithium-ion batteries (LIBs), and supercapacitors (SCs), etc. Nowadays, the SCs has been attracted much attention, because they embrace the great potential in an extensive range of applications **[8-10]**.

Supercapacitors with their fast charge/discharge efficiency, good cycling life (> 500,000) and high power density (>10 kW kg^{-1}) offer remarkable properties

as energy storage devices compared to conventional energy storage systems. The most trustworthy carbon-based supercapacitor achieved a power density of 8500 W kg^{-1}, with hardly 20 % capacitance decay after 1,000,000 cycles, **[11]** but the energy density is restricted to less than 7.4 Wh kg^{-1}. A supercapacitor consists of positive and negative electrodes, and they are electrically isolated using a separator (like an aqueous and non-aqueous electrolyte, porous membrane, etc.). The working procedure of supercapacitors **(Figure 1.1)** is based on collecting ions from the electrolyte on electrode surface known as an electrical double layer (EDL). Supercapacitors are widely used in hybrid vehicles, telecommunication devices (remote communication, cell phones, walkie-talkies, satellites, etc.), memory backup systems, pace-maker, portable electronic devices, etc. **[12, 13]**.

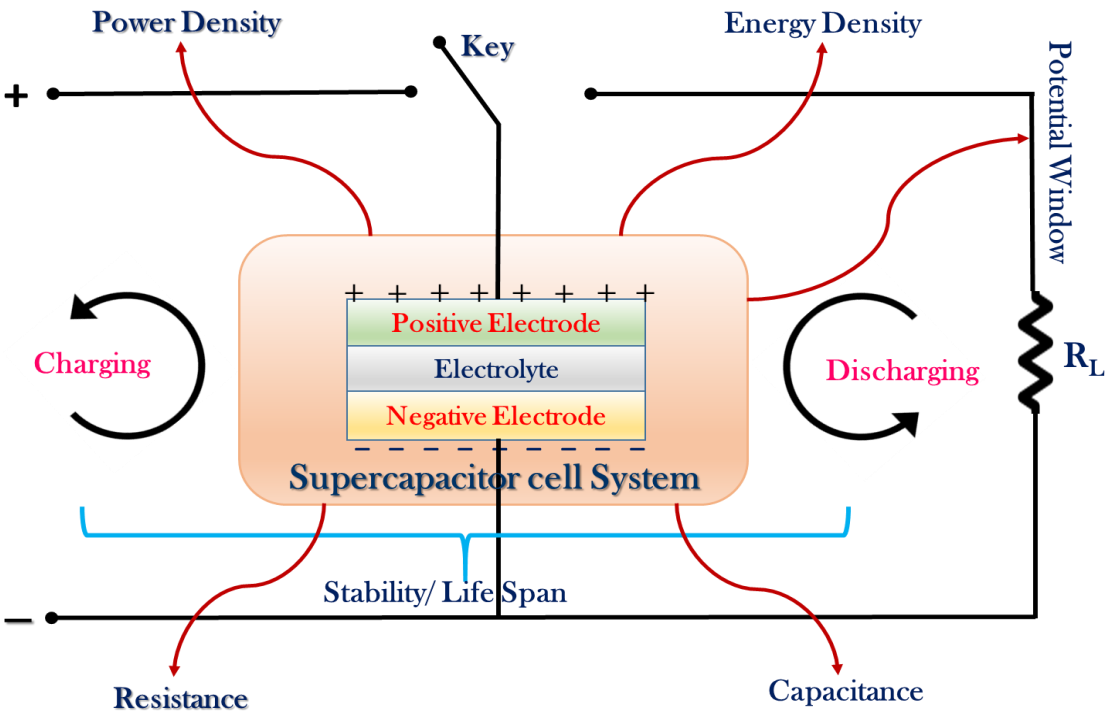

Figure 1.1: Schematic presentation of supercapacitor working procedure and related parameters **[11]**.

Supercapacitors can store electrical energy like batteries and deliver like conventional capacitors, but they utilize different storage mechanisms. Electricity

in the batteries is chemically stored, while supercapacitors are storing physically via separating positive and negative charges, therefore, they are highly reversible and can be repeated for several charge-discharge cycles. Also, they can be operated at a broad temperature scale (-40 to +50°C). The superior performance of energy storage devices can be described in terms of their ability to deliver power as well as energy densities **[14, 15]**.

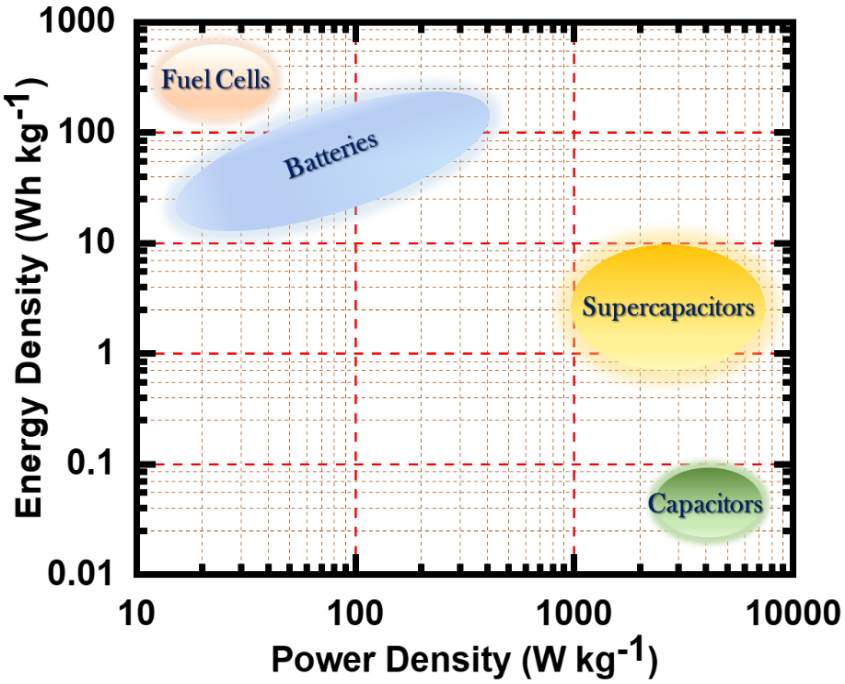

Figure 1.2: Comparative Ragone plot of several energy storage devices with their respective energy and power density.

Figure 1.2 shows the simplified Ragone plot which compares available energy storage devices, such as conventional capacitor, fuel cell, supercapacitor and battery in terms of their energy and power density. In comparison, a supercapacitor is situated between the conventional capacitor and batteries. The energy density of battery is extremely high as compared to capacitor and supercapacitor **[16]**. However, the conventional capacitor gives a low energy density but offers high power density. Supercapacitors maintain an important area

in the Ragone plot, they fulfilled the gap amongst batteries as well as fuel cells and conventional capacitors. However, supercapacitors deliver higher power than a battery and store high energy than the conventional capacitor. In addition, supercapacitors have long term cyclic stability as compared to batteries, high capacitance and low internal resistance than the conventional capacitors **[17, 18]**. Moreover, a recent application in low emission hybrid electric vehicles has shown that supercapacitors are equally important as batteries for future electrical energy storage systems **[16]**.

Table 1.1: Comparative table of basic characteristics of batteries, conventional capacitors and supercapacitors. **[19-23]**.

Sr. No.	**Factors**	**Batteries**	**Conventional Capacitors**	**Supercapacitors**
1.	Charging time	h	ps - ms	ms to s
2.	Discharging time	h	ps - ms	ms to s
3.	Specific power ($W\ kg^{-1}$)	~50 - 200	>10,000	~1000 - 2000
4.	Specific energy ($Wh\ kg^{-1}$)	~20 - 100	< 0.1	~1 - 10
5.	Cycle life (cycles)	~500 - 2000	Almost infinite	> 5,00,000
6.	Charge-discharge efficiency (%)	~70 - 85	~ 100	Up to 99

Note: ps: picosecond, ms: millisecond, s: second, h: hours.

Table 1.1 reveals the detailed performance variations of different energy storage (battery, conventional capacitor and supercapacitor) devices. In available energy storage devices, batteries have the most attention of researchers, because they can store a great amount of energy and provide proper levels of power for many applications **[14]**. However, the charge-discharge processes in batteries usually include irreversible redox reactions at the electrode-electrolyte interfaces, which change the molecular structure of active materials. For this reason, the

durability of batteries is normally restricted to only several hundred/thousand charge-discharge cycles and so it possesses less cyclic performance **[24]**. On the contrary, active materials in supercapacitors do not participate in redox reactions; therefore there are no significant chemical changes in electrode materials during cycling. As a result, an almost unlimited cyclability is frequently obtained in this highly reversible storage mechanism **[25]**. Moreover, much higher power distribution can be achieved for short times in supercapacitors. However, because of the faradaic processes in batteries, charge-discharge mechanisms are much slower than supercapacitors **[26]**. Furthermore, supercapacitors can be charged-discharged in few seconds whereas batteries require at least several hours or more to release their energy and recharge **[27]**. Nevertheless, the main adequacy of supercapacitors is their analogously less energy compared to batteries **[28]**. Due to high power, supercapacitors have been confirmed to be a budding approach to overcome the growing power interest of multi-functional devices in the twenty-first century.

1.1.2 Historical Background and Current Status of Supercapacitors:

The history of supercapacitors began with the first practical use of double layer capacitors was reported in 1957 by General Electric Company for electrolytic capacitor by applying porous carbon electrodes **[29]**. It is known that, this capacitor exhibited a surprisingly high capacitance and believed that the energy stored in pores of carbon, but the mechanism of charge storage of supercapacitor was anonymous at that time. So, this device was not marketed because of its impracticable design and flooded battery market, in which both the electrodes required to be immersed in an electrolyte vessel. Besides, in 1966 the Standard Oil Company of Ohio (SOHIO) was achieved development in energy storage devices by

manipulating the high surface area of carbon materials in tetra-alkyl ammonium electrolytes **[30]**. But SOHIO failed to commercialize their invention, so Nippon Electric Company (NEC), which after marketed all outcomes (supercapacitors) to provide backup power for maintaining computer memory and various consumer appliances under the license of SOHIO in 1978. In 1975, B. E. Conway formed a new scheme of charge storage mechanisms based on fast and reversible redox reactions arising near surface of electrode material. The development of first pseudocapacitor (a supercapacitor is also known as pseudocapacitor) is composed of ruthenium oxide (RuO_2) films as an electrode **[31-33]**. At present, the capacitors available in the market contain both carbon material with high surface area (activated carbon) in addition to highly redox active RuO_2 **[34]**. Many companies ventured in the 1980's manufacturing electrochemical capacitors. Panasonic (previously known as Matsushita Electric Industrial Co.) invented "Gold capacitor" **[35]**. The main difference between Panasonic and NEC devices was the electrolyte, NEC used an aqueous electrolyte while Panasonic used a non-aqueous electrolyte. In 1987, ELNA begun to produce double-layer capacitor by the name of "Dyna capacitor" **[36]**. In 1982, "PRI Ultracapacitors" developed first high power double-layer capacitors utilizing metal-oxide electrodes **[37]**. In 1990, the entire research field in supercapacitor become more concerned to develop supercapacitor devices with high performance. The revelation of supercapacitor devices generated curiosity, so the United States Department of Energy (DoE) started a study in the context of hybrid electric vehicles, and by 1992, a development program of ultracapacitor was started at Maxwell Laboratories **[36]**. There were four companies representing the supercapacitor's market until 1998 and they are NEC-Token, Maxwell Technologies, Panasonic, and Elena Capacitors. Further, several

vendors were providing supercapacitors as per global demand from 1999 to 2013, which was much higher than the market growth value. In year 2013, forty companies were competing in the carbon dielectric supercapacitor market worldwide (according to Paomanok's analysis data, the usage of EDLC supercapacitors worldwide has grown by 275 %, while the several vendors providing the market has risen by 1000 %) **[38]**. Composite based hybrid supercapacitor commercially manufactured by several companies are summarised in **Table 1.2**.

Table 1.2: Summary of world-wide commercially available supercapacitor **[39].**

Company	Country	Product Name	Voltage Range (V)	Capacitance Range (F)
Cooper Bussmann	US	Powerstor	2.5-5.5	0.07-100
Evans	US	Capattery	5.5, 11	0.47-1.5
AVX	US	Bestcap	3.6-16	0.010-1
Maxwell	US	Boostcap	2.2-125	1-3000
IOXUS	US	Ultracapacitor Cell	2.3-16	58-5000
IOXUS	US	Hybrid Capacitor	1-2.3	220-1000
Tarvima	Canada	ESCap	14-300	2-160
Cornell Dubilier	UK	CDE	2.1-5.5	0.022-70
SAFT-ESMA	France	Saft Nickel Capacitor	7-29	500-1200
WIMA	Germany	Supercap	2.5, 2.7	110-6500
Cap-xx	Australia	Cap-xx	2.3-5.5	0.09-120
Cellergy	Israel	Cellery	2.1-12	0.01-0.12
Panasonic	Japan	Gold Capacitor	2.1-5.5	0.015-70
NEC-Tokin	Japan	Supercapacitor	2.7-12	0.01-100
Elna	Japan	Dynacap	2.5-5.5	0.047-100
Nichicon	Japan	Evercap	2.5, 2.7	0.47-4000
Nesscap	Korea	EDLC	2.3-2.7	5-60
Nesscap	Korea	Pseudocapacitor	2.3	50-300
VINATECH	Korea	HY-CAP	2.3-5.4	0.75-800

Currently, products from Japan, US, and Russia occupy almost the entire supercapacitor market. Every nation’s supercapacitor products have their own

features and benefits like capacity, power, price and so on. According to Bosch's (2007–2022 research report on the current status and investment prospects of china's supercapacitor market), the international supercapacitor market has reached \$16 × 10^9 USD in 2015, and analysts predict that the supercapacitor market will exceed \$92.3 × 10^9 USD by 2020. Currently, the market addresses a large majority of symmetric supercapacitors using activated carbon as material for electrodes **[40, 41]**. Currently, IOXUS and Soft-ESMA are trying to commercialize asymmetric hybrid capacitors, exhibiting their capability to compete with the currently available lithium-ion hybrids and asymmetric nickel-carbon based supercapacitors **[42]**.

1.1.3 Modern Tendency of Research in Supercapacitors:

One of the new emerging energy storage technology is a supercapacitor, which is going to play a significant role in the future of energy systems. The main feature of supercapacitors is the high energy storage capacities, which makes it an essential option for different manufacturers **[43]**. With constant improvement in research, supercapacitors are achieving more attention in markets all over the world. For example, rail sections and automobiles are opening new possibilities in emerging sections such as grid energy storage. Hybrid vehicles are in demand, because of strict government rules concerning carbon emissions which inspire the growth of supercapacitors market **[44]**. The new consumer's electronic devices like cell phones and sensors required different power demands because of their various functionalities. Batteries react very slowly due to their chemical reactions. As a result, in most cases, the batteries do not supply the full energy requirement for all electronic devices. The increase in interest of supercapacitors at the industry level due to their benefits over battery in terms of power density and durability.

Supercapacitors can deliver large amounts of energy at high power and fast charge-discharge rates, making them fit for supplying high power to multifunctional electronic devices. Even, with these great features of supercapacitors, the industrial practicability of supercapacitors is limited by low energy density. Currently, researchers are trying to enhance the energy density by applying various approaches without interrupting the other features of supercapacitors.

In last few decades, carbon based materials are generally used in commercial supercapacitors **[45]**. But, carbon-based materials limit commercial use because of its low specific capacitance. Contemporary research suggests that, pseudocapacitive transition metal oxides are more promising electrode materials for supercapacitors because of their cost-effectiveness, lower resistance, and environmental friendly nature **[46]**. Furthermore, reversible and fast surface redox reactions of pseudocapacitive materials remarkably improved energy storage capacity of supercapacitors. However, the cycling life time of pseudocapacitive material is less due to the decomposition of active material in the liquid electrolyte during cyclic stability. Therefore, solid-state supercapacitors are investigated with a greater interest in which solid polymer (gel-type) electrolyte is used. Solid-state supercapacitors have several benefits over aqueous capacitors, as they overcome the problem of electrolyte leakage, flexibility, and ease of handling **[47]**. Moreover, the present research has focused on the improvement of supercapacitors using various ionic liquid electrolytes. These electrolytes are more beneficial, since they are non-toxic and thermally stable. Further, the voltage range of supercapacitors with these ionic liquid electrolytes can be increased up to 4 to 6 V **[48]**. The electrochemical performance of supercapacitor is not only subject to the electrode material, but also to the electrolyte, separator and current collector. The choice of

proper electrode material (non-toxic and low-cost) with corresponding electrolyte increases specific capacitance and energy density of a supercapacitor **[49]**.

1.1.4 Working Principle of Supercapacitor:

The conventional capacitor and electrochemical capacitor have same charge storage mechanisms but the difference is in separating medium (dielectric and electrolyte). The conventional capacitors store electrical energy in dielectric separator material that is carried by two metal plates work as terminals for the device. Similarly, electrochemical capacitors store energy in an electric double-layer formed at electrode-electrolyte interface. Formed an electric double-layer separated by a distance order of few Angstrom is depends on the used electrolytes. The schematic diagram of the energy storage mechanism of an electrochemical capacitor is shown in Figure 1.3. An electrochemical capacitor is composed of two electrodes coated with electroactive materials separated by an electrolyte.

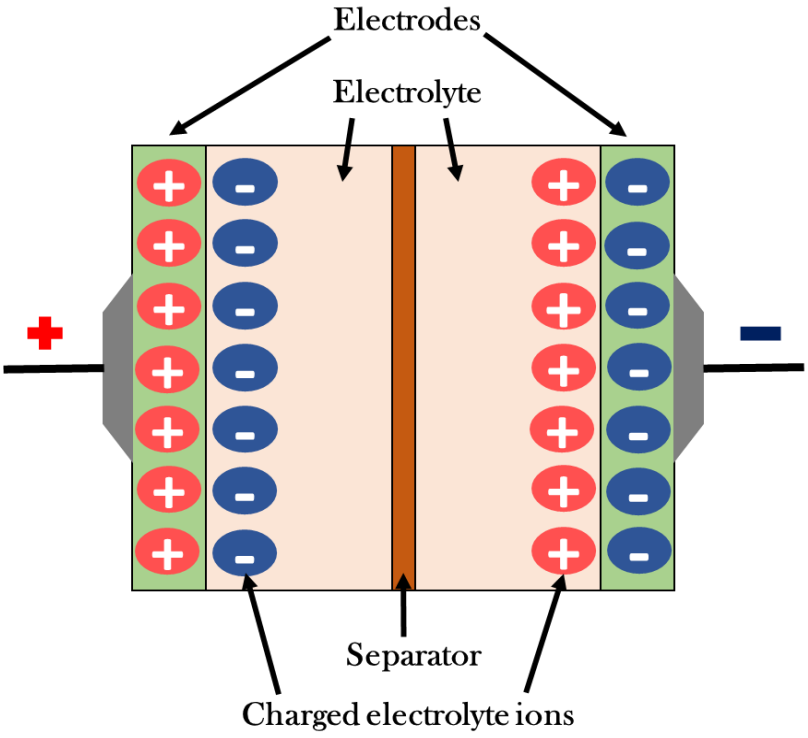

Figure 1.3: Schematic diagram of electrochemical capacitor.

When electrode surface is exposed to the electrolyte, the layers of charges formed at both sides of electrode-electrolyte interface. The total charge stored regarding the operating potential is called capacitance **(Eqⁿ. 1.1) [50]**.

$$C = \frac{Q}{V} \quad 1.1$$

where, 'C' is the specific capacitance (F g^{-1}), 'Q' is the stored charges (coulomb) and 'V' is the operating potential (V). In case of an electrochemical capacitor, 'C' is inversely proportional to the thickness of a double layer and directly proportional to the electroactive surface area of each electrode; **[14]**

$$C = \frac{\varepsilon_r}{d} A \quad 1.2$$

where, 'ε_r' is the relative permittivity, 'A' is specific surface area of electrode and '*d*' is thickness of electric double layer.

Also, the energy and power density of electrochemical capacitor is measured by the following equations: **[51]**

$$E = {}^{1}/_{2}\, CV^2 \quad \text{and} \quad 1.3$$

$$P = \frac{E}{\Delta t} \quad 1.4$$

where, E - energy density (Wh Kg^{-1}), C - specific capacitance, V - operating voltage, P - power density (W kg^{-1}) and Δt - discharging time.

Capacitance is a determination of the energy storing ability of capacitor which can be assessed using the above mentioned **Eqⁿ. (1.1)**. The energy delivered per unit time is known as power density. Generally, the resistance of physical elements (e.g., auxiliary substrate, electrode material, and electrolyte, etc.) in a supercapacitor needs to be considered while determining the energy density of the supercapacitor. Supercapacitors (electrochemical capacitors) have a similar

fundamental principle as conventional capacitors. Nevertheless, they include electrodes with an effective thickness of electric double layer (*d*) and larger surface areas (A) and resulted in enhanced capacitance and energy density **(Eq^{n}. (1.2)** and **(1.3))**. Also, the power density is calculated by the above **Eq^{n}. (1.4)**.

1.1.5 Types of Supercapacitor and Electrode Materials:

Chart 1.1 describes the classification of electrochemical supercapacitors with various types and subtypes. Depend on the charge storage mechanism, supercapacitors mainly classified into three categories namely, electrochemical double-layer capacitors (EDLCs), pseudocapacitors and hybrid capacitors. The charge storage mechanism includes faradic, non-faradic and composition of these two processes. In the faradic process, redox reaction occurs between electrode-electrolyte interfaces facilitated by transfer of charge. Conversely, chemical reactions do not happen in the non-faradic process, the charges are collected on the electrode surface by a physical process that does not involve breaking or forming a chemical bond. EDLCs based electrodes store charges electrostatically into a Helmholtz double-layer created by carbon-based materials using a non-faradic mechanism **[52-54]**. Pseudocapacitors store charges using a faradaic mechanism occurring close to the surface and in bulk of existing materials **[55]**. Usually, pseudocapacitors are comprised of metal oxides/hydroxides, sulfides, phosphates, and conducting polymers **[56-58]**.

The hybrid capacitors are operating on faradaic and non-faradaic (both) mechanisms. Hybrid capacitors are constructed by including carbon-based materials with conducting polymers or metal oxides or both **[59-61]**. It is known that, electrode material plays a vital role to reach the superior electrochemical performance of supercapacitors. So, supercapacitor electrode needs properties like

large specific area, high thermal and chemical stability, higher porosity and electrical conductivity. Several materials are applied as electrodes for supercapacitor and they have widely categorized in the below section.

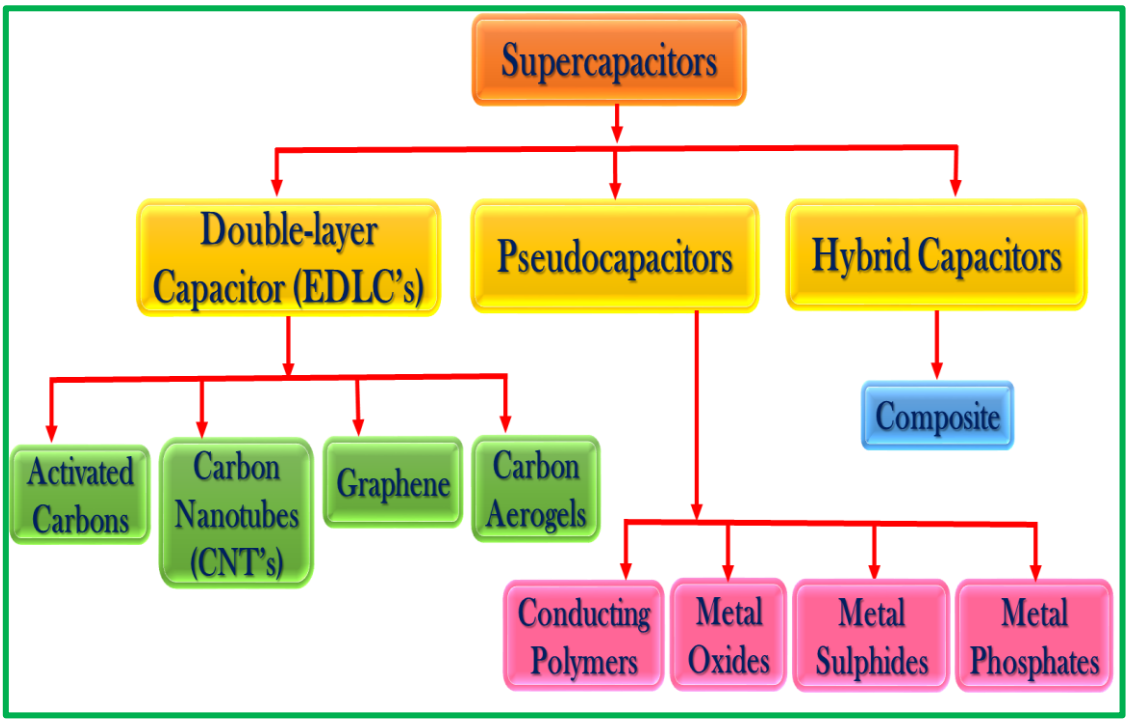

Chart 1.1: Classification of supercapacitors.

1.1.5.1 Electric Double Layer Capacitors (EDLCs):

The energy storage mechanism in EDLCs is non-faradic, there is no charge transfer at the electrode-electrolyte interface, and which is equivalent to a conventional capacitor. This indicates that, the electrolyte concentration remains constant after charging-discharging process **[62]**. Using voltage across electrochemical capacitor, both electrodes in the capacitor produce an electrical double-layer. These double-layers consist of two layers of charge: one electronic layer is in lattice structure at electrode surface and second with opposite polarity arises from solvated ions dissolved in the electrolyte. Both layers are differentiated by a single layer of the solvent (water as solvent) molecule, termed the inner Helmholtz plane. So in this process, charge transfer in electrode-electrolyte is

restricted and forces that cause adhesion are electrostatic forces (not chemical bonds) **[62, 63]**. The schematic representation of energy storage mechanism in EDLCs is displayed in **Figure 1.4 (a)**. A highly reversible EDLC capacitor delivers high cycling stability. EDLCs achieve higher capacitance due to the higher surface area of electrodes. Moreover, EDLCs can also provide higher specific power density due to faster discharge rate, and superior cycle life due to the absence of charge transfer chemical reactions **[64]**.

For carbon-based electrodes, all operating potentials are electrochemically inert. The decomposition potential (1-5 V) of electrolyte is very essential for determining the operating voltage range of EDLC. Accordingly, the electrical energy storage ability of EDLC depends on electrolytes (aqueous or non-aqueous). The ionic conductivity of the aqueous electrolyte is high as compared with a non-aqueous electrolyte which enhances the specific power density of a capacitor. Carbon based materials such as graphene, activated carbon, carbon aerogel, and carbon nanotubes are generally utilized as EDLC materials.

A) Activated Carbon (AC):

Generally, activated carbon is used as electrode materials in EDLCs due to its well-known characteristics such as low cost, feasible and scalable synthesis, higher surface area (>1000 m^2g^{-1}), excellent electrical conductivity and chemical stability **[65]**. Activated carbons are obtained from various carbon-based organic precursors, such as coal, wood, peat, nutshells, leaves, and charcoal. Normally, the process of AC activation can be achieved by chemical, physical (also called thermal) and hybrid activation methods, and it improves specific surface area along with capacitive performance **[22]**. Enhanced performance of supercapacitors using activated carbon depends on the surface area, distribution of pores, pore length as

well as pore size. Even though capacitance depends on surface area, the experimental result implies that all surface area of activated carbon does not contribute in capacitance of device. Mostly, activated carbon in the organic electrolyte shows capacitive performance in range of 50 to 150 F g^{-1}, and 100 to 200 F g^{-1} in aqueous electrolytes. The high capacitive performance (energy density of 10 Wh kg^{-1} and power density of 1.0 kW kg^{-1}) in aqueous electrolytes is associated with smaller size of solvated ions **[16, 66]**.

B) Carbon Nanotubes (CNTs)

Current research trends imply that, there is an expanding interest in the use of CNTs as EDLCs electrode material. The development of CNTs electrodes due to their excellent properties including higher porosity, excellent electrical conductivity, good mechanical integrity, high thermal and chemical stability, unique open tubular structure, a high aspect ratio of CNTs make them good electrode than other materials. Therefore, it has led to being widely researched for supercapacitor applications. CNTs have been studied to offer new opportunities for carbon electrodes in several applications like a supercapacitor, hydrogen storage, batteries, sensors, etc. CNTs are nothing but an allotrope of carbon arranged in a cylindrical hollow nanostructure. CNTs are generally observed in three forms, multi-walled (MWNTs), single-walled (SWNTs) and double-walled (DWNTs) nanotubes. CNTs are widely used as electrode material for supercapacitor devices because of their lower ESR (equivalent series resistance) than AC electrodes and show the enhanced power and energy density of a supercapacitor **[67, 68]**.

Current progress for the utilization of CNTs in supercapacitor application as conductivity enhancers and that can replace carbon black. The investigation on replacing carbon black with CNTs in EDLC electrodes showed a 90 % decrease in

ESR **[24]**. The novel structure of stuck nanotube electrodes achieves a range of specific capacitance between 80 and 130 F g^{-1} **[69]**.

C) Graphene:

Geim and Novoselov won the Nobel Prize (Physics) for their ground breaking research on graphene. Graphene is a promising candidate for the EDLCs electrode material and it is a two-dimensional (2D) single layer sheet arrangements of sp^2 carbon atoms in a hexagonal lattice, which shows superior electrical conductivity, large surface area, high carrier mobility, suitable pore size distribution, chemical and thermal stability, mechanical strength, etc. **[70]**. It is quite promising that, in near future it would draw a revolution in electrical, semiconductor, and biochemical research. Graphene-based electrochemical capacitors are highly demanded in energy storage device applications based on their superior mechanical, chemical and electrical properties.

Up to date, several methods have been employed for the preparation of graphene which can be widely categorized as a top-down and bottom-up approach. Among them, the effective approaches include mechanical exfoliation **[70]**, chemical vapor deposition (CVD) **[71]**, epitaxial growth **[72]**, thermal reduction and so on. The modified Hummers method is generally used for preparation of graphene oxide (GO) **[73]**, it can provide a higher level of oxidation in presence of strong acids and oxidants to form graphitic layered structure functionalized with covalently connected oxygen-containing groups such as hydroxyl, epoxide, carboxyl groups **[74]**. The modified Hummers method has been employed in present work for preparation of a GO based electrode. The prepared GO is hydrophilic in nature **[75]** and one important advantage is that, GO can be simply dispersed in various solutions like water, ethylene glycol, ethanol, tetrahydrofuran,

n-methyl-2-pyrrolidone (NMP), dimethylformamide, etc **[76]**. Graphene has extensively studied as electrode material in various electrolytes including organic electrolyte (TEATFB), inorganic electrolyte (H_2SO_4, KOH, Na_2SO_4) **[77, 78]**, and ionic liquid (N-butyl-N-methylpyrrolidiniumbis (trifluoromethanesulfonyl) imide (PYR14TFSI), IMIMTFB) **[79, 80]**.

Normally, reduced graphene oxide (rGO) is another option for graphene in practical application. In rGO, carbon planes are restored by carbon atoms except for few defects at the edges. The structure of rGO alters because of small variations in the adopted reduction paths. Nevertheless, GO sheets commonly represent a lower electrical conductivity owing to the effect of higher disorder **[81]** and remaining oxygen-containing groups. Theoretically, a monolayer of sp^2 bonded carbon atoms can exhibit theoretical specific capacitance up to ~550 F g^{-1}, high intrinsic mobility of 200,000 cm^2 Vs^{-1}, large surface area of 2675 m^2 g^{-1}, and optical transmittance around 97.7 % **[82]**, and they are essentially fixed the higher limit for all carbon materials. Compared to the other carbon-based material such as carbon nanotubes and activated carbon, graphene is a highly interesting material due to its quick electron-transfer kinetics, large surface area, and longer stability **[83]**. Hence, specific attention has been dedicated to the improvement of highly efficient synthesis approaches of graphene for excellent electrochemical performance.

In recent years, many researchers prepared graphene by different methods and obtained high specific capacitance, such as Yin et al. **[84]** prepared GO sheets by modified hummer's method and obtained maximum specific capacitance of 326 F g^{-1} for activated graphene. Ahmed et al. **[85]** prepared Nitrogen-doped mesoporous graphene hydrogel (MGHG) via a hydrothermal method. The as-

prepared MGHG shows a high 595.7 F g^{-1} specific capacitance. Moreover, Xian et al. **[86]** prepared graphene nanosheets (GSs) from graphite oxide via thermal exfoliation process and good supercapacitive performance (233.1 F g^{-1}) in a 6 mol L^{-1} KOH electrolyte. Therefore, there is particular interest in developing approaches for more effective synthesis of graphene, to achieve better electrochemical performance.

As the carbon-based materials (like ACs, carbon aerogel, graphene, CNTs, etc.) store energy only on surface of an electrode, the specific capacitance of those materials is relevant to the characteristics of electrode surfaces.

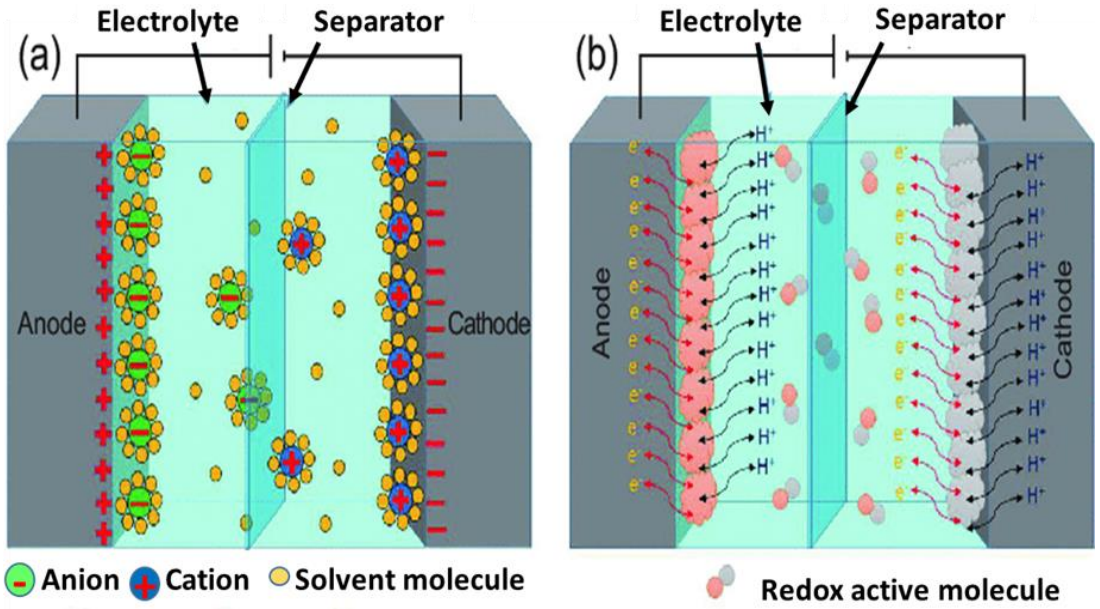

Figure 1.4: Schematic diagram of two different electric charge storage mechanisms, (a) Electrical double-layer capacitor (EDLCs) and (b) Pseudocapacitor **[87]**.

1.1.5.2 Pseudocapacitors:

In converse with EDLCs supercapacitor, the energy storage mechanism of pseudocapacitors is based on a transfer of charges by reversible faradaic reactions between electrode and electrolyte. The schematic illustration of a pseudocapacitor

with an oxidation/reduction reaction is exhibited in **Figure 1.4 (b)**. Generally, the metal oxides, sulphides, conducting polymers, and phosphates are used as pseudocapacitor materials **[88-92]**. The charge storing capacity of the pseudocapacitors electrode surface is higher than EDLCs, which means that it produces 10 times more capacitance and higher energy density than the EDLCs. However, several factors are affecting the pseudocapacitors like surface area of electrode, conductivity and porosity of materials, particle sizes, etc. Also, pseudocapacitors suffer from a lower life cycle span than EDLCs due to delamination of active material through electrochemical redox reactions. However, the pseudocapacitive materials are growing interest, because of their high specific capacitance, high energy density with fast and reversible redox reactions **[93, 94]**.

A) Conducting Polymer:

Conducting polymers are gaining much attention as an electrode material to improve the performance of supercapacitors. They give relatively higher specific capacitance, as redox reactions have not only the surface but also bulk material is involved in the charge storage mechanism and further, they have high porosity, better electric conductivity and broad potential window than carbon-based materials **[95, 96]**. The conducting polymers electrode materials like polyaniline (PANI), polypyrrole (PPy), and polythiophene (PTh) are the most usually studied materials for supercapacitors. Furthermore, the highest capacitances of PANI, PPy, and PTh are 750, 620 and 485 F g^{-1}, respectively **[97]**. Interestingly, electrolytic ions get absorbed to the surface of polymers during charging and released while discharging. However, the reduction of the polymer during an electrochemical reaction is a major issue resulting in disintegration of nanostructure and consequently decrease specific capacitance. The conducting polymers are charged

positively or negatively during oxidation or reduction (also called doping) reactions. The conducting polymer electrodes were investigated using ionic liquid electrolytes, and it shows better electrochemical performance **[98]** but, much lower cycle life than carbon electrodes, since redox sites in conducting polymer are not adequately stable. The proper operating potential window is a very crucial factor for polymers. Conducting polymers degrade and lose their conductivity by operating in an improper potential window. Accordingly, the potential range is very important for the excellent supercapacitive performance of conducting polymers.

Recently, many scientists prepared different polymers by different methods, such as Deshmukh et al. **[99]** prepared polyaniline (PANI) electrode via microwave-assisted chemical bath deposition method (CBD) and obtained maximum 753 F g^{-1} specific capacitance at a scan rate of 5 mV s^{-1}. Hryniewicz et al. **[100]** synthesized polypyrrole nanotubes by direct electro-synthesis method on flexible mesh electrode and obtained a maximum specific capacitance of 423 F g^{-1} at a current density of 0.5 A g^{-1}. Patil et al. **[101]** prepared polythiophene thin films at room temperature using CBD method. Polythiophene thin film showed a maximum specific capacitance of 300 F g^{-1} at 5 mV s^{-1}. It is known that, conducting polymers are less stable, therefore the composites can save mechanical breaking of polymers during long cycle life.

B) Metal Oxides:

Metal oxide materials are attractive electrode material for pseudocapacitors, because of their good cyclic stability as compared to conducting polymers along with high theoretical specific capacitance, high energy and power density. Pseudocapacitance obtained because of reversible redox reaction at

interface of metal oxide materials and electrolytes. Charging/discharging processes of metal oxides are able to convert into different oxidation states and ions can be inserted/deserted in the active electrode material. The different transition metal oxides could give high possibilities to manipulate the physical as well as chemical properties. Different metal oxides like TiO_2 **[102]**, RuO_2 **[103]**, MnO_2 **[104]**, Fe_2O_3 **[105]**, Co_3O_4 **[106]**, and NiO **[107]** are extensively studied as electrode materials for pseudocapacitors. Among these transition metal oxides, RuO_2 is the most popular active material as supercapacitor electrodes because of its higher specific capacitance (2192 F g^{-1} at 2 mV s^{-1} scan rate) with low ESR, good electrical conductivity, and broad potential window (0.0-1.0 V) **[108, 109]**. However, RuO_2 electrode material utilization has restricted by its toxicity and high cost.

1.1.5.3 Hybrid Capacitors:

A new third type of capacitor, developed by the co-operation of EDLC and pseudocapacitors is known as a hybrid capacitor and it accumulates charge through both faradic and non-faradic reaction mechanisms. EDLC provides a quite higher surface area by employing carbon-based materials as compared to pseudocapacitive materials. Moreover, EDLCs show comparatively less capacitive performance which hinders energy densities and further application in supercapacitors. The energy density of pseudocapacitors is more than EDLCs, but they have restrictions for the long life cycles, electrical conductivity, and power densities **[110-114]**. Researchers are trying to develop hybrid materials as supercapacitor electrodes which have higher specific capacitance, high energy with high power density without sacrificing the cyclic stability and life of the device. Asymmetric hybrid capacitors consist of EDLC and pseudocapacitor electrodes in

the same cell **[115]**. The hybrid electrode system consists of a combination of carbon-based materials with metal oxides/conducting polymers that lead to benefit of EDLC and pseudocapacitive charge storage mechanisms collectively in a single electrode. Usually, a high surface area of carbon materials improves the interaction amongst pseudocapacitive materials and electrolyte, whereas faradaic reactions enhance the charge storing ability of composite electrodes. Therefore, the coupling of carbon-based electrode materials and pseudocapacitive materials has obtained huge importance due to a large enhancement in the capacitance of devices **[116]**.

1.1.6 Basics of Metal Phosphate Materials:

The phosphate (also called orthophosphate) ion $[PO_4]^{3-}$ is obtained from phosphoric acid by the elimination of three protons (H^+). Phosphate is a salt of phosphoric acid. Phosphorus can react with many elements in the periodic table and produce different phosphates and phosphides **[117]**. A functional group contains one phosphorus atom bonded with four oxygen atoms in a tetrahedral structure (one double and three single bonds). Metal phosphate-based materials exhibit enormous potential as favorable electrode materials for the utilization of energy storage devices. Several lithium-based metal phosphate materials have been previously reported for commercialization in battery production, **[118, 119]** while nickel and cobalt phosphates are widely studied as a cathode material in energy storage devices. Metal phosphates provide excellent charge storage capacity and ionic conductivity due to their wide channels and open structure with cavities and high chemical stability according to strong P-O covalent bonds **[117]**. The phosphate-based materials show a pseudocapacitive type behaviour almost similar to the oxide-based materials.

Moreover, a lot of research on polymers, metal oxides/hydroxides and sulfides have been done and found out limitations of these pseudocapacitive materials. Metal oxides are much stable than metal hydroxides, sulfides and conducting polymers, but suffers from poor conductivity. Now a day's peoples are in a thrust of new emerging materials to overcome deficiencies of metal oxides, hydroxides and polymers applicable for supercapacitor, which can be completed by metal phosphate materials **[120]**. Metal phosphates are new emerging materials in supercapacitor application and show better electrochemical performance, conductivity more than metal oxides, hydroxides and sulfide materials. Therefore, transition metal phosphate attracted great attention in many fields such as an electrochemical supercapacitor, solar cell, Li-ion batteries, as catalysts, etc., because of their distinctive morphology, excellent mechanical and electrical properties.

To date, several efforts have been carried out to produce metal phosphate (transition metal phosphates) based electrodes for energy storage devices **[121]**. Moreover, transition metal phosphates are favorable electrode materials for supercapacitors, because of their rich redox behavior and open structure framework **[122]**. Generally, various types of monometallic phosphates are produced by different chemical methods for supercapacitor applications. However, recently researcher's attention has been focused on the production of bimetallic phosphates, such as Ni-Co phosphates, Co-Mn phosphates **[123, 124]**, which have given improved electrochemical performance compared to monometallic phosphates, due to synergy between different metal ions.

1.2 A Review of Literature:

Transition metal phosphate such as cobalt phosphate and manganese phosphate have been studied for supercapacitor applications because of good conductivity, redox behavior and open frame structure. In addition, the supercapacitor performance depends on the surface morphology of electrode material, also a potential window playing a vital role in increasing specific capacitance as well as the energy density of electrode material.

Hereafter, the earlier published different types of monometallic and bimetallic phosphate-based electrode materials are summarized, such as Wang et al. **[125]** prepared cobalt hydrogen phosphate nanosheets via a facile and eco-friendly, low-temperature hydrothermal method and achieved maximum specific capacitance of 411.2 F g^{-1} at a current density of 1 A g^{-1}. Marje et al. **[126]** synthesized nickel phosphate by CBD method and exhibited highest specific capacitance of 1031 F g^{-1} at 0.5 mA cm^{-2} current density. Furthermore, Xiao et al. **[127]** synthesized Co-Ni phosphate nanocages by metal-organic frameworks as a template. Due to the synergistic effect of Co and Ni species, prepared Co-Ni phosphate electrode showed a high specific capacitance of 1616 F g^{-1} at 1 A g^{-1} and excellent capacitance retention of 72.46 % after 2000 GCD cycles. Mirghni et al. **[128]** have been recently published a research paper on the preparation of $NiMn(PO_4)_2$/GF cubic rods by facile hydrothermal method and achieved a maximum specific capacity of 97 mAh g^{-1} at 0.5 A g^{-1}. Moreover, Mao et al. **[124]** successfully synthesized $Co_2Mn(PO_4)_2$ nanorods via a mild temperature method, which showed a specific capacitance of 525 F g^{-1} at 1.0 A g^{-1}. Also, Wang et al. **[129]** synthesized $Ba_xNi_{3-x}(PO_4)_2$ nanofibers and reported maximum specific capacitances of 1058 F g^{-1} at 0.5 A g^{-1}. In these reported works, compared to

monometallic phosphate, bimetallic phosphate-based electrode materials exhibited maximum specific capacitance, high cyclic stability, and better electrochemical performance, because of the synergy between different metal ions. **Table 1.3, 1.4, 1.5, 1.6 and 1.7** displays electrochemical properties (literature review) of cobalt phosphate, manganese phosphate, and cobalt manganese phosphate, respectively.

1.2.1 Literature Survey on Cobalt Phosphate:

Cobalt phosphate is the most important and attractive electrode material for supercapacitors due to its high specific capacitance, multiple oxidation states, natural abundance, non-toxic nature, and environmental compatibility **[51, 130]**. The structural parameters are important to optimize electrochemical performance of cobalt phosphate electrode. Cobalt phosphate thin films are used for supercapacitor applications, synthesized by various chemical methods, such as solvothermal **[131]**, hydrothermal **[132]**, chemical precipitation **[130]**, etc.

Theerthagiri et al. **[120]** synthesized hierarchical nanoflakes of $Co_3(PO_4)_2$ by simple co-precipitation method and reported a specific capacitance of 188 F g^{-1} at 3 Ag^{-1}. Also, Pang et al. **[122]** investigated the electrochemical supercapacitor properties of $K_2Co_3(P_2O_7)_2{\cdot}2H_2O$ nanocrystalline whiskers and obtained specific capacitance of 1100 mF cm^{-2} at a current density of 0.001 A cm^{-2}. Wang et al. **[125]** studied the capacitive performance of flowers-like $Co(H_2PO_4)_2$ electrodes prepared via a hydrothermal method. The $Co(H_2PO_4)_2$ exhibits a maximum capacitance of 411.2 F g^{-1} at 1 A g^{-1}. Pang et al. **[130]** successfully synthesized different morphologies from nano-microflowers/plates-like of $NH_4CoPO_4.H_2O$ via co-precipitation method and achieved specific capacitance of 369.4 F g^{-1} at 0.6 A g^{-1}. Xi et al. **[131]** synthesized $Co_3(PO_4)_2$ nanowires which shows a high specific

capacitance of 1174 F g^{-1} at 2 A g^{-1}. Recently, Sankar et al. **[132]** reported 15,687 mF cm^{-2} specific capacitance for $Co_3(PO_4)_2$ electrode synthesized via hydrothermal method. The flower-like morphology of $Co_3(PO_4)_2.8H_2O$ synthesized via green-precipitation method, which shows specific capacitance of 350 F g^{-1} at 1 A g^{-1} current density and better cycle life (102 % cyclic stability over 1000 cycles) **[133]**. Pang et al. **[134]** prepared the $CoHPO_4.3H_2O$ electrode and reported a specific capacitance of 413 F g^{-1} at 1.5 A g^{-1}. The $Co_3P_2O_8.8H_2O$ onto nickel foam substrate has been prepared via chemical precipitation method by Liu et al. **[135]** and demonstrated high cyclic stability (106 %) of the electrode. Li et al. **[136]** synthesized $Co_3P_2O_8.8H_2O$ nanoparticles by chemical co-precipitation method and electrochemical properties were tested. Cobalt phosphate hydrate nanoflakes were directly grown on nickel foam using a hydrothermal method and utilized as binder less electrode for high-performing supercapacitors (1578.7 F g^{-1} at 5 A g^{-1}) by Shao et al. **[137]**. The uniform ultralong nano-ribbons like $Co_{11}(HPO_3)_8(OH)_6$ architecture have been synthesized via hydrothermal method without any additive and reported specific capacitance of 321 F g^{-1} by Pang et al. **[138]**. Lee et al. **[139]** prepared dumbbell-shaped $Co_{11}(HPO_3)_8(OH)_6$ on Ni foam by a one-pot hydrothermal route and specific capacitance of 226 F g^{-1} at 1 A g^{-1} was obtained. Wang et al. **[140]** reported chemical precipitation of $NH_4CoPO_4.H_2O$ microflowers and it exhibits high cyclic durability of 99.4 % over 400 cycles. Cobalt phosphate ($Co_3(PO_4)_2$) material was successfully prepared using the hydrothermal method by Tang et al. **[141]** and reported a specific capacitance of 247.7 F g^{-1} at 0.25 A g^{-1}. Wang et al. **[142]** synthesized $NH_4CoPO_4.H_2O$ electrode by hydrothermal method and 662 F g^{-1} specific capacitance was achieved at 1.5 A g^{-1}. The cobalt phosphate nanoflakes were deposited onto nickel foam substrate by facile hydrothermal

method without using any surfactant and 410 F g^{-1} specific capacitance was achieved by Mao et al. **[143]**. The flake-like $Co_3(PO_4)_2.4H_2O$/GF was synthesized by a single-step hydrothermal process by Mirghni et al. **[144]** and reported a specific capacity of 39.8 mAh g^{-1} in 6 M KOH. The rod-shaped $Co_7(PO_4)_2(HPO_4)_4$ treated by N-Methyl-2-Pyrrolidone (NMP) on nickel foam was fabricated using an ultrasonic treatment route by Wang et al. **[145]** and obtained specific capacitance of 345 F g^{-1} at a current density of 1 A g^{-1}. Patil et al. **[146]** synthesized cobalt cyclotetraphosphate ($Co_2P_4O_{12}$) nanoparticles on carbon cloth substrate via solid-state sintering method. The achieved specific capacitance for cobalt cyclotetraphosphate is 437 F g^{-1} at 2.5 A g^{-1} current density. The preparation of Ni-doped $Co_{11}(HPO_3)_8(OH)_6$ nanowire arrays by Hydro(solvo)thermal method on nickel foam substrate and specific capacity of 159 mAh g^{-1} at 0.5 A g^{-1} current density was reported by Dan et al. **[147]**. Duraisamy et al. **[148]** obtained a specific capacitance of 203.4 C g^{-1} at 2 A g^{-1} for amorphous $Co_3(PO_4)_2$ anisotropic nano/micro rectangular architecture. Furthermore, Hou et al. **[149]** prepared the one-dimensional (1D) $Co_2P_2O_7$ using a temperature treatment method which gives specific capacitance of 483 F g^{-1} in 3 M KOH. Khan et al. **[150]** reported the synthesis of $Co_2P_2O_7$ on carbon paper by hydrothermal method and 580 F g^{-1} specific capacitance was achieved for the nanosheets structured surface. The nanoflakes like $Co_3(PO_4)_2$ synthesized by Shao et al. **[151]** for pseudocapacitor applications. It exhibits a specific capacitance of 1990 F g^{-1} at 5 mA. Moreover, Liang et al. **[152]** reported the synthesis of $KCoPO_4 \cdot H_2O$ electrode by hydrothermal method and achieved a specific capacitance of 229 F g^{-1}. Liu et al. **[153]** prepared $NaCoPO_4.H_2O$ by microwave-heated deposition method on nickel foam substrate and obtained a specific capacitance of 154.8 F g^{-1} at 1 A g^{-1}. Mahmoud et al. **[154]**

synthesized agglomerated grains of $Co_3(PO_4)_2$/GF by co-precipitation synthesis method. Tian et al. **[155]** synthesized $Co_{11}(HPO_3)_8(OH)_6$ flower-like microstructure on nickel foam substrate via a solvothermal method. The specific capacitance of 1532.2 F g^{-1} is obtained for $Co_{11}(HPO_3)_8(OH)_6$ at 1 A g^{-1} current density.

Moreover, a literature study of cobalt phosphate-based symmetric and asymmetric devices is summarized in **Table 1.4**, such as Pang et al. **[122]** manufactured solid-state micro-supercapacitors of $K_2Co_3(P_2O_7)_2{\cdot}2H_2O$//Graphene device and it exhibits specific capacitance of 6.0 F cm^{-3} at 10 mA cm^{-3} in PVA-KOH electrolyte. The cyclic stability of micro-supercapacitor device was 94.4 % over 5000 cycles. Xi et al. **[131]** manufactured $Co_3(PO_4)_2$//AC asymmetric device and obtained specific capacitance of 169.35 F g^{-1} at 2 A g^{-1} and also it exhibits superior cycling stability (85.8 % over 4000 cycles) with a little deterioration. Sankar et al. **[132]** fabricated $Co_3(PO_4)_2$//AC asymmetric device and achieved specific capacitance of 85 F g^{-1} at 1 A g^{-1} and energy (26.66 Wh kg^{-1}) and power (750 W kg^{-1}) density. Li et al. **[136]** assembled $Co_3P_2O_8.8H_2O$//AC asymmetric device and achieved a specific capacitance of 55 F g^{-1} at a current density of 0.5 A g^{-1}. Furthermore, the device offers high energy (11.9 Wh kg^{-1}) and power (3.59 kW kg^{-1}) density. Moreover, Shao et al. **[137]** fabricated $Co_3(PO_4)_2.8H_2O$//AC asymmetric device and it delivers a gravimetric capacitance of 111.2 F g^{-1} at 5 mA cm^{-2}. Wang et al. **[142]** assembled $NH_4CoPO_4.H_2O$//graphene asymmetric device and achieved energy and power density of 26.6 Wh kg^{-1} and 852 W kg^{-1}, respectively. Furthermore, Mao et al. **[143]** fabricated a flexible symmetric [$Co_3(PO_4)_2$//$Co_3(PO_4)_2$] device with PVA-KOH electrolyte and it exhibited a specific capacitance of 165 F g^{-1} at 0.5 A g^{-1} with cyclic stability of 96.1 % over 2000 cycles.

Also, Mirghni et al. **[144]** assembled $Co_3(PO_4)_2.4H_2O$/GF//C-FP hybrid asymmetric cell consist of $Co_3(PO_4)_2.4H_2O$ on graphene foam (GF) as positive and carbonized Fe adsorbed polyaniline (PANI) as a negative electrode. The $Co_3(PO_4)_2.4H_2O$/GF//C-FP hybrid device displayed excellent cycling stability of ~99 % with less distortion up to 10,000 cycles and energy density of 24 Wh kg^{-1} at a power density of 468 W kg^{-1} was achieved for device. Moreover, Wang et al. **[145]** fabricated $Co_7(PO_4)_2(HPO_4)_4$//AC asymmetric device and exhibited specific capacitance of 84.34 F g^{-1} at 0.5 A g^{-1} with better cycling stability of 93.08 % over 2500 cycles in 3 M KOH. Patil et al. **[146]** fabricated a $Co_2P_4O_{12}$//AC cell with an extended potential window (1.8 V). The reported specific capacitance of 156 F g^{-1} at 2.5 A g^{-1} and the cell deliver battery-level energy of 70 Wh kg^{-1} at 2300 W kg^{-1} power density. Dan et al. **[147]** fabricated Ni-doped $Co_{11}(HPO_3)_8(OH)_6$//AC asymmetrical supercapacitor and displays a specific capacity of 55 mAh g^{-1} at a current density of 0.5 A g^{-1} and good cycling stability of 90.5 % after 10,000 cycles. Duraisamy et al. **[148]** assembled supercapattery device combining $Co_3(PO_4)_2$ and activated carbon (AC) as a cathode and anode electrode, respectively and exhibited 174 C g^{-1} specific capacity at 0.4 A g^{-1} current density with specific energy (35.5 Wh kg^{-1}) and power (293.9 W kg^{-1}) density. Also, Shao et al. **[151]** developed a low cost and scalable prototype supercapattery of $Co_3(PO_4)_2$//AC and it delivers high energy (43.2 Wh kg^{-1}) and power density (5.8 W kg^{-1}) with excellent cyclic stability (68 % retention over 1,00,000 cycles). Mahmoud et al. **[154]** made an asymmetric device using $Co_3(PO_4)_2$/GF and biomass-derived activated carbon from pepper seed (ppAC) as a cathode and anode, respectively, which provided energy density of 52 Wh kg^{-1}. The $Co_3(PO_4)_2$/GF//ppAC asymmetric device exhibited capacity retention of 80 % over 10,000 cycles. Tian et al. **[155]** fabricated asymmetric

supercapacitor of $Co_{11}(HPO_3)_8(OH)_6$//AC and exhibits specific capacitance of 65.3 C g^{-1} at 1 A g^{-1}. The asymmetric device shows cycling stability of 83.5 % over 7800 cycles.

Electrochemical performance of cobalt phosphate-based single electrodes and symmetric as well as asymmetric devices with their specific capacitance, energy and power density, and the synthesis method are summarized in **Tables 1.3** and **1.4**. Also, some articles on cobalt phosphide-based single electrode materials and devices are summarized in **Tables 1.3** and **1.4**, respectively **[156-166]**. A literature survey indicates that, cobalt phosphate electrodes have low energy density than current battery technology. Hence, some extra efforts are needed to enhance the electrochemical performance of cobalt phosphate-based electrodes.

1.2.2 Literature Survey on Manganese Phosphate:

In recent years, manganese phosphate has got a significant technical and scientific importance, due to its electrochemical properties, such as long-term cyclic stability, energy density, and wide potential window, in energy storage devices **[167]**. Several deposition methods have been summarized for the preparation of manganese phosphate materials as an electrode for supercapacitors, such as hydrothermal method **[168]**, sol-gel technique **[169]**, electrodeposition **[170]**, solvothermal method **[171]**, chemical precipitation **[167]**, etc. Most of these studies focused on synthesis methods with the purpose of achieving enhanced specific capacitance and long-term cycling behavior. The electrochemical properties of manganese phosphate-based single electrodes and symmetric and asymmetric devices are summarized in **Tables 1.5 and 1.6.**

Dai et al. **[167]** synthesized $Mn_3(PO_4)_2 \cdot 3H_2O$ on Ni foam using co-precipitation method and it obtained a specific capacitance of 370 F g^{-1} at 0.5 A g^{-1}. Mirghni et al. **[168]** synthesized hexagonal micro-rods like $Mn_3(PO_4)_2$/GF by a facile hydrothermal method. This $Mn_3(PO_4)_2$/GF electrode displays specific capacitance of 270 F g^{-1} with excellent cyclic stability (99 % after 1000) retention. Priyadharsini et al. **[169]** obtained 516 F g^{-1} specific capacitance for $KMnPO_4.H_2O$ over SS substrate prepared by sol-gel method. Furthermore, Hao et al. **[170]** prepared PMn (phosphating manganese oxide) nanosheets array onto indium doped tin oxide (ITO) substrate by electrodeposition process exhibited specific capacitance of 6.7 mF cm^{-2} at 5 mV s^{-1} in 0.1 M Na_2SO_4. Xu et al. **[171]** prepared $LiMnPO_4$ nano-particles via PVP-assisted solvothermal process and obtained a specific capacitance of 217 C g^{-1} at 0.5 A g^{-1}. Moreover, Pang et al. **[172]** reported $NH_4MnPO_4.H_2O$ micro-nano structure via heat treatment and 35 F g^{-1} specific capacitance at a scan rate of 10 mV s^{-1}. Yan et al. **[173]** synthesized $MnPO_4.H_2O$/GO on Ni-foam using the hydrothermal method and obtained specific capacitance of 287.9 F g^{-1}. Ma et al. **[174]** reported long-term cycling (10,000 cycles) behavior with 91.1 % stable performance and highest specific capacitance (203 F g^{-1} at 0.5 A g^{-1}) for $Mn_3(PO_4)_2$ electrode. Also, Lee et al. **[175]** prepared $Mn_3(PO_4)_2$/PANI nanoparticles using the sonochemical method and specific capacitance of 347 C g^{-1} at 1 A g^{-1} discharge rate. Yang et al. **[176]** reported $Mn_3(PO_4)_2.3H_2O$/graphene synthesis by exfoliation precipitation based on the chemical reaction of ammonium phosphate with manganese chloride in an aqueous solution and reported 152 F g^{-1} specific capacitance. Also, it obtained energy and power density of 0.17 μWh cm^{-2} and 46 μW cm^{-2}, respectively. Raju et al. **[177]** prepared $NH_4MnPO_4.H_2O$ nanosheets by a microwave-assisted method and obtained capacitance of 423 F g^{-}

^{1} at scan rate of 5 mV s^{-1}. Also, cyclic stability after 10,000 cycles of electrode is 97 %. Moreover, Senthilkumar et al. **[178]** synthesized $NaMnPO_4$ microparticles over graphite sheet by solution combustion synthesis and reported specific capacitance of 163 F g^{-1} at 2 mA cm^{-2} current density. Sharmila et al. **[179]** prepared manganese phosphate by hydrothermal method on nickel foam substrate and reported a specific capacitance of 290 F g^{-1} in 0.5 V potential window. Also, it obtained energy and power density of 15 Wh kg^{-1} and 350 W kg^{-1}, respectively. Also, Raja et al. **[180]** prepared $NH_4MnPO_4.H_2O$-rGO clusters of flake slabs by a microwave-assisted method and obtained capacitance of 705 F g^{-1} at a current density of 1 A g^{-1}. Also, cycling stability over 5000 cycles of an electrode is 85 %. Recently, Zhang et al. **[181]** prepared $Mn(PO_3)_2$ ultrathin porous nanosheets on N, P doped graphene (NPG) framework by hydrothermal method. The $Mn(PO_3)_2$/NPG hybrid electrode delivers excellent specific capacitance of 2073.4 F g^{-1} at 1 A g^{-1} and good capacity retention of 92.9 % over 10,000 cycles.

Furthermore, a literature study of manganese phosphate-based symmetric and asymmetric devices are summarized, such as Dai et al. **[167]** assembled $Mn_3(PO_4)_2.3H_2O$//AC asymmetric cell consists of $Mn_3(PO_4)_2.3H_2O$ and activated carbon (AC) as a cathode and anode, respectively. The $Mn_3(PO_4)_2.3H_2O$//AC device showed better cycling stability of ~65.22 % with small degradation up to 2000 cycles. The energy density of 32.32 Wh kg^{-1} at a power density of 4250 W kg^{-1} was achieved for the device. Mirghni et al. **[168]** fabricated $Mn_3(PO_4)_2$/GF//AC asymmetric cell device within the potential window of 0.0-1.4 V and achieved a specific capacitance of 28 F g^{-1} at a current density of 0.5 A g^{-1} in 6 M KOH. The energy and power density of $Mn_3(PO_4)_2$/GF//AC device is 7.6 Wh kg^{-1} and 3528 W kg^{-1}, respectively. Xu et al. **[171]** assembled $LiMnPO_4$/rGO//rGO asymmetric

device and achieved excellent energy (16.46 Wh kg^{-1}) and power (0.38 kW kg^{-1}) density. The $LiMnPO_4$/rGO//rGO device maintains 91.2 % of initial capacity over 10,000 cycles and it displays high rate performance and long cycling stability. Moreover, Yan et al. **[173]** assembled $MnPO_4.H_2O$/GO//$MnPO_4.H_2O$/GO symmetric device. The reported specific capacitance of symmetric device is 115.63 F g^{-1} at 0.625 A g^{-1} current density. Furthermore, the device offers high energy (5.78 Wh kg^{-1}) and power density (150 kW kg^{-1}). Ma et al. **[174]** fabricated symmetric ($Mn_3(PO_4)_2$//$Mn_3(PO_4)_2$) and asymmetric ($Mn_3(PO_4)_2$//AC) devices exhibit specific capacitance of 53.7 F g^{-1} and 46.8 F g^{-1} respectively at 0.5 A g^{-1}, in 1 mol L^{-1} Na_2SO_4 electrolyte. Also, Lee et al. **[175]** manufactured $Mn_3(PO_4)_2$/PANI//AC and reported specific capacity of 73 C g^{-1} at 0.5 A g^{-1} with 80 % capacitive retention after 3000 charge-discharge cycles. Yang et al. **[176]** fabricated symmetric $Mn_3(PO_4)_2.3H_2O$/Graphene//$Mn_3(PO_4)_2.3H_2O$/Graphene device and displayed specific capacitance of 152 F g^{-1} (0.5 mV s^{-1}) in PVA-KOH solid polymer electrolyte with cyclic stability of 100 % over 2000 GCD cycles. Furthermore, Raju et al. **[177]** fabricated symmetric ($NH_4MnPO_4.H_2O$//$NH_4MnPO_4.H_2O$) and asymmetric ($NH_4MnPO_4.H_2O$//AC) devices having a voltage of 1.2 V and 1.8 V, respectively. The achieved specific capacitance for symmetric and asymmetric device is 48.4 F g^{-1} and 65.4 F g^{-1} (at 5 mV s^{-1} scan rate), respectively. Also, maximum energy and power density were achieved by symmetric (9.7 Wh kg^{-1}, 262 kW kg^{-1}) and asymmetric (29.4 Wh kg^{-1}, 133 kW kg^{-1}) devices. Also, Raja et al. **[180]** fabricated $NH_4MnPO_4.H_2O$/rGO//rGO asymmetric cell and reported 336 F g^{-1} specific capacitance at 1 A g^{-1}, the cell delivers maximum energy of 151 Wh kg^{-1} at 448 W kg^{-1} power density in 3 M H_2SO_4. Zhang et al. **[181]** fabricated an asymmetric hybrid device using $Mn(PO_3)_2$ as positive and MoO_2 as negative electrodes (on N, P

dual-doped graphene (NPG) framework), and revealed specific capacitance of 213.8 F g^{-1} at 0.8 A g^{-1} current density with high specific energy (96.2 Wh kg^{-1}) and power (726.7 W kg^{-1}) density.

1.2.3 Literature Survey on Cobalt Manganese Phosphate:

Nowadays, technology is dedicated to the development of emerging active materials for supercapacitors that meet specific requirements in terms of their capacitive efficiency. The design and fabrication of supercapacitor electrodes require high specific capacitance, high power density, wide potential window, and fast charging-discharging rate. Therefore, combining advantages of both metal phosphates (cobalt and manganese phosphate) is a very effective strategy to optimize each metal phosphate for improving their electrochemical performance. Accordingly, the cobalt manganese phosphate is the proper electrode material for construction of supercapacitors, since it has multiple redox sites, good electrolyte stability and better electron transport/diffusion, so it can give an excellent electrochemical performance. The reported electrochemical capacitive performance of cobalt manganese phosphates-based electrodes are summarized in **Table 1.7.**

Mao et al. **[124]** prepared cobalt manganese phosphate ($Co_2Mn(PO_4)_2$) on a nickel foam substrate by the mild chemical method. They exhibit significantly improved electrochemical performance (525 F g^{-1} at 1 A g^{-1}) and good capacitive retention (95.3 %) for supercapacitor application. Moreover, Chinnadurai et al. **[182]** reported a hydrothermal method for synthesis of $Mn_xCo_{3-x}(PO_4)_2{\cdot}8H_2O$ nanoflowers and it shows 979.9 F g^{-1} capacitance at a current density of 2 A g^{-1} in a 3 M KOH.

A literature study reveals that, only a few reports are available on cobalt phosphate, manganese phosphate, and cobalt manganese phosphate preparation by chemical methods. So, our aim is to prepare cobalt manganese phosphate using simple chemical methods, such as hydrothermal and successive ionic layer adsorption and reaction (SILAR). These are promising methods for the preparation of metal phosphate thin films over stainless steel substrate. Those methods are probably easiest, low cost, and suitable to prepare large-area, binder-free thin film electrodes for supercapacitor applications.

Table 1.3: Comparative literature survey of electrochemical capacitive performance of cobalt phosphate based electrodes.

Sr. No.	Material (Nano/Micro structure)	Sub-strate	Method of deposition	Electro-lyte	Capacitance at current density	Energy density	Power density	Cycles	Stability	Ref.
1.	$Co_3(PO_4)_2$ (Nanoflakes)	Carbon Paper	Co-precipitation	3 M KOH	188 F g^{-1} at 3 A g^{-1}	32.6 Wh kg^{-1}	420 W kg^{-1}	800	95 %	**120**
2.	$K_2Co_3(P_2O_7)_2 \cdot 2H_2O$ (Nanocrystal whiskers)	Nickel Foam	Hydrothermal	3 M KOH	1100 mF cm^{-2} at 1.0 mA cm^{-2}	--	--	--	--	**122**
3.	$Co(H_2PO_4)_2$ (Nanoflower)	Nickel Foam	Hydrothermal	2 M KOH	411.2 F g^{-1} at 1 A g^{-1}	--	--	10000	97.6 %	**125**
4.	$NH_4CoPO_4.H_2O$ (Nano/Microflowers/ plates)	Nickel Foam	Chemical precipitation	3 M KOH	369.4 F g^{-1} at 0.625 A g^{-1}	10.4 Wh kg^{-1}	1407 W kg^{-1}	400	99.7 %	**130**
5.	$Co_3(PO_4)_2$ (Nanowires)	Nickel Foam	Solvothermal	3 M KOH	1174 F g^{-1} at 2 A g^{-1}	--	--	4000	--	**131**
6.	$Co_3(PO_4)_2$ (Nanograss)	Nickel Foam	Hydrothermal	1 M KOH	15,687 mF cm^{-2} at 6 A g^{-1}	0.41 mWh cm^{-2}	1.065 mW cm^{-2}	6000	89 %	**132**
7.	$Co_3(PO_4)_2.8H_2O$ (Flower like)	Nickel Foam	Green-precipitate process	3 M KOH	350 F g^{-1} at 1 A g^{-1}	--	--	1000	102 %	**133**
8.	$CoHPO_4.3H_2O$ (Layered)	Nickel Foam	Hydrothermal	3 M KOH	413 F g^{-1} at 1.5 A g^{-1}	8.7 Wh kg^{-1}	3225 W kg^{-1}	3000	58.1 %	**134**
9.	$Co_3P_2O_8.8H_2O$ (Flakes)	Nickel Foam	Chemical precipitation	6 M KOH	205 F g^{-1} at 1 A g^{-1}	--	--	1000	106 %	**135**

10.	$Co_3P_2O_8.8H_2O$ (Nanoparticles)	Nickel Foam	Chemical precipitation	3 M KOH	446 F g^{-1} at 0.5 A g^{-1}	--	--	1000	100 %	**136**
11.	$Co_3(PO_4)_2.8H_2O$ (Nanoflakes)	Nickel Foam	Hydrothermal	1 M NaOH	1578.7 F g^{-1} at 5 A g^{-1}	--	--	1000	72.8 %	**137**
12.	$Co_{11}(HPO_3)_8(OH)_6$ (Nano-ribbons)	Nickel Foam	Hydrothermal	3 M KOH	321 F g^{-1} at 1.25 A g^{-1}	--	--	3000	89.4 %	**138**
13.	$Co_{11}(HPO_3)_8(OH)_6$ (Dumbbell like shape)	Nickel Foam	Hydrothermal	3 M KOH	226 F g^{-1} at 1 A g^{-1}	--	--	30	76 %	**139**
14.	$NH_4CoPO_4.H_2O$ (Microflowers)	Nickel Foam	Chemical precipitation	1 M KOH	525 F g^{-1} at 0.625 A g^{-1}	11.9 Wh kg^{-1}	1377 W kg^{-1}	400	99.4 %	**140**
15.	$Co_3(PO_4)_2$ (Mesoporous)	Nickel Foam	Hydrothermal	2 M KOH	247.7 F g^{-1} at 0.25 A g^{-1}	--	--	--	--	**141**
16.	$NH_4CoPO_4.H_2O$ (Microbundles)	Nickel Foam	Hydrothermal	3 M KOH	662 F g^{-1} at 1.5 A g^{-1}	26.6 Wh kg^{-1}	852 W kg^{-1}	3000	92.7 %	**142**
17.	$Co_3(PO_4)_2$ (Leaf like, Nanoflakes)	Nickel Foam	Hydrothermal	3 M KOH	410 F g^{-1} at 1 A g^{-1}	--	--	2000	96.1 %	**143**
18.	$Co_3(PO_4)_2.4H_2O$/GF (Flakes)	Nickel Foam	Hydrothermal	6 M KOH	39.8 mAh g^{-1} at 10 A g^{-1}	--	--	--	--	**144**
19.	$Co_7(PO_4)_2(HPO_4)_4$ /NMP (rod-shaped)	Nickel Foam	Ultrasonic treatment	3 M KOH	345 F g^{-1} at 1 A g^{-1}	--	--	2000	80.14 %	**145**
20.	$Co_2P_4O_{12}$ (Nanoparticles)	Carbon Cloth	Solid-state sintering	2 M KOH	437 F g^{-1} at 2.5 A g^{-1}	--	--	3000	90 %	**146**
21.	Ni-doped $Co_{11}(HPO_3)_8(OH)_6$ (nanowire arrays)	Nickel Foam	Hydro(solvo) thermal	2 M KOH	159 mAh g^{-1} at 0.5 A g^{-1}	--	--	8000	71.1 **%**	**147**

22.	$Co_3(PO_4)_2$ (Anisotropic nano/micro rectangular)	Nickel Foam	Sonochemical	1 M KOH	203.4 C g^{-1} at 2 A g^{-1}	--	--	--	--	**148**
23.	$Co_2P_2O_7$ (Nanorods)	Nickel Foam	Temperature treatment	3 M KOH	483 F g^{-1} at 1 A g^{-1}	--	--	3000	90 %	**149**
24.	$Co_2P_2O_7$ (Nanosheets)	Carbon paper	Hydrothermal	3 M KOH	580 F g^{-1} at 1 A g^{-1}	--	--	5000	96 %	**150**
25.	$Co_3(PO_4)_2$ (Nanoflakes/flower)	Nickel Foam	Hydrothermal	3 M KOH	1990 F g^{-1} at 5 mA	--	--	20000	80.4 %	**151**
26.	$KCoPO_4 \cdot H_2O$ (Plate-like)	Nickel Foam	Hydrothermal	1 M KOH	229 F g^{-1} at 1.5 A g^{-1}	--	--	100	123 %	**152**
27.	$NaCoPO_4.H_2O$ (Particles)	Nickel Foam	Microwave-heated	1 M KOH	154.8 F g^{-1} at 1 A g^{-1}	--	--	3000	95.5 %	**153**
28.	$Co_3(PO_4)_2$/GF (Agglomerated grains)	Nickel Foam	Co-precipitation	1 M KOH	57 mAh g^{-1} at 0.5 A g^{-1}	--	--	5000	89 %	**154**
29.	$Co_{11}(HPO_3)_8(OH)_6$ (Flower-like microstructure)	Nickel Foam	Solvothermal	2 M KOH	1532.2 F g^{-1} at 1 A g^{-1}	--	--	1000	64 %	**155**
30.	CoP (Nanowire arrays)	Carbon Cloth	Hydrothermal	1 M LiCl	571.3 mF cm^{-2} at 1 mA cm^{-2}	--	--	5000	82 %	**156**
31.	CoP (Nanotube arrays)	Carbon Cloth	Hydrothermal	6 M KOH	610 F g^{-1} at 1.0 A g^{-1}	--	--	10000	99 %	**157**
32.	Co_2P (Nanoshuttles)	Nickel Foam	Hydrothermal	6 M KOH	246 F g^{-1} at 1 A g^{-1}	--	--	1000	72 %	**158**
33.	Co_2P (Nanoflowers)	Nickel Foam	Thermal decomposition	6 M KOH	416 F g^{-1} at 1 A g^{-1}	--	--	--	--	**159**

34.	Co_2P (Nanoflowers)	Nickel Foam	Thermal decomposition	6 M KOH	412.7 F g^{-1} at 1 A g^{-1}	--	--	10000	124.7 %	**160**
35.	CoP (Nanosheets)	Nickel Foam	Solvothermal	6 M KOH	416 F g^{-1} at 2 A g^{-1}	--	--	900	97 %	**161**
36.	CoP (Microcubes)	Nickel Foam	Low-temperature	6 M KOH	560 F g^{-1} at 1 A g^{-1}	--	--	10000	91.2 %	**162**
37.	CoP (Nanoprism array)	Nickel Foam	Hydrothermal	6 mol L^{-1} KOH	1349 F g^{-1} at 1 A g^{-1}	--	--	5000	85 %	**163**
38.	CoP (Nanowires)	Stainless Steel Wire	Hydrothermal-oxidation-phosphidation	2 M KOH	558 F g^{-1} at 1 A g^{-1}	23.4 Wh Kg^{-1}	274.4 W Kg^{-1}	5000	98 %	**164**
39.	CoP (Nanoparticles)	Stainless Steel	Mechanical alloying	6 M KOH	447.5 F g^{-1} at 1 A g^{-1}	--	--	5000	84.3 %	**165**
40.	Mn-CoP (Nanowire decorated nanosheets cluster arrays)	Nickel Foam	Hydrothermal	6 M KOH	8.66 F cm^{-2} at 1 mA cm^{-2}	--	--	2000	82.1 %	**166**

Table 1.4: Literature survey of cobalt phosphate based symmetric and asymmetric devices.

Sr. No.	**Material (Nano/micro-structure)**	**Sub-strate**	**Electro-lyte**	**Capacitance at a current density**	**Energy density**	**Power density**	**Cycles**	**Stability**	**Ref.**
1.	$K_2Co_3(P_2O_7)_2{\cdot}2H_2O$ nanocrystalline whisker//Graphene nanosheets	Nickel Foam	PVA-KOH	6.0 F cm^{-3} at 10 mA cm^{-3}	0.96 mWh cm^{-3}	54.5 mW cm^{-3}	5000	94.4 %	**122**

2.	$Co_3(PO_4)_2$//AC (Nanowires)	Nickel Foam	3 M KOH	169.35 F g^{-1} at 2 A g^{-1}	--	--	4000	85.8 %	**131**
3.	$Co_3(PO_4)_2$//AC (Nanograss)	Nickel Foam	1 M KOH	85 F g^{-1} at 1 A g^{-1}	26.66 Wh kg^{-1}	750 W kg^{-1}	6000	80 %	**132**
4.	$Co_3P_2O_8$. $8H_2O$//AC (Nanoparticles)	Nickel Foam	3 M KOH	55 F g^{-1} at 0.5 A g^{-1}	11.9 Wh kg^{-1}	3.59 kW kg^{-1}	1000	--	**136**
5.	$Co_3(PO_4)_2.8H_2O$//AC (Nanoflakes)	Nickel Foam	1 M NaOH	111.2 F g^{-1} at 5 mA cm^{-2}	5.33 Wh kg^{-1}	4687 W kg^{-1}	--	--	**137**
6.	$NH_4CoPO_4.H_2O$//graphene (Microbundles//nanosheets)	Nickel Foam	3 M KOH	--	26.6 Wh kg^{-1}	852 W kg^{-1}	--	--	**142**
7.	$Co_3(PO_4)_2$ //$Co_3(PO_4)_2$ (Leaf like, Nanoflakes)	Nickel Foam	PVA-KOH	165 F g^{-1} at 0.5 A g^{-1}	52.8 Wh kg^{-1}	756 W kg^{-1}	2000	96.1 %	**143**
8.	$Co_3(PO_4)_2.4H_2O$/GF// C-FP	Nickel Foam	6 M KOH	24 mAh g^{-1} at 10 A g^{-1}	24 Wh kg^{-1}	468 W kg^{-1}	10000	99 %	**144**
9.	$Co_7(PO_4)_2(HPO_4)_4$ /NMP//AC (rod-shaped)	Nickel Foam	3 M KOH	84.34 F g^{-1} at 0.5 A g^{-1}	26.04 Wh kg^{-1}	372.75 W kg^{-1}	2500	93.08 %	**145**
10.	$Co_2P_4O_{12}$//AC (Nanospheres)	Carbon Cloth	KI-added KOH	156 F g^{-1} at 2.5 A g^{-1}	70 Wh kg^{-1}	2300 W kg^{-1}	5000	94 %	**146**
11.	Ni-doped $Co_{11}(HPO_3)_8(OH)_6$//AC (nanowire arrays)	Nickel Foam	2 M KOH	55 mAh g^{-1} at 0.5 A g^{-1}	58.7 Wh kg^{-1}	532 W kg^{-1}	10000	90.5 %	**147**
12.	$Co_3(PO_4)_2$//AC (Anisotropic nano/ micro rectangular)	Nickel Foam	1 M KOH	174 C g^{-1} at 0.4 A g^{-1}	35.5 Wh kg^{-1}	293.9 W kg^{-1}	3000	93 %	**148**

13.	$Co_3(PO_4)_2$//AC (Nanoflakes/Flower)	Nickel Foam	3 M KOH	107.7 F g^{-1} at 5 mA	43.2 Wh kg^{-1}	5.8 W kg^{-1}	100000	68 %	**151**
14.	$Co_3(PO_4)_2$/GF//ppAC (Agglomerated grains)	Nickel Foam	1 M KOH	--	52 Wh kg^{-1}	847 W kg^{-1}	10000	80 %	**154**
15.	$Co_{11}(HPO_3)_8(OH)_6$// AC (Flower-like microstructure)	Nickel Foam	2 M KOH	65.3 C g^{-1} at 1 A g^{-1}	14.5 Wh kg^{-1}	799.4 W kg^{-1}	7800	83.5 %	**155**
16.	CoP//MnO_2 (Nanowire arrays //nanowire)	Carbon Cloth	PVA-LiCl	1.94 F cm^{-3} at 1 mA cm^{-2}	0.69 mWh cm^{-3}	10.1 mW cm^{-3}	5000	82 %	**156**
17.	CoP//CoP (Nanowire arrays)		PVA-LiCl	35.4 mF cm^{-2} at 1 mA cm^{-2}	--	--	5000	87.05 %	
18.	Co(P,S)/CC//PCP/rGO (Nanowires)	Nickel Foam	6 M KOH	109.5 F g^{-1} at 1.0 A g^{-1}	39 Wh kg^{-1}	0.8 kW kg^{-1}	50000	86.4 %	**157**
19.	Co_2P//Graphene (Nanoflowers)	Nickel Foam	6 M KOH	76.8 F g^{-1} at 0.4 A g^{-1}	24 Wh kg^{-1}	300 W kg^{-1}	6000	97 %	**159**
20.	Co_2P//AC (Hollow nanoflowers)	Nickel Foam	6 M KOH	75.9 F g^{-1} at 1 A g^{-1}	30.5 Wh kg^{-1}	850 W kg^{-1}	10000	108 %	**160**
21.	CoP//N-doped graphene (Microcubes)	Nickel Foam	6 M KOH	68.8 F g^{-1} at 0.5 A g^{-1}	21.4 W h kg^{-1}	373 W kg^{-1}	6000	81.2 %	**162**
22.	CoP//CMK-3 (ordered mesoporous carbon) (Nanoprism array)	Nickel Foam	6 mol L^{-1} KOH	--	24 Wh kg^{-1}	325 W kg^{-1}	5000	93 %	**163**
23.	CoP (Nanoparticles)	Stainless Steel	6 M KOH	70 F g^{-1} at 0.5 A g^{-1}	19 Wh kg^{-1}	350.8 W kg^{-1}	5000	96.7 %	**165**

24.	Mn-CoP//AC (Nanowire decorated nanosheet cluster arrays)	Nickel Foam	6 M KOH	98.9 F g^{-1} at 5 mA cm^{-2}	35.21 Wh kg^{-1}	193 W kg^{-1}	4000	88.9%	**166**

Table 1.5: Comparative literature survey of electrochemical capacitive performance of manganese phosphate based electrodes.

Sr. No.	**Material (Nano/micro-structure)**	**Sub-strate**	**Method of deposition**	**Electro-lyte**	**Capacitance at current density/ scan rate**	**Energy density**	**Power density**	**cycles**	**stability**	**Ref.**
1.	$Mn_3(PO_4)_2{\cdot}3H_2O$ (Nanosheets)	Nickel Foam	Chemical precipitation	2 M KOH	370 F g^{-1} at 0.5 A g^{-1}	--	--	2000	74 %	**167**
2.	$Mn_3(PO_4)_2$/GF (Hexagonal Micro-rods)	Nickel Foam	Hydrothermal	6 M KOH	270 F g^{-1} at 0.5 A g^{-1}	--	--	1000	99 %	**168**
3.	$KMnPO_4.H_2O$ (Submicron sized particles)	Stainless Steel	Sol-Gel method	1 M KOH	516 F g^{-1} at 2 mV s^{-1}	--	--	1000	82 %	**169**
4.	PMn (Nanosheets array)	ITO	Electro-deposition	0.1 M Na_2SO_4	6.7 mF cm^{-2} at 5 mV s^{-1}	--	--	5000	87.6 %	**170**
5.	$LiMnPO_4$ (Nanoparticles)	Nickel Foam	Solvothermal	1 M LiOH	217 C g^{-1} at 0.5 A g^{-1}	--	--	--	--	**171**
6.	$NH_4MnPO_4.H_2O$ (Micro-Nano Structure)	Nickel Grid	Heat Treatment	1 mol L^{-1} Na_2SO_4	35 F g^{-1} at 10 mV s^{-1}	--	--	--	--	**172**

7.	$MnPO_4.H_2O$/GO (Nanowires)	Nickel Foam	Hydrothermal	3 M KOH	287.9 F g^{-1} at 0.625 Ag^{-1}	--	--	--	--	**173**
8.	$Mn_3(PO_4)_2$ (Nanosheets)	Nickel Foam	Hydrothermal	1 mol L^{-1} Na_2SO_4	203 F g^{-1} at 0.5 A g^{-1}	--	--	10000	91.1 %	**174**
9.	$Mn_3(PO_4)_2$/PANI (Nanoparticle)	Nickel Foam	Sonochemical method	1 M KOH	347 C g^{-1} at 1 A g^{-1}	--	--	3000	60 %	**175**
10.	$Mn_3(PO_4)_2.3H_2O$ /Graphene (Nanosheets)	Nickel Foam	Exfoliation Precipitation	6 M KOH	152 F g^{-1} at 0.5 A g^{-1}	0.17 µWh cm^{-2}	46 µW cm^{-2}	2000	100 %	**176**
11.	$NH_4MnPO_4.H_2O$ (Nanosheets)	Nickel Foam	Microwave assisted	3 M KOH	423 F g^{-1} at 5 mV s^{-1}	--	--	10000	97 %	**177**
12.	$NaMnPO_4$ (Microparticles)	Graphite Sheet	Solution combustion synthesis	1 M NaOH	163 F g^{-1} at 2 mA cm^{-2}	--	--	1000	93 %	**178**
13.	$MnPO_4 \cdot H_2O$ (Nanosheets)	Nickel Foam	Hydrothermal	0.2 M KOH	290 F g^{-1} at 2 A g^{-1}	15 Wh kg^{-1}	350 W kg^{-1}	5000	93.3 %	**179**
14.	$NH_4MnPO_4.H_2O$–rGO (Clusters of flake slabs)	Graphite	Microwave route	2 M H_2SO_4	705 F g^{-1} at 1 A g^{-1}	--	--	5000	85 %	**180**
15.	$Mn(PO_3)_2$ (Ultrathin porous nanosheets)	N, P dual-doped Graphene (NPG)	Hydrothermal	6 M KOH	2073.4 F g^{-1} at 1 A g^{-1}	--	--	10000	92.9 %	**181**

Table 1.6: Comparative literature survey of manganese phosphate based symmetric/asymmetric device.

Sr. No.	Material (Nano/micro-structure)	Substrate	Electro-lyte	Capacitance at a current density/scan rate	Energy density	Power density	cycles	stability	Ref.
1.	$Mn_3(PO_4)_2.3H_2O$//AC (Nanosheets)	Nickel Foam	2 M KOH	--	32.32 Wh kg^{-1}	4250 W kg^{-1}	2000	65.22 %	**167**
2.	$Mn_3(PO_4)_2$/GF//AC (Hexagonal Micro-rods)	Nickel Foam	6 M KOH	28 F g^{-1} at 0.5 A g^{-1}	7.6 Wh kg^{-1}	3528 W kg^{-1}	10000	96 %	**168**
3.	$LiMnPO_4$/rGO//rGO (Nanoparticles)	Nickel Foam	1 M LiOH	79 C g^{-1} at 0.5 A g^{-1}	16.46 Wh kg^{-1}	0.38 kW kg^{-1}	10000	91.2 %	**171**
4.	$MnPO_4.H_2O$/GO// $MnPO_4.H_2O$/GO (Nanowires)	Nickel Foam	3 M KOH	115.63 F g^{-1} at 0.625 A g^{-1}	5.78 Wh kg^{-1}	150 kW kg^{-1}	1000	85.3 %	**173**
5.	$Mn_3(PO_4)_2$//AC (Nanosheets)	Nickel Foam	1 mol L^{-1} Na_2SO_4	46.8 F g^{-1} at 0.5 A g^{-1}	16.64 Wh kg^{-1}	7984.48 W kg^{-1}	10000	90 %	**174**
6.	$Mn_3(PO_4)_2$//$Mn_3(PO_4)_2$		1 mol L^{-1} Na_2SO_4	53.7 F g^{-1} at 0.5 A g^{-1}	19.09 Wh kg^{-1}	8033 W kg^{-1}	10000	90 %	
7.	$Mn_3(PO_4)_2$/PANI//AC (Nanoparticle)	Nickel Foam	1 M KOH	73 C g^{-1} at 0.5 A g^{-1}	14.7 Wh kg^{-1}	2988 W kg^{-1}	3000	80 %	**175**
8.	$Mn_3(PO_4)_2.3H_2O$/Graphene//$Mn_3(PO_4)_2.3H_2O$/ Graphene (Nanosheets)	Nickel Foam	PVA-KOH	152 F g^{-1} at 0.5 mV s^{-1}	35.5 Wh kg^{-1}	365 W kg^{-1}	2000	100 %	**176**
9.	$NH_4MnPO_4.H_2O$// NH4$MnPO_4.H_2O$ (Nanosheets)	Nickel Foam	3 M KOH	65 F g^{-1} at 5 mV s^{-1}	9.7 Wh kg^{-1}	262 kW kg^{-1}	10000	98 %	**177**

10.	$NH_4MnPO_4.H_2O$//AC (Nanosheets)		PVA-KOH	48.4 F g^{-1} at 5 mV s^{-1}	29.4 Wh kg^{-1}	133 kW kg^{-1}	100000	93 %	
11.	$NH_4MnPO_4.H_2O$/rGO//rGO (Clusters of flake slabs)	Graphite	3 M H_2SO_4	336 F g^{-1} at 1 A g^{-1}	151 Wh kg^{-1}	448 W kg^{-1}	5000	80 %	**180**
12.	$Mn(PO_3)_2$/NPG-2// MoO_2/NPG (Ultrathin Porous nanosheets //nanocrystal array)	N, P dual-doped graphene (NPG)	6 M KOH	213.8 F g^{-1} at 0.8 A g^{-1}	96.2 Wh kg^{-1}	726.7 W kg^{-1}	10000	91.52 %	**181**

Table 1.7: Comparative literature survey of electrochemical capacitive performance of cobalt manganese phosphate based electrodes.

Sr. No.	Material (Nano/micro-structure)	Sub-strate	Method of deposition	Electro-lyte	Capacitance at current density	Energy density	Power density	Cycles	Stability	Ref.
1.	$Co_2Mn(PO_4)_2$ (Nanorods)	Nickel Foam	Mild chemical method	3 M KOH	525 F g^{-1} at 1 A g^{-1}	--	--	5000	95.3 %	**124**
2.	$Mn_xCo_{3-x}(PO_4)_2 \cdot 8H_2O$ (Nanoflowers)	Nickel Foam	Hydrothermal	3 M KOH	979.91 F g^{-1} at 2 A g^{-1}	--	--	--	--	**182**

1.3 Orientation and Purpose of the Dissertation:

Modern investigation on supercapacitor provides an idea about advanced energy storage devices, which are utilized in hybrid electric vehicles, portable electronic devices, laptops, and power backup, etc. Therefore, supercapacitors have been considered to be a widespread alternative to batteries. Supercapacitors offer many potential benefits to their efficiency, including higher energy as well as power density, better lifetime, and faster charge-discharge rates. Moreover, a comparatively quick response is necessary for supercapacitor to deliver pulse power, which can be achieved by lowering equivalent series resistance (ESR). Therefore, the design and development of active electrode materials to satisfying the above requirements become an interesting aspect for many electrochemists.

The trend of recent research is focused on producing binary metal phosphate materials to achieve superior electrochemical efficiency with a high value of energy and power density. Binary metal phosphate-based supercapacitors are an important incoming class of electrochemical capacitors, likely to deliver high energy density at high charging-discharging rates. Improvements in the operating potential window, specific capacitance and energy density of binary metal phosphate-based electrodes significantly increase the overall electrochemical efficiency of the supercapacitor. In addition, the lack of one active (cobalt) material can be accomplished by another active (manganese) material, and synergy between both (cobalt manganese phosphate) materials can result in increased electrochemical performance. The cobalt and manganese with their multiple oxidation states and high electrical conductivity help to increase working potential window, capacitance and thereby energy and power density of supercapacitor devices containing aqueous or neutral electrolytes. In preparation of such

electrode materials, a simple, inexpensive and convenient chemical way to maintain the cost of supercapacitor cells is important. Among various other deposition methods, hydrothermal and SILAR have many advantages. Chemical methods produce pinhole-free, well adherent and uniformly deposited thin films. The nucleation and growth in chemical systems play an important part in the formation of nanocrystalline materials. Also, these methods are generally used for large area deposition, which is beneficial for device fabrication.

The literature study clarifies that, a new class of cobalt manganese phosphate based electrode materials can be synthesized and asymmetric devices can be fabricated using flexible SS substrates and polymer gel electrolytes. Metal phosphates (cobalt phosphate, manganese phosphate, cobalt manganese phosphate) with various types of morphologies could be prepared by simple chemical methods and utilized as electrode materials in supercapacitors. The purpose behind construction of asymmetric supercapacitors is to test the practicability of active electrode material at device level. Our prior aim is that, synthesis of cobalt manganese phosphate thin films by simple chemical methods and characterize these thin films with various physico-chemical characterization techniques. The preparative parameters like pH, concentration, temperature of solution, and deposition time are optimized. The simple chemical methods (Hydrothermal and SILAR) can provide binder-free and additive-less thin film electrodes by improving the interfacial contact of active material and stainless steel (SS) substrates. Also, corrosion and oxidation of metallic substrates can be restricted using low temperature deposition methods.

Furthermore, well adherent and uniform cobalt manganese phosphate thin films are evaluated for phase analysis, structural interpretation, compositional

analysis, surface, and microstructural analysis. The X-ray diffraction (XRD) technique was utilized for phase confirmation of material and chemical bonding in prepared material was studied by fourier transform infrared spectroscopy analysis (FTIR). The morphological evaluation of thin film material was carried out using field emission scanning electron microscopy (FE-SEM) technique. The energy-dispersive X-ray spectroscopy (EDS) technique is used for confirmation of elemental composition. The X-ray photoelectron spectroscopy (XPS) technique is employed for the identification of oxidation states, chemical composition, and confirmation of material formation. The electrochemical capacitive performances of the electrodes are investigated by cyclic voltammetry (CV), galvanostatic charge-discharge measurement (GCD), and electrochemical impedance spectroscopy (EIS) using an electrochemical workstation. The supercapacitive performance of cobalt manganese phosphate thin film electrodes and asymmetric device is evaluated with different electrochemical parameters such as potential window, specific capacitance, specific power, specific energy, and cycle stability.

1.4 References:

1. A. Du, Pasquier, I. Plitz, J. Gural, S. Menocal, G. Amatucci, J. Power Sources, 113, (2003), 62-71.
2. J. Tao, N. Liu, W. Ma, L. Ding, L. Li, J. Su, Y. Gao, Sci. Rep., 3, (2013), 1-7.
3. J. H. Kim, K. H. Lee, L. J. Overzet, G. S. Lee, Nano Lett., 11, (2011), 2611-2617.
4. Y. Zhu, J. Li, J. Liu, J. Power Sources, 351, (2017), 17-25.
5. Z. Zhang, X. Zhang, W. Chen, Y. Rasim, W. Salman, H. Pan, Y. Yuan, C. Wang, Appl. Energy, 178, (2016), 177-188.
6. H. Jiang, P. S. Lee, C. Li, Energy Environ. Sci., 6, (2013), 41-53.
7. L. L. Zhang, Y. Gu, X. S. Zhao, J. Mater. Chem. A, 1, (2013), 9395-9408.
8. S. Maiti, A. Pramanik, S. Chattopadhyay, G. De, S. Mahanty, J. Colloid Interf. Sci., 464, (2016), 73-82.
9. D. G. Gromadskyi, J. H. Chae, S. A. Norman, G. Z. Chen, Appl. Energy, 159, (2015), 39-50.
10. H. Jung, H. Wang, T. Hu, J. Power Sources, 267, (2014), 566-575.
11. H. Shao, Nanostructure materials based supercapattery for next generation pacemaker. PhD Thesis, University College Cork (2018).
12. C. Zhou, Y. Zhang, Y. Li, J. Liu, Nano Lett., 13, (2013), 2078-2085.
13. W. Lu, R. Hartman, L. Qu, L. Dai, J. Phys. Chem. Lett., 2, (2011), 655-660.
14. A. Burke, J. Power Sources, 91, (2000), 37-50.
15. B. E. Conway, "Electrochemical supercapacitors: scientific fundamentals and technological applications", Kluwer–Plenum, New York (1999)
16. P. Simon and Y. Gogotsi, Nat. Mater., 7, (2008), 845–854.
17. J. Xu, D. Zhang, Electrochim. Acta, 224, (2017), 105-112.
18. D. Xu, C. Mu, J. Xiang, F. Wen, C. Su, C. Hao, W. Hu, Y. Tang, Z. Liu, Electrochim. Acta, 220, (2016), 322-330.
19. M. V. Kiamahalleh, S. H. S. Zein, G. Najafpour, S. A. Sata, S. Buniran, Nano, 7, (2012), 1-27.
20. M. Hashemi, M. S. Rahmanifar, M. F. El-Kady, A. Noori, M. F. Mousavi, R. B. Kaner, Nano Energy, 44, (2018), 489-498.
21. T. C. Mendes, F. Zhou, A. J. Barlow, M. Forsyth, P. C. Howlett, D. R. MacFarlane, Sustain. Energy Fuels, 2, (2018), 763-771.

22. A. G. Pandolfo, A. F. Hollenkamp, J. Power Sources, 157, (2006), 11–27.
23. L. Ren, G. Zhang, J. Lei, Y. Wang, D. Hu, J. Colloid Interf. Sci., 512, (2018), 300-307.
24. P. J. Hall, M. Mirzaeian, S. I. Fletcher, F. B. Sillars, A. J. R. Rennie, G. O. Shitta-Bey, G. Wilson, A. Cruden, R. Carter, Energy Environ. Sci., 3, (2010), 1238-1251.
25. A. K. Shukla, S. Sampath, K. Vijayamohanan, Curr. Sci., 79, (2000), 1656-1661.
26. H. D. Abruña, Y. Kiya, J. C. Henderson, Phys. Today, 61, (2008), 43-47.
27. J. R. Miller, A. F. Burke, Electrochem. Soc. Interface, 17, (2008), 53-57.
28. M. Jayalakshmi, K. Balasubramanian, Int. J. Electrochem. Sci., 4, (2009), 878-886.
29. H. I. Becker, Low voltage electrolytic capacitors. U.S., Patent 2800616 (1957).
30. R. A. Rightmire, Electrical energy storage apparatus. U.S., Patent 3288641 (1966).
31. S. Hadz¯i-Jordanov, H. Angerstein-Kozlowska, M. Vukovič, B. E. Conway, J. Electrochem. Soc., 125, (1978), 1471.
32. S. Trasatti, G. Buzzanca, J. Electroanal. Chem. Interf. Electrochem., 29, (1971), A1-A5.
33. D. Galizzioli, F. Tantardini, S. Trasatti, J. Appl. Electrochem., 5, (1975), 203–214.
34. C. C. Hu, K. H. Chang, M. C. Lin, Y. T. Wu, Nano Lett., 6, (2006), 2690–2695.
35. A. Yoshida, K. Imoto, H. Yoneda, A. Nishimo, IEEE Transactions on Components, Hybrids, and Manufacturing Technology, 15, (1992), 133-138.
36. http://services.eng.uts.edu.au/cempe/subjects_JGZ/eet/SuperCap_1_11_05.pdf, J. G. Zhu, (2012) Supercapacitors.
37. G. L. Bullard, H. B. Sierra-Alcazar, H. L. Lee, J. L. Morris, IEEE Transactions on Magnetics, 25, (1989), 102-106.
38. https://www.ttiinc.com/content/ttiinc/en/resources/marketeye/categories/passives/me-zogbi-20130403.html, D. M. Zogbi, Supercapacitors the Myth, the Potential and the Reality.
39. M. Y. Ho, Transition metal oxide and phosphate-based/carbon composites as supercapacitor electrodes. PhD thesis, University of Nottingham (2017).

40. S. Huang, X. Zhu, S. Sarkar, Y. Zhao, APL Mater., 7, (2019), 1-9.
41. A. Davies, A. Yu, Can J. Chem. Eng., 89, (2011), 1342-1357.
42. J. Ledge, "Saft and ESMA to cooperate on supercapacitor development, production and commercialisation," Saft Press Release (2009).
43. S. I. Kim, S. W. Kim, K. Jung, J. B. Kim, J. H. Jang, Nano Energy, 24, (2016), 17-24.
44. A. Castaings, W. Lhomme, R. Trigui, A. Bouscayrol, Appl. Energy, 163, (2016), 190-200.
45. L. L. Zhang, X. S. Zhao, Chem. Soc. Rev., 38, (2009), 2520-2531.
46. C. D. Lokhande, D. P. Dubal, O. S. Joo, Curr. Appl. Phys., 11, (2011), 255-270.
47. H. Pang, X. Li, Q. Zhao, H. Xue, W. Y. Lai, Z. Hu, W. Huang, Nano Energy, 35, (2017), 138-145.
48. L. Miao, H. Duan, M. Liu, W. Lu, D. Zhu, T. Chen, L. Li, L. Gan, Chem. Eng., 317, (2017), 651-659.
49. C. Guan, X. Qian, X. Wang, Y. Cao, Q. Zhang, A. Li, J. Wang, Nanotechnology, 26, (2015), 1-7.
50. D. P. Dubal, O. Ayyad, V. Ruiz, P. Gómez-Romero, Chem. Soc. Rev., 44, (2015), 1777–1790.
51. P. K. Katkar, S. J. Marje, S. S. Pujari, S. A. Khalate, A. C. Lokhande, U. M. Patil, ACS Sustain. Chem. Eng., 7, (2019), 11205-11218.
52. T. Chen, L. Dai, Mater. Today, 16, (2013), 272-280.
53. W. Wang S. Wu, Appl. Surf. Sci., 396, (2017), 1360-1367.
54. X. Li, Y. Zhao, Y. Bai, X. Zhao, R. Wang, Y. Huang, Q. Liang, Z. Huang, Electrochim. Acta, 230, (2017), 445-453.
55. Y. Wang, Y. Song, Y. Xia, Chem. Soc. Rev., 45, (2016), 5925-5950.
56. B. Zhang, W. Li, J. Sun, G. He, R. Zou, J. Hu, Z. Chen, Mater. Lett., 114, (2014), 40-43.
57. W. Li, G. He, J. Shao, Q. Liu, K. Xu, J. Hu, I. P. Parkin, Electrochim. Acta, 186, (2015), 1–6.
58. A. Xie, F. Tao, C. Jiang, W. Sun, Y. Li, L. Hu, X. Du, S. Luo, C. Yao, J. Electroanal. Chem., 789, (2017), 29-37.
59. Y. Li, X. Wang, Q. Yang, M. S. Javed, Q. Liu, W. Xu, C. Hu, D. Wei, Electrochim. Acta, 234, (2017), 63-70.

60. M. G. Hosseini, E. Shahryari, J. Colloid Interf. Sci., 496, (2017), 371-381.
61. M. Gopalakrishnan, G. Srikesh, A. Mohan, V. Arivazhagan, Appl. Surf. Sci., 403, (2017), 578-583.
62. H. Ji, X. Zhao, Z. Qiao, J. Jung, Y. Zhu, Y. Lu, L. L. Zhang, A. H. MacDonald, R. S. Ruoff, Nat. Comm., 5, (2014).
63. B. K. Kim, S. Sy, A. Yu, J. Zhang, Handbook of Clean Energy Systems, (2015), 1–25.
64. M Jayalakshmi, K Balasubramanian, Int. J. Electrochem. Sci., 3, (2008), 1196–1217.
65. V. Dodevski, B. Janković, M. Stojmenović, S. Krstić, J. Popović, M. C. Pagnacco, M. Popović, S. Pašalić, Colloid Surf. A, 522, (2017), 83-96.
66. E. Raymundo-Piñero, F. Leroux, F. Béguin, Adv. Mater., 18, (2006), 1877-1882.
67. C. Xiong, T. Li, T. Zhao, A. Dang, H. Li, X. Ji, W. Jin, S. Jiao, Y. Shang, Y. Zhang, Compos. B. Eng., 116, (2017), 7-15.
68. W. Liu, Y. Tang, Z. Sun, S. Gao, J. Ma, L. Liu, Carbon, 115, (2017), 754-762.
69. K. Jurewicz, S. Delpeux, V. Bertagna, F. Béguin, E. Frackowiak, Chem. Phys. Lett., 347, (2001), 36-40.
70. K. S. Novoselov, Science, 306, (2004), 666–669.
71. K. S. Kim, Y. Zhao, H. Jang, S. Y. Lee, J. M. Kim, K. S. Kim, J. H. Ahn, P. Kim, J. Y. Choi, B. H. Hong, Nature, 457, (2009), 706–710.
72. K. V. Emtsev, A. Bostwick, K. Horn, J. Jobst, G. L. Kellogg, L. Ley, J. L. McChesney, T. Ohta, S. A. Reshanov, J. Röhrl, E. Rotenberg, A. K. Schmid, D. Waldmann, H. B. Weber, T. Seyller, Nature Mater., 8, (2009), 203–207.
73. W. S. Hummers, R. E. Offeman, J. Am. Chem. Soc., 80, (1958), 1339–1339.
74. N. I. Kovtyukhova, P. J. Ollivier, B. R. Martin, T. E. Mallouk, S. A. Chizhik, E. V. Buzaneva, A. D. Gorchinskiy, Chem. Mater., 11, (1999), 771-778.
75. A. Buchsteiner, A. Lerf, J. Pieper, J. Phys. Chem. B, 110, (2006), 22328-22338.
76. J. I. Paredes, S. V. Rodil, A. M. Alonso, J. M. D. Tascón, Langmuir, 24, (2008), 10560–10564.
77. M. D. Stoller, S. Park, Y. Zhu, J. An, R. S. Ruoff, Nano Lett., 8, (2008), 3498–3502.

78. S. Ghosh, T. Mathews, B. Gupta, A. Das, N. G. Krishna, M. Kamruddin, Nano-Struct. Nano-Objects, 10, (2017), 42–50.
79. S. R. C. Vivekchand, C. S. Rout, K. S. Subrahmanyam, A. Govindaraj, C. N. R. Rao, J. Chem. Sci., 120, (2008), 9–13.
80. C. Liu, Z. Yu, D. Neff, A. Zhamu, B. Z. Jang, Nano Lett., 10, (2010), 4863–4868.
81. I. Jung, D. A. Dikin, R. D. Piner, R. S. Ruoff, Nano Lett., 8, (2008), 4283–4287.
82. Y. Zhu, S. Murali, W. Cai, X. Li, J. W. Suk, J. R. Potts, R. S. Ruoff, Adv. Mater., 22, (2010), 3906–3924.
83. L. L. Zhang, R. Zhoua, X. S. Zhao, J. Mater. Chem., 20, (2010), 5983-5992.
84. C. Yin, C. Tao, F. Cai, C. Song, H. Gong, J. Wang, Carbon, 109, (2016), 558-565.
85. N. Ahmed, A. Amer, B. A. Ali, A. H. Biby, Y. I. Mesbah, N. K. Allam, SM&T, 25, (2020), 1-9.
86. H. Xian, T. Peng, H. Sun, J. Wang, Nano-Micro Lett., 7, (2015), 17–26.
87. X. Chen, R. Paul, L. Dai, Natl. Sci. Rev., 4, (2017), 453-489.
88. Z. Wen, W. She, Y. Li, R. Che, J. Mater. Chem. A, 2, (2014), 20729-20738.
89. L. L. Xing, K. J. Huang, L. X. Fang, Dalton Trans., 45, (2016), 17439-17446.
90. J. Xu, T. Xiao, X. Tan, P. Xiang, L. Jiang, D. Wu, J. Li, S. Wang, J. Alloys Compd., 706, (2017), 351-357.
91. W. Chen, R. B. Rakhi, H. N. Alshareef, Nanoscale, 5, (2013), 4134-4138.
92. S. Lyu, H. Chang, F. Fu, L. Hu, J. Huang, S. Wang, J. Power Sources, 327, (2016), 438-446.
93. V. Augustyn, P. Simon, B. Dunn, Energy Environ. Sci., 7, (2014), 1597-1614.
94. J. S. Shayeh, M. Sadeghinia, S. O. R. Siadat, A. Ehsani, M. Rezaei, M. Omidi, J. Colloid Interf Sci., 496, (2017), 401-406.
95. D. Aradilla, F. Estrany, C. Alemán, J. Phys. Chem. C, 115, (2011), 8430-8438.
96. Y. Huang, M. Zhu, Z. Pei, Y. Huang, H. Geng, C. Zhi, ACS Appl. Mater. Interfaces, 8, (2016), 2435-2440.
97. G. A. Snook, P. Kao, A. S. Best, J. Power Sources, 196, (2011), 1–12.
98. S. R. Sivakkumar, D.-W. Kim, J. Electrochem. Soc., 154, (2007), A134-A139.
99. P. R. Deshmukh, S. N. Pusawale, V. S. Jamadade, U. M. Patil, C. D. Lokhande, J. Alloys Compd., 509, (2011), 5064-5069.
100. B. M. Hryniewicz, R. V. Lima, F. Wolfart, M. Vidotti, Electrochim. Acta, 293, (2019), 447-457.

101. B. H. Patil, S. J. Patil, C. D. Lokhande, Electroanalysis, 26, (2014), 2023-2032.
102. H. Zhou, Y. Zhong, Z. He, L. Zhang, J. Wang, J. Zhang, C. Cao, J. Alloys Compd., 597, (2014), 1-7.
103. U. M. Patil, S. B. Kulkarni, V. S. Jamadade, C. D. Lokhande, J. Alloys Compd., 509, (2011), 1677-1682.
104. V. J. Mane, D. B. Malavekar, S. B. Ubale, V. C. Lokhande, C. D. Lokhande, Inorg. Chem. Commun., 115, (2020), 1-17.
105. P. M. Kulal, D. P. Dubal, C. D. Lokhande, V. J. Fulari, J. Alloys Compd., 509, (2011), 2567-2571.
106. A. D. Jagadale, V. S. Kumbhar, R. N. Bulakhe, C. D. Lokhande, Energy J., 64, (2014), 234-241.
107. U. M. Patil R. R. Salunkhe, K. V. Gurav, C. D. Lokhande, Appl. Surf. Sci., 255, (2008), 2603-2607.
108. S. Jeon, J. H. Jeong, H. Yoo, H. K. Yu, B. H. Kim, M. H. Kim, ACS Appl. Nano Mater., 3, (2020), 3847–3858.
109. B. Y. Fugare, B. J. Lokhande, Mater. Sci. Semicond. Process., 71, (2017), 121-127.
110. X. Zhao, L. Zhang, S. Murali, M. D. Stoller, Q. Zhang, Y. Zhu, R. S. Ruoff, ACS Nano, 6, (2012), 5404-5412.
111. C. T. Hsieh, W. Y. Lee, C. E. Lee, H. Teng, J. Phys. Chem. C, 118, (2014), 15146-15153.
112. T. L. Chen, Y. A. Elabd, Electrochim. Acta, 229, (2017), 65-72.
113. T. Nguyen, M. Boudard, M. J. Carmezim, M. F. Montemor, Energy J., 126, (2017), 208–216.
114. W. Shaheen, M. F. Warsi, M. Shahid, M. A. Khan, M. Asgharb, Z. Ali, M. Sarfraz, H. Anwar, M. Nadeem, I. Shakir, Electrochim. Acta, 219, (2016), 330-338.
115. H. G. Jung, N. Venugopal, B. Scrosati, Y. K. Sun, J. Power Sources, 221, (2013), 266-271.
116. J. Liu, J. Essner, J. Li, Chem. Mater., 22, (2010), 5022-5030.
117. X. Li, A. M. Elshahawy, C. Guan, J. Wang, Small, 13, (2017), 1-24.
118. J. Li, Y. Cheng, M. Jia, Y. Tang, Y. Lin, Z. Zhang, Y. Liu, J. Power Sources, 255, (2014), 130-143.
119. Y. Ye, Y. Shi, A. A. O. Tay, J. Power Sources, 217, (2012), 509-518.

120. J. Theerthagiri, K. Thiagarajan, B. Senthilkumar, Z. Khan, R. A. Senthil, P. Arunachalam, J. Madhavan, M. Ashokkumar, ChemistrySelect, 2, (2017), 201-210.
121. N. Srinivasan, S. Mandal, Angew. Chem. Int. Ed., 47, (2008), 4798-4828.
122. H. Pang, Y. Zhang, W. Y. Lai, Z. Hu, W. Huang, Nano Energy, 15, (2015), 303-312.
123. J. Zhang, Y. Yang, Z. Zhang, X. Xua, X. Wang, J. Mater. Chem. A, 2, (2014), 20182-20188.
124. H. Mao, Y. Qian, Z. Jin, Y. Zhang, Mater. Lett., 228, (2018), 258-261.
125. Y. Wang, W. Li, L. Zhang, X. Zhang, B. Tan, J. Hao, J. Zhang, X. Wang, Q. Hu, X. Lu, J. Power Sources, (2020), 449, 227487.
126. S. J. Marje, P. K. Katkar, S. S. Pujari, S. A. Khalate, P. R. Deshmukh, U. M. Patil, Mat. Sci. Eng. B, 261, (2020), 114641.
127. Z. Xiao, Y. Bao, Z. Li, X. Huai, M. Wang, P. Liu, L. Wang, ACS Appl. Energy Mater., 2, (2019), 1086–1092.
128. A. A. Mirghni, K. O. Oyedotun, O. Fasakin, B. A. Mahmoud, D. J. Tarimo, N. Manyala, J. Energy Storage, 31, (2020), 1-9.
129. T. Wang, Q. Hao, J. Liu, J. Zhao, J. Bell, H. Wang, RSC Adv., 6, (2016), 45986-45992.
130. H. Pang, Z. Yan, W. Wang, J. Chen, J. Zhang, H. Zheng, Nanoscale, 4, (2012), 5946-5953.
131. Y. Xi, B. Dong, Y. Dong, N. Mao, L. Ding, L. Shi, R. Gao, W. Liu, G. Su, L. Cao, Chem. Mater. 28, (2016), 1355-1362.
132. K. V. Sankar, S. C. Lee, Y. Seo, C. Ray, S. Liu, A. Kundu, S. C. Jun, J. Power Sources, 373, (2018), 211-219.
133. H. Li, H. Yu, J. Zhai, L. Sun, H. Yang, S. Xie, Mater. Lett., 152, (2015), 25-28.
134. H. Pang, S. Wang, W. Shao, S. Zhao, B. Yan, X. Li, S. Li, J. Chen, W. Du, Nanoscale, 5, (2013), 5752-5757.
135. M. C. Liu, J. J. Li, Y. X. Hu, Q. Q. Yang, L. Kang, Electrochim. Acta, 201, (2016), 142-150.
136. J. J. Li, M. C. Liu, L. B. Kong, M. Shi, W. Han, L. Kang, Mater. Lett., 161, (2015), 404-407.

137. H. Shao, N. Padmanathan, D. McNulty, C. O' Dwyer, K. M. Razeeb, ACS Appl. Mater. Interfaces, 8, (2016), 28592-28598.
138. H. Pang, Y. Liu, J. Li, Y. Ma, G. Li, Y. Ai, J. Chen, J. Zhang, H. Zheng, Nanoscale, 5, (2013), 503-507.
139. D. H. Lee, M. Kang, S. M. Paek, H. Jung, Bull. Korean Chem. Soc., 37, (2016), 192-199.
140. X. Wang, Z. Yan, H. Pang, W. Wang, G. Li, Y. Ma, H. Zhang, X. Li, J. Chen, Int. J. Electrochem. Sci., 8, (2013), 3768-3785.
141. Y. Tang, Z. Liu, W. Guo, T. Chen, Y. Qiao, S. Mu, Y. Zhao, F. Gao, Electrochim. Acta, 190, (2016), 118-125.
142. S. Wang, H. Pang, S. Zhao, W. Shao, N. Zhang, J. Zhang, J. Chen, S. Li, RSC Adv., 4, (2014), 340-347.
143. H. Mao, F. Zhang, X. Liu, J. Qiu, B. Li, Z. Jin, J. Mater. Sci. Mater. Electron., 29, (2018), 16721-16729.
144. A. A. Mirghni, D. Momodu, K. O. Oyedotun, J. K. Dangbegnon, N. Manyala, Electrochim. Acta, 283, (2018), 374-384.
145. D. Wang, Y. Xu, W. Sun, X. Guo, L. Yang, F. Wang, Z. Yang, Electrochim. Acta, 337, (2020), 1-10.
146. D. R. Patil, B. Koteswararao, K. Begari, A. Yogi, M. Moussa, D. P. Dubal, ACS Appl. Energy Mater., 2, (2019), 2972-2981.
147. H. Dan, K. Tao, Q. Zhou, Y. Gong, J. Lin, ACS Appl. Mater. Interfaces, 10, (2018), 31340-31354.
148. N. Duraisamy, N. Arshid, K. Kandiah, J. Iqbal, P. Arunachalam, G. Dhanaraj, K. Ramesh, S. Ramesh, J Mater Sci: Mater Electron, 30, (2019), 7435-7446.
149. L. Hou, L. Lian, D. Li, J. Lin, G. Pan, L. Zhang, X. Zhang, Q. Zhang, C. Yuan, RSC Adv., 3, (2013), 21558-21562.
150. Z. Khan, B. Senthilkumar, S. Lim, R. Shanker, Y. Kim, H. Ko, Adv. Mater. Interfaces, 4, (2017), 1-7.
151. H. Shao, N. Padmanathan, D. McNulty, C. O' Dwyer, K. M. Razeeb, ACS Appl. Energy Mater., 2, (2019), 569-578.
152. B. Liang, Y. Chen, J. He, C. Chen, W. Liu, Y. He, X. Liu, N. Zhang, V. A. L. Roy, ACS Appl. Mater. Interfaces, 10, (2018), 3506-3514.

153. M. Liu, N. Shang, X. Zhang, S. Gao, C. Wang, Z. Wang, J. Alloy Compd., 791, (2019), 929-935.
154. B. A. Mahmoud, A. A. Mirghni, K. O. Oyedotun, D. Momodu, O. Fasakin, N. Manyala, J. Alloys Compd., (2020), 818, 1-36.
155. Y. Tian, X. Lian, Y. Wu, W. Guo, S. Wang, CrystEngComm, 22, (2020), 5218-5225.
156. Z. Zheng, M. Retana, X. Hu, R. Luna, Y. H. Ikuhara, W. Zhou, ACS Appl. Mater. Interfaces, 9, (2017), 16986-16994.
157. A. M. Elshahawy, C. Guan, X. Li, H. Zhang, Y. Hu, H. Wu, S.J. Pennycook, J. Wang, Nano Energy, 39, (2017), 162-171.
158. F. Liang, L. Huang, L. Tian, J. Li, H. Zhang, S. Zhang, CrystEngComm, 20, (2018), 2413-2420.
159. X. Chen, M. Cheng, D. Chen, R. Wang, ACS Appl. Mater. Interfaces, 8, (2016), 3892-3900.
160. M. Cheng, H. Fan, Y. Xu, R. Wang, X. Zhang, Nanoscale, 9, (2017), 14162–14171.
161. J. Wang, X. Ren, L. Chen, B. Wang, Int. J. Electrochem. Sci., 13, (2018), 10904-10910.
162. W. Wang, L. Zhang, G. Xu, H. Song, L. Yang, C. Zhang, J. Xu, D. Jia, Inorg. Chem., 57, (2018), 10287-10294.
163. Q. Zhang, W. B. Zhang, P. Hei, Z. Hou, T. Yang, J. Long, Appl. Surf. Sci., (2020), 1-11.
164. Y. Jin, C. Zhao, Q. Jiang, C. Ji, Colloids Surf. A, (2018), 553, 58-65.
165. Y. Hu, M. Liu, Q. Yang, L. Kong, L. Kang, J. Energy Chem., (2017), 26, 49-55.
166. G. Zhu, L. Yang, W. Wang, M. Ma, J. Zhang, H. Wen, D. Zheng, Y. Yao, Chem. Commun., 54, (2018), 9234-9237.
167. Y. H. Dai, L. B. Kong, K. Yan, M. Shi, Y. C. Luo, L. Kang, Ionics, 22, (2016), 1461–1469.
168. A. A. Mirghni, M. J. Madito, T. M. Masikhwa, K. O. Oyedotun, A. Bello, N. Manyala, J. Colloid Interf. Sci., 494, (2017), 325-337.
169. N. Priyadharsini, A. Shanmugavani, L. Vasylechko, R. Kalai Selvan, Ionics, 24, (2018), 2073–2082,.

170. J. Hao, W. Li, X. Zuo, D. Zheng, X. Liang, Y. Qiang, B. Tan, B. Xiang, X. Zou, J. Mater Sci., 54, (2018), 625-637.
171. L. Xu, S. Wang, X. Zhang, T. He, F. Lu, H. Li, J. Ye, Appl. Surf. Sci., 428, (2018), 977-985.
172. H. Pang, Z. Yan, W. Wang, Y. Wei, X. Li, J. Li, J. Chen, J. Zhang, H. Zheng, Int. J. Electrochem. Sci., 7, (2012), 12340-12353.
173. B. Yan, D. Bin, F. Ren, Z. Xiong, K. Zhang, C. Wang, Y. Du, Catalysts, 6, (2016), 1-15.
174. X. J. Ma, W. B. Zhang, L. B. Kong, Y. C. Luob, L. Kang, RSC Adv., 6, (2016), 40077-40085.
175. C. C. Lee, F. S. Omar, A. Numan, N. Duraisamy, K. Ramesh, S. Ramesh, J. Solid State Electrochem., 21, (2017), 3205-3213.
176. C. Yang, L. Dong, Z. Chen, H. Lu, J. Phys. Chem. C, 118, (2014), 18884-18891.
177. K. Raju, H. Han, D. B. Velusamy, Q. Jiang, H. Yang, F. P. Nkosi, N. Palaniyandy, K. Makgopa, Z. Bo, K. I. Ozoemena, ACS Energy Lett., 5, (2020), 23-30.
178. B. Senthilkumar, K. V. Sankar, L. Vasylechko, Y. S. Lee, R. K. Selvan, RSC Adv., 4, (2014), 53192–53200.
179. V. Sharmila, M. Parthibavarman, J Mater Sci: Mater Electron, 30, (2019), 19813-19825.
180. T. A. Raja, P. Vickraman, A. S. Justin, B. J. Reddy, J Mater Sci., 55, (2020), 14447-14463.
181. M. Zhang, H. Liu, T. Ma, Z. Song, S. Shao, Chem. Eng. J., 403, (2020), 1-12.
182. D. Chinnadurai, A. R. Selvaraj, R. Rajendiran, G. R. Kumar, H. J. Kim, K. K. Viswanathan, K. Prabakar, ACS Omega, 3, (2018), 1718-1725.

CHAPTER -2

THEORETICAL BACKGROUND OF HYDROTHERMAL, SILAR METHOD AND THIN FILM CHARACTERIZATION TECHNIQUES

CHAPTER 2

Theoretical Background of Hydrothermal, SILAR Method and Thin Film Characterization Techniques

Sr. No.	Title		Page No.
2.1	**Introduction of Thin Films**		**59**
2.2	**Hydrothermal Method**		**62**
	2.2.1	*Theoretical Background*	**62**
	2.2.2	*Basics of Hydrothermal Method*	**63**
	2.2.3	*Effect of Preparative Parameters*	**65**
	2.2.4	*Advantages*	**67**
2.3	**Successive Ionic Layer Adsorption and Reaction (SILAR) Method**		**68**
	2.3.1	*Theoretical Background*	**68**
	2.3.2	*Basics of SILAR Method*	**69**
	2.3.3	*Effect of Preparative Parameters*	**73**
	2.3.4	*Advantages*	**74**
2.4	**Thin Film Characterization Techniques**		**75**
	2.4.1	*X-Ray Diffraction (XRD)*	**75**
	2.4.2	*Fourier Transform-Infrared Spectroscopy (FT-IR)*	**78**
	2.4.3	*X-Ray Photoelectron Spectroscopy (XPS)*	**80**
	2.4.4	*Field Emission-Scanning Electron Microscopy (FE-SEM)*	**82**
	2.4.5	*Energy Dispersive X-Ray Spectroscopy (EDS)*	**85**
2.5	**Electrochemical Techniques**		**86**
	2.5.1	*Cyclic Voltammetry (CV)*	**88**
	2.5.2	*Galvanostatic Charge-Discharge (GCD)*	**90**
	2.5.3	*Electrochemical Impedance Spectroscopy (EIS)*	**91**
2.6	**References**		**95**

2.1 Introduction of Thin Films:

Nowadays, thin film science has spread globally into a major research area. Presently, the fast-growing demand for thin film materials and their devices is developing new opportunities for the evolution of new processes, materials, and technologies. Consequently, significant considerations have been given to prepare advanced material in thin film form to enhance the capability of existing energy storage devices. In 1838, the electrolysis method was used to prepare first thin solid films. For the past several decades, organic and inorganic materials have been produced in thin film configuration and used for various applications **[1-3]**.

As the name implies 'thin film' is thin in nature which is any liquid or solid system that has a maximum two-dimensional order or periodicity, and this thin film material thickness ranging from nanometers to micrometers. The thin layers of material can be deposited on any kind (conducting and non-conducting) of substrates through atom by atom or ion by ion, which originates from a purely physical or chemical process. The benefits of thin films and scientific interest in 2D solids are the main reasons for creating enormous attention in science and technology studies of thin films as shown in **Figure 2.1**. In addition, the usage of thin film technology has transformed the area of electronics, optics, energy storage devices (like supercapacitors), sensors and magnetism, etc. **[4-7]**. The nanomaterial offers improved electrochemical capacitive performance because of its capability to obtain both bulk and surface properties. The benefits of nanomaterials for energy storage devices have mostly concentrated on the advantages related to short charge transfer length. Nanocrystalline thin film materials give different advantages like large surface area, lower thermal conductivity, higher electrical conductivity, enhanced diffusivity, increased

strength, high thermal expansion coefficient is compared with conventional coarse-grained materials **[8]**.

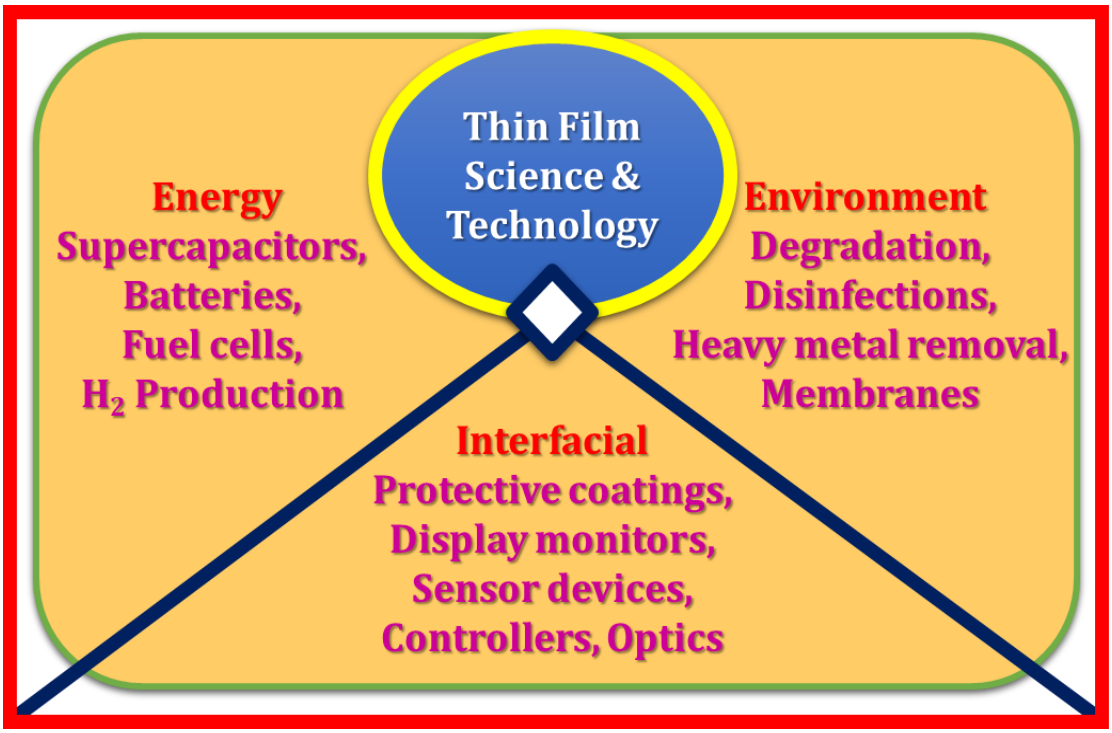

Figure 2.1: Innovations and applications related to thin film materials and devices.

Moreover, the synthesis method of thin films is very important for the required properties and versatility. There are two main branches of thin film deposition methods that exist to grow nanomaterials in thin film forms; it can be widely categorized as either physical *(top-down)* or chemical *(bottom-up)* methods **[9, 10]**. The physical *(top-down)* methods involve sputtering, vacuum evaporation, etc. In these methods, depositing material is transferred into the gaseous phase by the evaporation process and deposited on a substrate by condensing. A wide categorization of thin film preparation methods is described in **Chart 2.1**. Also, the chemical method involves gas and liquid phase. The gas-phase chemical methods consist of various types such as chemical, laser chemical, photochemical, plasma-enhanced chemical, and metal organo-chemical vapor deposition (CVD). The liquid

phase chemical method involves successive ionic layer adsorption and reaction (SILAR), chemical bath deposition (CBD), hydrothermal, anodization, electrodeposition, electroless deposition, sol-gel method, spray pyrolysis, etc. The requirement of vacuum, higher deposition temperature, sophisticated instrumentation, wastage of depositing material and small area deposition are major drawbacks of physical method. Whereas, the chemical-based methods are facile, inexpensive, and efficient for large area preparation of various materials in thin film form.

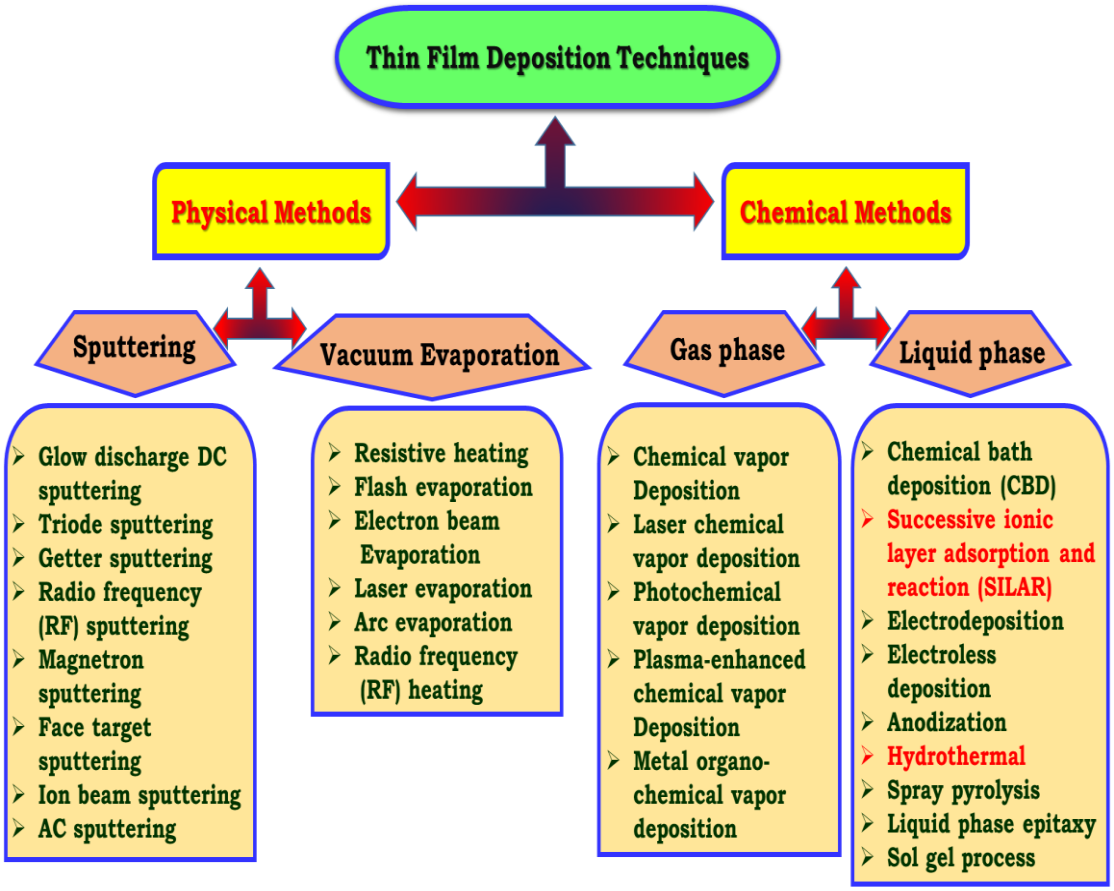

Chart 2.1: Classification of thin film preparation methods.

The preparative parameters of chemical methods like pH of solution, deposition time, concentration of reactants and temperature can be easily controlled. The metallic substrates get oxidized and corroded in the physical

method and it can be prevented by using low-temperature chemical deposition methods. The chemical method can produce adherent and uniform deposition of thin film. Therefore, these chemical methods are widely used to produce nanostructured materials for various applications.

The present chapter describes theoretical background of hydrothermal and SILAR methods are used for thin film preparation and different characterization (Structural, morphological, and electrochemical) techniques.

2.2 Hydrothermal Method:

2.2.1 Theoretical Background:

A hydrothermal method is the most popular one and gathering attention from technologists and researchers of diverse fields for various applications. The hydrothermal concept is originated from a geological subject. A common explanation of the hydrothermal word is, 'hydro' defines water, and 'thermal' defines heat. Sir Roderick Murchison (British Geologist) (1792-1871) used this word for the first time in order to describe the activity of water at high pressure and temperature for alterations in the earth crust, which leads to production of several minerals and rocks **[11, 12]**. In presence of water, high pressure and temperature, most minerals formed in post-magmatic and metasomatic stages and said to be of hydrothermal origin. It is well-known that, biggest single crystal (>100 gm of beryl crystals) made in nature and man-made crystals by single experimental run (several hundreds of grams of quartz crystal) both have a hydrothermal origin. In the hydrothermal process, heterogeneous reaction carried out in aqueous solvents or minerals at high pressure and temperature, to dissolve and re-crystallize in materials that are relatively insoluble under normal conditions. Although the hydrothermal technique has made great progress, there is still no

unanimity in its interpretation. In literature, different interpretations were proposed for a hydrothermal method by different scientists. According to Morey and Niggli (1913), "In a hydrothermal method, the mechanisms are subjected to behavior of water at temperatures usually close or marginally above critical temperature of water (~370°C) in closed bombs, and consequently under high pressures developed by such solutions" **[13]**. Laudise **[14]** defined it as "hydrothermal growth means growth from aqueous solution at ambient or near ambient conditions." Rabenau in 1985 defined as, "hydrothermal synthesis as the heterogeneous reactions in aqueous media above 100°C temperature and 1 bar pressure" **[15]**. Lobachev defined it as, "A method where crystallization is carried out from superheated aqueous solution at high pressure" **[16]**. Yoshimura **[17]** defined it as "reactions taking place under the conditions of high temperature and pressure (>100 °C, >1 atm) in aqueous solutions in a closed system".

2.2.2 Basics of Hydrothermal Method:

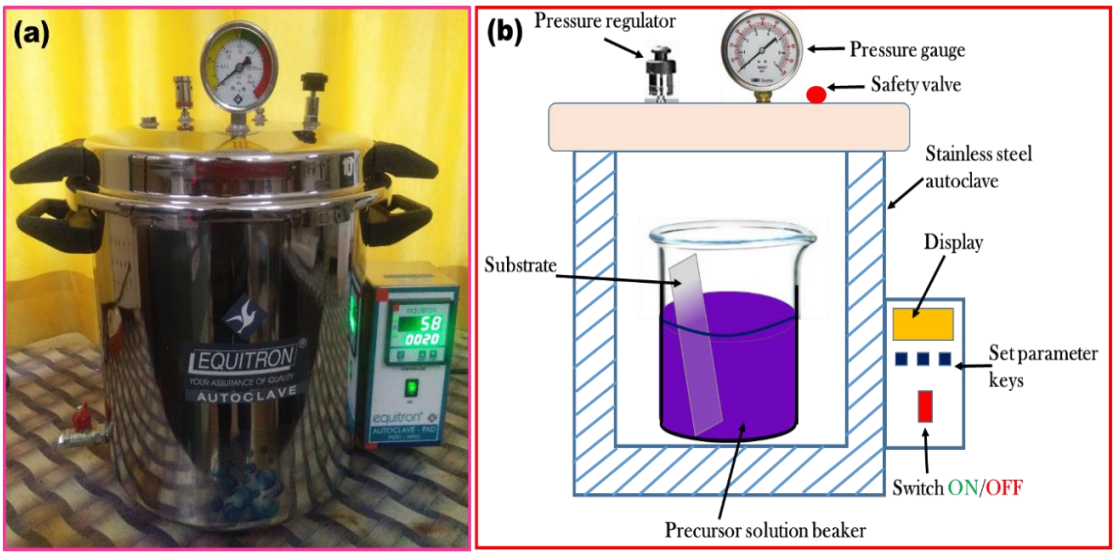

Figure 2.2: (a) The actual autoclave used for hydrothermal deposition and (b) Schematic diagram of hydrothermal method.

The hydrothermal method is a typical phenomenon of a solvothermal process which is generally considered as a chemical reaction that occurs in a solvent at temperatures beyond the boiling point of the solvent and at a pressure above 1 bar **[18]**. **Figure 2.2 (a, b)** shows the actual and schematic diagram of autoclave utilized for hydrothermal deposition. Important features of the hydrothermal method, such as ionic product, thermal conductivity, heat capacity, viscosity, and dielectric constant depend on extreme temperature and pressure. Therefore, by regulating synthesis parameters, certain properties can be easily manipulated.

Water is of utmost significant solvent existing abundance in nature and it has extraordinary characteristics as a reaction media in hydrothermal conditions. Water is environmentally benign and less expensive than other solvents and acts as a catalyst to produce the required material by altering pressure and temperature. Another benefit is that the water is highly volatile, so it can be easily separated from the material. In the conventional hydrothermal synthesis process, precursors are simply dissolved in a water bath then the bath is placed in an autoclave which can endure high temperature and pressure. A reaction container called an autoclave is needed for crystal growth under hydrothermal conditions. The autoclave is sealed and heated to the necessary temperature, most of the time pressure is autogenously generated. Depend on the level of autoclave filling, a pressure of several hundred bars can be easily obtained at low temperatures. Highly corrosive salts are utilized to synthesize inorganic substances for long duration reactions in hydrothermal method. The capacity of autoclave differs from several milliliters for laboratory synthesis to hundreds of liters for large scale materials production in industries. The highest temperature and pressure can be

as high as 1000 °C and 500 bar. However, for commercial applications temperature below 500 °C are usually preferred **[19]**. High temperature also contributes to a high reaction rate. Depending on the requirements of deposition, the film can be grown by the ion-by-ion accumulation of material or adsorption of colloidal particles on a substrate from solution. The hydrothermal method is especially useful for growth of large and fine crystals while their structure can be well controlled.

2.2.3 Effect of Preparative Parameters:

The chemical reaction kinetics performs a vital role in the disposition of well adherent and uniform thin films. The growth process depends on the growth kinetics, ions concentration, and a number of nucleation centres on dipped substrates. The impact of different deposition parameters like substrate, pH of solution, concentration of solution, complexing agent and temperature, etc. briefly explained as follows;

a) Substrate:

The formation of thin film strictly depends on the nature and surface of substrate material. It acts an important role in optimizing the rate of deposition and thickness of thin film. Therefore, substrate purification is initial important step in the procedure of thin film preparation. Also, a good match of lattice between the substrate and deposited layer on a substrate is a significant factor and that helps crystal growth. The supporter substrates contribute a conducive framework for better adhesion of active material with a current collector. Generally, conducting (stainless steel) and non-conducting (glass) materials can be utilized as substrates. The growth of active materials on the conducting substrate begins direct electrical

contact with a substrate, which helps to enhance the more efficient electrochemical reactions.

b) Temperature & Pressure:

The reaction kinetics mostly depends on the temperature and pressure of the precursor solution. The dissociation rate of complex cation and anion depends on solution temperature. This results in to increase or decrease in formation of anions and cations, and the rate of deposition. The dissociation of corrosive salts and complex ions can be increased at higher temperatures, so that excess ions are accessible for reaction and thus higher thickness can be achieved. The thickness of thin film increases to a particular reaction temperature after that the thickness of thin film decreases at higher temperatures.

c) ***Concentration of Solution:***

An increase in concentration of ionic precursors increases the concentration of cation or anion. If the concentration of ionic precursors is increased up to optimum value, the thickness of thin film can be high to a certain extent. After this limitation, rate of precipitation increases due to higher reaction rates leads to decrease film thickness. However, if concentration of ionic precursors is less than its optimum value, then the deposition cannot take place. So, the optimum concentrations of precursors are important for thin film formation.

d) Complexing Agent:

Generally, the complexing agent holds the metal cation and thus they prevent rapid material precipitation. Also, the production of complexes allows us to enhance the dissolution of moderately soluble salts. Furthermore, the complexing agent serves to decrease the concentration of unreacted metal ions in

a solution bath. Moreover, the precipitation is reduced, which results in the forming of diverse morphologies with an increasing terminal thickness of the thin film.

2.2.4 Advantages:

The hydrothermal synthesis method offers several benefits over other methods, which are listed below: **[20, 21]**

- This method is eco-friendly because it is performed in a closed system and the material can be easily retrieved and reused, once it has cooled to room temperature.
- The necessary equipment and processing are simpler and process is less energy consuming.
- By controlling the hydrothermal temperature and pressure, different crystalline products, structure, and morphology can be obtained.
- A hydrothermal method is unique for the preparation of thermodynamically metastable phases.
- Crystalline size and morphologies can be changed into nanoscale by adjusting preparation parameters e.g. precursor concentration, temperature, deposition time, pH, etc.
- A variety of morphologies and particle sizes are possible through hydrothermal processing.
- It can be combined with other methods like ultrasound, microwave, optical radiation, hot-pressing, and mechano-chemistry to expand benefits such as improvement of reaction kinetics and enhance the capability to produce novel materials.
- It doesn't require any seeds and catalyst, thus it is useful for low-cost and large area deposition with high-quality thin films.

- This process can be simply done as per industrial demand because in principle hydrothermal synthesis offers the opportunity for reproducible production of high-quality ceramic powder at a large industrial level. Hydrothermal methods are more environment friendly than most synthesis methods, which can be ascribed to less energy-conservation, low processing temperature, absence of grinding, ability to recycle waste, safe and convenient disposal of waste that cannot be recycled.

2.3 Successive Ionic Layer Adsorption and Reaction (SILAR) Method:

2.3.1 Theoretical Background:

During the 1980s, successive ionic-layer absorption and reaction (SILAR) process were developed to deposit a variety of thin films **[22-27]**. Besides, the comparable SILAR technique was reported for preparation of oxide thin films by Ristov et al. **[28].** The characteristic feature of SILAR is that, it consists of alternative aqueous cationic (metal salt solution) and anionic (hydrolyzing solution) baths. In principle, it is expected to grow thin film using an ion-by-ion mechanism through subsequent adsorption and reaction of a single atomic layer. In the last few years, cobalt and manganese based oxide, sulfide thin film has been produced using SILAR method **[29]**.

In most chemical methods, a thin film is formed on a substrate when heterogeneous precipitation takes place on a substrate surface and homogeneous precipitation takes place in a solution or bath. Nevertheless, the chemical method results in unnecessary formation of precipitate in solution and it cannot be avoided. To avoid such a problem; the CBD method is modified and developed in a new method that is known as SILAR method. **Figure 2.3** and **2.4** shows the actual used and schematic presentation of SILAR method, respectively. In this modified

method, thin films are prepared from the insertion of a substrate in distinctly placed cationic and anionic precursors, and the substrate is rinsed with ion-exchange water during each immersion.

The basic and theoretical background of SILAR is described in detail in the review article of Pathan and Lokhande **[30]**. The SILAR method basically depends on adsorption followed by reaction of ions in a solution of precursors and rinsing in double distilled water (DDW) during each immersion to avoid homogeneous precipitation. Adsorption is a fundamental backbone of the SILAR system. It is expected that, contact between heterogeneous phases expedites the growth of material. Therefore, there are three adsorption systems - liquid-solid, gas-solid, and gas-liquid. SILAR system used in this work based on adsorption in a liquid-solid system. Adsorption is a surface phenomenon (exothermic) facilitated by the attractive forces (cohesive or Van-der Waals or chemical attraction) between solution ions and the surface of a substrate. Due to the cohesive or Van-der Waals or chemical attractive forces, the cations adsorbed on a substrate surface leading to the development of a monolayer. In the step of reaction, the adsorbed ion reacted with desired anions leading to the monolayer formation of desired material. By repeating such subsequent cycles layer-by-layer formation of film occurs on the substrate surface. As the adsorption process is highly influenced by the physical parameters like temperature, nature of substrate, concentration of solution, area of substrate, etc., thus physico-chemical characteristics of a thin film can be altered by varying the above parameters.

2.3.2 Basics of SILAR Method:

In the past few years, metal, semiconductors, polymers, superconductors, ceramics, etc. have been prepared in thin film form using the SILAR method **[31-**

33]. SILAR method is able to form a thin nanocrystalline compact layer over conducting and non-conducting substrates.

Figure 2.3: The photograph of programmable SILAR coating system used for preparation of thin films.

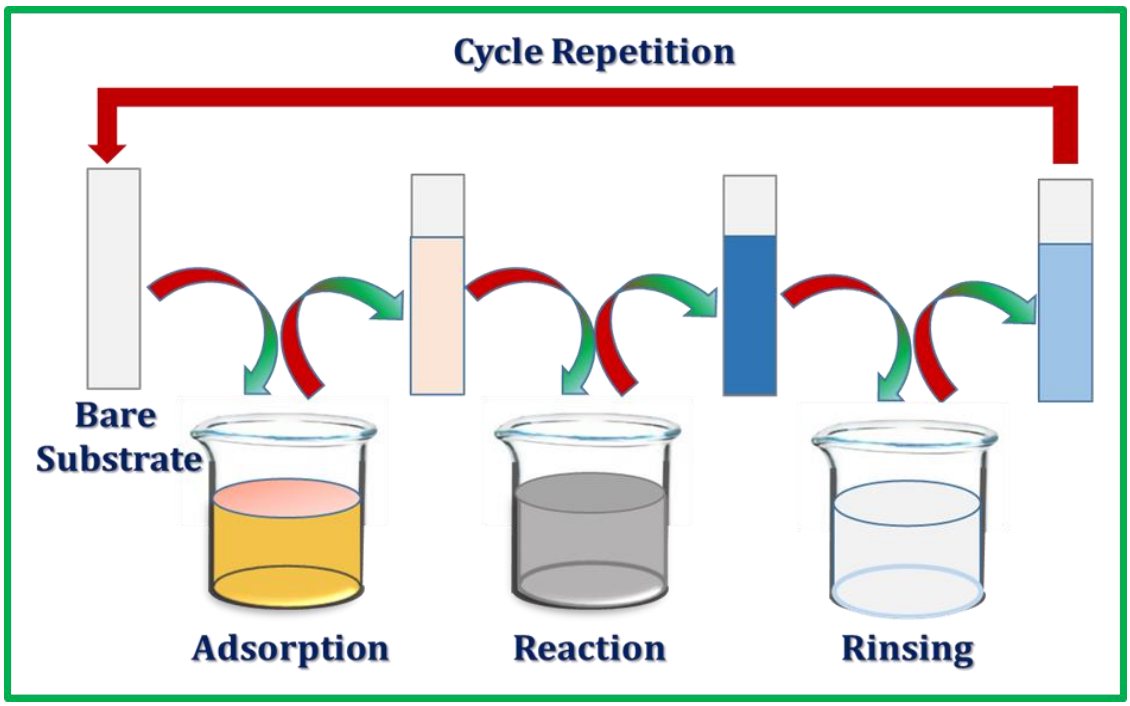

Figure 2.4: Schematic diagram of modified SILAR method

In the manually operated SILAR process, the researcher needs to immerse substrate for numbers of repeated cycles in the solution and water. So, it is relatively difficult to manage the time and number of dips in the manually operated SILAR process. In the automatic unit, the researcher only needs to suspend substrate in a holder and program the controller for required dip cycles and duration. The SILAR equipment (Holmarc Opto-Mechatronics Pvt Ltd. India, Model: HO-TH-03A) consists of six beakers on the circular metal tray, of 100 ml each (see **Figure 2.3**). Each rinsing beaker can be placed between cationic and anionic salt solutions. Then, substrates can be set on the line with the help of vertical tweezers and supported on the spindle. The spindle rotates and slides into the Teflon bearing driven by a stepping motor. Dipping and retrieval speed as well as period can be set for each beaker. The vertical movement of spindle is variable, it has different rotation speeds (1-200 rpm) **[34]**.

SILAR method is expected to produce thin films of metal compounds of the CyDm type through a heterogeneous chemical reaction on the solid surface via a reaction between adsorbed yC^{a+} (cations) and mD^{y-} (anion), as per the following reaction,

$$yC^{a+} + zA^{n-} + n'B^{z'+} + mD^{y-} \rightarrow CyDm_S \downarrow + zA^{n-} + n'B^{z'+} \quad 2.1$$

With $my = nz = n'z'$.

Where, C: cation (Co^{2+}, Mn^{2+}, Ni^{2+}, Fe^{3+}, Cu^{+}, etc.); y: number of cations, a: numerical value of charge on cation, A: an ion in cationic precursors having a negative charge (A = Cl^{2-}, SO_4^{2-}, NO_3^{2-} etc.) z: number of A in cationic precursors and n: numerical value of charges on A, z': numerical value of charge on B, B: the ion in anionic

precursor having a positive charge, *n'*: number of *B* in the anionic solutions, *D*: anion (O^-, OH^- and PO_4^{3-}), m: the number of anions.

SILAR method basically consists of four beakers system, which is generally used for deposition of metal oxide, sulfide films, and this system has been modified into a three-beaker system for deposition of binary metal phosphate films. **Figure 2.4** represents a schematic illustration of a modified SILAR method. In the present work, the chemical coating involves at least three distant steps; 1) Adsorption of cations from a cationic bath, 2) Reaction with anions from the anionic bath, and 3) Rinsing for removal of weakly adsorbed particles in DDW.

1. ***Adsorption:***

This is the first step where cations adsorbed on surface of immersed substrate from a solution of cationic salts, along with the formation of Helmholtz double layer at a solid-solution interface. The Helmholtz layer is consists of two layers: the inner layer contains a polarized solvent and the outer layer contains solvated cations.

2. ***Reaction:***

In this second step of reaction, the chemical interaction among solvated adsorbed cations and anions by immersing the substrate in the solution causes growth of material. Because of the less stability of ions, a solid material is produced at the interface (C_yD_m). In this step, yC^{a+}surface cations react with mD^{y-} anions from solution.

3. ***Rinsing:***

In order to remove the unreacted species and loosely bonded particles from the film, rinsing is used in this last step.

After a few cycles, depending on the concentration of solution and immersion and rinsing time the substrate completely coated by CyDm layer (theoretical monolayer), and also the thickness of film increases with repeating each cycle. Two criteria of film formation by SILAR method are (a) minimum single ion must be assigned specifically to substrate interface and; (b) growth rate per immersion should not surpass the interplanar distance of compound and grow along with prescribed direction. The homogeneous precipitation may take place in the solution, when the growth rate surpasses the lattice constant of material. In the SILAR process, a substrate is immersed sequentially in cationic and anionic baths containing a soluble salt of material to be deposited. After anionic immersion, a growing film over a substrate is rinsed in DDW **[30]**.

2.3.3 Effect of Preparative Parameters:

In the SILAR method, growth kinetics can be controlled by ions concentration, substrate nature, adsorption, reaction, and rinsing time. The impact of different preparative parameters on film formation are described below:

a) ***Concentration of Cation and Anion:***

With an increase in precursor concentration, the 'C' and 'D' ion concentration increases and yields a film of 'CD' with a higher thickness. Also, the reaction rate is higher for a high concentration of cation and anion, which leads to an increase in homogeneous precipitation and results in deposition of less 'CD' over the substrate. Therefore, the thickness of film decreases at a high concentration of precursors. Stoichiometric deposition of material can be achieved by varying precursor concentrations.

b) Adsorption and Reaction Time:

The time period of adsorption and reaction plays a crucial role in the production of a thin film. The same adsorption and reaction time, resulting in a consistent reaction and continuous growth that provides the production of a uniform film.

c) Rinsing Time:

In a rinsing bath, the poorly bonded species detached from a substrate surface. A good quality film can be prepared by adequate rinsing time, which is free from unreacted species and loosely bonded compounds.

2.3.4 Advantages:

Apart from saving material cost, preparation of thin films using a modified SILAR method has the following advantages:

- SILAR is a simple, inexpensive method and it is efficient for deposition over a large area.
- Various kinds of substrates like metals, semiconductors, insulators, and polymers can be used, because it is a low-temperature process. This prevents corrosion or oxidation of metallic substrates.
- This method is very feasible to dope any element with the required proportion in the film.
- The deposition rate, morphology, and film thickness can be efficiently manipulated by varying the preparative conditions.
- A comparatively uniform film can be deposited on any kind of substrate having a complex configuration.

- Drawbacks like contamination, interdiffusion, and dopant redistribution, due to high temperature deposition techniques can be avoided in this low temperature deposition technique.

Along with the above advantages, SILAR has attractive features that material can be directly deposited from aqueous and non-aqueous baths and used to produce binary metal phosphate materials.

2.4 Thin Film Characterization Techniques:

In the last few years, the improvement in materials science and technology has taken place mainly with the contribution to the progress of new materials. Advanced and reliable characterization techniques are essential for the investigation of physico-chemical properties of materials. Characterization is a highly crucial step in the progress of advanced functional materials. The set of characterization e.g. phase analysis, compositional characterization, structural analysis, and surface characterization, can be useful to investigate properties of final material. Thus, in the material science field, various advanced techniques are emerged to probe the various aspects of final material. **Section 2.4** describes the operation and working principle of various analytical characterization techniques use to investigate various properties of thin films.

2.4.1 X-Ray Diffraction (XRD):

X-ray diffraction (XRD) analysis is a popular analytical technique, used to identify the crystal structure of investigated sample and provide information about unit cell dimensions and phase of material **[35]**. Structure identification, lattice parameters, strain, grain size, epitaxy, defect structure and preferred orientation of the materials can be determined by the X-ray diffraction pattern. It is a non-destructive and non-contact technique and provides useful information based on

the scattering of X-rays from long-range order structures **[36]**. Due to enhanced detection techniques of X-rays, specific monochromators, and intense micro-focused X-ray beam, the X-ray diffraction technique has been using to probe thin films of 100 Å thickness **[37]**. The intensity measured by XRD can provide quantitative and accurate knowledge about the atomic arrangement at the interface (e.g. in multilayer). The photograph of Rigaku Miniflex-600 X-Ray diffractometer is displayed in **Figure 2.5.** The schematic of XRD diffractometer is presented in **Figure 2.6**, where the diffraction angle 2Θ is the angle between incident and diffracted X-rays. The X-ray wavelength is in the scanning up to 145°, which corresponds to X-ray energies. Many researchers have used an X-ray diffraction system for the structural investigation of thin films. In the XRD technique, a diffraction beam provided by chromator is diffracted from the film surface and detected by an oscillating detector around the mean diffraction position.

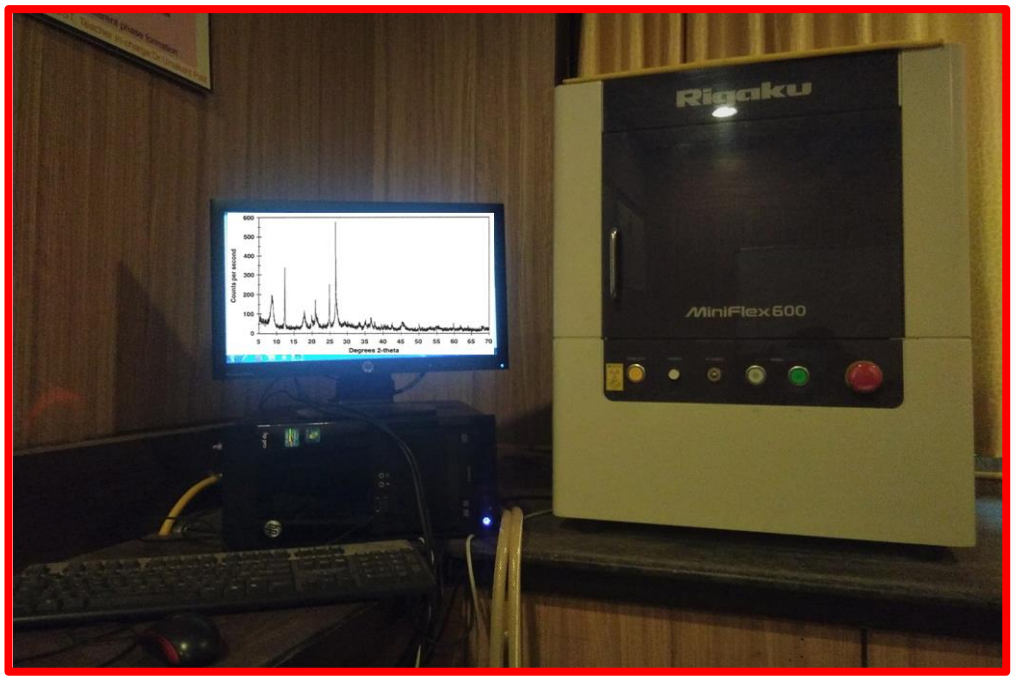

Figure 2.5: Photograph of Rigaku Miniflex-600 X-Ray diffractometer.

The basic requirement of XRD technique is monochromatic radiation since the interplanar distance can be measured from a diffraction angle, according to Bragg's law as exhibited following equation **[38];**

$$2d \sin\theta = n\lambda \qquad 2.2$$

Where, 'd' is interplanar distance, 'λ' is wavelength of X-ray, 'n' is order of diffraction, and 'θ' is diffraction angle. The X-ray powder diffraction data achieved from the diffractometer is compared with Joint Committee Powder Diffraction Standards (JCPDS) or American Standards for Testing of Materials (ASTM) to identify phases of materials **[39]**. The powder, single crystal, or thin film sample can be identified by XRD technique.

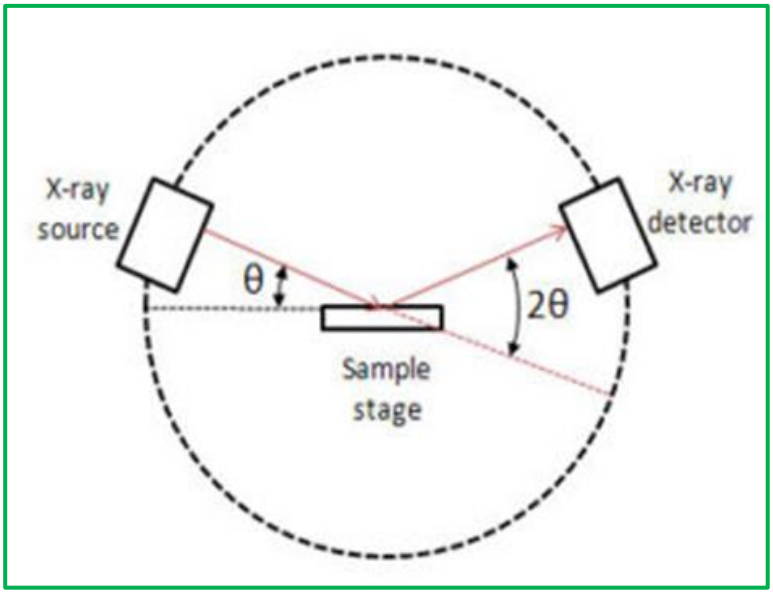

Figure 2.6: Schematic diagram of XRD diffractometer **[40]**

Thin films contain many grains or crystallites that have a distribution of orientation. If the distribution is completely random, then there are diffraction from any of the crystallites which have the correct orientation that satisfy the diffraction conditions. The diffracted X-rays emerge out as cones about the incident beam with an angle $2\theta_{hkl}$, creating a powder diffraction pattern Furthermore, all

crystallites in a film may have the same atomic planes parallel or randomly oriented to the substrate surface. Though, the XRD technique effectively investigates the structural properties e.g. structure of a material, lattice dimensions, crystallite size, etc. However, it is not unable to determine quantitative compositional analysis.

2.4.2 Fourier Transform Infrared Spectroscopy (FTIR):

Fourier-Transform Infrared Spectroscopy (FTIR) is a powerful analytical tool for identifying functional groups and covalent bond information. The spontaneous orientation of the dipole moment in materials is studied by the non-destructive tool using infrared spectroscopy that can provide information about inter-atomic forces within the crystal lattice. There are six different ways an organic/inorganic compound can vibrate: symmetrical and anti-symmetrical stretching, wagging, rocking, scissoring, and twisting **[41]**. FTIR spectrometer; Alpha (II) Bruker model is used for characterization and the ray diagram of the FTIR is displayed in **Figure 2.7**.

The infrared vibrational frequencies and inter-atomic forces correlated and so it is used to investigate functional groups in the material. According to Planck-Einstein relation, energy transfer between different energy states of molecules can be written as the following equation,

$$\Delta E = h\nu \qquad 2.3$$

Where h is Planck constant and ν is frequency. The positive ΔE means molecule absorbs energy; when ΔE is negative means it emits energy in form of radiation, and thus emission spectrum is obtained.

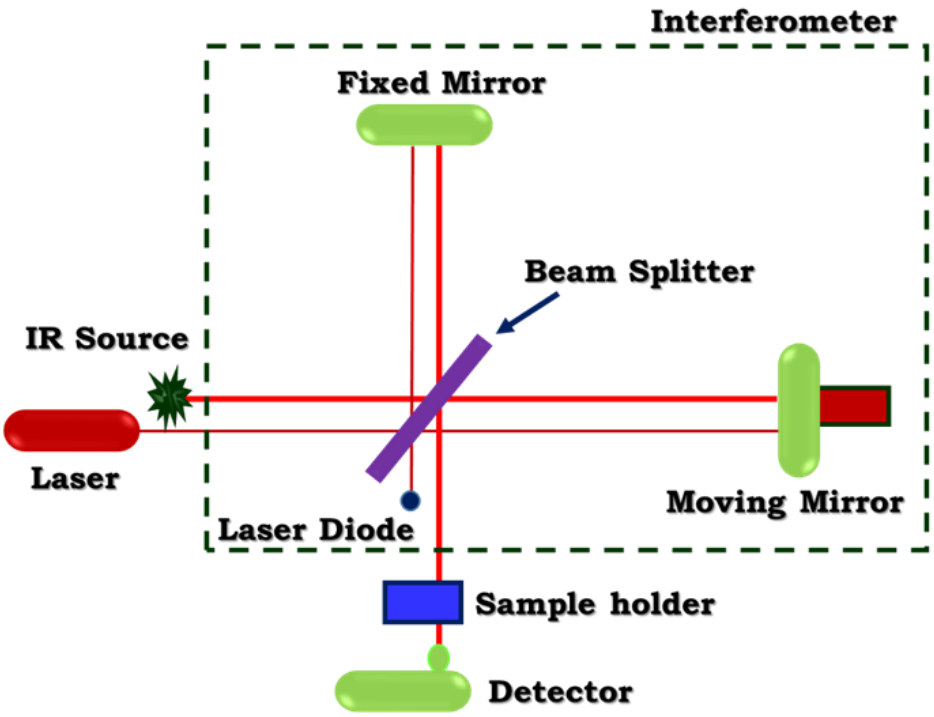

Figure 2.7: Basic ray diagram of FT-IR Spectrometer

When **Eqⁿ 2.3** is satisfied, an absorption spectrum is obtained, which is particular to a molecule under investigation. The spectrum is normally presented as an intensity plot versus frequency and absorption peaks obtain, when **Eqⁿ 2.3** is satisfied. A spectrum close to a visible region (comparatively small portion) is used for spectroscopic investigations. This portion incorporates UV-Visible and IR regions (10 nm to 1 mm). The different absorption spectra can be observed from atoms and molecules, because of nature of energy levels in transition. The transition of electrons between orbitals of atoms takes place due to the absorption of energy. However, the atoms vibrate in a molecule and it moves due to the absorption of energy **[42, 43]**. A few transition energies such as rotational, vibrational, and electronic are possible to measure. Usually, translational energy can be ignored, since it is sufficiently small. The vibrational spectrum is believed to

be a unique physical characteristic of molecules. Therefore, the IR spectrum is supposed as a fingerprint for the identification of material **[44]**.

2.4.3 X-Ray Photoelectron Spectroscopy (XPS):

In 1950, the first successful study of photoelectron spectroscopy has performed by Kai Siegbahn and for this work, he received the Nobel prize (Physics, 1981) **[45]**. Siegbahn et al. coined the term Electron Spectroscopy for Chemical Analysis (ESCA) are also known as X-ray photoelectron spectroscopy (XPS) and it has the fundamental ability to know surface properties of materials or thin films. This technology works on the principle of photoelectric effects in which soft X-rays are used as the source of monochromatic photons and the characteristics of emitted electrons from the surface are studied **[46]**. When X-rays are allowed to fall on the material, it causes electrons to release from a surface layer of material and these electrons are called photoelectrons. Elements in a sample are identified from the kinetic energy of those photoelectrons. Furthermore, the concentration of relative components is evaluated by the intensity of the photoelectron. The kinetic energy of photoelectron is given by the following relation **[47]**,

$$K.E. = h\nu - B.E. - \phi_s \qquad 2.4$$

Where, K.E. is kinetic energy of ejected photoelectron, hν is photon energy, B.E. is binding energy of atomic orbital, ϕ_s is work function of spectrometer.

In XPS, the photon is incident by an atom in a molecule, which causes ionization and ejection of electrons from core shell. Each element has distinctive binding energy corresponds with individual core atomic orbital, which means that each element gives a characteristic peak in the photoelectron spectrum. The kinetic energy is calculated by photon energy and corresponding binding energy.

Normally, aluminium Kα radiation hν = 1486.6 eV, magnesium Kα radiation hν = 1253.6 eV and zirconium Kα radiation hν = 2042.4 eV are used as targets in the X-ray source of radiation **[48]**.

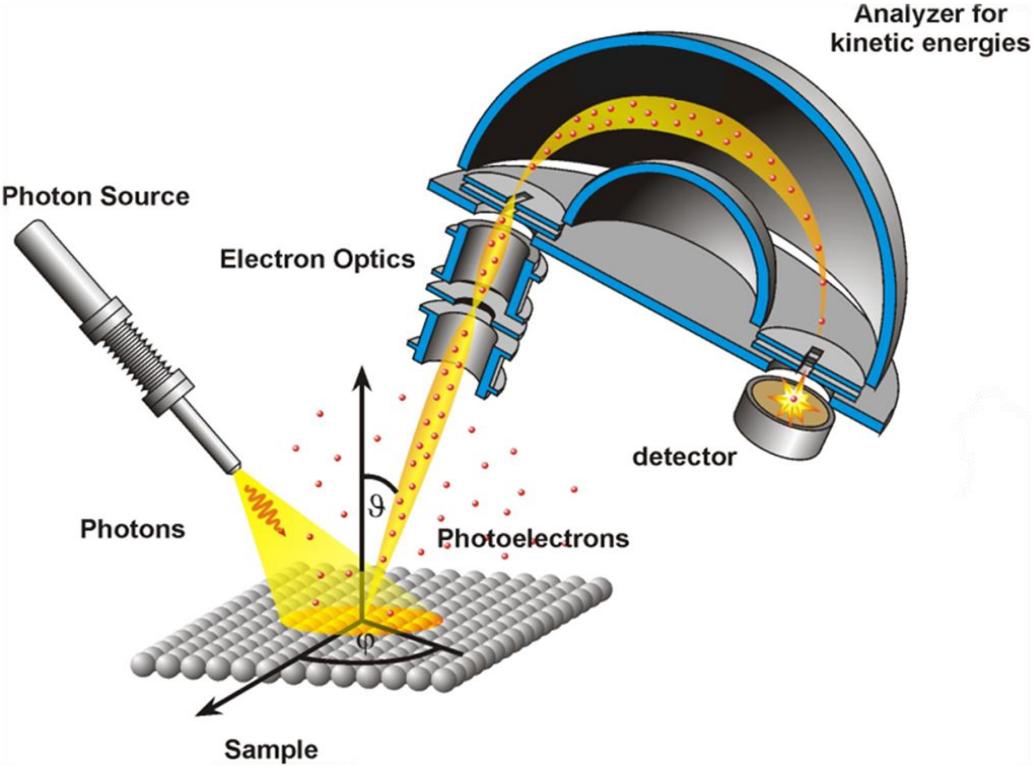

Figure 2.8: Schematic diagram of an XPS instrument **[49]**

XPS is mainly used to identify compounds using energy shifts due to chemical composition in the sample. Measurements are made on the total accessible energies known as a survey scan. This ensures presence of all elements in the sample. Although, the XPS measures of kinetic energy of emitted electrons, it is actually binding energy of electrons plotted to create the energy spectrum. Thus, the XPS spectrum contains a number of electrons identified respective with their binding energy. The number of electrons gives the quantity of that element in the sample. Chemical elements are distinguished by the position of energy peaks at particular binding energy on XPS spectrum. These characteristic energy peaks are related to the electronic configuration of atoms, such as 1s, 2s, 2p, 3p, 3s, 3d, etc.,

to identify valence state of that element. The schematic of XPS technique is presented in **Figure 2.8.** XPS is a surface-sensitive and quantitative spectroscopic technique, it gives information about elemental composition (at parts thousand range), electronic state of elements, empirical formula, and chemical states of the material. XPS is not a purely chemical analysis technique; some signals arise from certain atomic layers of the surface, while a small number of signals exit the solid part of an element, and used to investigate the surface chemistry of material at its receiving state or after some amplification treatment (shown in **Figure 2.8**).

2.4.4 Field Emission-Scanning Electron Microscopy (FE-SEM):

Field emission scanning electron microscopy (FE-SEM) is the most extensively utilized microscopy technique because of its versatility. Its various imaging techniques and easy interpretation of images make visualize the specimen surface scanned by a focused high-energy electron beam **[50]**. The FE-SEM produces clear images, with low electrostatic distortion and spatial resolution of ~1 nm (that means 3-6 times better resolution than regular SEM).

Generally, electrons incident on atoms, and it produces signals which give information about materials surface topography, elemental analysis, grain size, particle size, etc. **[51]**. In a vacuum, the electrons created by the field emission source and accelerate in the field gradient. The bombardment resulted in a variety of emissions from the specimen. The detector captures the secondary electrons, which are useful for the generation of sample surface image (**Figure 2.9**). The ray diagram of FE-SEM displays in **Figure 2.9**. The ray diagram of emitted different types of electrons and X-rays during a scan is presented in **Figure 2.10**. The electron either goes away without any interaction or the electron is dispersed within the cloud with potential. The ejection of electrons from a specimen occurs

due to the number of interactions of a specimen with an electron beam. This interaction involves the emission of Auger electrons, back-scattered electrons, secondary electrons, and elemental X-rays (shown in **Figure 2.10**). Depend on energies, the secondary electrons and backscattered electrons are separated out. The detector collects secondary electrons and produces electrical signals, these electrical signals are amplified and converted into video scan images that can appear on the monitor screen as a digital image of a sample surface.

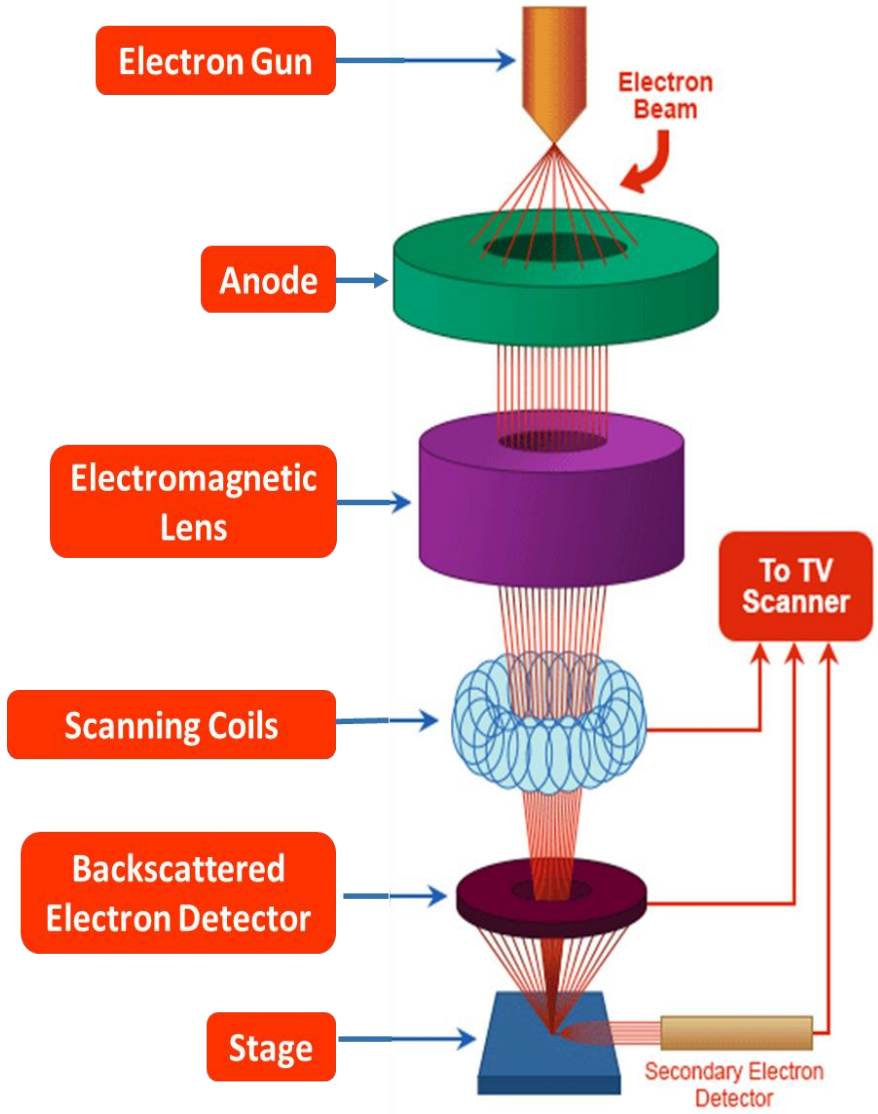

Figure 2.9: Ray diagram of field emission scanning electron microscope **[52]**.

Highly energetic primary electron beam interacts in elastic and inelastic ways, providing a variety of signals. The kinetic energy of an electron does not affect even when its trajectory has been changed, so it is called elastic scattering. However, in inelastic scattering, energy transfer to atoms in a sample from an electron beam, and reduces the energy of electron with a smaller trajectory deviation. If the transmitted energy surpasses the work function of sample material, the electrons can exit the sample surface. If the energy is less than 50 eV of an emitted electron, then it is considered as the secondary electron. Generally, secondary electrons are generated by the upper layer of the sample. The emitted electrons that have energy above 50 eV are known as back-scattered electrons **[53]**.

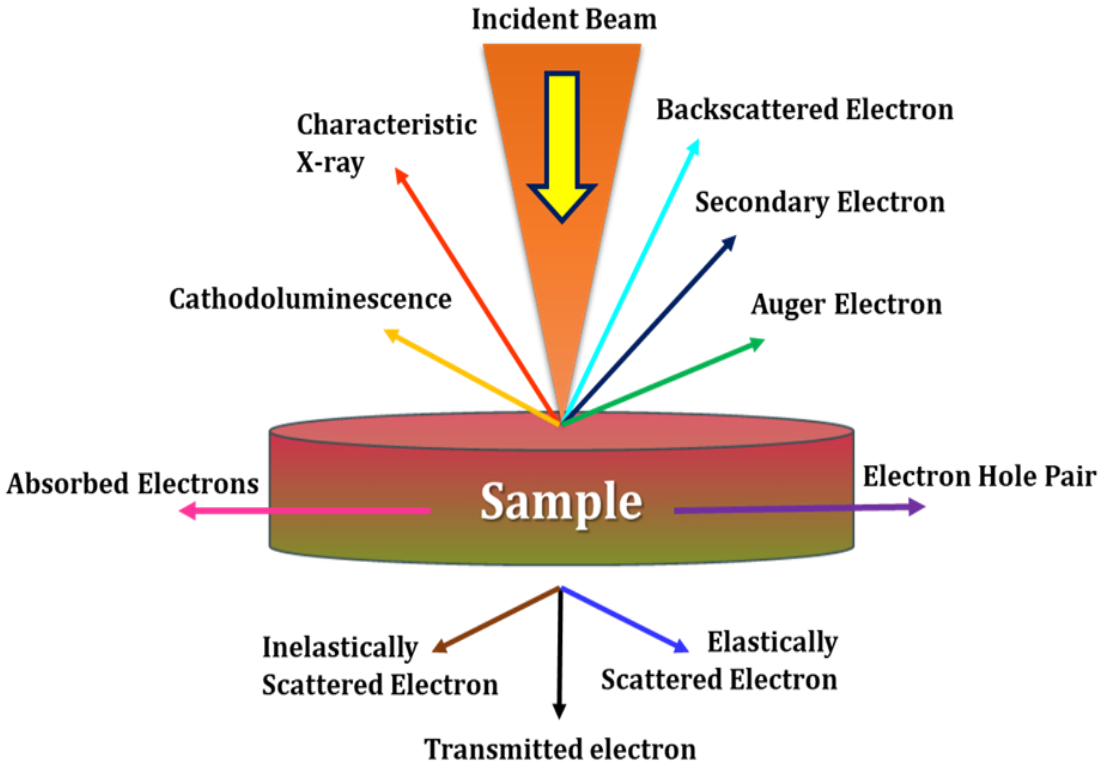

Figure 2.10: Ray diagram for the emission of diverse forms of electrons during scanning **[54]**.

Low voltage FE-SEM used to measure the image without conductive coatings to prevent beam-induced damage to the surface **[50]**. FE-SEM equipment consists of the following components; excitation source (electron beam), detector, pulse processor, and analyzer, etc. Information about the underlying structure of the sample cannot be found by FE-SEM, because it is a surface analysis technique.

2.4.5 Energy Dispersive X-Ray Spectroscopy (EDS):

Energy dispersive X-ray spectroscopy (EDX or EDS) is used to identify the elemental composition or elemental analysis of the specimen. It is organized in conjunction with FE-SEM. The EDS applications include qualitative X-ray mapping, line scans and spot analysis. EDS has mainly based on the concept that a specific atomic structure of elements can exhibit a distinct set of peaks in its emission spectrum. **Figure 2.11** displays a schematic representation of K, L and M electron shells around nucleus of an atom.

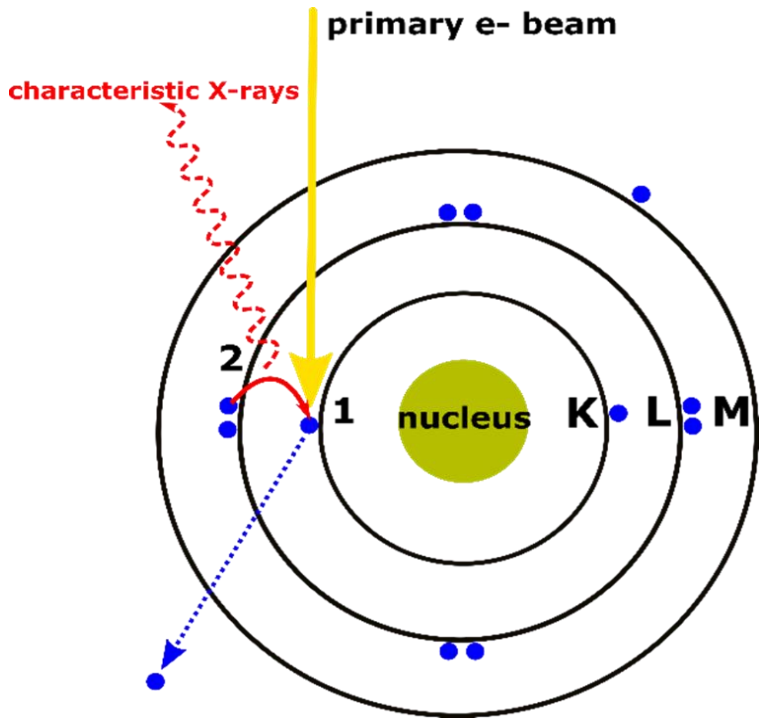

Figure 2.11: A schematic representation of K, L and M electron shells around nucleus of an atom **[55]**.

A high energy beam of electrons or protons or a beam of X-rays is focused on the sample to initiate the ejection of characteristics X-ray. Initially, atom in a specimen consists of unexcited electrons that are a ground-state electron at discrete energy levels. The x-rays are created, when incident electrons cause ejection of an electron from inner shell and outer shell electron fulfils the hole and releases energy **[56]**. The amount and energy of X-rays ejected from a sample are determined by an energy dispersive spectrometer. The energy of X-ray is identical with the energy difference between two shells in atomic structure of the emitted electron and this allows to determine the elemental composition of specimen. The low detection limit varies from ~0.1 to several atomic percentages, depending on the element and sample matrix. Radiation can be analyzed in an X-ray spectrometer and the elements available in sample identified by their characteristics wavelength.

2.5 Electrochemical Techniques:

Generally, the three-electrode (half-cell) system is used in electrochemical investigations to determine specific electrochemical properties of a material, while a two-electrode (full-cell) is suggested for performance evaluation of supercapacitor device **[57]**. The half-cell consists of three electrodes submerged in an electrolyte, namely working electrode, reference electrode, and counter electrode. The schematic of three-electrode cell system described in **Figure 2.12 (a)**. The electrochemical workstation controllers potential difference between reference and working electrodes and measures the current flowing from counter to working electrode. The obtained current is proportional to voltage developed among working electrode and a reference electrode, then converted to a voltage by a current-to-voltage (I/E) converter and recorded with respect to time by the data-acquisition system. It is noted that, the electrical resistance of an ideal electrometer

should be large enough so that it has zero input current. Since, when current passes through a reference electrode, it can change actual potential which in turn affects the precision of data **[58]**.

In the two-electrode (full-cell) systems, two working electrodes sandwiched with a solid electrolyte and it acts as a separator. **Figure 2.12 (b)** shows a schematic of a two-electrode configuration similar to a packaged supercapacitor cell that provides a better presentation for electrochemical performance of electrode in the device **[57]**. It should be noted that, at the given potential range on the electrochemical system, the working electrodes of the three-electrode systems were twice the potential range that applied to the electrodes in the two-electrode cells.

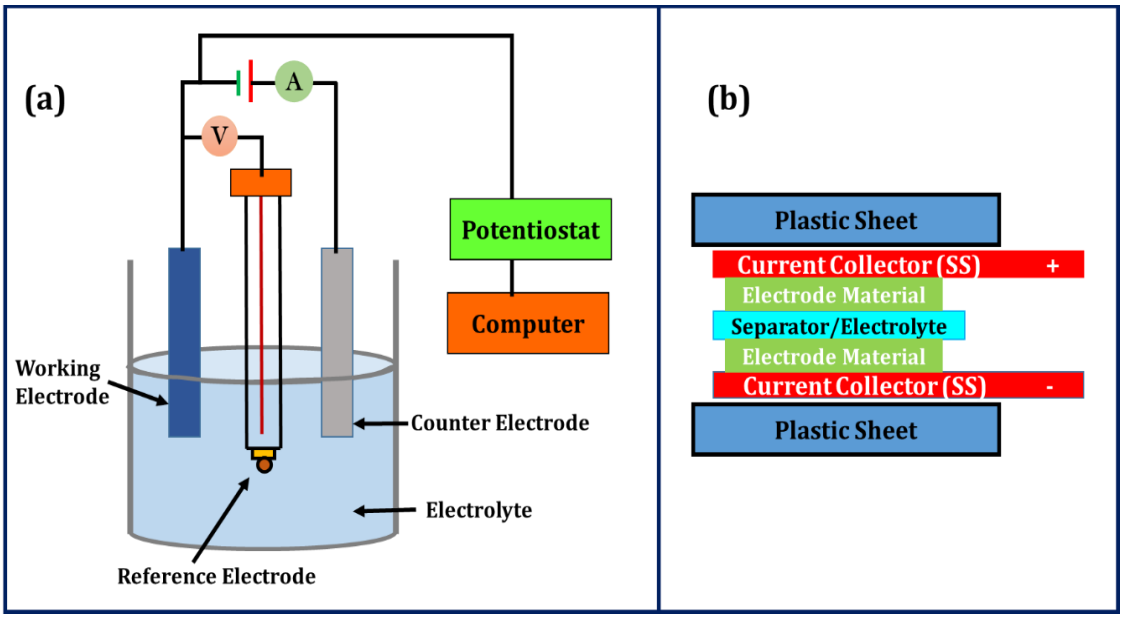

Figure 2.12: Schematic diagram of (a) three-electrode electrochemical (half-cell) system and, (b) two-electrode (full-cell) systems.

Lastly, the capacitance of two or three-electrode based supercapacitors is calculated by the following relation; **[59, 60]**

$$C_s = \frac{\int I(v)\mathrm{dV}}{m \times v \times \Delta V} \quad \text{(For CV)} \qquad 2.5$$

where, C_s is specific capacitance (F g^{-1}), v is scan rate (mV s^{-1}), I (v) is current response (mA), ΔV is operating potential window (V), and m is deposited material mass (g) on electrodes.

$$C_s = \frac{I \times \Delta t}{m \times \Delta V} \quad \text{(For GCD)} \qquad 2.6$$

Where, C_s is specific capacitance (F g^{-1}), I represents current density (mA cm^{-2}), ΔV is a potential window (V), m is deposited material mass (g), and Δt is discharging time (s). As discussed in previous Chapter 1, the energy and power density of supercapacitor can be calculated using the **equation (1.3)** and **(1.4)**, respectively. The capacitance and operational potential window of supercapacitors must be large in order to achieve the maximum value of specific energy. However, the capacitance and potential window of a supercapacitor depend on working electrode material and electrolyte.

A number of techniques including CV, GCD, and EIS studies can be employed to probe the electrochemical capacitive performance of developed materials. For the utilization of thin films as an active electrode for supercapacitor devices, the electrochemical characteristics of thin film are significant.

2.5.1 Cyclic Voltammetry (CV):

Cyclic voltammetry (CV) is electroanalytical technique, it is also called as two way linear sweep voltammetry (LSV). CV is generally used to probe electrochemical evaluation of active material in an electrolyte solution for a supercapacitor. It is a potentiodynamic technique whereby the potential of working electrode sweeping between two voltage limits at a fixed voltage scan rate, as display in **Figure 2.13** and generates basic information about redox behavior,

specific capacitance, charge transfer kinetics, reversibility and material stability, etc. **[61].**

Firstly, the selection of initial and final potential is a very significant factor for CV measurement. The three-electrode system is used to minimize the ohmic resistance. The potential is applied between a reference electrode and working electrode and current is measured among the working electrode and a counter electrode. The range of operating potentials for a CV in the different electrolytes can varies and not only depends on electrode material but also on the composition of electrolytes. Moreover, an operational potential window of working electrode depends on redox potential of material and decomposition capacity of electrolytes. In general, a positive potential limit is caused by high current arising from oxidation of electrolyte as well as reduction of electrolyte brings negative potential limitation.

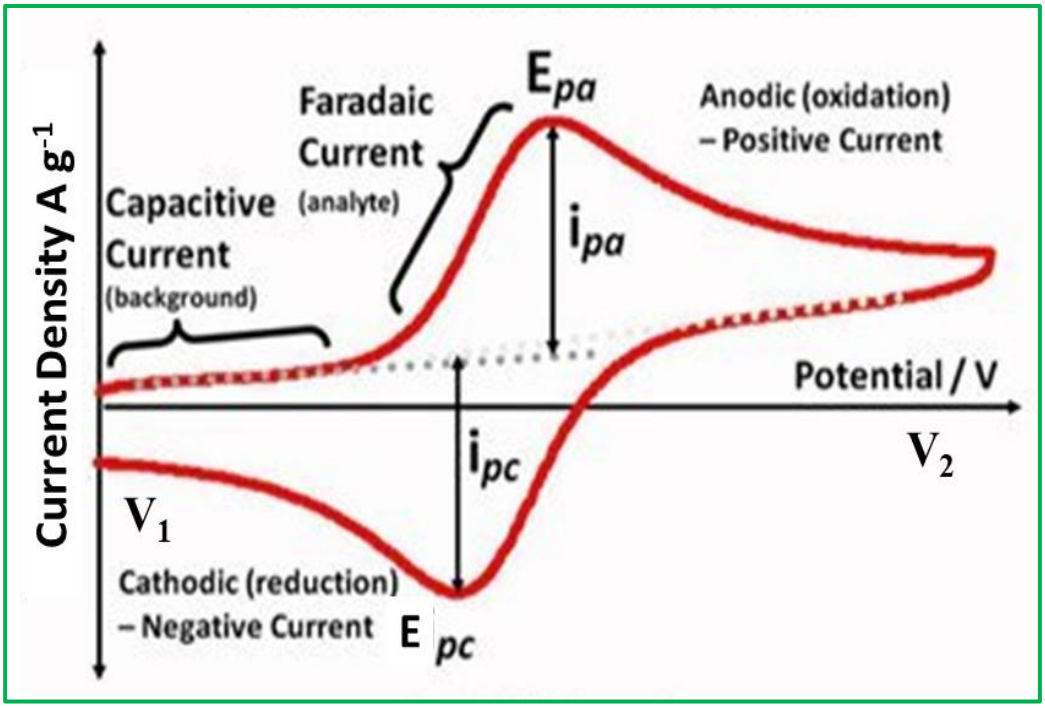

Figure 2.13: Typical CV curve of single electrode with reversible redox reaction **[62].**

In CV, the potential is swept within two fixed values (i.e. in a given potential window). When the voltage achieves point V_2, the scan swept back and voltage reversed to point V_1. Where, V_1 and V_2 are the potential limits, i_{pc} and i_{pa} represent the cathodic and anodic peak currents and E_{pc} and E_{pa} are the cathodic and anodic peak voltages of resulted voltammogram. During the forward scan, a current increases as potential reaches oxidation potential of the electroactive material, but it decreases as potential further increases due to high concentration of electrolytic ions at the electroactive sites. In reversible redox couple, the product produced in initial oxidation reaction reduces during applied reverse potential and generates reverse polarity current.

2.5.2 Galvanostatic Charge-Discharge (GCD):

Galvanostatic charge-discharge (GCD) also called chronopotentiometry (CP) is a well-known measurement technique that can provide useful information about capacitance, energy density, power density, equivalent series resistance as well as cycle life. In GCD technique, a constant current is provided to working electrode, and the corresponding potential with respect to a reference electrode is measured. When the working electrode charge and discharge at fix current density, the quantity of charge transferred among the electrode remains constant. Change in potential and time are measured and varies based on applied current density. The schematic of charge-discharge curve is shown in **Figure 2.14**.

However, to characterize the cycle life of supercapacitors, the two electrode test cell is favorable because it is analogous to the more practical operating conditions. The nature of charge-discharge curve reveals the charge storage mechanism of a specified electrode. If the charge-discharge curve is linear in nature, then the charges are stored by an electric double-layer mechanism

otherwise non-linear nature indicates that the charges are stored by a pseudocapacitive mechanism **[63]**.

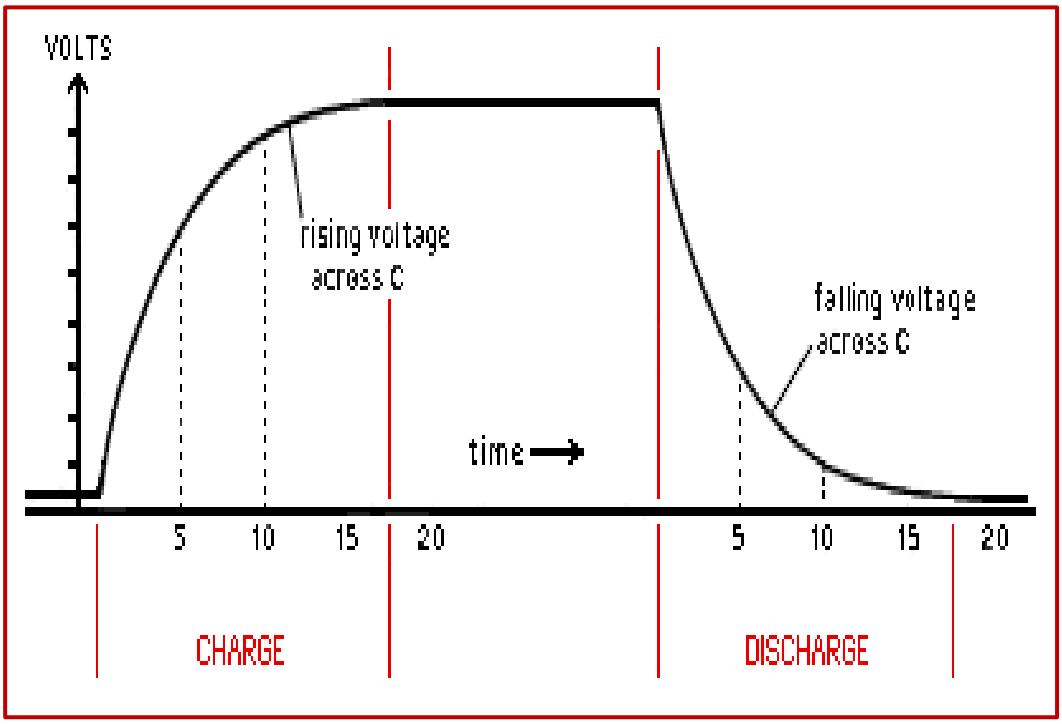

Figure 2.14: Schematic of galvanostatic charge-discharge curve **[64].**

2.5.3 Electrochemical Impedance Spectroscopy (EIS):

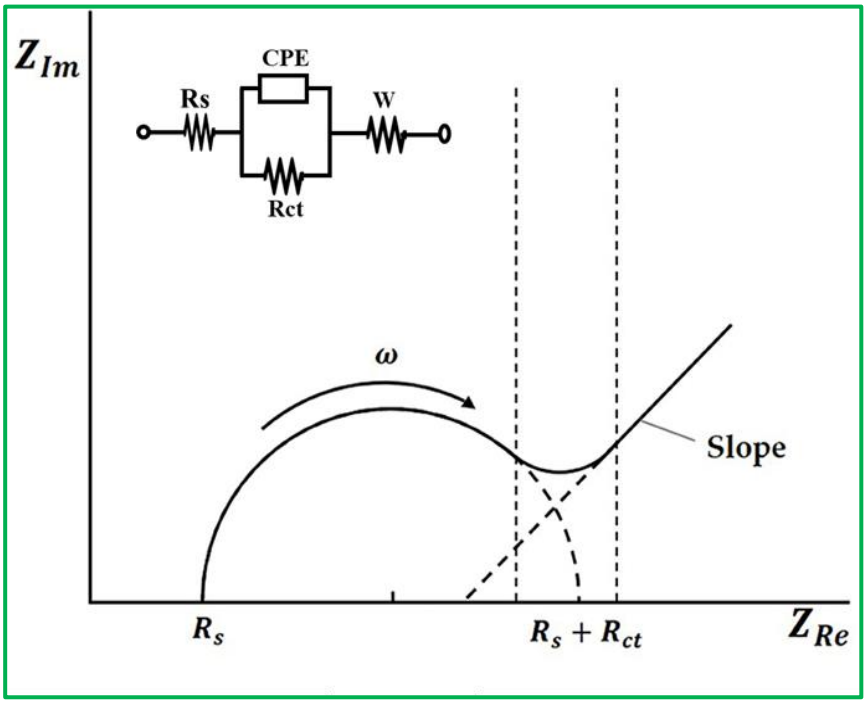

Figure 2.15: Nyquist plot with electrical equivalent circuit **[65].**

Electrochemical impedance spectroscopy (EIS) determines the impedance of material in a set of frequencies and beneficial to provide information about the resistance of electrode-electrolyte interface and charge transfer process **[66]**. The small AC signal (5 to 50 mV) is applied to the supercapacitor cell over a set of frequencies from 10 μHz to 1 MHz. The output signals are a current response of applied AC signals. The EIS spectra can be analyzed and interpreted by Nyquist and bode plot **[67]**.

Figure 2.15 illustrates a Nyquist plot with equivalent circuits and involves the following circuit elements: R_s: ohmic resistance, R_s+R_{ct}: charge transfer resistance, CPE: constant phase element and W: Warburg impedance element. The EIS technique is essential because it determines the frequency dependent and independent electrical components from Nyquist plot. Equivalent circuit models based on basic electric circuit elements such as capacitors and resistors are used to simulate complicated electrochemical processes near the electrode-electrolyte interface **[68]**. Components of equivalent circuits and the equations of their current-voltage relationships are illustrated in **Table 2.1**. The resistor is not dependent on the frequency and does not contain imaginary elements. Furthermore, inductor and capacitor have an imaginary element of impedance **[69]**.

Table 2.1: Common electrical elements.

Component	Current Vs. Voltage	Impedance
Resistor	E= IR	Z = R
Inductor	E = L di/dt	Z = jωL
Capacitor	I = C dE/dt	Z = 1/jωC

The imaginary and real parts of impedance are described in Nyquist plot shown in **Figure 2.15**. In Nyquist plot, the real and imaginary parts are plotted on X and Y axis, respectively. The inset diagram displays a fitted equivalent circuit associated with the Nyquist plot. In this figure, the semi-circular loop is associated with resistance of charge transfer. In addition, solution resistance is an important term in the impedance of electrochemical cell. The resistance of electrolytic solution depends on concentration of ions, type of ion, temperature and geometry of region in which the electric current flows. Also, transfer of these charges has fixed kinetics and the kinetics depend on reaction type, temperature, concentration, and potential of reaction products. Furthermore, ionic diffusion can create an impedance called Warburg impedance. Also, impedance is based on the frequency of potential irritability.

The Warburg impedance is smaller at higher frequencies, because the diffusing reactant does not need to go very far. Also, real-axis intercept (at high frequencies) corresponds to the ohmic resistance. At lower frequencies, the reactors have to diffuse more distance, increases the Warburg-impedance. In Nyquist plot, Warburg impedance described by diagonal line with an inclination of 45° arises due to mass transport of ions. In EIS study, capacitors are normally not ideally behave, rather they act as constant phase elements (CPE) **[69]**. In short, a supercapacitor behaves as a capacitor and pure resistor at low and high frequencies, respectively. Moreover, in the medium-frequency range, the physical and morphological properties of electroactive material play a crucial role in achieving the capacitance value and serving as an association of resistors and capacitors **[70]**. The impedance response mainly depends on the operating voltage **[71]**. The obtained data fitted with different interface parameters by algorithms

with minimum chi-square value. EIS is employed as an important characterization technique for applications to many material systems such as plating, corrosion, fuel cells, batteries, etc. Also, EIS gives the opportunity to determine the capacitance as a function of frequency **[72]**.

All electrochemical tests described in **Section 2.5** were analyzed using ZIVE MP1 electrochemical workstation. The collected data was utilized to evaluate specific capacitance of electrodes. The EIS was measured under the following circumstances: (i) Open circuit potential condition in the frequency range: 100 kHz-100 MHz; (ii) 10 mV AC-perturbation amplitude of a sinusoidal signal. To analyze typical physical processes, "ZSimpWin" equivalent circuit editor was used to fit the equivalent circuit in accordance with the experimental Nyquist spectra.

2.6 Reference:

1. B. E. Conway, J. Electrochem. Soc., 138, (1991), 1539-1548.
2. B. E. Conway, Electrochemical Supercapacitors: Scientific Fundamentals and Technological Applications, Kluwer-Plenum, New York, (1999), pp. 1-697.
3. B. E. Conway, V. I. Birss, J. Wojtowicz, J. Power Sources, 66, (1997), 1-14.
4. X. Cui, Y. Xu, X. Zhang, X. Cheng, S. Gao, H. Zhao, L. Huo, Sensor Actuat B-Chem, 247, (2017), 681-690.
5. G. Brammertz, B. Vermang, H. ElAnzeery, S. Sahayaraj, S. Ranjbar, M. Meuris, J. Poortmans, Thin Solid Films, 616, (2016), 649-654.
6. D. A. Minkov, G. M. Gavrilov, E. Marquez, S. M. Fernandez Ruano, A. V. Stoynova, Optik, 132, (2017), 320-328.
7. M. Feinaeugle, P. Gregorčič, D. J. Heath, B. Mills, R. W. Eason, Appl. Surf. Sci., 396, (2017), 1231-1238.
8. I. Gurrappa, L. Binder, Sci. Technol. Adv. Mater., 9, (2008), 1-11.
9. K. L. Chopra, I. J. Kaur, Thin film Device Application, Plenum Press, New York (1983), pp. 101.
10. J. George, Preparation of Thin Films, Marcel Dekker, Inc., New York, (1992), pp. 13-19.
11. K. Byrappa, T. Adschiri, Prog. Cryst. Growth Ch., 53, (2007), 117–166.
12. K. Byrappa, N. Keerthiraj, S. M. Byrappa, Handbook of Crystal Growth (2nd Edition), Bulk Crystal Growth, (2015), 535-575.
13. G. W. Morey, P. Niggli, A Review, J. Am. Chem. Soc., 35, (1913), 1086–1130.
14. R. A. Laudise, The Growth of Single Crystals, Prentice-Hall, Englewood Cliffs, NJ, (1970), pp. 278–281.
15. A. Rabenau, Angew. Chem. Int. Ed., 24, (1985), 1026–1040.
16. A. N. Lobachev, (ed.), Crystallization Processes under Hydrothermal Conditions, Consultants Bureau, New York, (1973), pp. 1–255.
17. M. Yoshimura, H. Suda, Hydrothermal Processing of Hydroxyapatite: Past, Present, and Future in: Hydroxyapatite and Related Materials (P. W. Brown and B. Constanz, eds.), CRC Press, Inc, (1994), pp. 45–72.
18 M. Yoshimura, K. Byrappa, J. Mater. Sci., 43, (2008), 2085–2103.
19. R. I. Walton, Chem. Soc. Rev., 31, (2002), 230-238.

20. W. L. Suchanek, R. E. Riman, Adv. Sci. Tech, 45, (2006), 184–193.
21. M. Shandilya, R. Rai, J. Singh, Adv. Appl. Ceram, 115, (2016), 354-376.
22. Y. F. Nicolau, Appl. Surf. Sci., 22-23, (1985), 1061-1074.
23. S. S. Kale, R. S. Mane, H. M. Pathan, A. V. Shaikh, O. S. Joo, S. H. Han, Appl. Surf. Sci., 253, (2007), 4335-4337.
24. S. D. Sartale, C. D, Lokhande, Mater. Chem. Phys., 72, (2001), 101-104.
25. H. M. Pathan, S. S. Kale, C. D. Lokhande, S. H. Han, O. S. Joo, Mater. Res. Bull., 42, (2007), 1565-1569.
26. T. P Niesen, M. R. De Guire, Solid State Ion., 151, (2002), 61-68.
27. T. P. Niesen, M. R. De Guire, J. Electroceram., 6, (2001), 169–207.
28. M. Ristov, Gj. Sinadinovski, I. Grozdanov, Thin Solid Films, 123, (1985), 63-67.
29. S. G. Kandalkar, C. D. Lokhande, R. S. Mane, S. H. Han, Appl. Surf. Sci., 253, (2007), 3952-3956.
30. H. M. Pathan, C. D. Lokhande, Bull. Mater. Sci., 27, (2004), 85–111.
31. R. R. Salunkhe, D. S. Dhawale, T. P. Gujar, C. D. Lokhande, Mater. Res. Bull., 44, (2009), 364-368.
32. V. D. Patake, C. D. Lokhande, Appl. Surf. Sci., 254, (2008), 2820-2824.
33. R. R. Salunkhe, C. D. Lokhande, Sensor Actuat B-Chem, 129, (2008), 345-351.
34. https://holmarc.com/silar_controller_with_stirrer.php, SILAR machine.
35. G. Hodes, Chemical Solution Deposition of Semiconductor Films, Marcel Dekker Inc., New York (2001), pp. 64.
36. C. Hu, X. Dang, S. Hu, J. Electroanal. Chem., 572, (2004), 161-171.
37. K. L. Chopra, Thin Film Phenomena, McGraw Hill Book Co. New York, (1969), pp. 864.
38. A. A. Bunaciu, E. gabriela Udriştioiu, H. Y. Aboul-Enein, Crit. Rev. Anal. Chem, 45, (2015), 289–299.
39. B. D. Cullity, Elements of X-rays Diffraction, 3rd Edition, Prentice Hall, (2001), 664.
40. http://xrd.co/component-parts-x-ray-diffractometer, Component parts of an x-ray diffractometer.
41. F. Settle, J. Liq. Chromatogr. R. T., (1998), 3072-3076.

42. J. Preudhomme, P. Tarte, Spectrochim Acta A, 27, (1971), 1817-1835.
43. R. A. Nyquist, R. O. Kagel, Infrared Spectra of Inorganic Compounds, 1st edition, Academic Press INC, New York, (1971), pp. 500.
44. G. R. Chatwal, S. K. Anand, Instrumental methods of chemical analysis, 5th Edition, Himalaya Publishing group, (2002), pp. 794.
45. C. Nordling, S. Hagström, K. Siegbahn, Z. Physik, 178, (1964), 433–438.
46. C. D. Wagner, W. M. Riggs, L. E. Davis, J. F. Moulder, X-ray Photoelectron Spectroscopy in: G. E. Muilenberg (Eds.), X-ray Photoelectron Spectroscopy, Perkin Elmer Corporation, Minnesota, (1979), pp. 1-28.
47. S. J. Kerber, T. L. Barr, G. P. Mann, W. A. Brantley, E. Papazoglou, J. C. Mitchell, J. Mater. Eng. Perform. 7, (1998), 334–342.
48. S. Hüfner, Photoelectron Spectroscopy, Principles and Applications, 2nd edition, Springer-Verlag, Germany, (1995).
49. https://epm.univie.ac.at/research/low-dimensional-quantum-solids/methods/, X-Ray Photoemission Spectroscopy.
50. T. Pradeep, Nano: The Essentials, Understanding Nanoscience and Nanotechnology. US: McGraw-Hill Education, (2007).
51. http://photometrics.net/field-emission-scanning-electronmicroscopy-fesem/, FE-SEM explanation.
52. https://www.nanoimages.com/sem-technology-overview/sem_img2/, FE-SEM image.
53. M. Broussely, G. Pistoia, Industrial Applications of Batteries: From Cars to Aerospace and Energy Storage, 1st edition, (2007).
54. https://www.azom.com/article.aspx?ArticleID=16146, Interaction electron beam with sample.
55. https://www.thermofisher.com/blog/microscopy/edx-analysis-with-sem-how-does-it-work/, EDX Analysis with SEM: How Does it Work?
56. D. C. Bell, A. J. Garratt-Reed, Energy Dispersive X-ray Analysis in the Electron Microscope. Microscope Handbooks Series. New York: BIOS Scientific, (2003), pp. 160.
57. M. D. Stollera, R. S. Ruoff, Energy Environ. Sci., 3, (2010), 1294-1301.

58. D. A. Skoog, Voltammetry, in Principles of Instrumental Analysis, ed. Fort Worth, Texas Saunders College Pub., (1992).
59. A. Bard, L. Faulkner, Electrochemical Methods: Fundamentals and Applications, 2nd edition, John Wiley & Sons, Inc, (2001), pp. 864.
60. S. S. Pujari, S. A. Kadam, Y. R. Ma, P. K. Katkar, S. J. Marje, S. A. Khalate, A. C. Lokhande, U. M. Patil, J. Electron. Mater., 49, (2020), 3890–3901.
61. N. Aristov, A. Habekost, World J. Chem. Educ., 3, (2015), 115-119.
62. M. S. Khan, A. Asif, S. Khawaldeh, A. Tekin, J. Electr. Bioimpedance, 9, (2018), 3-9.
63. H. Gao, J. Xiang, Y. Cao, Appl. Surf. Sci., 413, (2017), 351-359.
64. http://www.michaelsharris.com/electronics/images/capRCcurve.gif, Charge-discharge graph.
65. C. Song, Z. Peng, X. Lin, H. Luo, M. Song, L. Jin, X. Xiao, H. Ji, Front. Chem., 8, (2020), 1-9.
66. A. Chu, P. Braatz, J. Power Sources, 112, (2002), 236-246.
67. M. E. Orazem, B. Tribollet, Preliminary Graphical Methods in: Electrochemical Impedance Spectroscopy, A John Wiley & Sons, Inc., New Jersey, (2008), pp. 333.
68. R. de Levie, Electrochim. Acta, 9, (1964), 1231-1245.
69. https://www.gamry.com/application-notes/EIS/basics-of-electrochemical-impedance-spectroscopy/, Basics of electrochemical impedance spectroscopy.
70. V. Ganesh, S. Pitchumani, V. Lakshminarayanan, J. Power Sources, 158, (2006), 1523-1532.
71. D. J. Lee, W. W. Lin, AIChE Journal, 41, (1995), 2314–2317.
72. C. Gabrielli, Use and application of electrochemical impedance techniques, technical report number 24, Solartron analytical, France, (1997).

CHAPTER -3

SYNTHESIS, CHARACTERIZATION AND SUPERCAPACITIVE PERFORMANCE OF COBALT MANGANESE PHOSPHATE THIN FILM BY HYDROTHERMAL METHOD

CHAPTER 3

Synthesis, Characterization and Supercapacitive Performance of Cobalt Manganese Phosphate Thin Film by Hydrothermal Method

Sr. No.	Title		Page No.
3.1	**Introduction**		99
	SECTION – A **Hydrothermal Synthesis and Characterization of Cobalt Manganese Phosphate Thin Films**		
3.2.A.1	**Introduction**		101
3.2.A.2	**Experimental Details**		102
	3.2.A.2.1	*Substrate*	102
	3.2.A.2.2	*Substrate Cleaning*	103
	3.2.A.2.3	*Chemicals*	103
	3.2.A.2.4	*Synthesis of Cobalt Manganese Phosphate Thin Films*	104
	3.2.A.2.5	*Materials Characterization*	105
3.2.A.3	**Results and Discussion**		106
	3.2.A.3.1	*Film Formation and Reaction Mechanism*	106
	3.2.A.3.2	*XRD Study*	108
	3.2.A.3.3	*FTIR Study*	109
	3.2.A.3.4	*XPS Study*	111
	3.2.A.3.5	*FE-SEM Study*	112
	3.2.A.3.6	*EDS Study*	115
3.2.A.4	**Conclusions**		116
	SECTION – B **Supercapacitive Performance Evaluation of Cobalt Manganese Phosphate Thin Films**		
3.2.B.1	**Introduction**		117
3.2.B.2	**Experimental Setup for Supercapacitive Studies**		117

3.2.B.3	**Results and Discussion**		**118**
	3.2.B.3.1	*CV Study*	**118**
	3.2.B.3.2	*GCD Study*	**122**
	3.2.B.3.3	*EIS Study*	**125**
	3.2.B.3.4	*Stability Study*	**127**
3.2.B.4	**Conclusions**		**128**
3.3	**References**		**129**

3.1 Introduction:

The increase in consumption of fossil fuel and environmental deterioration requires not only efficient, clean, and sustainable energy sources, but also new technologies related to energy transformation and storage have been developed to fulfill the increasing societal demands **[1]**. Among the number of energy storage devices, supercapacitor (SCs) is emerged as a new class of energy storage device, due to its fast and highly reversible storage as well as electrical energy, high power density, high charge-discharge cycle life, low fabrication cost, and safe operation. So, it attracts more attention in the area of high power applications **[2, 3]**. However, energy density of SC's is lower (compared to batteries), to satisfy the increasing demand for the industries. Therefore, to enhance energy density of supercapacitor: the potential window, capacitance or both must be extended **[4]**. Binary transition metal-based oxides/hydroxides, sulfides, and phosphates have high electrochemical activity due to their complex chemical composition. Furthermore, the synergetic effects of binary transition metals can contribute to high specific capacitance **[5]**. So far, there are numerous reports on the preparation of transition metal oxides (TMOs) **[6]** and transitional metal phosphates (TMPs) **[7]** as active materials for supercapacitor electrodes. Generally, TMPs are superior in specific capacitances compared to carbon-based materials and better in cycling efficiency than conductive polymers. Metal phosphate-based materials can be used efficiently due to their exceptional electrochemical properties and polar nature. TMPs as pseudocapacitive materials are inexpensive, electrochemically active materials that have been prepared for use in SCs as well as they exhibit a broad range of potential applications (e.g. batteries, solar cells, etc.) **[8-10]**.

In particular, metal phosphates with transition metal elements such as Co, Mn, and Ni can produce more redox states, which are helpful for pseudocapacitors. Therefore, researchers have found many electrochemically active TMPs, such as $Ni_2P_2O_7$ **[11]**, $Mn_3(PO_4)_2$ **[12]**, and $Co_3(PO_4)_2$ **[13]** as energy storage materials. Especially, cobalt phosphate and manganese phosphate are promising electrodes for SCs due to their rich redox behaviour, high energy density, superior cyclic stability and low cost **[13, 14]**. However, cobalt phosphate also has some shortcomings like poor electrical conductivity and poor cycling life and the specific capacitance of manganese phosphate is also low. So, the combination of cobalt and manganese phosphate resolves these drawbacks and provides an effective way to achieve high electrochemical performance (cyclic stability, specific capacitance) **[5, 15]**. Cobalt manganese phosphate was studied for supercapacitor applications, because of multiple oxidation states (Co^{2+}, Co^{3+}, Mn^{2+}, Mn^{3+}, Mn^{4+}) of cobalt and manganese, and different structural possibilities **[15, 16]**. The excellent supercapacitive behavior of cobalt manganese phosphate is ascribed to the synergy between multi-metals in electrode and enhanced oxidation states with uniform distribution of Mn and Co elements due to its unique homogeneous composition. Depend on combined advantages, cobalt manganese phosphate shows outstanding electrochemical performance (well-defined redox behaviour) for supercapacitor applications.

Inspired by research interests in the synergistic effect of binary TMPs for SCs application, cobalt manganese phosphate (Co-Mn Phosphate) thin films are deposited directly (binder-free approach) on stainless steel (SS) substrate at different concentrations of cobalt (Co) and manganese (Mn) using hydrothermal method. Further, the influence of Co and Mn concentrations on physico-chemical

properties of Co-Mn Phosphate thin films are studied. This chapter is distributed into two parts (Section A and B). Section 'A' deals with the synthesis of Co-Mn Phosphate thin films by hydrothermal method and their structural and morphological characterization. Section 'B' is related to the supercapacitor performance evaluation of Co-Mn Phosphate thin film electrodes.

SECTION – A

Hydrothermal Synthesis and Characterization of Cobalt Manganese Phosphate Thin Films

3.2.A.1 Introduction:

Some successful efforts have been done to prepare cobalt manganese phosphate thin films by hydrothermal method **[15]**. A hydrothermal method is extensively utilized to develop functional nano/micro materials with definite shapes and sizes. The expected nano/microstructured thin films can be simply achieved by regulating the rate of reaction and growth through hydrothermal method. According to the literature survey, a study on the preparation of cobalt manganese phosphate material by a hydrothermal method for energy-related (supercapacitor) applications is rarely investigated. So, there is a chance to investigate the performance of a novel cobalt manganese phosphate electrode. The attractive strategy for supercapacitor electrode preparation is the direct growth of nano/micro-architectures on stainless steel (SS) conductive substrate by a binder-free hydrothermal synthesis method. These unique binder-less electrodes can reduce internal resistance, enhance the use of active materials and maintain a faster redox reaction **[13, 17]**. This chapter is about the synthesis and

characterization of cobalt manganese phosphate electrodes by hydrothermal method with varying concentrations of cobalt and manganese.

3.2.A.2 Experimental Details:

3.2.A.2.1 Substrate:

It is known that, a good lattice match among substrate and layer deposited on the substrate are a significant factors and that helps to growth of material **[18]**. Also, mechanical flexibility, high porosity, excellent conductivity, and high surface area of support substrates effectively increase the performances of SC's. Different substrates such as stainless steel (SS), carbon cloth, carbon-based paper, Ti foil, graphene sponge, nickel foam, Indium doped Tin Oxide (ITO) coated substrate, etc. act as a conductive backbone to support the active materials in SC's **[19]**. The supporter substrates contribute a conducive framework for better adhesion to the active material. The growth of active materials on the conducting substrate introduces direct electrical contact with a substrate, which helps to enhance the more efficient electrochemical reaction than the traditional binder enriched casting method. Lately, stainless steel has been comprehensively used as a substrate for the preparation of supercapacitor electrodes.

In this investigation, SS substrate is employed as a current collector for direct growth of TMP's (cobalt manganese phosphate) thin film, since SS substrate offers a 2D surface for deposition and doesn't participate in an electrochemical reaction. Additionally, it eludes usage of polymer binders and additives in active material coating. Binder less electrode shows high conductivity than electrodes prepared by slurry coating technique and consequently displays better electrochemical efficiency. Previous reports have revealed that, the improved

structure and morphology of active materials with good adhesion on the current collector helps the charge transfer process more effectively **[20, 21].**

3.2.A.2.2 Substrate cleaning:

Substrate cleaning plays a very essential role in the deposition of good quality thin films. Utmost cleansed substrate is essential for deposition of thin films, as the cleaned substrate surface gives nucleation centres that help to grow uniform films. A high conducting substrate is a basic requirement to investigate the supercapacitive performance of thin film electrodes. So, the SS substrate is appropriate for supercapacitors by the reason of its high conductivity and low cost. Stainless steel (SS) substrates were cleansed according to the following procedure;

- ❒ The substrates were mirror-polished applying polish paper (zero grade).
- ❒ The substrates were washed using detergent and cleaned with double distilled water (DDW).
- ❒ After that, substrates were ultra-sonically cleaned in DDW for 20 min, and
- ❒ Subsequently, the substrate was dried in ambient condition and utilized for the deposition of active materials.

3.2.A.2.3 Chemicals:

For the synthesis of cobalt manganese phosphate thin film, cobalt chloride hexahydrate ($CoCl_2 \cdot 6H_2O$), manganese chloride tetrahydrate ($MnCl_2.4H_2O$), and potassium dihydrogen orthophosphate (KH_2PO_4) (Sigma Aldrich) were used as received. Urea [$CO(NH_2)_2$], potassium hydroxide (KOH), and sodium sulfate (Na_2SO_4) were provided by Alfa Aesar. All reagents were analytical reagent (AR) grade and used as received (without further purification). The commercially available SS substrate (304 grade) was used as a current collector.

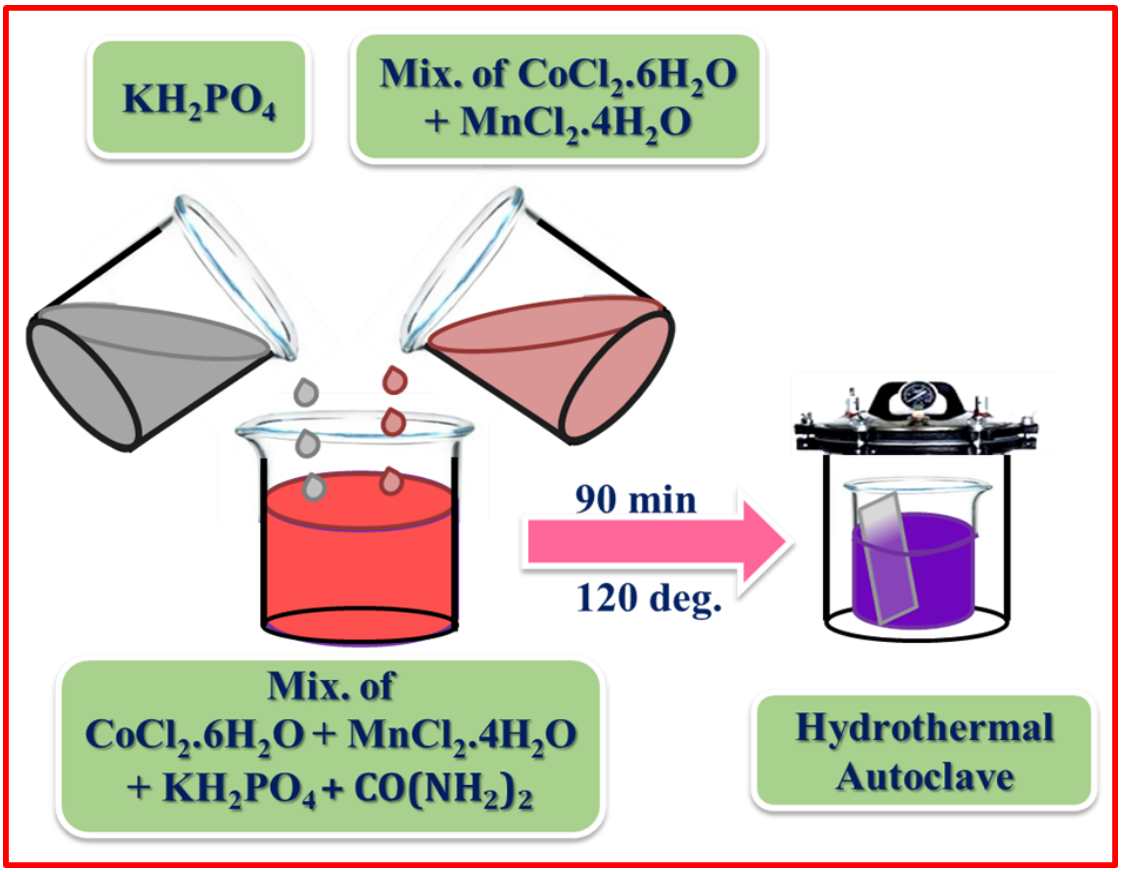

Figure 3.1: Schematic diagram of hydrothermal method for cobalt manganese phosphate thin film deposition.

3.2.A.2.4 Synthesis of Cobalt Manganese Phosphate Thin Films:

The preparation of Co-Mn Phosphate on SS substrate via hydrothermal method is shown in schematic **Figure 3.1**. In a typical synthesis, five distinct baths are prepared with different molar concentrations of $CoCl_2 \cdot 6H_2O$, $MnCl_2.4H_2O$, and KH_2PO_4 in 60 mL DDW, as described in **Table 3.1** and denoted as H-CMP-1, H-CMP-2, H-CMP-3, H-CMP-4, H-CMP-5. Then, 0.050 M of $CO(NH_2)_2$ was added in above mentioned five solution baths and stirred vigorously to form a transparent solution. The well cleaned SS substrates dipped vertically in prepared solutions and these baths were transferred to a hydrothermal autoclave and maintained in 120°C for 90 min. After 90 min, violet to milky white-colored films (as shown in **Figure 3.2**) of cobalt manganese phosphate was collected on SS substrates, then

rinsed with DDW several times to eliminate loosely bonded particles and dried at room temperature. The prepared thin film electrodes of cobalt manganese phosphate on SS substrates were directly used for further characterization.

Table 3.1: Different compositions of cobalt and manganese precursors for synthesis of cobalt manganese phosphate thin film and corresponding notations.

Sr. No.	$CoCl_2.6H_2O$ (M)	$MnCl_2.4H_2O$ (M)	KH_2PO_4 (M)	$CO(NH_2)_2$ (M)	Notation
1)	0.030	0.000	0.020	0.050	H-CMP-1
2)	0.023	0.007	0.020	0.050	H-CMP-2
3)	0.015	0.015	0.020	0.050	H-CMP-3
4)	0.007	0.023	0.020	0.050	H-CMP-4
5)	0.000	0.030	0.020	0.050	H-CMP-5

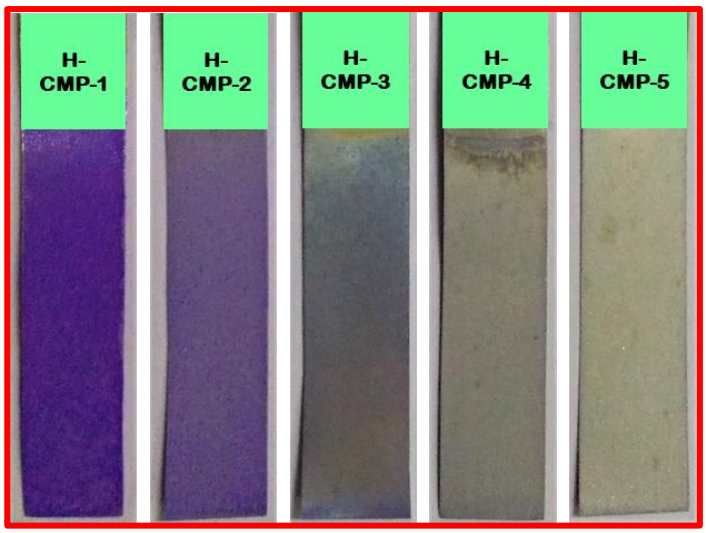

Figure 3.2: Photographs of hydrothermally synthesized cobalt manganese phosphate thin films (H-CMP-series) for different concentrations of Co:Mn.

3.2.A.2.5 Materials Characterization:

The prepared electrodes were characterized structurally by X-ray diffraction (XRD), (Rigaku Miniflex-600) using target Cu Kα (λ = 1.5418 Å) radiation source in the 2θ range from 5° to 80°. Fourier transform infrared (FT-IR) spectroscopy analysis was carried out on Alpha (II) Bruker unit (Bruker

Corporation) using a KBr pellet at ambient temperature to study the available functional groups in material. The elements and their valence state were probed by X-ray photoelectron spectroscopy (XPS, K-alpha, and Thermo Fisher, UK). The morphology of prepared electrodes was probed using field emission scanning electron microscopy (FE-SEM, model JEOL-JSM 6360) equipped with an X-ray energy-dispersive spectrometer (EDS). The electrochemical measurements were carried out by WonATech made ZIVE MP1 electrochemical workstation.

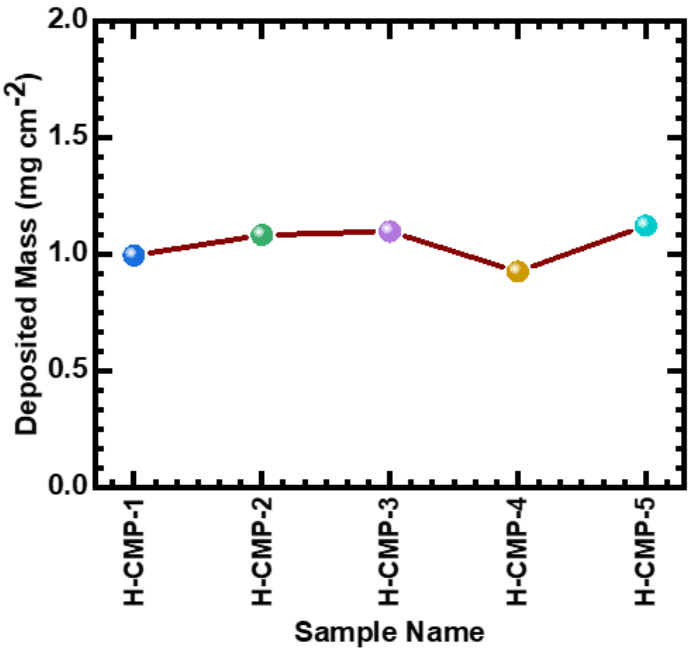

Figure 3.3: Cobalt manganese phosphate thin film thickness for different compositions of Co:Mn.

3.2.A.3 Results and Discussion:

3.2.A.3.1 Film Formation and Reaction Mechanism:

The deposition of Co-Mn Phosphate thin films are carried out using different Co and Mn concentrations via a hydrothermal method. In hydrothermal synthesis, the aqueous solutions of dissolved precursors are utilized for deposition of thin film on SS substrate. Cobalt chloride/manganese chloride and potassium

dihydrogen phosphate are used as precursors of cobalt-manganese and phosphate along with urea as a hydrolyzing agent. The Co-Mn Phosphate solid thin films are prepared from a supersaturated precursor solution baths. In a solution bath, heterogeneous nucleation is essential for rapid growth of film on SS substrate **[22, 23]**. In typical thin film formation, initially, decomposition of urea takes place above 90°C by producing CO_2 and NH_4^+ ions **(Eq^n. 3.1) [23, 24]**.

$$CO(NH_2)_2 + 3H_2O \xrightarrow{\Delta} 2NH_4^+ + CO_2\uparrow + 2OH^- \quad 3.1$$

According to the above reaction, the released NH_4^+ ions perform as a complexing agent in the bath, and Co^{2+} and Mn^{2+} ions available in solution get complexed by means of $[Co_xMn_{3-x}(NH_3)]^{6+}$ **[Eq^n. (3.2)]**. This complex slowly releases Co^{2+}/Mn^{2+} ions to prevent rapid nucleation and subsequent homogeneous nucleation in the solution and control the reaction rate.

$$(x)CoCl_2 + (3\text{-}x)MnCl_2 + NH_4OH \xrightarrow{\Delta} [Co_xMn_{3-x}(NH_3)]^{6+} + H_2O + 6Cl^- \quad 3.2$$

On other hand, phosphate decomposes as per **(Eq^n. 3.3),**

$$KH_2PO_4 \xrightarrow{\Delta} H_2PO_4^- + K^+ \quad 3.3$$

Finally, Co^{2+}/Mn^{2+} ions from cobalt/manganese complex and $H_2PO_4^-$ ions from phosphate precursor react with each other and produces $Co_xMn_{3-x}(PO_4)_2.nH_2O$ material in thin film form, as per the following reaction **(Eq^n. 3.4),**

$$[Co_xMn_{3-x}(NH_3)]^{6+} + 2H_2PO_4^- + nH_2O \xrightarrow{\Delta} Co_xMn_{3-x}(PO_4)_2.nH_2O + 2H_2^+ + NH_3\uparrow \quad 3.4$$

The mass of deposited Co-Mn Phosphate material on SS substrate with different Co:Mn compositions is measured by weight difference method **(Figure 3.3)**. For samples H-CMP-1, H-CMP-2, H-CMP-3, H-CMP-4, and H-CMP-5, the deposited weights are 0.997, 1.085, 1.10, 0.928, and 1.125 mg cm^{-2}, respectively. It is seen that, the rising concentration of manganese gradually increases the weight

of thin films may be due to the faster growth kinetics of manganese than cobalt phosphate.

3.2.A.3.2 XRD Study:

The XRD patterns of cobalt manganese phosphate (H-CMP-1 to H-CMP-5) electrodes prepared by hydrothermal method at different concentration ratios of Co and Mn are illustrated in **Figure 3.4**. The H-CMP-1 and H-CMP-5 are pristine cobalt phosphate and manganese phosphate samples, respectively. The characteristic diffraction peaks of H-CMP-1 sample at the angles (2θ) of 9.42, 10.95, 13.64, 20.73, 21.65, 26.88, 35.97 and 55.41° attributes to the (001), (110), (020), (011), (130), (121), (231) and (501) planes, respectively for the monoclinic phase of cobalt phosphate hydrate [$Co_3(PO_4)_2.8H_2O$] (JCPDS card No. 00-033-0432), indicated as "▲" in **Figure 3.4**. Also, the characteristic diffraction peaks indicated as "●" in H-CMP-5 sample at the angles (2θ) of 10.21, 11.18, 19.55, 20.54, 21.59, 24.52, 28.08, 29.58, 31.55, 34.18, 41.38, 51.92, and 63.92° corresponds to the planes ($\bar{1}02$), (100), (022), ($\bar{1}15$), (023), (210), (123), (033), ($\bar{3}15$), (133), ($\bar{4}16$), (153) and (004), respectively for the manganese phosphate of monoclinic phase [$Mn_3(PO_4)_2$] (JCPDS card No. 01-073-1088). It is seen that, the diffraction peaks belong to cobalt phosphate are more prominent in H-CMP-1 and H-CMP-2 than others, where cobalt concentration is higher than manganese in cobalt manganese phosphate films. In addition, peaks correspond to manganese phosphate are more dominant than cobalt phosphate for sample H-CMP-3 to H-CMP-5, since manganese concentration is higher. Observed peaks and crystal planes indicate, the formation of monoclinic crystal structure of cobalt phosphate and manganese phosphate in H-CMP-series thin films. So, it confirms the formation of cobalt manganese phosphate material. The existence of sharp diffraction peaks in the patterns

suggests that, cobalt manganese phosphate is highly crystalline. Additionally, good crystallinity of cobalt manganese phosphate may beneficial for enhancing the cycle life of electrodes, as its stable crystal structure is not easy to damage throughout electrochemical processes **[25]**.

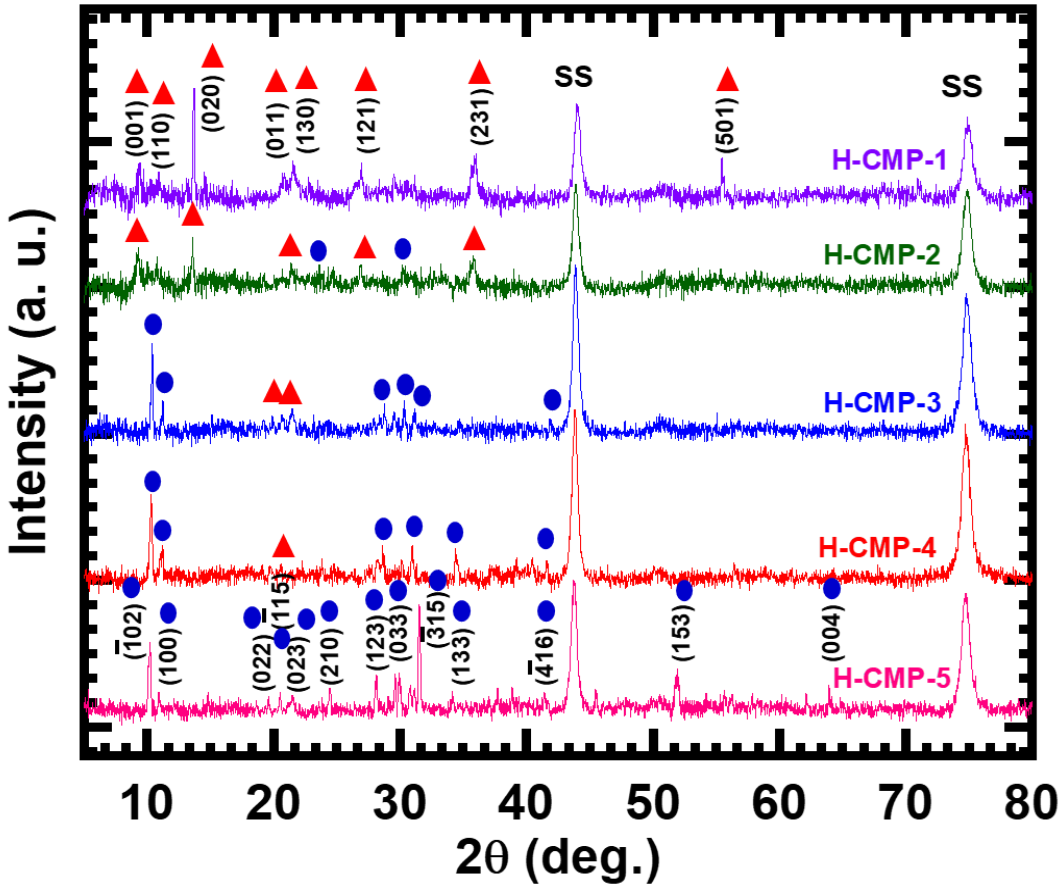

Figure 3.4: XRD patterns of cobalt manganese phosphate (H-CMP-series) thin films.

3.2.A.3.3 FTIR Study:

The molecular bond vibrations in H-CMP-series were investigated and the corresponding FTIR spectra are displayed in **Figure 3.5**. In FTIR spectra, the characteristic peak at 580 cm^{-1} is allied to Mn-O bending vibration and Co-O vibration band **[20, 26]**. Further, the peak at 740 cm^{-1} is attributed to P-O-P bending mode **[27]**. The weak band at 789 cm^{-1} is assigned to lattice vibration

mode of Co-O **[28]**. Also, the absorption peaks at 951 and 1111 cm^{-1} are ascribed to P-O symmetric stretching vibration, and 1022 cm^{-1} is antisymmetric stretching of PO_4^{3-} group **[13, 28, 29]**. The bending mode of H-O-P group at an absorption peak of 1340 cm^{-1} **[30]**. The peak at 1648 cm^{-1} represents the H-O-H bending vibration. Furthermore, wide bands at 3067 and 3456 cm^{-1} are associated with the O-H stretching vibration mode from water molecules coordinated/entrapped in a structure during synthesis **[20, 26, 30]**. The results of FTIR study confirm presence of entrapped water in the prepared cobalt manganese phosphate thin films. The FTIR investigation implies that, successful synthesis of the cobalt manganese phosphate thin films.

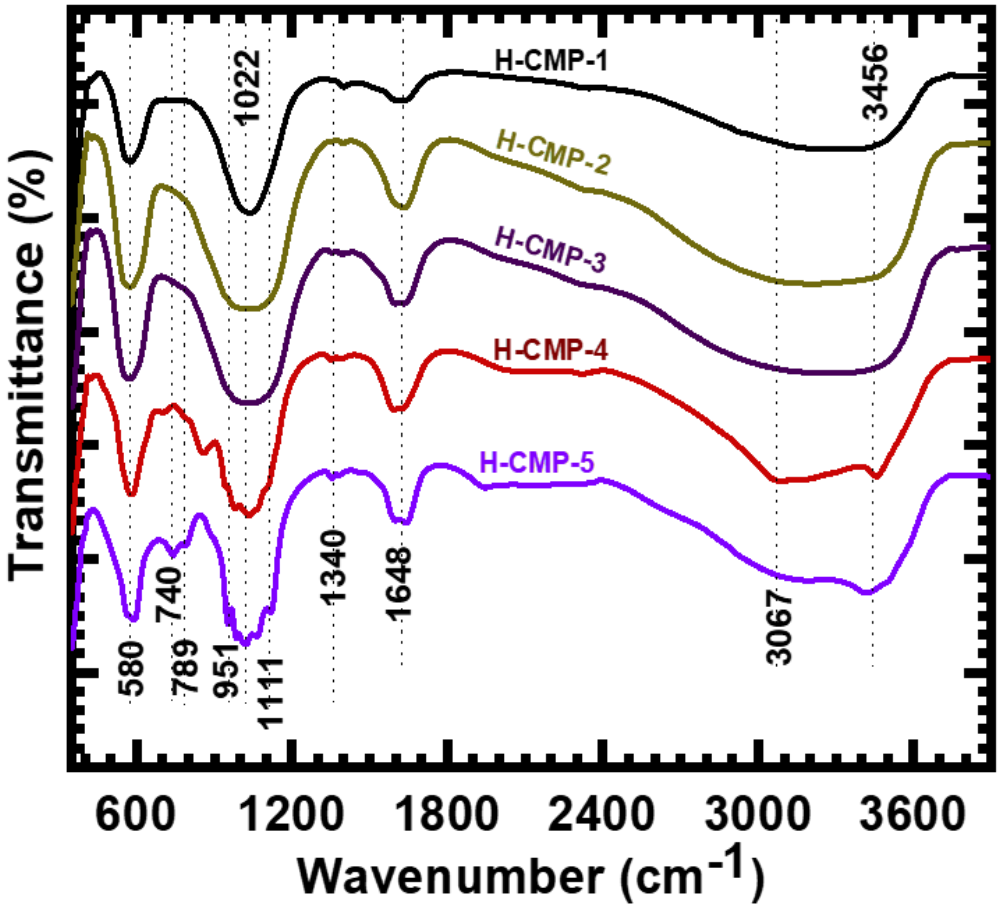

Figure 3.5: FTIR spectra of cobalt manganese phosphate (H-CMP-series) thin films.

3.2.A.3.4 XPS Study:

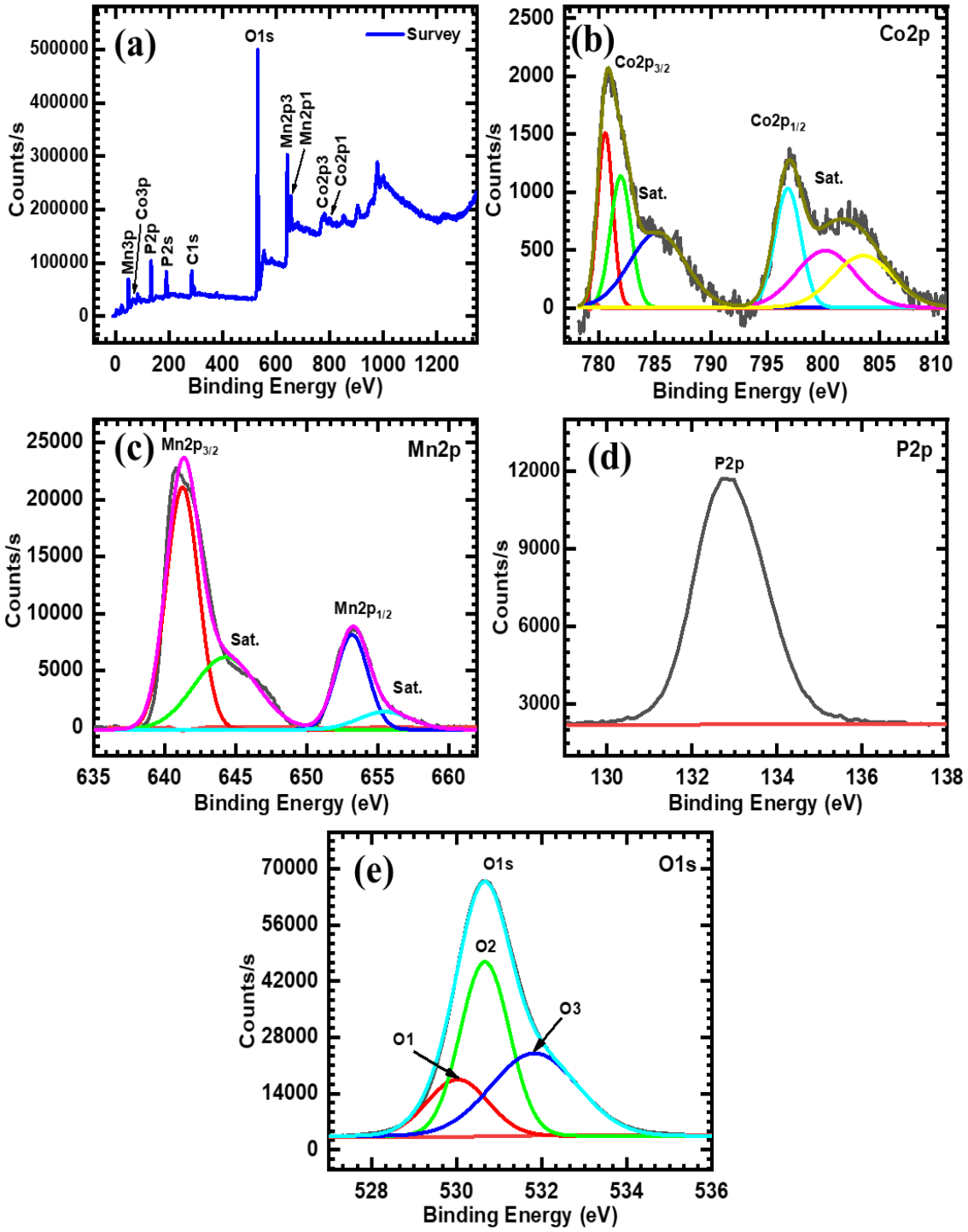

Figure 3.6: XPS spectra of H-CMP-2 electrode: (a) survey spectrum, (b) Co 2p, (c) Mn 2p, (d) P 2p, and (e) O 1s spectrum.

X-ray photoelectron spectroscopy (XPS) analysis is conducted to investigate elements along with their valence states of the cobalt manganese phosphate (H-

CMP-2) thin film **(Figure 3.6 (a-e))**. The full survey spectrum **(Figure 3.6 (a))** indicates and confirms characteristic peaks of Co 2p, Mn 2p, P 2p, and O 1s elements. The Co 2p spectrum in **Figure 3.6 (b)** is fitted for two main binding energies of Co $2p_{3/2}$ at 780.9 eV and Co $2p_{1/2}$ at 797.0 eV along with two satellite peaks at 785.5 eV and 802.1 eV, respectively, which are identified as Co^{2+} and Co^{3+} states of cobalt **[31]**. Furthermore, the spectrum of Mn 2p in cobalt manganese phosphate is displayed in **Figure 3.6 (c)**, where two intense peaks at 641.4 and 653.3 eV are belong to Mn $2p_{3/2}$ and Mn $2p_{1/2}$, respectively with their satellite peaks at 644.4 and 655.4 eV, and these binding energies are corresponding to Mn^{2+} and Mn^{3+} states of manganese **[20, 32]**. Also, the P 2p spectrum exhibits a peak at a binding energy of 132.7 eV is belongs to $2P_{3/2}$ state **(Figure 3.6 (d))**, and confirms pentavalent state of phosphorous (PO_4^{3-}) **[33, 34]**. Moreover, **Figure 3.6 (e)** exhibits XPS spectrum of O 1s, the fitted peaks located at binding energies of 530.0, 530.6 and 531.8 eV are assigned to the metal-oxygen species, phosphate species (P-O), and oxygen of OH group, respectively in Co-Mn Phosphate thin film **[13, 35]**. These XPS results confirm that, the obtained material in thin film form is a hydrous Co-Mn Phosphate compound.

3.2.A.3.5 FE-SEM Study:

It is known that, the performance of active material is extensively related to morphology of electrode material. The material with nano/micro-structured morphology may improve specific surface area allowing easy adsorption/desorption of electrolytic ions and it enhances electrochemical performance of electrode **[36]**. The FE-SEM images of H-CMP-series thin films on the SS substrate at two different magnifications (1,000x and 30,000x) are shown in **Figure 3.7 (a-j)**.

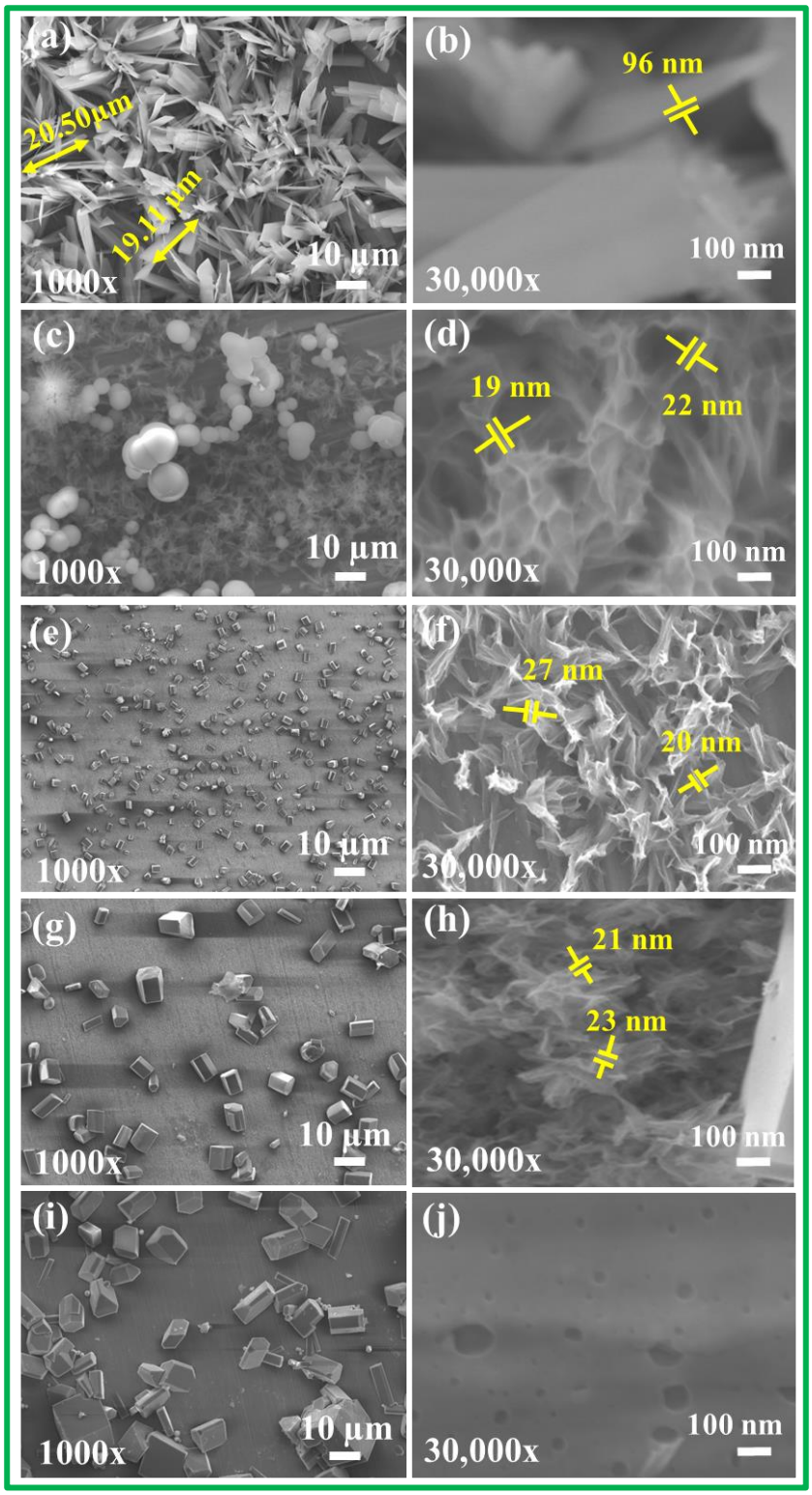

Figure 3.7: FE-SEM micrographs of cobalt manganese phosphate electrodes: (a, b) H-CMP-1, (c, d) H-CMP-2, (e, f) H-CMP-3, (g, h) H-CMP-4, and (i, j) H-CMP-5 at two magnifications (1000x and 30,000x).

The FE-SEM images clearly reveal the strong correlation between the composition of Co:Mn and resulting surface morphology. The FE-SEM images of H-CMP-1 for pristine cobalt phosphate shown in **Figure 3.7 (a, b)**, indicate microflowers-like structure consists of uniform microplates of length between 19 to 21 μm and thickness of about 96 nm. The FE-SEM image of H-CMP-2 electrode is shown in **Figure 3.7 (c),** the increased concentration of manganese for H-CMP-2 thin film changes the nano/microstructure from microflower to nanoflakes-like morphology. **Figure 3.7 (d)** reveals a nanoflakes-like structure having a thickness of 19-22 nm. Also, these nanoflakes are connected to each other resulting into interconnected networks. Further increase in the concentration of manganese for H-CMP-3 to H-CMP-5 thin film, nanoflakes like morphology with some individual overgrown microrods are obtained. The H-CMP-3 thin film **(Figure 3.7 (e, f))** shows a nanoflakes-like structure with a thickness of 20-27 nm.

Similarly, the H-CMP-4 thin film **(Figure 3.7 (g, h))** shows a nanoflakes-like structure with a thickness of 21-23 nm. FE-SEM images of H-CMP-5 for pristine manganese phosphate are shown in **Figure 3.7 (i, j)**, indicating that the sample consists of overgrown microrods with an uneven porous structure having compact morphology. Most importantly, the nanoflakes are interconnected with each other, which helps to efficiently carry electrons from active material to the current collector. Finally, H-CMP-series thin films surface morphology with microflower to nanoflakes-like structure contribute largely accessibility of active sites in electrochemical reactions to produce high specific capacitance **[37]**.

3.2.A.3.6 EDS Study:

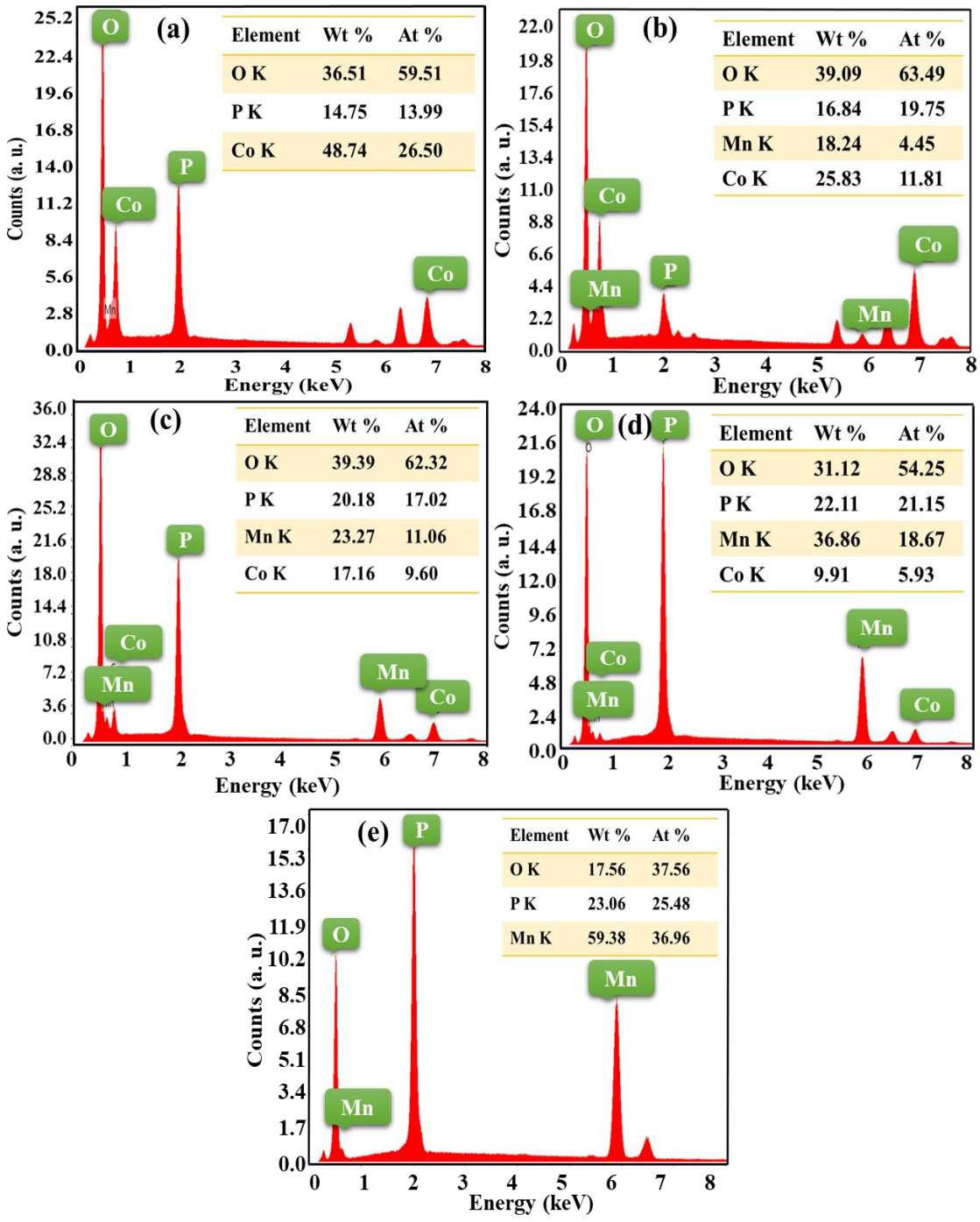

Figure 3.8: EDS spectra of cobalt manganese phosphate electrodes: (a) H-CMP-1, (b) H-CMP-2, (c) H-CMP-3, (d) H-CMP-4, and (e) H-CMP-5.

The chemical composition of Co-Mn Phosphate is investigated by energy-dispersive X-ray spectroscopy (EDS) and presented in **Figure 3.8 (a-e)**. The EDS

spectra confirm the presence of Co, Mn, P, and O elements in a material without any other impurity. The observed Co:Mn atomic ratios of H-CMP-1 to H-CMP-5 electrodes along with experimental chemical compositions are given in **Table 3.2**. The cobalt manganese phosphate material formation in thin film form was confirmed from the EDS analysis.

Table 3.2: Experimental and observed Co and Mn atomic ratio with an obtained phase of H-CMP-series thin films.

Sample Name	Experimental Ratio (Co:Mn)	Observed Ratio (Co:Mn)	Obtained Phase
H-CMP-1	1:0	1:0	$Co_3(PO_4)_2$
H-CMP-2	0.75:0.25	0.72:0.28	$Co_{2.16}Mn_{0.84}(PO_4)_2$
H-CMP-3	0.50:0.50	0.47:0.53	$Co_{1.41}Mn_{1.59}(PO_4)_2$
H-CMP-4	0.25:0.75	0.24:0.76	$Co_{0.72}Mn_{2.28}(PO_4)_2$
H-CMP-5	0:1	0:1	$Mn_3(PO_4)_2$

3.2.A.4 Conclusions:

In summary, the nano/microstructured H-CMP-series thin films are directly deposited on SS substrate using a facile hydrothermal method at 120 °C for 90 min. H-CMP-series thin films show different morphologies from microflower to nanoflakes and they can significantly influence their electrochemical performance. The XRD study confirms, monoclinic crystal structure and FTIR reveals the hydrous nature of cobalt manganese phosphate thin films. Also, XPS results confirm that the obtained material is a cobalt manganese phosphate compound. Furthermore, EDS confirms that the chemical composition of cobalt manganese phosphate varies from H-CMP-1 to H-CMP-5. The overall results confirm that, the obtained material in thin film form is hydrous cobalt manganese phosphate.

SECTION – B

Supercapacitive Performance Evaluation of Cobalt Manganese Phosphate Thin Films

3.2.B.1 Introduction:

In this section, hydrothermally synthesized cobalt manganese phosphate thin films are used as supercapacitor electrodes for electrochemical testing. The concentration effect of cobalt and manganese on the electrochemical performance of cobalt manganese phosphate thin films are examined in conventional three-electrode systems by different electrochemical measurements such as CV, GCD, cyclic stability, and EIS.

3.2.B.2 Experimental Setup for Supercapacitive Studies:

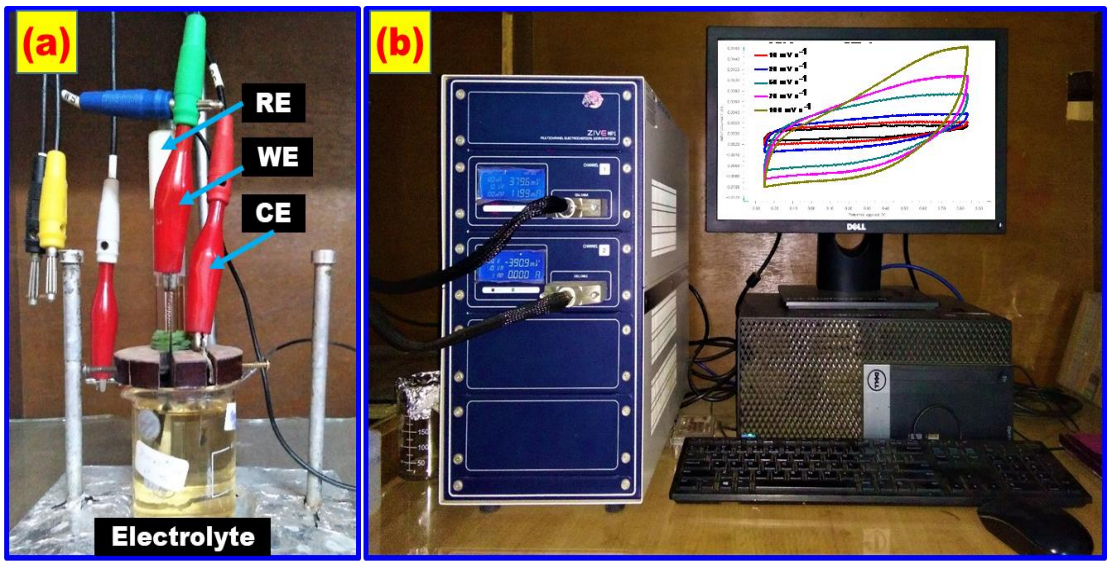

Figure 3.9: Photograph of (a) Three electrode system and, (b) experimental set up consisting of an electrochemical workstation.

Electrochemical analyses were conducted in the three-electrode configuration at ambient temperature. The cobalt manganese phosphate on SS substrate (1 cm × 1 cm) and the platinum plate was used as a working and counter

electrodes, respectively and Hg/HgO was used as a reference electrode. To design working electrodes for electrochemical measurements, the thin-film is covered with insulating tape except an area of 1 cm^2. The actual experimental set up used to evaluate supercapacitor performance is shown in **Figure 3.9 (a)**. The electrochemical properties are measured by CV, GCD, and EIS in 1M KOH and Na_2SO_4 electrolytes. EIS analysis was performed at open-circuit potential (OCP) with 10 mV AC amplitude in set of frequencies from 100 kHz to 100 mHz. Electrochemical workstation (ZIVE MP1) (displayed in **Figure 3.9 (b))** used to perform CV, GCD, and EIS studies.

Cyclic voltammetry is an important technique for deciding redox potentials and electronic transfer redox reactions **[38]**. The specific capacitance (Cs) is calculated from CV curves using **Eqⁿ 2.5** given in **Chapter 2**. Also, the GCD technique is used to determine the supercapacitive performance of electrode material in terms of specific capacitance, energy and power density of electrode. Furthermore, charge storage mechanism of electrode material is decided by the nature of GCD curves **[11]**. The specific capacitance **(Eqⁿ. 2.6),** energy (SE) and power (SP) density **(Eqⁿ. 1.3** and **1.4)** of electrode material are determined from GCD analysis given in **Chapter 1** and **2.**

3.2.B.3 Results and Discussion:

3.2.B.3.1 CV Study:

It is known that, the morphology of materials plays a crucial role in their electrochemical performance. Different morphologies deliver different active surface areas, which leads to different electrochemical properties. The electrochemical performance of Co-Mn Phosphate thin film electrode (H-CMP-4) tested in different aqueous electrolytes (1 M KOH and 1 M Na_2SO_4) by CV technique

in a three-electrode system. **Figure 3.10 (a)** displays the CV measurement for H-CMP-4 electrode tested in 1 M Na_2SO_4 and KOH aqueous electrolytes within a potential range of 0.0-1.0 V and 0.0-0.6 V, respectively at a scan rate of 50 mV s^{-1}.

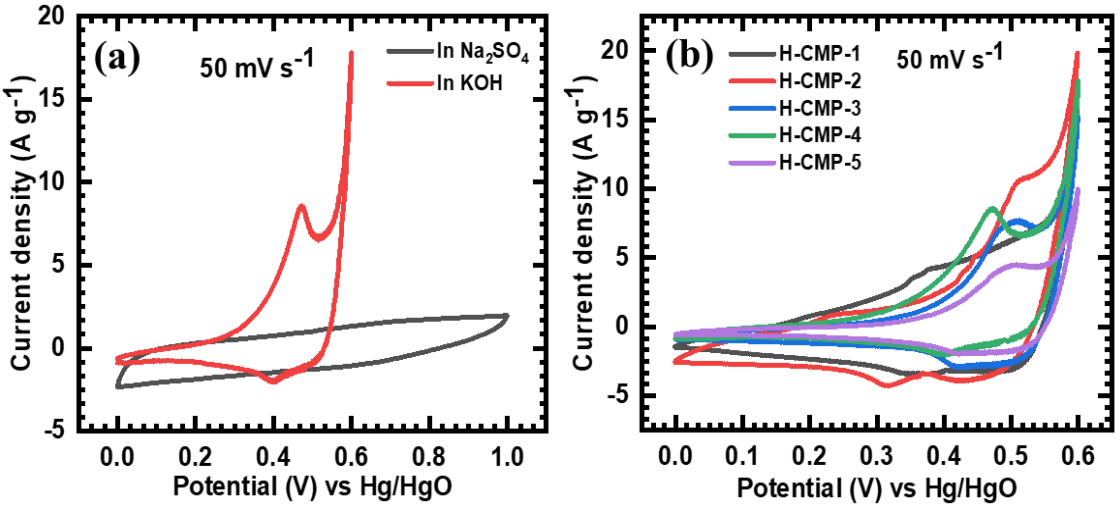

Figure 3.10: CV plots of (a) H-CMP-4 electrode in 1 M Na_2SO_4 and KOH electrolyte and, (b) H-CMP-series thin film electrodes in 1 M KOH electrolyte at a scan rate of 50 mV s^{-1}.

The result shows that, H-CMP-4 electrode obtain the highest electroactive area and store more charges in KOH as compared to Na_2SO_4 electrolyte, which indicates that easy accessibility to KOH electrolyte ions in the electrochemically active site of an electrode for electrochemical redox reactions. Since, KOH as a strongly alkaline electrolyte has high ionic conductivity, and less equivalent series resistance (ESR). Therefore, KOH electrolyte was preferred for further electrochemical studies of Co-Mn Phosphate electrode. The CV curves of H-CMP-series thin film electrodes in 1 M KOH aqueous electrolyte at 50 mV s^{-1} scan rate are shown in **Figure 3.10 (b)**.

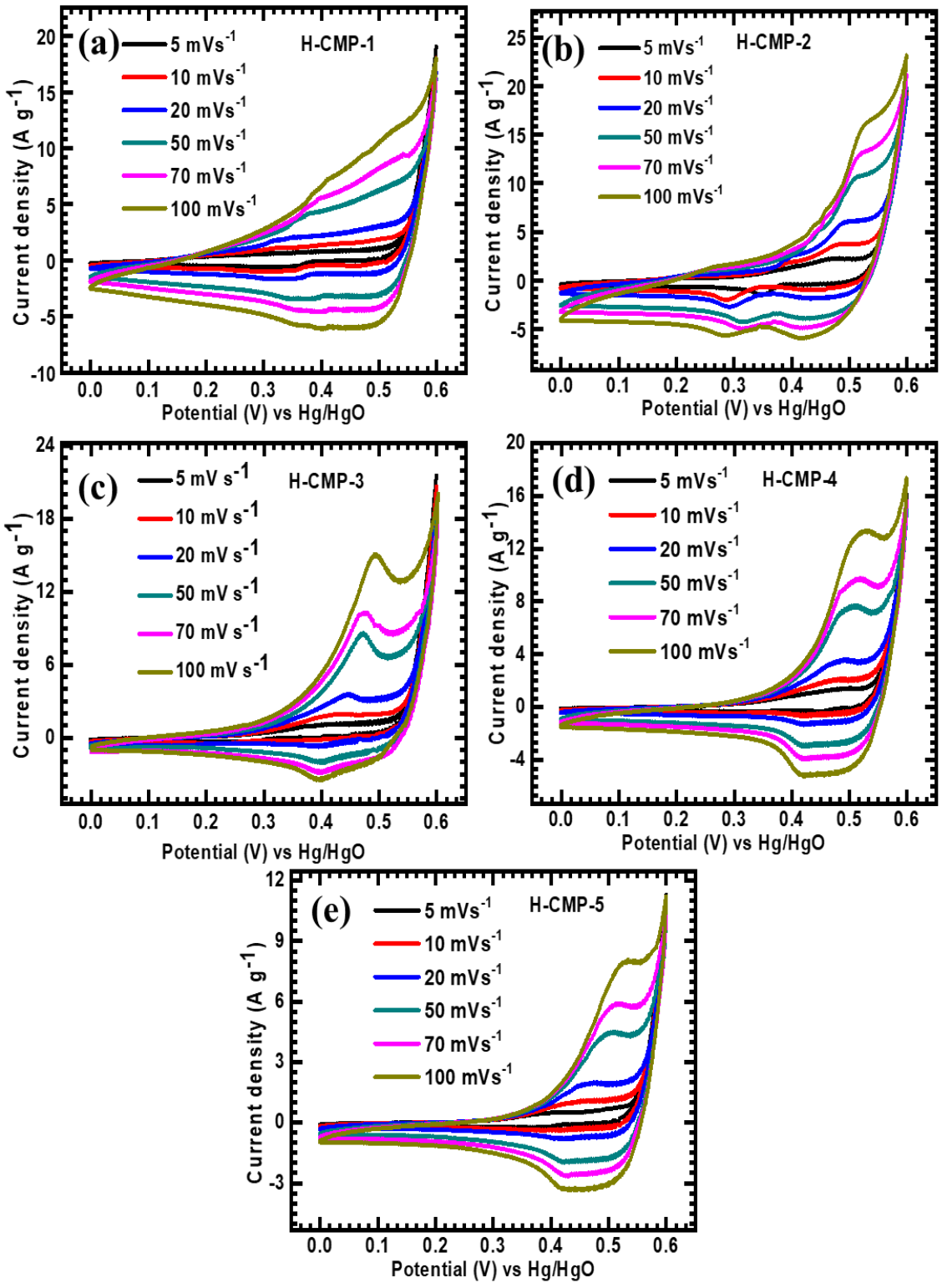

Figure 3.11: (a-e) CV plots of cobalt manganese phosphate (H-CMP-series) at different scan rates (5-100 mV s^{-1}) in 1 M KOH electrolyte.

In this study, Co-Mn Phosphate (H-CMP-2) thin film electrode exhibits good electrochemical performance than other thin films from the series. Further, the CV curves of H-CMP-series electrodes in 1 M KOH electrolyte at different scan rates (5-100 mV s^{-1}) are shown in **Figures 3.11 (a-e)**. It can be noted that, all CV curves of H-CMP-series electrodes having quasi-reversible redox peaks in KOH electrolyte. Furthermore, all CV curves of Co-Mn Phosphate thin films indicate intercalation pseudocapacitive behavior with sufficiently fast, as well as a relatively better stability of electronic and ionic transport rates. Also, they retain their shape even at high scan rates, show the high-rate performance of the material **[39-43]**.

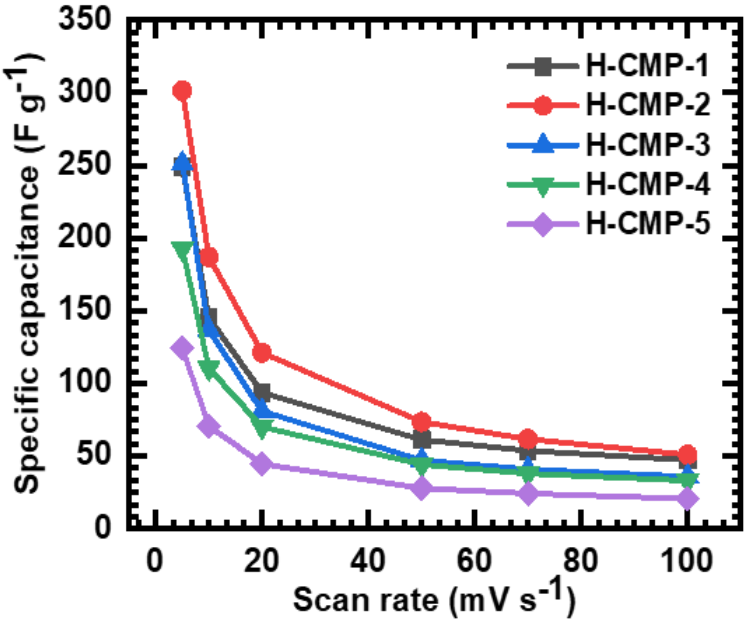

Figure 3.12: Specific capacitance of cobalt manganese phosphate electrodes (H-CMP-series) at various scan rates (5-100 mV s^{-1}).

The specific capacitance of H-CMP-series thin films is calculated using **Eqⁿ. (2.5)**. The variation of specific capacitance with different scan rates is shown in **Figure 3.12**. The specific capacitance of H-CMP-1, H-CMP-2, H-CMP-3, H-CMP-4 and H-CMP-5 thin films decreases from 248-47, 301-51, 251-36, 193-33 and 124-21 F g^{-1} with increasing scan rate (5-100 mV s^{-1}), respectively. The highest specific

capacitance (301 F g^{-1}) is achieved for H-CMP-2 as compared to pristine cobalt phosphate (H-CMP-1) or manganese phosphate (H-CMP-5) electrode. The good electrochemical performance of H-CMP-2 electrode implies that surface morphology (nanoflakes) and the synergistic effect of Co and Mn ions composition (0.75:0.25) provides high specific capacitances, which is advantageous for supercapacitors.

3.2.B.3.2 GCD Study:

The electrochemical capacitive performance of H-CMP-series electrodes was investigated by the GCD technique. The corresponding GCD curves of H-CMP-series electrodes at 2.2 A g^{-1} constant current density, in a potential range of 0.0 to 0.55 V vs Hg/HgO (1 M KOH electrolyte) are shown in **Figure 3.13**. The highest discharge time is observed for H-CMP-2 electrode compared with other electrodes, which indicates excellent electrochemical performance. The non-linear (quasi-triangular) behavior of the charge and discharge curves reveals the intercalation pseudocapacitive characteristic of Co-Mn Phosphate thin films **[40]**. Also, the GCD curves of H-CMP-series electrodes in the KOH electrolyte at different current densities (2.2-2.8 A g^{-1}) are shown in **Figure 3.14 (a-e)**. The discharging region of all GCD curve shows intercalated pseudocapacitive behavior. Moreover, good symmetrical features of GCD curves explains that, Co-Mn Phosphate material produces excellent electrochemical potential and redox reversibility during charge-discharge for the total range of potential **[40, 44]**.

The specific capacitances of H-CMP-series thin films determined from the GCD plots according to **Eq^{n}. (2.6)** are 468, 571, 436, 329, and 178 F g^{-1} at a current density of 2.2 A g^{-1}. The determined specific capacitance values at different current densities are displayed in **Figure 3.15**. The H-CMP-2 electrode exhibits the

maximum specific capacitance of 571 F g^{-1} at 2.2 A g^{-1} current density as compared to the H-CMP-series electrodes. The better electrochemical capacitive performance of H-CMP-2 electrode is originated from synergistic effect of Co and Mn ions (high amount of cobalt) and high surface area provided by nanoflakes-like morphology. Moreover, the decreasing trend of capacitance with increasing charge-discharge rate indicates that the inner surface of electrode material is not accessible at a higher charge-discharge rate.

So far, only two articles are available on cobalt manganese phosphate-based supercapacitors such as Mao et al. **[45]** synthesized $Co_2Mn(PO_4)_2$ nanorods by the mild chemical method and reported 525 F g^{-1} specific capacitance at 1 A g^{-1} current density. In addition, Chinnadurai et al. **[15]** synthesized $MnCo_2(PO_4)_2{\cdot}8H_2O$ nanoflowers via a hydrothermal method and reported 979.91 F g^{-1} specific capacitance at a current density of 2 A g^{-1}.

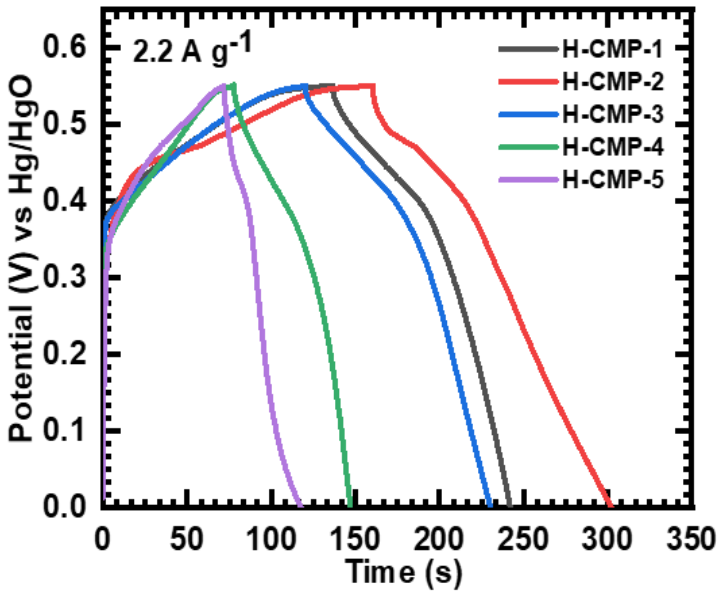

Figure 3.13: GCD curves of H-CMP-series thin films in 1 M KOH electrolyte at 2.2 A g^{-1} current density.

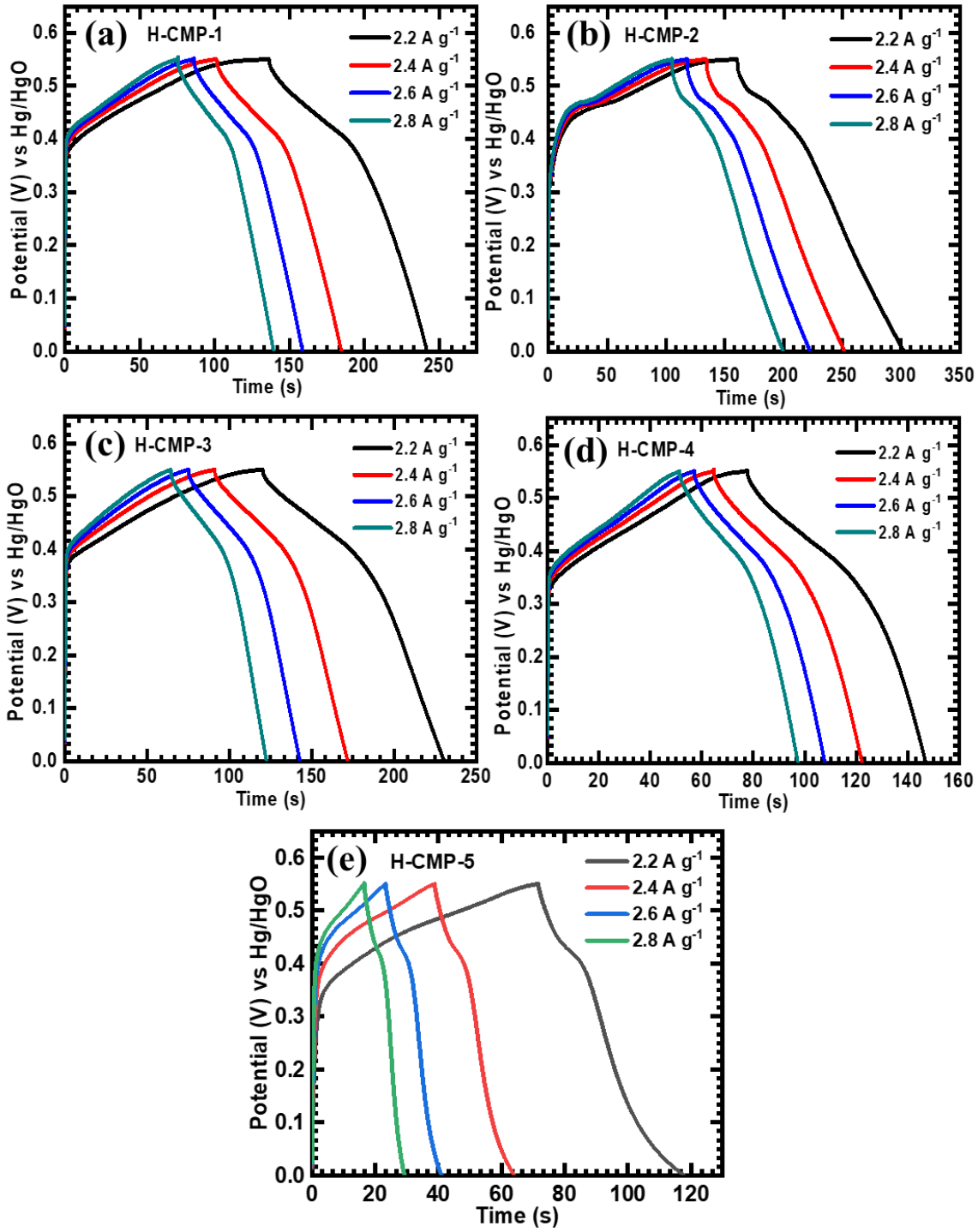

Figure 3.14: GCD curves of H-CMP-series thin films for (a) H-CMP-1, (b) H-CMP-2, (c) H-CMP-3, (d) H-CMP-4 and (e) H-CMP-5 at different current densities (2.2-2.8 A g^{-1}).

The specific capacitance obtained in present work is less than the reported capacitance by Chinnadurai et al., since they used nickel foam as a current collector

and it might contribute to an electrochemical analysis by adding self-capacitance **[46]**. In this work, Co-Mn Phosphate series thin films are prepared on SS current collector and this substrate allows a 2D surface (unlike 3D nickel foam) and does not participate in electrochemical reactions. Therefore, the obtained specific capacitance in present work is thoroughly exhibited by only the Co-Mn Phosphate material and not by a current collector (SS).

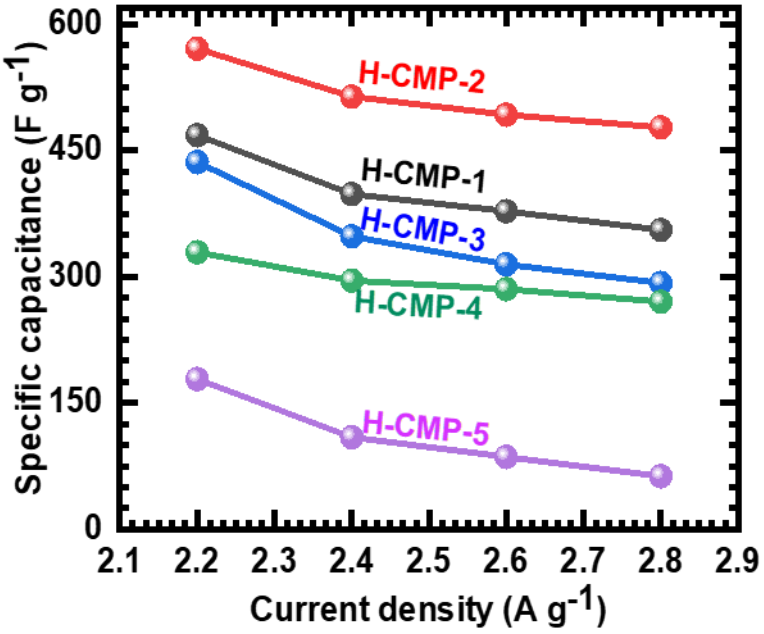

Figure 3.15: Specific capacitance of H-CMP-series thin films at various current densities (2.2-2.8 A g^{-1}).

3.2.B.3.3 EIS Study:

To investigate the electrochemical impedance properties of cobalt manganese phosphate (H-CMP-series) thin films, EIS analyses were carried out. **Figure 3.16** shows Nyquist plots of H-CMP-series thin films in a set of frequencies between 100 kHz to 100 mHz. Also, the inset **Figure 3.16** shows a magnified image of a Nyquist plot in a higher frequency region. The electrochemical impedance spectral data is fitted in an equivalent circuit (as shown in inset **Figure 3.16**) by a

charge transfer resistance (R_{ct}), electrolyte resistance (R_s), Warburg resistance (W) of electrolytic ions in a host material, and a constant phase element (CPE) to account for the capacitance **[47, 48]**. All plots are identical, like forming a vertical line in the low frequency region and a semicircle in the high frequency region. An escalation in semicircle diameter means that it is more difficult to transfer the charge of the active species inside the electrode material. The R_s values of H-CMP-series electrodes are 1.24, 1.09, 1.13, 1.12, 1.1 Ω. Also, R_{ct} values of H-CMP-series electrodes are 22.06, 7.73, 22.67, 31.85, 76.33 Ω in 1 M KOH electrolyte. The H-CMP-2 electrode shows less charge transfer resistance compared to the other electrode materials, in fact, when the amount of Co increases, the R_{ct} value of H-CMP-series electrodes decreases.

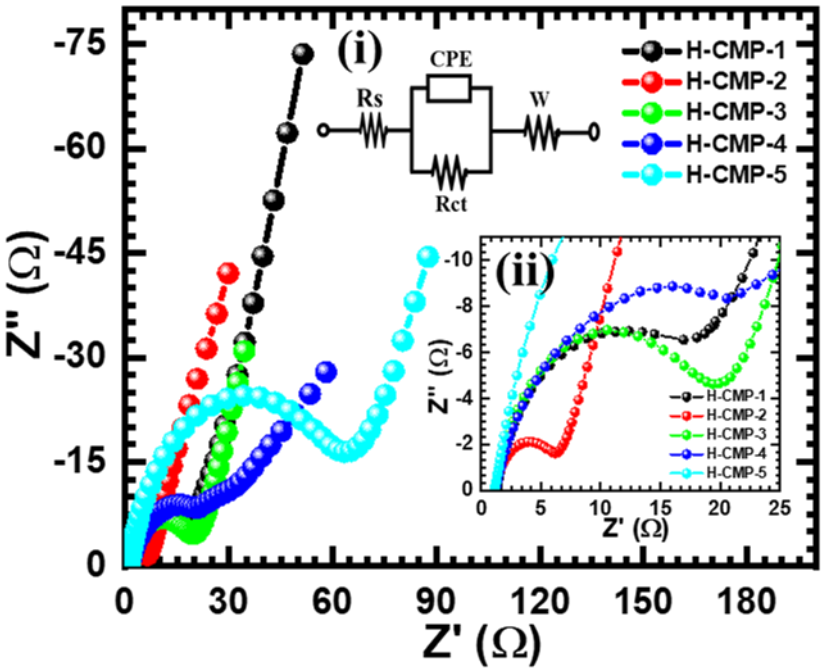

Figure 3.16: Nyquist plots of H-CMP-series thin films (Inset: (i) fitted equivalent circuit of H-CMP-2 thin film electrode, and (ii) enlarged Nyquist plots at a higher frequency).

Moreover, a comparatively small value of R_{ct} indicates good charge transfer kinetics of cobalt manganese phosphate electrode (H-CMP-2), which is advantageous for charge storage process and relatively good stability **[49]**. Therefore, the H-CMP-2 electrode exhibited better electrochemical performance compared to other electrodes from H-CMP-series.

3.2.B.3.4 Stability Study:

Cycling stability is one of the important factor for finding the usage of electrode materials in supercapacitor devices. The cyclic stability of best-performed H-CMP-2 electrode at 3.0 A g^{-1} current density within 0.0 to 0.55 V is shown in **Figure 3.17 (a)**. It displays excellent cyclic performance (capacitance retention) of 81 % after 4000 cycles. Furthermore, **Figure 3.17 (b)** shows the 1st, 2000th, and 4000th GCD curves for H-CMP-2 electrode. The capacitance loss is observed in the first 1500 cycles and then retains good stability up to 4000 cycles. Also, the charging and discharging of electrode results in a shrinking and swelling of material that causes to delaminate of a small amount of active material **[50-52]**.

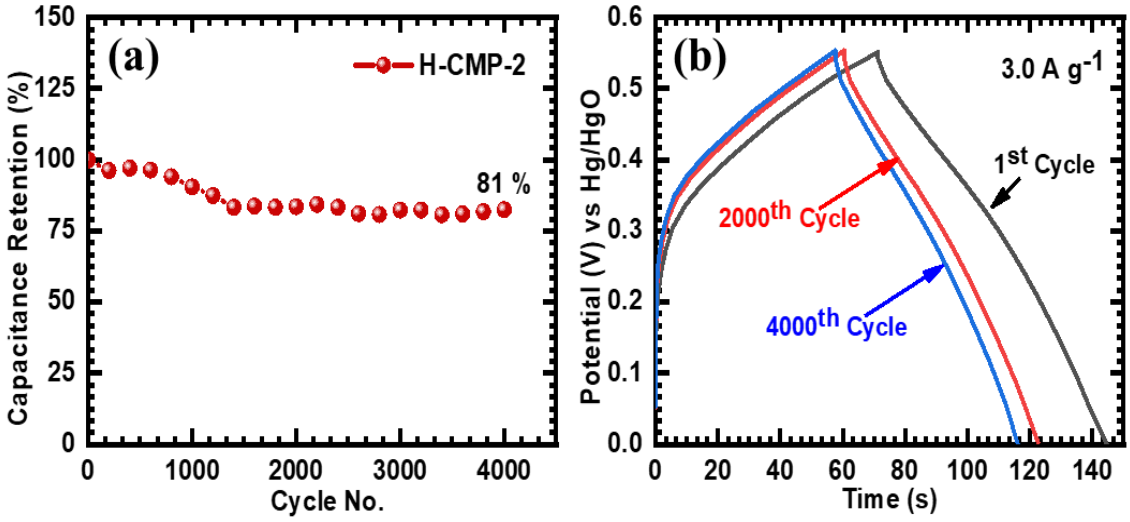

Figure 3.17: (a) GCD stability graph of H-CMP-2 electrode for 4000 cycles and (b) 1st, 2000th, and 4000th GCD cycles of H-CMP-2 electrode.

Moreover, the H-CMP-2 thin film shows excellent capacitance retention, due to binder-free synthesis of cobalt manganese phosphate thin film electrode. Since, binder-free approach for the synthesis of electrode enables to develop well contact between the current collector and sustainable nano/microstructure.

3.2.B.4 Conclusions:

In this section, the electrochemical performance of cobalt manganese phosphate (H-CMP-series) was tested by a three-electrode system in aqueous 1 M KOH and Na_2SO_4 electrolyte. The cobalt manganese phosphate electrodes show high performance in KOH electrolyte as compared to Na_2SO_4 electrolyte. The maximum specific capacitance of 571 F g^{-1} is obtained for H-CMP-2 ($Co_{2.16}Mn_{0.84}(PO_4)_2$) electrode at 2.2 A g^{-1} current density. Also, a small value of R_{ct} (7.73 Ω) indicates good charge transfer kinetics and high electrochemical conductivity of the H-CMP-2 electrode. Moreover, the H-CMP-2 electrode displays excellent capacitive retention of 81 % over 4000 cycles. The enhanced electrochemical performance of H-CMP-2 electrode is attributed to the interconnected nanoflakes-like structure of cobalt manganese phosphate over SS substrate, which provides more pathways for easy penetration of electrolyte into the interior of active material. Among H-CMP-series thin films, the H-CMP-2 electrode shows high electrochemical capacitive performance and it can be used as a cathode in asymmetric device fabrication.

3.3 References:

1. G. Wang, L. Zhang, J. Zhang, Chem. Soc. Rev., 41, (2012), 797-828.
2. C. Chen, N. Zhang, X. Liu, Y. He, H. Wan, B. Liang, R. Ma, A. Pan, V. A. L. Roy, ACS Sustain. Chem. Eng., 4, (2016), 5578–5584.
3. G. Zhang, X. W. (David) Lou, Adv. Mater., 25, (2013), 975-975.
4. A. Bello, K. Makgopa, M. Fabiane, D. D. Ahrin, K. I. Ozoemena, N. Manyala, J. Mater Sci., 48, (2013) 6707–6712.
5. C. Yuan, H. B. Wu, Y. Xie, X. W. (David) Lou, Angew. Chem. Int. Ed., 53, (2014), 1488-1504.
6. T. Liu, C. Jiang, W. You, J. Yu, J. Mater. Chem. A, 5, (2017), 8635-8643.
7. H. Li, H. Yu, J. Zhai, L. Sun, H. Yang, S. Xie, Mater. Lett., 152, (2015), 25-28.
8. G. Chen, W. Ma, X. Liu, S. Liang, G. Qiu, R. Ma, RSC Adv., 3, (2013), 3544-3547.
9. H. Chen, L. Hu, M. Chen, Y. Yan, L. Wu, Adv. Funct. Mater., 24, (2014), 934-942.
10. J. Wang, X. Sun, Energy Environ. Sci., 5, (2012), 5163-5185.
11. S. J. Marje, P. K. Katkar, S. S. Pujari, S. A. Khalate, A. C. Lokhande, U. M. Patil, Synth. Met., 259, (2020), 1-11.
12. C. Yang, L. Dong, Z. Chen, H. Lu, J. Phys. Chem. C, 118, (2014), 18884–18891.
13. P. K. Katkar, S. J. Marje, S. S. Pujari, S. A. Khalate, A. C. Lokhande, U. M. Patil, ACS Sustain. Chem. Eng., 7, (2019), 11205–11218.
14. P. Y. Chuang, C. C. Hu, Mater. Chem. Phys., 92, (2005), 138-145.
15. D. Chinnadurai, A. R. Selvaraj, R. Rajendiran, G. R. Kumar, H. J. Kim, K. K. Viswanathan, K. Prabakar, ACS Omega, 3, (2018), 1718–1725.
16. E. Rios, J. L. Gautier, G. Poillerat, P. Chartier, Electrochim. Acta, 44, (1998), 1491-1497.
17. P. Xu, K. Ye, D. Cao, J. Huang, T. Liu, K. Cheng, J. Yin, G. Wang, J. Power Sources, 268, (2014), 204-211.
18. K. Sato, S. Umino, K. Tsubouchi, N. Mikoshiba, IEEE 1985 Ultrasonics Symposium, Proceedings (Cat. No. 85CH2209-5), New York, NY, USA, (1985)
19. D. P. Dubal, J. G. Kim, Y. Kim, R. Holze, C. D. Lokhande, W. B. Kim, Energy Technol., 2, (2014), 325-341.
20. P. K. Katkar, S. J. Marje, S. S. Pujari, S. A. Khalate, P. R. Deshmukh, U. M. Patil, Synth. Met., 267, (2020), 1-13.

21. S. S. Pujari, S. A. Kadam, Y. R. Ma, P. K. Katkar, S. J. Marje, S. A. Khalate, A. C. Lokhande, U. M. Patil, J. Electron. Mater., 49, (2020), 3890–3901.
22. B. C. Bunker, P. C. Rieke, B. J. Tarasevich, A. A. Campbell, G. E. Fryxell, G. L. Graff, L. Song, J. Liu, J. W. Virden, G. L. McVay, Science, 264, (1994), 48-55.
23. Y. L. Zhao, J. M. Wang, H. Chen, T. Pan, J. Q. Zhang, C. N. Cao, Electrochim. Acta, 50, (2004), 91-98.
24. G. Briganti, S. Puvvada, D. Blankschtein, J. Phys. Chem., 95, (1991), 8989–8995.
25. C. Wang, L. Yin, D. Xiang, Y. Qi, ACS Appl. Mater. Interfaces, 4, (2012), 1636–1642.
26. B. R. Wiston, M. Ashok, Mat. Sci. Semicon. Proc., 103, (2019), 1-8.
27. Y. P. Zhu, Y. L. Liu, T. Z. Ren, Z. Y. Yuan, Nanoscale, 6, (2014), 6627-6636.
28. P. K. Katkar, S. J. Marje, S. B. Kale, A. C. Lokhande, C. D. Lokhande, U. M. Patil, CrystEngComm, 21, (2019), 884-893.
29. B. Liang, Y. Chen, J. He, C. Chen, W. Liu, Y. He, X. Liu, N. Zhang, V. A. L. Roy, ACS Appl. Mater. Interfaces, 10, (2018), 3506–3514.
30. D. Wang, Y. Xu, W. Sun, X. Guo, L. Yang, F. Wang, Z. Yang, Electrochim. Acta, 337, (2020), 1-10.
31. B. J. Tan, K. J. Klabunde, P. A. Sherwood, J. Am. Chem. Soc., 113, (1991), 855-861.
32. G. Neher, T. T. Salguero, Cryst. Growth Des., 17, (2017), 4864–4872.
33. G. R. Hu, X. R. Deng, Z. D. Peng, K. Du, Electrochim. Acta, 53, (2008), 2567-2573.
34. R. Yuan, J. Yuan, Y. Wu, P. Ju, L. Ji, H. Li, L. Chen, H. Zhou, J. Chen, Colloids Surf. A, 547, (2018), 56-63.
35. X. Liang, B. Zheng, L. Chen, J. Zhang, Z. Zhuang, B. Chen, ACS Appl. Mater. Interfaces, 9, (2017), 23222–23229.
36. L. Chang, F. Ren, C. Zhao, X. Xue, J. Electroanal. Chem., 778, (2016), 110-115.
37. X. J. Ma, W. B. Zhang, L. B. Kong, Y. C. Luo, L. Kang, RSC Adv., 6, (2016), 40077-40085.
38. S. B. Ubale, T. T. Ghogare, V. C. Lokhande, T. Ji, C. D. Lokhande, SN Appl. Sci., 2, (2020), 1-5.

39. J. Yan, Z. Fan, W. Sun, G. Ning, T. Wei, Q. Zhang, R. Zhang, L. Zhi, F. Wei, Adv. Funct. Mater., 22, (2012), 2632-2641.
40. N. R. Chodankar, H. D. Pham, A. K. Nanjundan, J. F. S. Fernando, K. Jayaramulu, D. Golberg, Y. K. Han, D. P. Dubal, Small, 16, (2020), 1-35,
41. X. Lu, M. Yu, G. Wang, T. Zhai, S. Xie, Y. Ling, Y. Tong, Y. Li, Adv. Mater., 25, (2013), 267-272.
42. C. Zhu, D. Wen, S. Leubner, M. Oschatz, W. Liu, M. Holzschuh, F. Simon, S. Kaskel, A. Eychmüller, Chem. Commun., 51, (2015), 7851-7854.
43. D. S. Sun, Y. H. Li, Z. Y. Wang, X. P. Cheng, S. Jaffer, Y. F. Zhang, J. Mater. Chem. A, 4, (2016), 5198-5204.
44. H. Kim, M. Y. Cho, M. H. Kim, K. Y. Park, H. Gwon, Y. Lee, K. C. Roh, K. Kang, Adv. Energy Mater., 3, (2013), 1500-1506.
45. H. Mao, Y. Qian, Z. Jin, Y. Zhang, Mater. Lett., 228, (2018), 258-261.
46. D. P. Dubal, G. S. Gund, C. D. Lokhande, R. Holze, ACS Appl. Mater. Interfaces, 5, (2013), 2446–2454.
47. A. Paravannoor, S. V. Nair, P. Pattathil, M. Manca, A. Balakrishnan, Chem. Commun., 51, (2015), 6092-6095.
48. S. Hassan, M. Suzuki, S. Mori, A. A. El-Moneim, RSC Adv., 4, (2014), 20479-20488.
49. X. J. Ma, L. B. Kong, W. B. Zhang, M. C. Liu, Y. C. Luo, L. Kang, Electrochim. Acta, 130, (2014), 660-669.
50. Y. L. Cheah, V. Aravindan, S. Madhavi, ACS Appl. Mater. Interfaces, 5, (2013), 3475–3480.
51. J. T. Zhang, S. Liu, G. L. Pan, G. R. Lia, X. P. Gao, J. Mater. Chem. A, 2, (2014), 1524-1529.
52. J. Xu, S.Gai, F. He, N. Niu, P. Gao, Y. Chen, P. Yang, J. Mater. Chem. A, 2, (2014), 1022-1031.

CHAPTER -4

SYNTHESIS, CHARACTERIZATION AND SUPERCAPACITIVE PERFORMANCE OF COBALT MANGANESE PHOSPHATE THIN FILM BY SILAR METHOD

CHAPTER 4

Synthesis, Characterization and Supercapacitive Performance of Cobalt Manganese Phosphate Thin Film by SILAR Method

Sr. No.	Title		Page No.
4.1	**Introduction**		**133**
SECTION – A **SILAR Synthesis and Characterization of Cobalt Manganese Phosphate Thin Films**			
4.2.A.1	**Introduction**		**135**
4.2.A.2	**Experimental Details**		**136**
	4.2.A.2.1	*Chemicals*	**136**
	4.2.A.2.2	*Synthesis of Cobalt Manganese Phosphate Thin Films*	**136**
4.2.A.3	**Results and Discussion**		**139**
	4.2.A.3.1	*Film Formation and Reaction Mechanism*	**139**
	4.2.A.3.2	*XRD Study*	**140**
	4.2.A.3.3	*FTIR Study*	**141**
	4.2.A.3.4	*XPS Study*	**142**
	4.2.A.3.5	*FE-SEM Study*	**144**
	4.2.A.3.6	*EDS Study*	**146**
4.2.A.4	**Conclusions**		**147**
SECTION – B **Supercapacitive Performance Evaluation of Cobalt Manganese Phosphate Thin Films**			
4.2.B.1	**Introduction**		**148**
4.2.B.2	**Results and Discussion**		**148**
	4.2.B.2.1	*CV Study*	**148**
	4.2.B.2.2	*GCD Study*	**151**
	4.2.B.2.3	*EIS Study*	**154**
	4.2.B.2.4	*Stability Study*	**155**
4.2.B.3	**Conclusions**		**156**
4.3	**References**		**157**

4.1 Introduction:

In recent years, research and technology are devoted to the synthesis of novel electrode materials with unique electrochemical properties for supercapacitor applications. Moreover, the properties of electrode material have a significant impact on the electrochemical performance of supercapacitor (SCs). Until now, various materials were investigated as electrodes for SCs, such as metal oxides **[1]**, carbon materials **[2-4]**, and conductive polymers **[5]**. Lately, transition metal phosphates (TMPs) are gaining much attention as an important division of electrode materials for SCs. Moreover, TMPs electrode materials offer several properties required for supercapacitor electrodes such as high theoretical capacitance, low-cost, large abundance and excellent ion conductivity with high energy density, redox activity, long cycling life span, and eco-friendly behavior. TMPs are widely applied in many industrial research areas because of open-framework structure with wide channels and long tunnels **[6, 7]**. Current research has shown that, the different redox-active TMPs are extensively explored as electrode materials for application in supercapacitors such as $Co_3(PO_4)_2$ **[8]**, $Mn_3(PO_4)_2$ **[9]**, $Ni_2P_2O_7$ **[10]**, $VOPO_4$ **[11]**, and Ag_3PO_4 **[12]**. In the family of transition metal phosphate, individual cobalt-based and manganese-based phosphate electrodes possess a higher specific capacitance and stable life cycle span, respectively. However, the ability to use these single metal phosphates is constrained by poor intrinsic conductivity, low energy density, poor durability, and limited rate capability **[7, 13-15]**. To surpass these shortcomings, a combination of two metal phosphate (binary metal phosphate) electrode materials can be used for a supercapacitor and may offer enhanced specific capacitance and stability. The synergy between different metal species offers high conductivity, feasible

oxidation states, more active sites and excellent supercapacitor properties instead of single metal phosphates **[16-19]**. The combination of Co and Mn-based phosphate electrode materials results in proficient pseudocapacitive behavior with excellent performance such as higher capacitance, higher rate capability. Therefore, the preparation of stable Co-Mn Phosphate materials is hugely beneficial for supercapacitor application **[20, 21]**. Some studies have reported cobalt manganese phosphate electrode for SCs application, although the limited capacitive performance and energy density is still a barrier to overcome **[20, 21]**. So, to improve the capacitance of Co-Mn Phosphate with the synergetic effects of cobalt and manganese species, different synthesis approaches are investigated and reported **[22, 23]**. Almost all efforts in this area have been focused on the preparation of binary metal phosphate materials, as these compounds have good electrochemical performance. However, supercapacitors made up of crystalline electrodes generally exhibit extremely poor cycle life, which limits their practical use. Therefore, it is essential to produce an amorphous structure of the material to extend the cycle life and to increase the capacitance of Co-Mn Phosphate.

In general, the deposition of cobalt manganese phosphate using the hydrothermal method has been achieved and reported by several authors, which requires high temperature, high pressure, and long-time processing **[20, 21]**. However, successive ionic layer adsorption and reaction (SILAR) method can be employed to overcome these difficulties by preparing amorphous supercapacitor electrodes. SILAR method is the simplest, economically feasible, most versatile and environment friendly process according to the soft chemical solution method in ambient conditions **[24]**. Also, SILAR is a relatively new and less investigated method for the preparation of Co-Mn Phosphate directly on the large-area

substrate in a thin-film form with a controlled thickness, without using unnecessary binders and additives **[24-27]**. For the design of supercapacitor electrodes, binder-free preparation is an effective approach to reduce internal resistance and enhance electrochemical performance. The novelty of this work lies mainly in the investigation of energy storage capacity of Co-Mn Phosphate depending on various operating parameters. However, there is no report available on Co-Mn Phosphate synthesized by SILAR method on SS substrate for supercapacitor application.

The present chapter is divided into two sections (sections A and B). Section 'A' contains the synthesis of Co-Mn Phosphate thin films by SILAR method and their characterizations. Section 'B' is related to the evaluation of supercapacitor performance of Co-Mn Phosphate thin film electrodes.

SECTION – A

SILAR Synthesis and Characterization of Cobalt Manganese Phosphate Thin Films

4.2.A.1 Introduction:

According to supercapacitors market for a wide range of working applicability, the electrode material must have high energy and power density, excellent cycle life and low cost. Hence, binder-free Co-Mn Phosphate thin films on SS substrate at ambient temperature are prepared using a convenient and simple SILAR method. The preparative parameters such as precursor concentration, adsorption, reaction, and rinsing time are optimized to obtain good quality Co-Mn Phosphate thin films. It offers several advantages such as layer-by-layer (LBL)

growth mode, superior precursor utilization efficiency, and deposition procedure is easy to control desired thickness film **[28, 29]**. Subsequently, Co-Mn Phosphate thin films are characterized using different characterization techniques such as XRD for structural study, FT-IR for chemical bonding study, XPS to determine oxidation states, FE-SEM for surface micro/nanostructural studies. The purpose of this work is to investigate synergistic effect in combined transition bimetallic phosphate (different concentrations of Co:Mn) on electrochemical performance.

4.2.A.2 Experimental details:

4.2.A.2.1 Chemicals:

Potassium hydrogen phosphate (K_2HPO_4), cobalt (II) chloride hexahydrate ($CoCl_2.6H_2O$), and manganese (II) chloride tetrahydrate ($MnCl_2.4H_2O$) was purchased from Sigma Aldrich. Potassium hydroxide (KOH) was bought from Alfa Aesar. Stainless steel (SS) substrate was bought from a local market in Kolhapur, India. All reagents were AR grade and utilized without any further purification.

4.2.A.2.2 Synthesis of Cobalt Manganese Phosphate Thin Films:

In the present study, synthesis of Co-Mn Phosphate thin film by SILAR method on SS substrate was achieved by successive immersion of the substrate in cationic and ionic precursor solutions separately. **Figure 4.1** presents the schematic of a modified SILAR method for synthesis of Co-Mn Phosphate on the SS substrate using a three-beaker system.

In SILAR synthesis, the first beaker contains 50 mL solution with different concentrations of (0.010-0.040 M) $CoCl_2.6H_2O$ and (0.010-0.040 M) $MnCl_2.4H_2O$, which serves as the cationic precursor source. The second beaker contains a 50 mL solution of (0.080 M) K_2HPO_4 and serves as an anionic precursor source. The third beaker contains 50 mL DDW which is used for rinsing purposes. Different

proportions of cobalt (Co) and manganese (Mn) precursors are used for deposition of cobalt manganese phosphate materials and the detailed compositions used in the experiment are exhibited in **Table 4.1**. In synthesis procedure, Co:Mn ions are adsorbed on mirror-polished SS substrate because of the attractive forces between ions in solution and surface of a substrate. The force of attraction can be a cohesive or van der Waals forces **[25]**. The SS substrate is then immersed in a phosphate source, where a reaction of PO_4^{3-} anions with Co:Mn ions occurs. Then, the loosely bonded excess ions (cations and anions)/particles are removed by rinsing substrate in a third beaker containing DDW. The concentration of precursor solution, duration of adsorption, reaction, and rinsing is important in the SILAR method. For deposition of Co-Mn Phosphate thin film, the adsorption period of 10 s, reaction period of 10 s, rinsing period of 20 s and the 80 number of cycles are optimized. After 80 deposition cycles, milky white to light violet-colored films were obtained on surface of SS substrates (shown in **Figure 4.2**). The thin film electrodes prepared by using different compositions given in **Table 4.1** are denoted as, S-CMP-1, S-CMP-2, S-CMP-3, S-CMP-4, and S-CMP-5.

Table 4.1: Different compositions of cobalt, manganese and phosphate precursors for synthesis of cobalt manganese phosphate thin film and corresponding notations.

Sr. No.	$CoCl_2.6H_2O$ (M)	$MnCl_2.4H_2O$ (M)	K_2HPO_4 (M)	Notation
1)	0.000	0.040	0.080	S-CMP-1
2)	0.010	0.030	0.080	S-CMP-2
3)	0.020	0.020	0.080	S-CMP-3
4)	0.030	0.010	0.080	S-CMP-4
5)	0.040	0.000	0.080	S-CMP-5

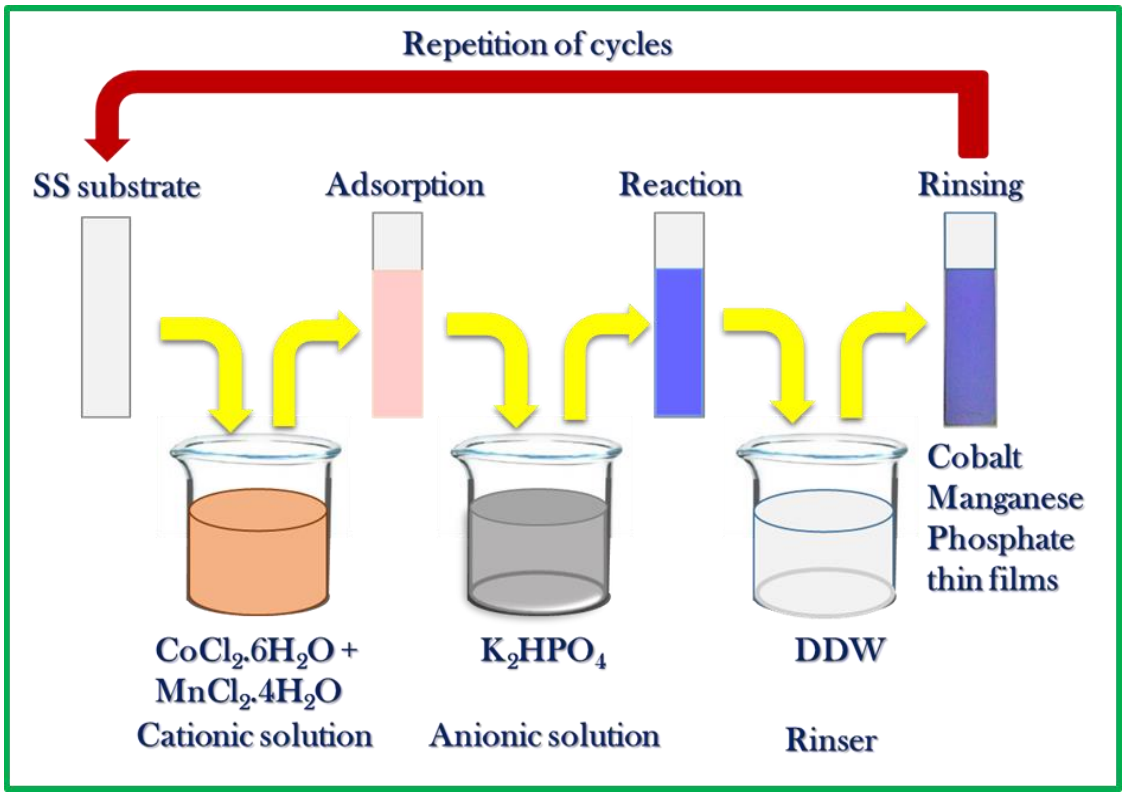

Figure 4.1: Schematic diagram of SILAR method for cobalt manganese phosphate thin films deposition.

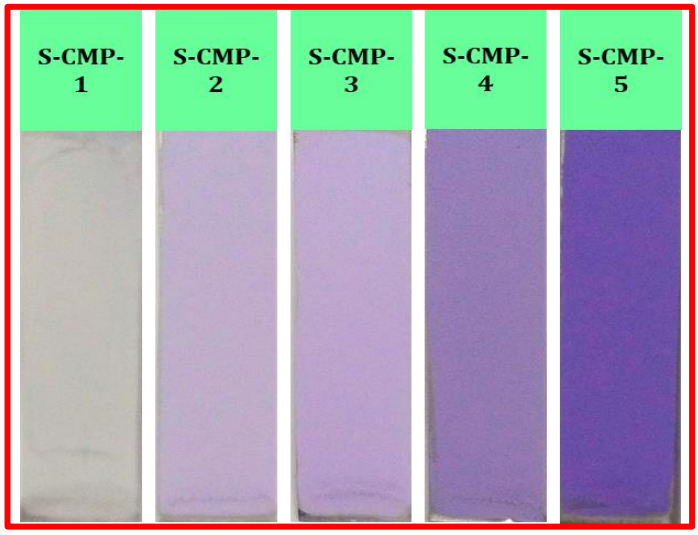

Figure 4.2: Photographs of SILAR synthesized cobalt manganese phosphate thin films (S-CMP-series) with different concentrations of Co:Mn.

4.2.A.3 Results and Discussion:

4.2.A.3.1 Film Formation and Reaction Mechanism:

Schematic **Figure 4.1** shows the preparation procedure of Co-Mn Phosphate thin films by SILAR method. In brief, a three-beaker arrangement is used, the first beaker contains a mixture of cobalt chloride and manganese chloride ($CoCl_2.6H_2O/MnCl_2.4H_2O$) aqueous solution with different compositions, as the cationic precursor. Then, the adsorbed ions react with an anionic precursor (K_2HPO_4) in the second beaker. Furthermore, DDW in third Beaker was utilized for rinsing purpose.

The explanation of reaction mechanism for cobalt manganese phosphate thin film produced by SILAR method is as follows; a thin layer of Co^{2+}/Mn^{2+} ions is applied to SS substrate by immersing the substrate in a cationic precursor solution kept at room temperature.

$$CoCl_2.6H_2O + MnCl_2.4H_2O \rightarrow Co^{2+} + Mn^{2+} + 4Cl^- + 10H_2O \quad 3.1$$

Moreover, an anionic precursor of dipotassium phosphate dissociates as per **Eqn. (3.2),**

$$K_2HPO_4 \rightarrow HPO_4^{2-} + 2K^+ \quad 3.2$$

Furthermore, the reaction occurs after immersion of the wet substrate in the K_2HPO_4 anionic solution, where a chemical reaction between HPO_4^{2-} and adsorbed Co^{2+}/Mn^{2+} ions leads to the deposition of adherent cobalt manganese phosphate layer as,

$$(x)[Co]^{2+} + (3\text{-}x)[Mn]^{2+} + 2HPO_4^{2-} \rightarrow Co_xMn_{3-x}(PO_4)_2 + 2H^+ \quad 3.3$$

Thus, the thin film is grown by the ions-by-ion growth mechanism, where film growth takes place by the deposition of ions at nucleation centre on immersed surface of a substrate. The weight of cobalt manganese phosphate on SS substrate

was measured by the gravimetric weight difference method **(Figure 4.3)**. The deposited weights of material for electrodes S-CMP-1, S-CMP-2, S-CMP-3, S-CMP-4, and S-CMP-5 are 0.809, 1.178, 0.956, 1.055, and 0.975 mg cm^{-2}, respectively.

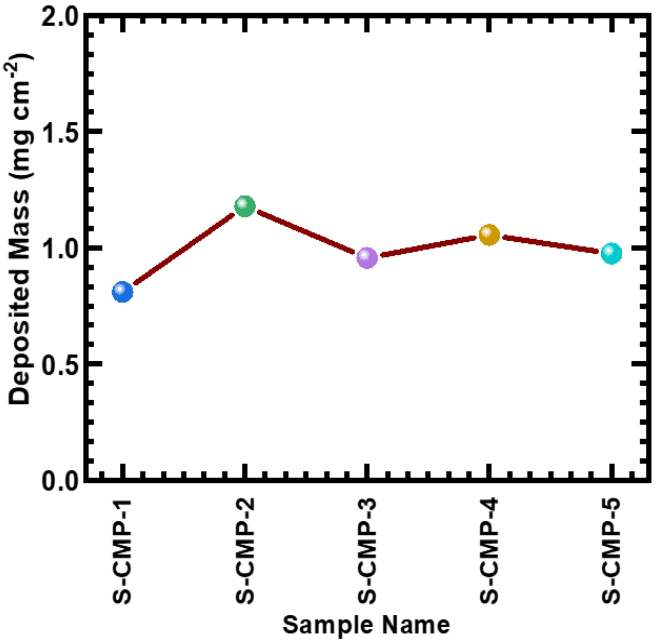

Figure 4.3: Cobalt manganese phosphate thin film thickness for different composition of Co:Mn.

4.2.A.3.2 XRD Study:

The crystallinity of S-CMP-1 to S-CMP-5 electrodes was analyzed by XRD analysis. As shown in **Figure 4.4**, amorphous phase of as-prepared cobalt manganese phosphate is observed, because no significant diffraction peaks were seen in the XRD patterns. The disorder may exist in the nanostructures resulting in lower or no crystallinity. The peaks labelled as 'SS' are corresponding to stainless steel conducting substrate. So, XRD results confirm the formation of amorphous cobalt manganese phosphate [$Co_xMn_{3-x}(PO_4)_2$] thin film by SILAR method. A well-crystallized structure has complexity in expansion and results in insufficient insertion and diffusion of ions. In contrast, amorphous materials allows a

continuous redox reaction on the surface, leading to higher performance compared to crystalline structures **[30]**.

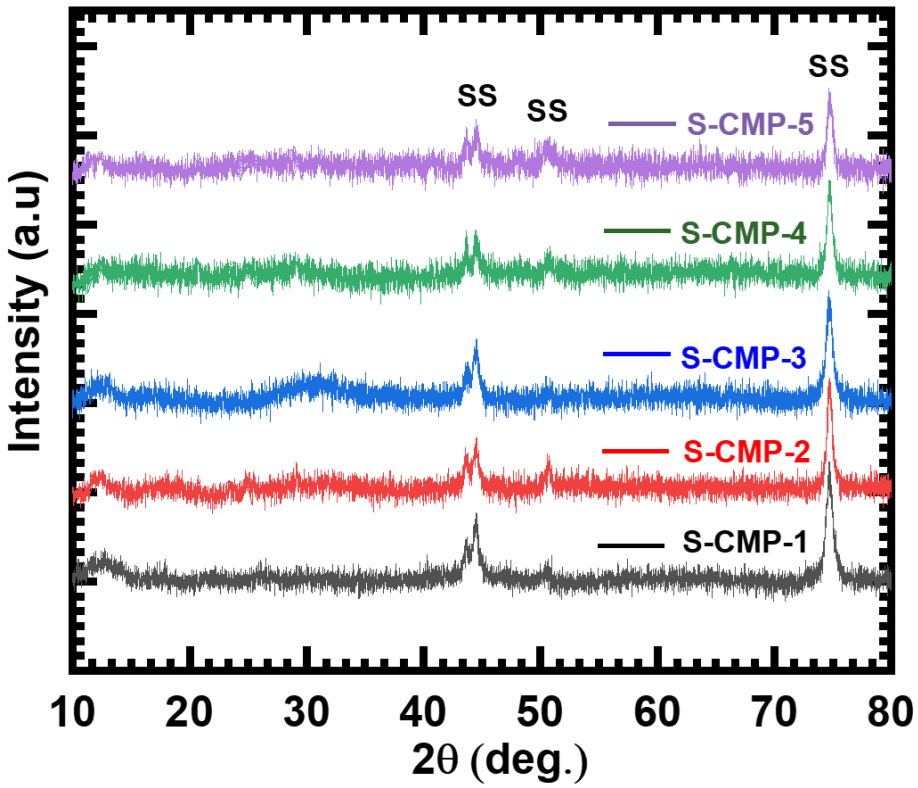

Figure 4.4: XRD patterns of cobalt manganese phosphate (S-CMP-series) thin films.

4.2.A.3.3 FTIR Study:

The chemical composition and surface purity are investigated via Fourier transform infrared (FTIR) spectroscopy. **Figure 4.5** illustrated FTIR spectra of S-CMP-series electrodes in region of 400 to 4000 cm^{-1}. FTIR spectra consist of the prominent characteristic peak at 589 cm^{-1} related to Mn-O as well as Co-O bending vibration bond **[9, 31]**. The weak band at 769 cm^{-1} is assigned to the lattice vibration mode of Co-O **[32]**. In addition, the sharp band at 1024 cm^{-1} is asymmetric stretching of PO_4^{3-} group and absorption peaks at about 949 and 1099 cm^{-1} attributed to P-O symmetric stretching vibration **[8, 32, 33]**. The bending

mode of H-O-P group is found at an absorption peak of 1354 cm^{-1} **[34]**. The peaks at approximately 1388 and 1630 cm^{-1} describe the H-O-H bending vibrations. Furthermore, a wide band at 3468 cm^{-1} is attributed to O-H stretching vibration mode from structural water molecules entrapped during synthesis **[9, 31, 32, 34]**. The spectra exhibit characteristic features of cobalt manganese phosphate and the results of FTIR analysis indicates successful formation of hydrous cobalt manganese phosphate.

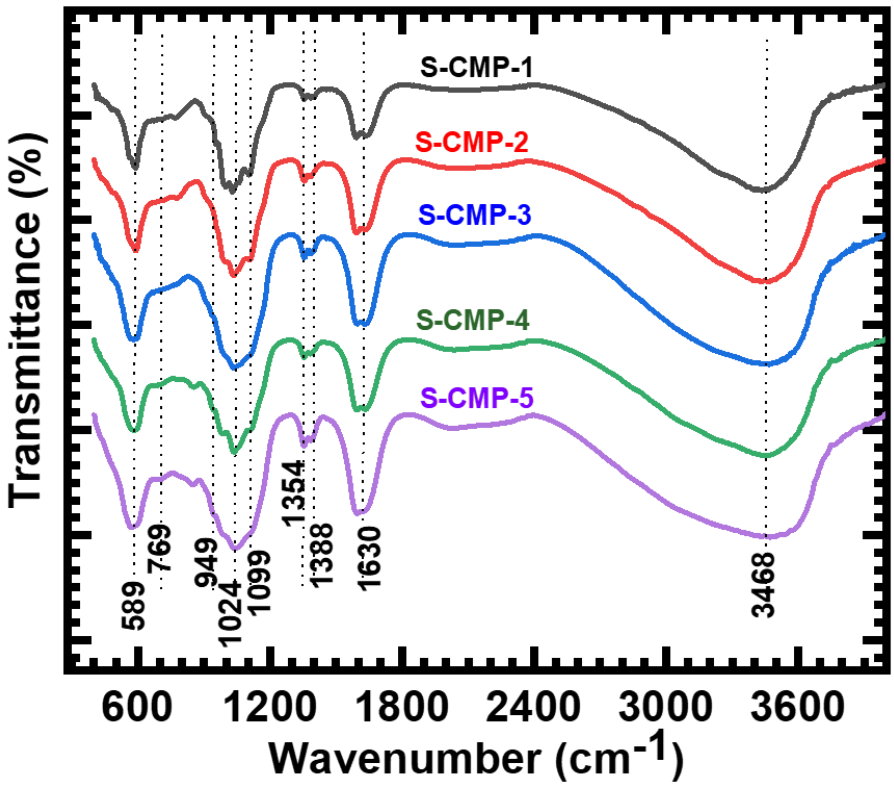

Figure 4.5: FTIR spectra of cobalt manganese phosphate (S-CMP-series) thin films.

4.2.A.3.4 XPS Study:

X-ray photoelectron spectroscopy (XPS) is used to evaluate elemental states of the as-synthesized electrode (S-CMP-4) **(Figure 4.6 (a-e))**. The existence of Co, Mn, P and O elements were identified from a survey scan of cobalt manganese phosphate for S-CMP-4 electrode **(Figure 4.6 (a))**. The main two peaks located at a binding energy of 781.3 eV for Co $2p_{3/2}$ and 797.1 eV for Co $2p_{1/2}$ **(Figure 4.6 (b))**

along with two satellite peaks, indicating the presence of Co^{2+} and Co^{3+} oxidation states **[35, 36]**.

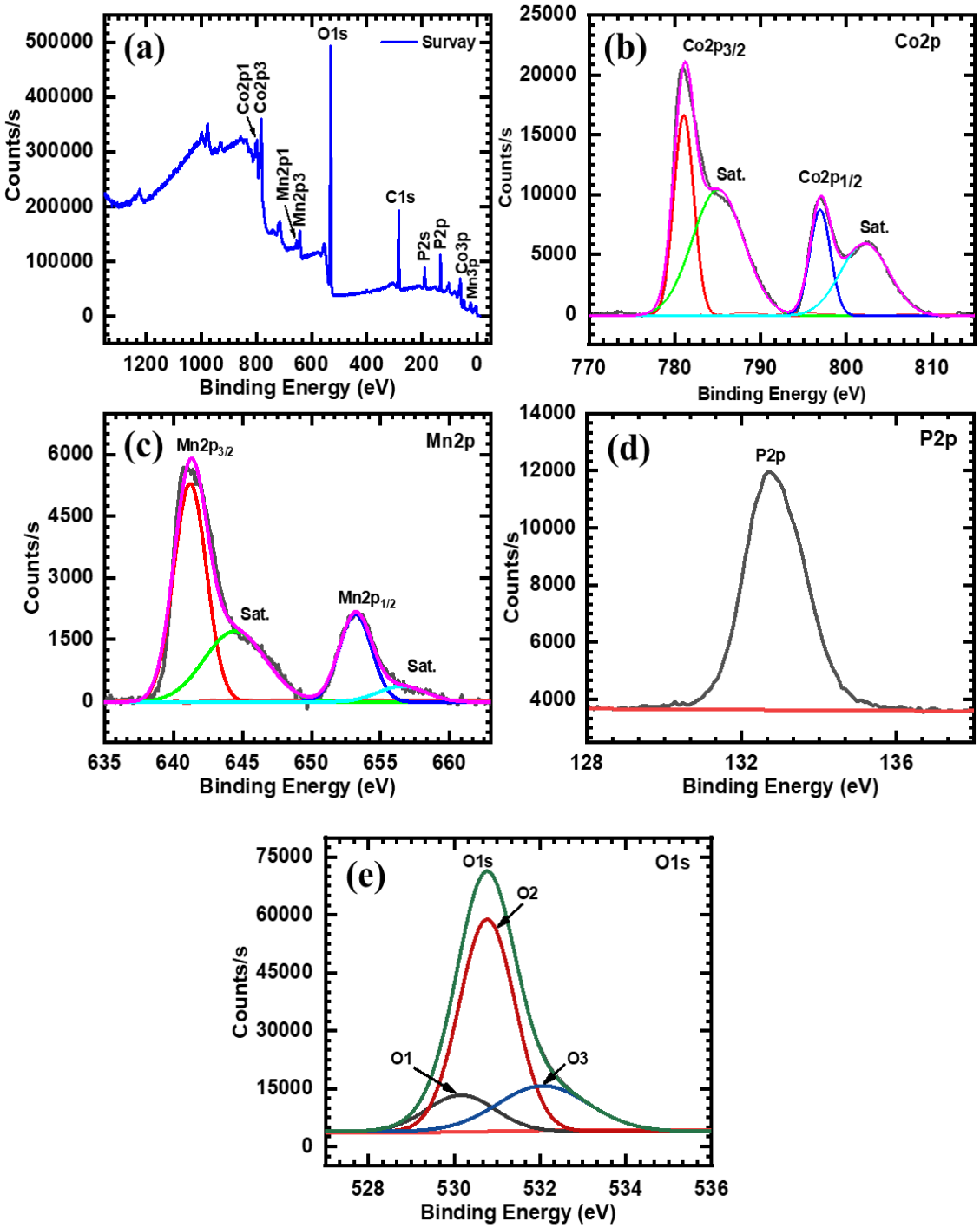

Figure 4.6: XPS spectra of S-CMP-4 electrode: (a) survey spectrum, (b) Co 2p, (c) Mn 2p, (d) P 2p and (e) O 1s spectrum.

In XPS spectrum of Mn 2p **(Figure 4.6 (c))**, the two different peaks located at 641.3 (Mn $2p_{3/2}$) and 653.1 eV (Mn $2p_{1/2}$) indicates the presence of Mn^{2+} and two satellite peaks at 644.6 and 656 eV represents the Mn^{3+} oxidation states in Co-Mn Phosphate **[9, 37]**. The XPS spectrum of P 2p **(Figure 4.6 (d))** exhibits a peak at 133.6 eV, which corresponds to the P $2p_{3/2}$ in Co-Mn Phosphate **[38].** Moreover, **Figure 4.6 (e)** shows XPS spectrum of O 1s, the fitted peak located at 530.0 eV is attributed to a metal-oxygen bond. Also, binding energies of 530.7 and 531.4 eV are assigned to phosphate species (P-O) and oxygen of O-H group, respectively in Co-Mn Phosphate **[8, 39]**. Finally, the XPS results confirmed that the cobalt manganese phosphate was successfully obtained.

4.2.A.3.5 FE-SEM Study:

The surface morphology of as-prepared S-CMP-series thin film electrodes are investigated via field emission scanning electron microscopy (FE-SEM). FE-SEM images show porous morphology consisting of a nanoparticle-like structure. This morphology can support the rapid diffusion of electrolytic ions in electrodes with faster electron transport even at a high charging rate. The FE-SEM images of cobalt manganese phosphate electrode at two magnifications (20,000x and 50,000x) are revealed in **Figure 4.7 (a1-e2)**. The FE-SEM images of pristine manganese phosphate (S-CMP-1) are shown in **Figure 4.7 (a1, a2)**, indicates that the sample consists of nanoparticle structure having a particle size between 225-295 nm. Similarly, nanoparticles-like morphology is observed for electrode **(Figure 4.7 (b1-d2))** S-CMP-2 (115-165 nm), S-CMP-3 (120-140 nm) and S-CMP-4 (90-140 nm) with different particle sizes. The FE-SEM images of pristine cobalt phosphate (S-CMP-5) **(Figure 4.7 (e1, e2))** indicate that thin film contains nanoparticle-like morphology having a particle size between 120-137 nm. Also,

such nanoparticles-like morphology with porous interconnected structure may promote the high surface area and easy electrolyte access during electrochemical reactions **[40-42]**.

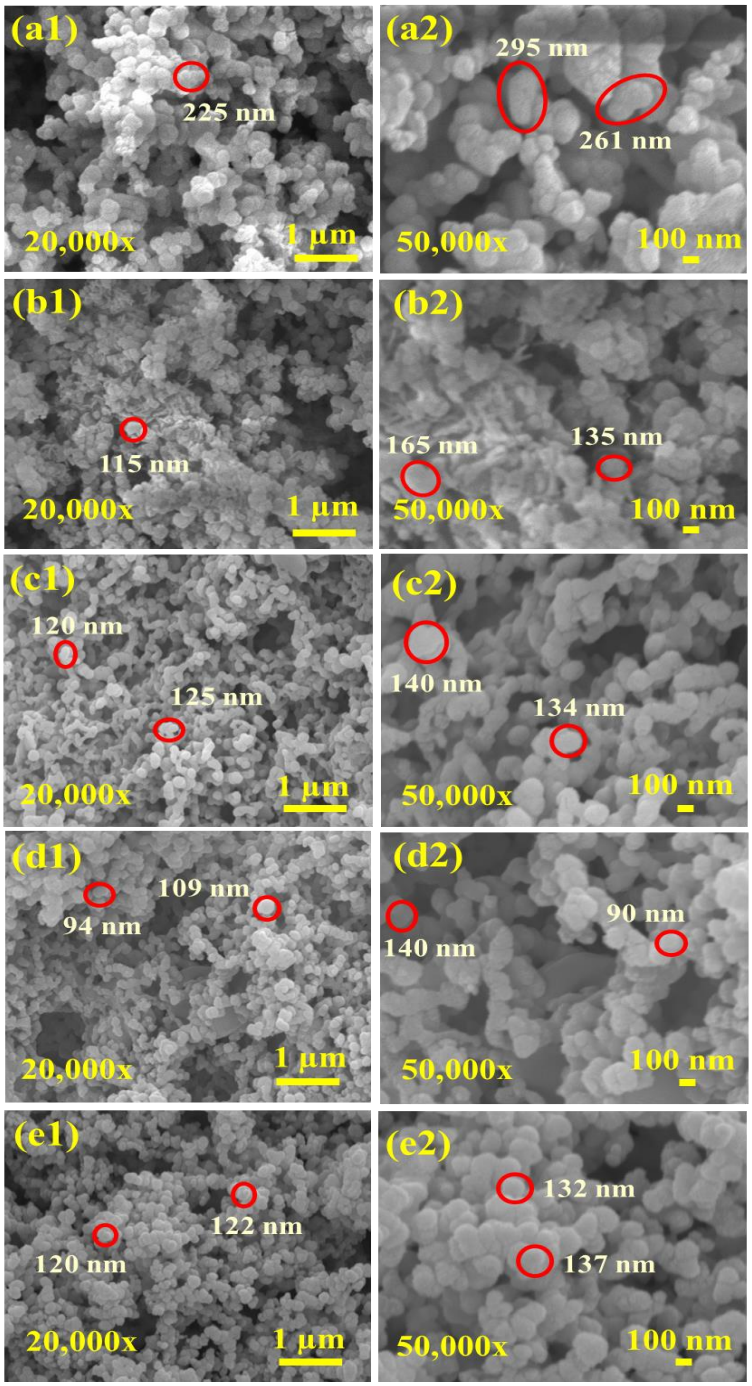

Figure 4.7: FE-SEM micrographs of cobalt manganese phosphate electrodes: (a1, a2) S-CMP-1, (b1, b2) S-CMP-2, (c1, c2) S-CMP-3, (d1, d2) S-CMP-4, and (e1, e2) S-CMP-5 at different magnifications (20,000x, and 50,000x).

4.2.A.3.6 EDS Study:

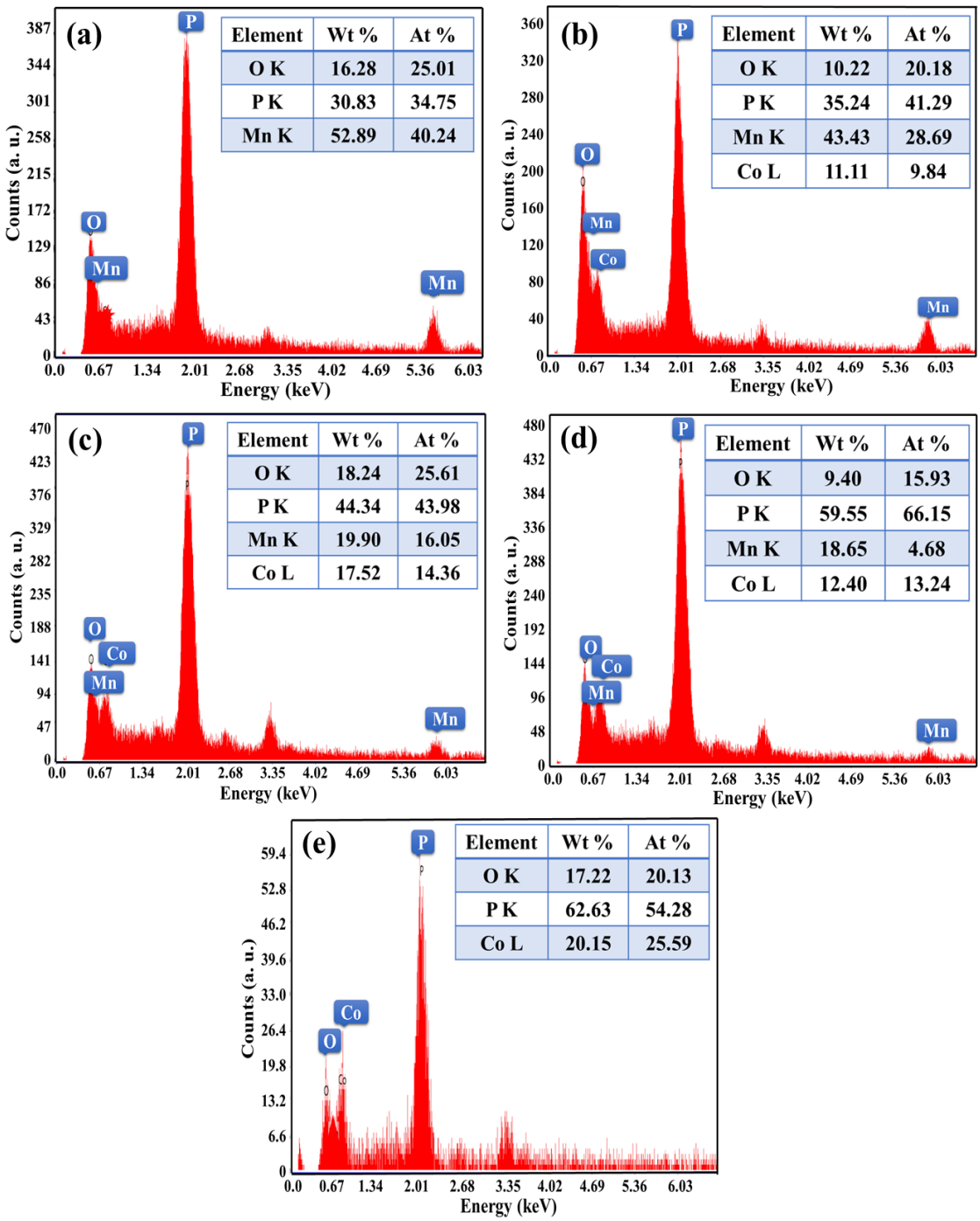

Figure 4.8: EDS spectra of cobalt manganese phosphate electrodes: (a) S-CMP-1, (b) S-CMP-2, (c) S-CMP-3, (d) S-CMP-4, and (e) S-CMP-5.

The elemental composition of Co-Mn Phosphate is investigated by energy-dispersive X-ray spectroscopy (EDS) and corresponding outcomes are exhibited in **Figure 4.8 (a-e)**. The EDS spectra confirm presence of Co, Mn, P, and O elements in

a material without any other impurity. **Table 4.2** shows experimental and observed Co:Mn atomic ratios by EDS analysis in S-CMP-1 to S-CMP-5 electrodes. Also it is observed that, the concentration of manganese decreases from S-CMP-1 to S-CMP-5 electrode, which matches with the experimental composition ratio. The phase formation of existing materials ($Co_xMn_{3-x}(PO_4)_2$) is confirmed from the EDS analysis.

Table 4.2: Experimental and observed cobalt and manganese atomic ratio in S-CMP-series thin films.

Sample Name	Experimental Ratio (Co:Mn)	Observed Ratio (Co:Mn)	Obtained Phase
S-CMP-1	0:1	0:1	$Mn_3(PO_4)_2$
S-CMP-2	0.25:0.75	0.26:0.74	$Co_{0.78}Mn_{2.22}(PO_4)_2$
S-CMP-3	0.50:0.50	0.47:0.53	$Co_{1.41}Mn_{1.59}(PO_4)_2$
S-CMP-4	0.75:0.25	0.74:0.26	$Co_{2.22}Mn_{0.78}(PO_4)_2$
S-CMP-5	1:0	1:0	$Co_3(PO_4)_2$

4.2.A.4 Conclusions:

In summary, the binder-free synthesis of cobalt manganese phosphate thin film electrodes (S-CMP-series) at ambient temperature is achieved by SILAR method. S-CMP-series thin films show nanoparticles-like morphology with porous channels and XRD analysis confirmed the formation of amorphous cobalt manganese phosphate. The compositions of existing S-CMP series thin film materials is confirmed from the EDS analysis with $Co_xMn_{3-x}(PO_4)_2$ (x= 0 to 3) phase. Also, the FTIR study confirms the structural water present in the prepared cobalt manganese phosphate thin films. The XPS results confirm that, the obtained material is a cobalt manganese phosphate compound. The overall results confirm that, the obtained material in thin film form is amorphous, porous and hydrous cobalt manganese phosphate [$Co_xMn_{3-x}(PO_4)_2$].

SECTION – B

Supercapacitive Performance Evaluation of Cobalt Manganese Phosphate Thin Films

4.2.B.1 Introduction:

In the present section, electrochemical measurement of cobalt manganese phosphate (S-CMP-1 to S-CMP-5) thin films in 1M KOH electrolyte was studied by CV, GCD and EIS techniques. Moreover, the effect of scan rate and current density on electrochemical performance of cobalt manganese phosphate thin films were investigated using above mentioned electrochemical techniques, to decide appropriate electrode material for the construction of supercapacitor device.

4.2.B.2 Results and Discussion:

4.2.B.2.1 Cyclic Voltammetry (CV) Study:

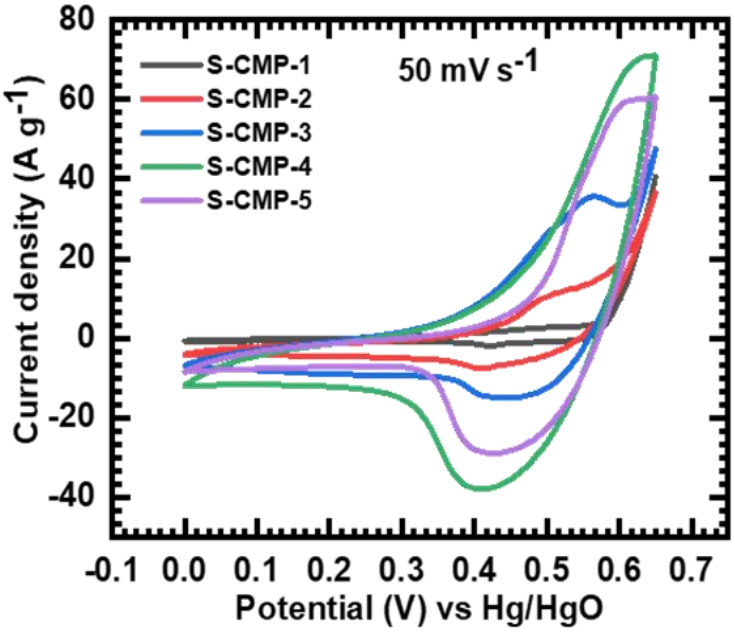

Figure 4.9: CV plots of S-CMP series thin films in 1 M KOH electrolyte at 50 mV s^{-1} scan rate.

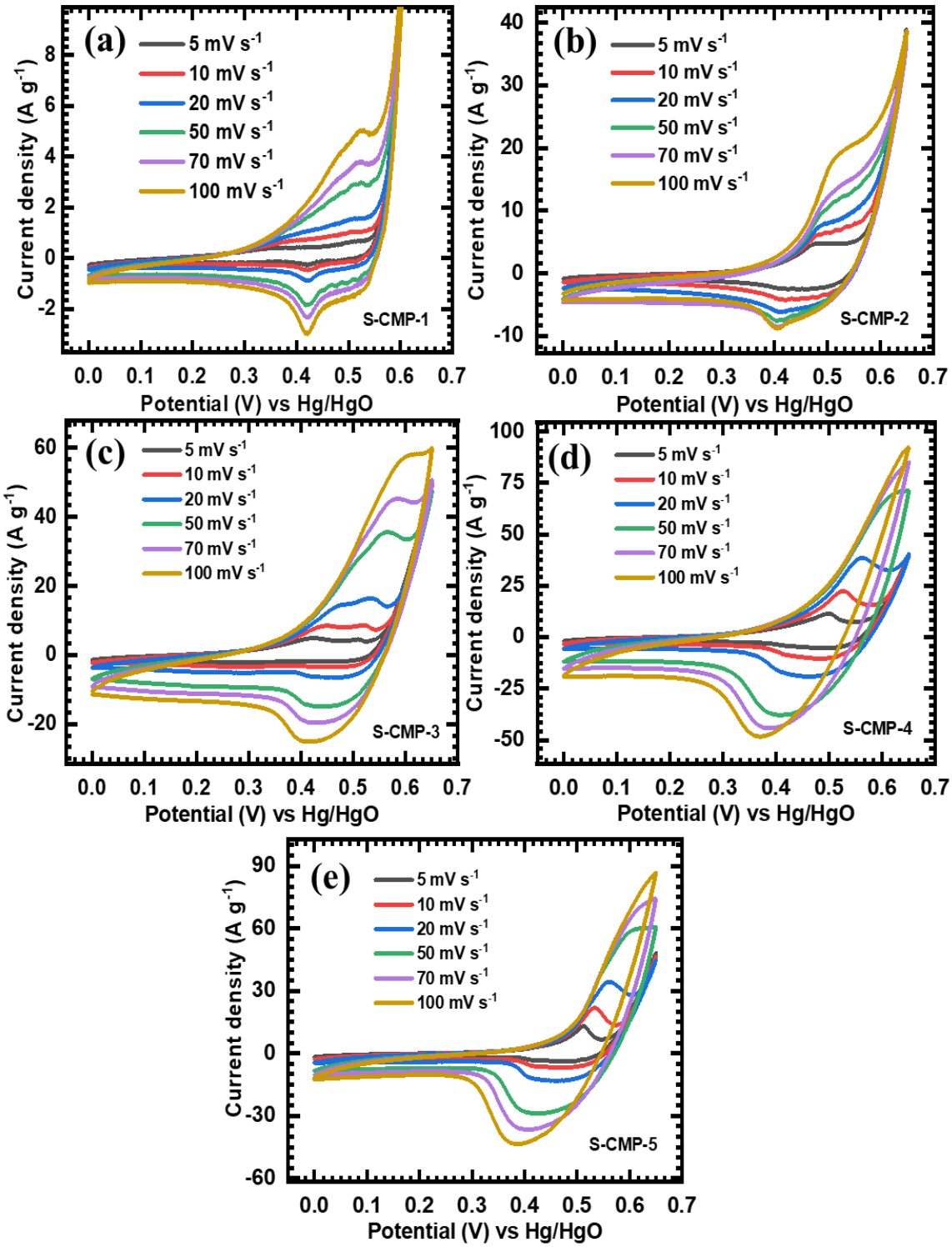

Figure 4.10: (a-e) CV plots of cobalt manganese phosphate (S-CMP-series) at different scan rates (5-100 mV s^{-1}).

The CV curves of S-CMP-series electrodes are investigated in a potential window of 0.0 to 0.65 V/Hg/HgO in aqueous 1 M KOH electrolyte at a fixed scan

rate of 50 mV s^{-1} and presented in **Figure 4.9**. The S-CMP series thin film electrodes in the KOH electrolyte exhibit pseudocapacitive behavior, which is different from the electric double-layer capacitors (EDLCs) **[43, 44]**. In these plots, the S-CMP-4 electrode contributes more area under the curve. Furthermore, the CV curves of S-CMP-series thin films at different scan rates from 5-100 mV s^{-1} are demonstrated in **Figure 4.10 (a-e)**. It is noted that, all CV curves of S-CMP-series electrodes displays the redox behaviour.

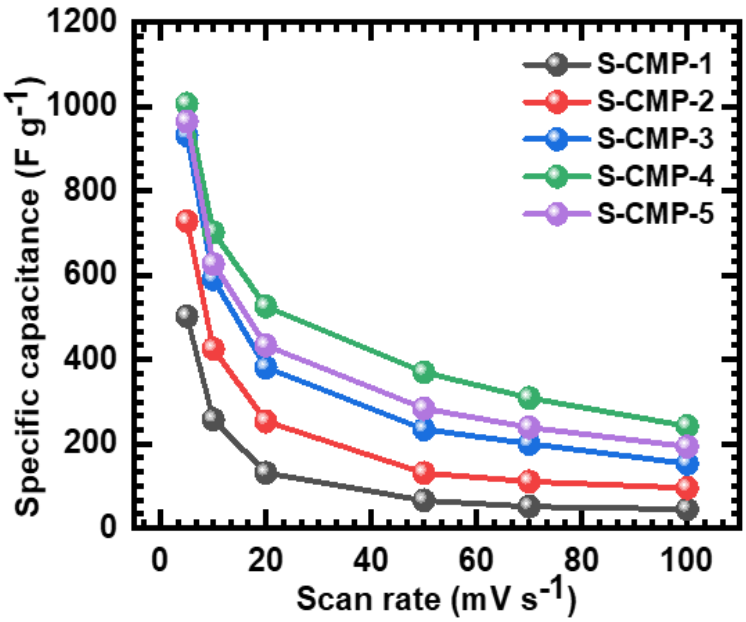

Figure 4.11: Specific capacitance of cobalt manganese phosphate (S-CMP-series) at various scan rates (5-100 mV s^{-1}).

The specific capacitance of S-CMP-series thin films is calculated using **Eq^{n}. (2.5)**. The values of specific capacitance for S-CMP-series thin films versus scan rate are plotted and presented in **Figure 4.11**. The highest specific capacitance is observed at a lower scan rate and it decreases at a higher scan rate. This is due to electrolytic ions at high scan rates diffuse only on the outer surface of Co-Mn Phosphate electrode, while the electrolytic ions at low scan rates diffuse both (outer and inner) surfaces of the thin film, resulting in efficient utilization of

electrode material. The obtained values of specific capacitance for S-CMP-1, S-CMP-2, S-CMP-3, S-CMP-4, and S-CMP-5 thin films at 5 mV s^{-1} are 502, 728, 932, 1005 and 964 F g^{-1}. Due to the synergy between cobalt and manganese ions and the high surface area offered by nanoparticles (90-140 nm), highest specific capacitance as compared to pristine cobalt phosphate or manganese phosphate electrode is observed for S-CMP-4 electrode.

4.2.B.2.2 Galvanostatic Charge-Discharge (GCD) Study:

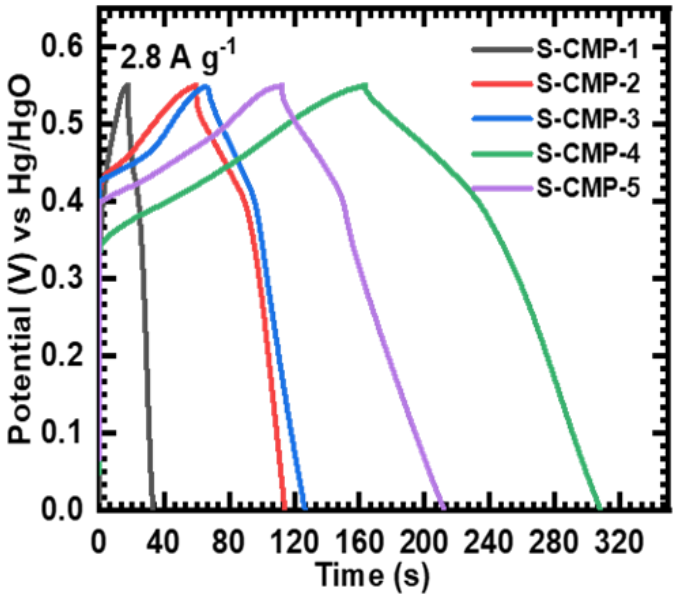

Figure 4.12: GCD curves of S-CMP-series thin film in 1 M KOH electrolyte at 2.8 A g^{-1} current density.

The GCD measurement is a very important method for calculating specific capacitance at different current densities. The charge-discharge behavior of the S-CMP-series electrodes was examined in the potential window of 0.0 to 0.55 V/Hg/HgO at 2.8 A g^{-1} current density in an aqueous 1 M KOH solution and shown in **Figure 4.12**. The GCD curves of S-CMP-series thin film electrodes show a potential drop during a discharging time. The S-CMP-4 thin film electrode shows a higher discharging time (**Figure 4.12**).

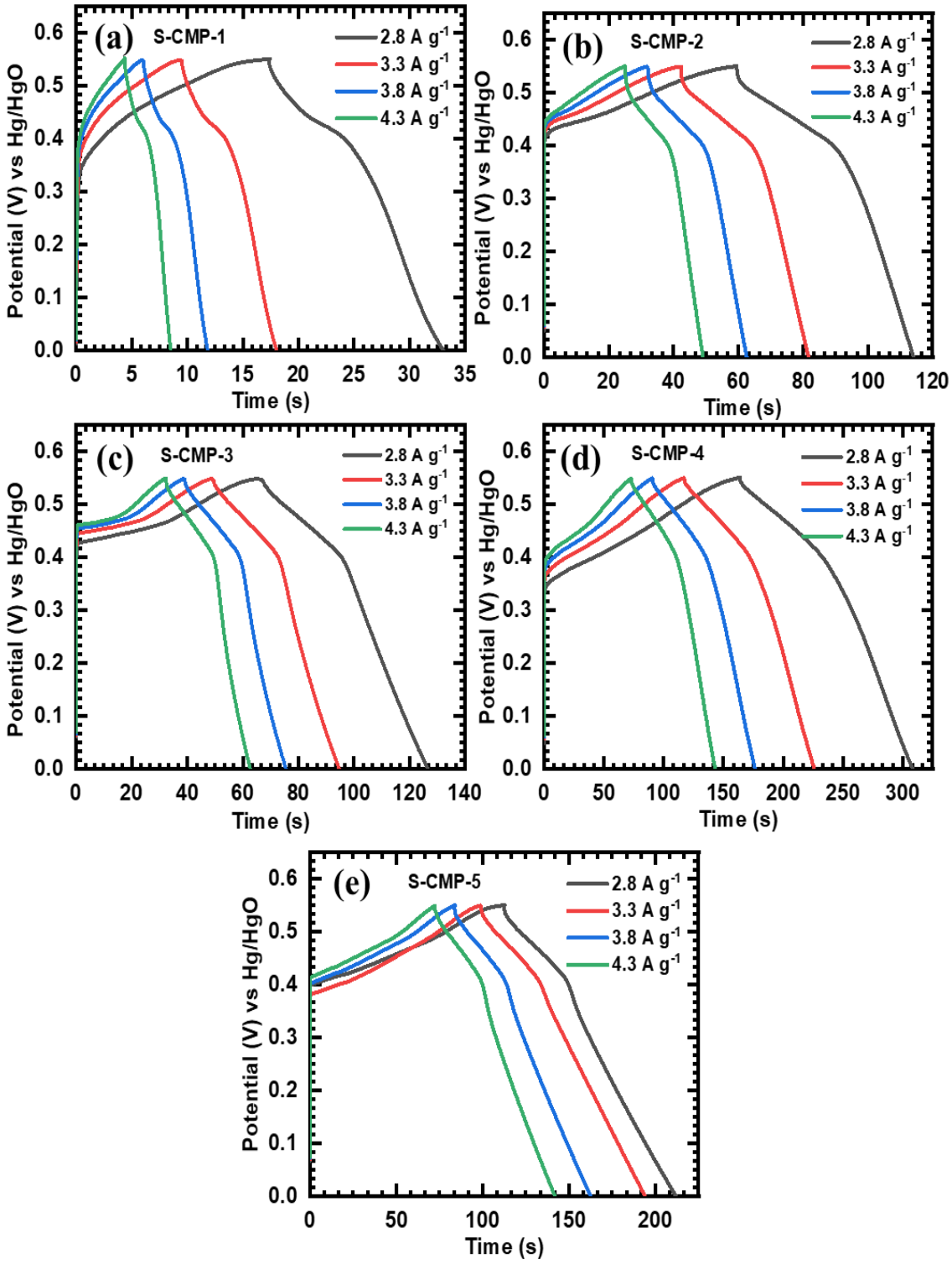

Figure 4.13: GCD curves of S-CMP series thin films for (a) S-CMP-1, (b) S-CMP-2, (c) S-CMP-3, (d) S-CMP-4, and (e) S-CMP-5 at different current densities (2.8 to 4.3 A g^{-1}).

The nanoparticles-like structured S-CMP-4 thin film electrode offers a number of electrochemically active sites compared to other S-CMP-series electrodes. Also, the quasi-triangular profile of the charge-discharge process in 1 M KOH is associated with Faradaic reaction **[45]**. Further, the GCD curves of S-CMP-series thin films at different current densities from 2.8 to 4.3 A g^{-1} are depicted in **Figure 4.13 (a-e)**. The non-linear behavior of charge-discharge curves reflects the electrochemical adsorption/desorption reaction at the interface between electrode and electrolyte and excellent reversible redox reactions.

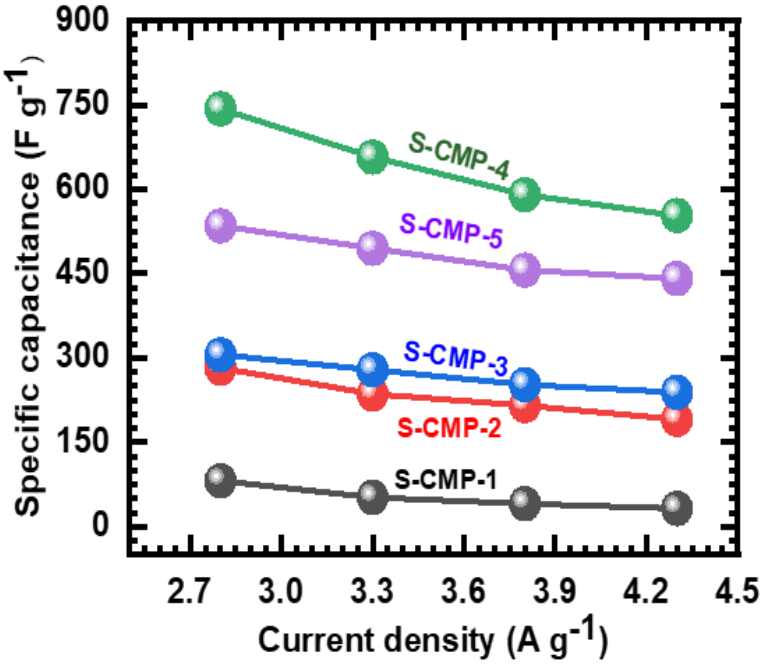

Figure 4.14: specific capacitance of S-CMP series thin films at various current densities (2.8 to 4.3 A g^{-1}).

The specific capacitance is calculated using **Eq^{n}. (2.6)** from the discharge curves of GCD cycles. **Figure 4.14** displays the plots of specific capacitance vs current density. The specific capacitance of S-CMP-1 to S-CMP-5 electrodes are 82, 282, 305, 743 and 535 F g^{-1} at 2.8 A g^{-1} current density. The rate of electrolytic ion diffusion during charging-discharging process is slow at low current densities.

Therefore, the electrolytic ions have enough time to disperse into Co-Mn Phosphate electrodes, resulting in the maximum possible insertion reaction which leads to better capacitive behavior at lower current densities. The capacitance values increased with increasing concentration of Co^{2+} ions in thin film (from S-CMP-1 to S-CMP-4). Furthermore, the S-CMP-4 electrode provides higher electrochemical performance and the results are comparable to reported work **[20, 21]**. It suggests that, S-CMP-4 electrode can be a potential candidate for supercapacitor applications.

4.2.B.2.3 Electrochemical Impedance Spectroscopy (EIS) Study:

The measured impedance quantitatively explores the electrochemical properties of electrodes and electrolytes **[46]**. **Figure 4.15 (a)** shows Nyquist plots of S-CMP-series thin films performed in 1 M KOH electrolyte. The equivalent circuit is shown in **Figure 4.15 (b)** and it is found to fit with experimental data of Co-Mn Phosphate thin film electrode. In general, all Nyquist plot reveals two different regions: the semi-circular arc present in high-frequency section, it is based on solution resistance (R_s) and faradic charge-transfer resistance (R_{ct}), and the plot ends in a vertical line with a capacitive slope in a low-frequency region associated with electrolytic ion diffusion in the porous structure of a material and denoted by Warburg element (W) **[47-49]**.

The ideal capacitive/pseudocapacitive behavior is described by the so-called constant phase element (CPE), which depends on the redox capacitance and diffusion effects of the porosity at a low frequency **[50, 51]**. The solution resistance (R_s= 0.99, 0.96, 1.18, 0.98 and 1.20 Ω) and charge transfer resistance (R_{ct}= 392.84, 114.68, 27.63, 6.32 and 8.44 Ω) are obtained for S-CMP-series electrodes.

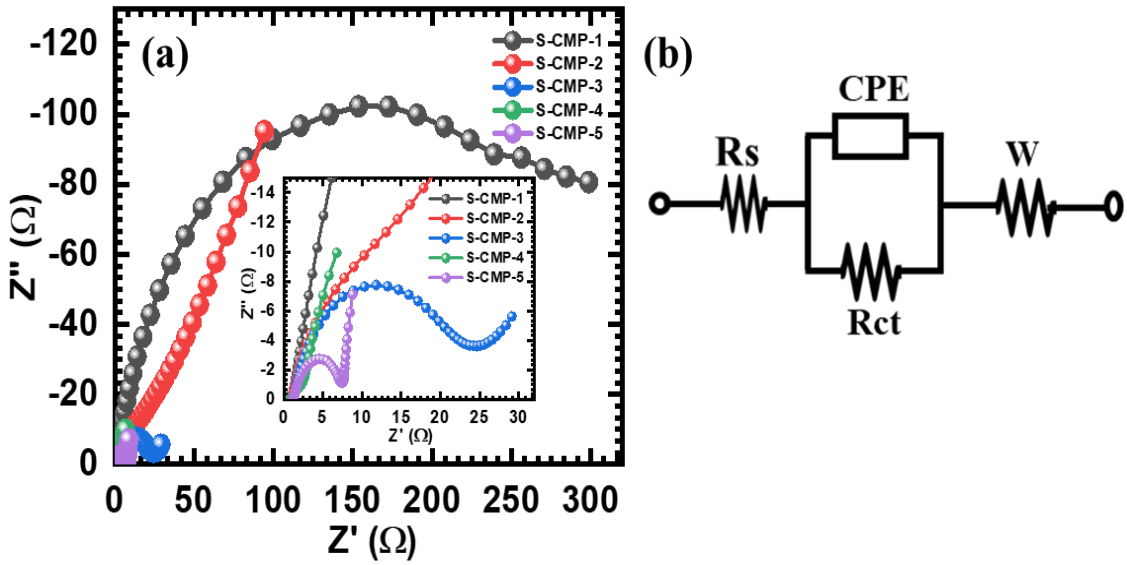

Figure 4.15: (a) Nyquist plots of S-CMP-series thin films (Inset: enlarged Nyquist plot at higher frequencies region), and (b) fitted equivalent circuit for Nyquist plot of thin film.

The small values of R_s and R_{ct} for S-CMP-series thin films indicate a good attachment of the active material with the current collector and the spontaneous electrochemical reaction between the active electrode material and electrolyte. It is manifesting that, the good conductivity of electrolyte and very low internal resistance of material leads to a high capacitance of S-CMP-4 electrode.

4.2.B.2.4 Stability Study:

The stability of electrode must be checked for long-term device application. **Figure 4.16 (a)** shows the cyclic stability of S-CMP-4 electrode at 3.8 A g^{-1} current density. Stability study reveals that, the S-CMP-4 electrode shows 90.6 % capacitive retention over 4000 cycles. The 1st, 2000th and 4000th GCD cycle of S-CMP-4 electrode shows a slight decrement in storing capacitance with cycles **(Figure 4.16 (b))**. Also, decrease in capacitive retention is observed may be due to the loss of

active material by the dissolution or detachment during the early charging/discharging cycles **[52]**.

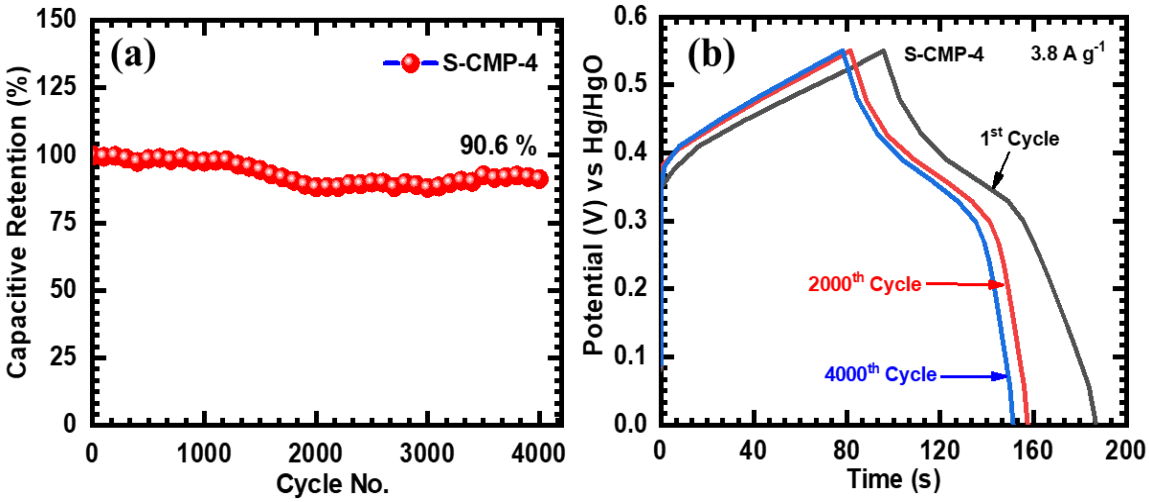

Figure 4.16: (a) GCD stability graph of S-CMP-4 electrode for 4000 cycles and (b) 1st, 2000th and 4000th GCD cycle of S-CMP-4 electrode.

4.2.B.3 Conclusions:

The electrochemical performance of cobalt manganese phosphate (S-CMP-series) depends on the different compositions of Co:Mn. The optimized Co-Mn phosphate ($Co_{2.22}Mn_{0.78}(PO_4)_2$) electrode exhibited the highest specific capacitance of 743 F g^{-1} at a current density of 2.8 A g^{-1} with good cyclic stability up to 90.6 % after 4000 GCD cycles. A small R_{ct} value (6.32 Ω) of S-CMP-4 electrode indicates good charge transfer kinetics and high electrical conductivity, which attributed to excellent capacitive performance. The electrochemical analysis indicates that, S-CMP-4 thin film electrode is suitable as a cathode for asymmetric supercapacitor device fabrication.

4.3 References:

1. J. L. Liu, L. Z. Fan, X. Qu, Electrochim. Acta, 66, (2012), 302-305.
2. L. Zhao, L. Z. Fan, M. Q. Zhou, Adv. Mater., 22, (2010), 5202–5206.
3. Z. Niu, L. Zhang, L. Liu, B. Zhu, H. Dong, X. Chen, Adv. Mater., 25, (2013), 4035-4042.
4. C. Choi, J. W. Park, K. J. Kim, D. W. Lee, M. J. de Andrade, S. H. Kim, S. Gambhir, G. M. Spinks, R. H. Baughman, S. J. Kim, RSC Adv., 2018, 8, 13112-13120.
5. Y. Wang, Y. Ding, X. Guo, G. Yu, Nano Res., 12, (2019), 1978–1987.
6. R. Bendi, V. Kumar, V. Bhavanasi, K. Parida, P. S. Lee, Adv. Energy Mater., 6, (2016), 1501833.
7. X. Li, A. M. Elshahawy, C. Guan, J. Wang, Small, 13, (2017), 170153.
8. P. K. Katkar, S. J. Marje, S. S. Pujari, S. A. Khalate, A. C. Lokhande, U. M. Patil, ACS Sustain. Chem. Eng., 7, (2019), 11205–11218.
9. P. K. Katkar, S. J. Marje, S. S. Pujari, S. A. Khalate, P. R. Deshmukh, U. M. Patil, Synth. Met., 267, (2020), 1-13.
10. S. J. Marje, P. K. Katkar, S. S. Pujari, S. A. Khalate, A. C. Lokhande, U. M. Patil, Synth. Met., 259, (2020), 1-11.
11. Z. Luo, E. Liu, T. Hu, Z. Li, T. Liu, Ionics, 21, (2015), 289–294.
12. S. Li, F. Teng, M. Chen, N. Li, X. Hua, K. Wang, M. Li, Chem. Phys. Lett, 601, (2014), 59.
13. B. Zhao, L. Zhang, Q. Zhang, D. Chen, Y. Cheng, X. Deng, Y. Chen, R. Murphy, X. Xiong, B. Song, C. P. Wong, M. S. Wang, M. Liu, Adv. Energy Mater., 8, (2018), 1702247.
14. J. Duay, S. A. Sherrill, Z. Gui, E. Gillette, S. B. Lee, ACS Nano, 7, (2013), 1200–1214.
15. B. Wang, J. S. Chen, Z. Wang, S. Madhavi, X. W. (David) Lou, Adv. Energy Mater., 2, (2012), 1188-1192.
16. Z. Xiao, Y. Bao, Z. Li, X. Huai, M. Wang, P. Liu, L. Wang, ACS Appl. Energy Mater., 2, (2019), 1086–1092.
17. X. Cheng, J. Zhang, J. Ren, N. Liu, P. Chen, Y. Zhang, J. Deng, Y. Wang, H. Peng, J. Phys. Chem. C, 120, (2016), 9685–9691.

18. Q. Li, Y. H. Li, H. R. Peng, X. Cui, M. Zhou, K. Y. Feng, P. Xiao, J. Mater. Sci., 51, (2016), 9946-9957.
19. Z. Yan, F. Wang, P. Deng, Y. Wang, K. Cai, Y. Chen, Z. Wang, Y. Liu, Biosens. Bioelectron., 109, (2018), 132-138.
20. H. Mao, Y. Qian, Z. Jin, Y. Zhang, Mater. Lett, 228, (2018), 258-261.
21. D. Chinnadurai, A. R. Selvaraj, R. Rajendiran, G. R. Kumar, H. J. Kim, K. K. Viswanathan, K. Prabakar, ACS Omega, (2018), 3, 1718–1725.
22. P. Xu, K. Ye, D. Cao, J. Huang, T. Liu, K. Cheng, J. Yin, G. Wang, J. Power Sources, 268, (2014), 204-211.
23. Y. Bai, L. Fang, H. Xu, X. Gu, H. Zhang, Y. Wang, Small, 13, (2017), 1-11.
24. R. B. Kale, C. D. Lokhande, Mater. Res. Bull., 39, (2004), 1829-1839.
25. H. M. Pathan, C. D. Lokhande, Bull. Mater. Sci., 27, (2004), 85–111.
26. S. D. Sartale, C. D. Lokhande, Mater. Chem. Phys., 65, (2000), 63-67.
27. D. P. Dubal, R. Holze, New J. Chem., 37, (2013), 403-408.
28. R. S. Patil, C. D. Lokhande, R. S. Mane, H. M. Pathan, O. S. Joo, S. H. Han, Mat. Sci. Eng. B, 129, (2006), 59-63.
29. S. S. Kale, R. S. Mane, H. Chung, M. Y. Yoon, C. D. Lokhande, S. H. Han, Appl. Surf. Sci., 253, (2006), 421-424.
30. Z. Jiang, W. Lu, Z. Li, K. H. Ho, X. Li, X. Jiao, D. Chen, J. Mater. Chem. A, 2, (2014), 8603-8606.
31. B. R. Wiston, M. Ashok, Mater. Sci. Semicond. Process., 103, (2019), 1-8.
32. P. K. Katkar, S. J. Marje, S. B. Kale, A. C. Lokhande, C. D. Lokhande, U. M. Patil, CrystEngComm, 21, (2019), 884-893.
33. B. Liang, Y. Chen, J. He, C. Chen, W. Liu, Y. He, X. Liu, N. Zhang, V. A. L. Roy, ACS Appl. Mater. Interfaces, 10, (2018), 3506–3514.
34. D. Wang, Y. Xu, W. Sun, X. Guo, L. Yang, F. Wang, Z. Yang, Electrochim. Acta, 337, (2020), 1-10.
35. T. Ma, S. Dai, M. Jaroniec, S. Qiao, J. Am. Chem. Soc., 136, (2014), 13925-13931.
36. J. Li, G. Wei, Y. Zhu, Y. Xi, X. Pan, Y. Ji, I. V. Zatovsky, W. Han, J. Mater. Chem. A, 5, (2017), 14828-14837.
37. G. Neher, T. T. Salguero, Cryst. Growth Des., 17, (2017), 4864–4872.
38. P. Arunachalam, M. N. Shaddad, A. S. Alamoudi, M. A. Ghanem, A. M. Al-Mayouf, Catalysts, 7, (2017), 1-11.

39. X. Liang, B. Zheng, L. Chen, J. Zhang, Z. Zhuang, B. Chen, ACS Appl. Mater. Interfaces, 9, (2017), 23222–23229.
40. X. J. Ma, W. B. Zhang, L. B. Kong, Y. C. Luo, L. Kang, RSC Adv., 6, (2016), 40077-40085.
41. L. Yu, B. Guan, W. Xiao, X. W. (David) Lou, Adv. Energy Mater., 5, (2015), 1-7.
42. F. Yunyun, L. Xu, Z. Wankun, Z. Yuxuan, Y. Yunhan, Q. Honglin, X. Xuetang, W. Fan, Appl. Surf. Sci., 357, (2015), 2013-2021.
43. Jaidev, R. I. Jafri, A. K. Mishra, S. Ramaprabhu, J. Mater. Chem., 21, (2011), 17601-17605.
44. X. Zhang, L. Ji, S. Zhang, W. Yang, J. Power Sources, 173, (2007), 1017-1023.
45. N. R. Chodankar, H. D. Pham, A. K. Nanjundan, J. F. S. Fernando, K. Jayaramulu, D. Golberg, Y. K. Han, D. P. Dubal, Small, (2020), 2002806.
46. P. R. Deshmukh, S. N. Pusawale, V. S. Jamadade, U. M. Patil, C. D. Lokhande, J. Alloys Compd., 509, (2011), 5064-5069.
47. J. Xiao, S. Yang, J. Mater. Chem., 22, (2012), 12253-12262.
48. B. Xie, Y. Chen, M. Yu, X. Shen, H. Lei, T. Xie, Y. Zhang, Y. Wu, Nanoscale Res. Lett, 10, (2015), 1-11.
49. P. Vela´squez, D. Leinen, J. Pascual, J. R. R. Barrado, P. Grez, H. Go´mez, R. Schrebler, R. D. Rı´o, R. Co´rdova, J. Phys. Chem. B, 109, (2005), 4977-4988.
50. A. I. Najafabadi, S. Yasuda, K. Kobashi, T. Yamada, D. N. Futaba, H. Hatori, M. Yumura, S. Iijima, K. Hata, Adv. Mater., 22, (2010), E235-E241.
51. D. E. Pacheco-Catalán, M. A. Smit, E. Morales, Int. J. Electrochem. Sci., 6, (2011), 78-90.
52. Y. K. Hsu, Y. C. Chen, Y. G. Lin, Electrochim. Acta, 139, (2014), 401-407.

CHAPTER -5

ASYMMETRIC SUPERCAPACITOR DEVICE FABRICATION AND PERFORMANCE EVALUATION

CHAPTER 5

Asymmetric Supercapacitor Device Fabrication and Performance Evaluation

Sr. No.	Title		Page No.
5.1	**Introduction**		**161**
SECTION – A **Synthesis, Characterization and Supercapacitive Performance Evaluation of Reduced Graphene Oxide (rGO) Electrode (As an Anode)**			
5.2.A.1	**Introduction**		**162**
5.2.A.2	**Experimental Details**		**162**
	5.2.A.2.1	*Chemicals*	**162**
	5.2.A.2.2	*Preparation of Reduced Graphene Oxide Electrode*	**162**
5.2.A.3	**Results and Discussion**		**164**
	5.2.A.3.1	*XRD Study*	**164**
	5.2.A.3.2	*Raman Study*	**164**
	5.2.A.3.3	*BET study*	**165**
	5.2.A.3.4	*FE-SEM Study*	**166**
5.2.A.4	**Supercapacitive Performance Evaluation**		**167**
	5.2.A.4.1	*CV Study*	**167**
	5.2.A.4.2	*GCD Study*	**168**
	5.2.A.4.3	*EIS Study*	**169**
	5.2.A.4.4	*Stability Study*	**170**
5.2.A.5	**Conclusions**		**171**
SECTION – B **Fabrication of Asymmetric Supercapacitor Devices**			
5.2.B.1	**Introduction**		**171**
5.2.B.2	**Experimental details**		**172**
	5.2.B.2.1	*Electrode preparation*	**172**
	5.2.B.2.2	*Preparation of PVA-KOH gel electrolyte*	**172**
	5.2.B.2.3	*Fabrication of asymmetric aqueous device*	**173**
	5.2.B.2.4	*Fabrication of asymmetric solid-state device*	**173**
5.2.B.3	**Conclusions**		**174**
SECTION – C **Electrochemical Performance Evaluation of Aqueous and Solid-State Devices (For S-CMP-4//rGO)**			
5.2.C.1	**Introduction**		**175**
5.2.C.2	**Results and Discussion**		**176**

	5.2.C.2.1	Electrochemical performance evaluation of S-CMP-4//KOH//rGO aqueous asymmetric device		**176**
		5.2.C.2.1.1	*CV study*	**176**
		5.2.C.2.1.2	*GCD study*	**178**
		5.2.C.2.1.3	*EIS study*	**179**
		5.2.C.2.1.4	*Ragone plot*	**180**
		5.2.C.2.1.5	*Stability study*	**181**
	5.2.C.2.2	Electrochemical performance evaluation of S-CMP-4//PVA-KOH//rGO asymmetric solid-state device		**182**
		5.2.C.2.2.1	*CV study*	**182**
		5.2.C.2.2.2	*GCD study*	**183**
		5.2.C.2.2.3	*EIS study*	**185**
		5.2.C.2.2.4	*Ragone plot*	**185**
		5.2.C.2.2.5	*Stability study*	**186**
		5.2.C.2.2.6	*Demonstration of S-CMP-4//PVA-KOH//rGO asymmetric solid-state device*	**187**
5.2.C.3	**Conclusions**			**188**
5.3	**References**			**190**

5.1 Introduction:

Advanced energy storage devices are an important part of electronics such as e-papers, mobile phones, hybrid vehicles, laptops, backup systems, etc. Accordingly, researchers are trying to develop energy storage devices having a long operation lifetime, high energy and power efficiency. At present, supercapacitors (SCs) are considered a promising energy storage device due to their superior capabilities such as excellent power density, fast charge-discharge capacity and long lifetime compared to battery technology **[1-4]**. In order to commercialize supercapacitors, it is important to raise the specific energy and potential window of supercapacitors without leaving out other features. The fabrication of solid-state supercapacitor becomes an attractive subject in the area of research for electrochemical energy storage systems **[5]**.

In this chapter, SILAR synthesized Co-Mn Phosphate and rGO are used as positive and negative electrodes, respectively to fabricate aqueous asymmetric (1 M KOH) and solid-state (PVA-KOH) devices. This chapter is distributed into three sections (A, B and C). Section 'A' describes the synthesis, structural and morphological characterization and electrochemical performance evaluation of rGO electrode. Further, Section 'B' deals with the fabrication of aqueous and solid-state asymmetric supercapacitor devices, whereas section 'C' is related to the electrochemical performance evaluation of S-CMP-4//rGO aqueous and solid-state asymmetric devices.

SECTION – A

Synthesis, Characterization and Supercapacitive Performance Evaluation of Reduced Graphene Oxide (rGO) Electrode (As an Anode)

5.2.A.1 Introduction:

Recently, various types of carbon materials have been employed as a negative (anode) electrode for asymmetric SCs **[6]** and which include reduced graphene oxide (rGO) **[7]**, carbon nanotubes (CNTs) **[8]** and activated carbon (AC) **[9]**. The carbon-based negative electrodes are used to make asymmetric supercapacitor devices because of their excellent electrical conductivity, higher power density, strong mechanical properties and better cycling stability **[10, 11]**. Among these materials, reduced graphene oxide (rGO) provides the ultrahigh specific surface area with strong mechanical strength, high electric conductivity and good chemical stability **[12, 13]**.

5.2.A.2 Experimental Details:

5.2.A.2.1 Chemicals:

Graphite flakes and sodium nitrate ($NaNO_3$) were purchased from Sigma-Aldrich. Sulfuric acid (H_2SO_4), potassium permanganate ($KMnO_4$), carbon black, N-Methyl-2-Pyrrolidone (NMP) and polyvinylidene fluoride (PVDF) were purchased from Sigma-Aldrich. Also, hydrogen peroxide (H_2O_2) and potassium hydroxide (KOH) were purchased from Alfa-Aesar. All the chemicals were AR grade and used without further purification.

5.2.A.2.2 Preparation of Reduced Graphene Oxide (rGO) Electrode:

Typically, graphene oxide (GO) was synthesized from graphite flakes using a modified Hummer's method **[14-16]**. In this process, graphite flakes (5 g) and sodium nitrate ($NaNO_3$) (2.5 g) were mixed with 120 mL of sulfuric acid (H_2SO_4) in

a 1000 mL flask and this mixture was stirred in an ice bath for 30 minutes. While continuing vigorous stirring, potassium permanganate ($KMnO_4$) (18 g) was mixed in the suspension gently and maintained the reaction temperature under 20°C. After $KMnO_4$ addition, the mixture was stirred continuously at ambient temperature overnight (12 h). As the reaction progresses the mixture gradually becomes paste-like and the colour changes from dark to a light brown. Then, 5 mL of hydrogen peroxide (30% H_2O_2) with 150 mL of DDW was dropped slowly into the mixture with continuous stirring and the light brown colour of the mixture turned yellow. For purification, the mixture was washed with double distilled water several times to eliminate an excess $KMnO_4$. After washing, the mixture was centrifuged using a centrifuge machine at 10000 rpm for 10 minutes. The washed and centrifuged graphene oxide (GO) is used for the preparation of rGO. The rGO was prepared by reducing the GO via a simple hydrothermal method. Briefly, the homogeneous suspension of GO in DDW (4 mg/mL of GO) was prepared by ultra-sonication and the prepared solution was heated at 150°C for 12 h in a hydrothermal autoclave. Once the reaction was over, it allowed to cool down at room temperature, and then the final product (rGO) was freeze-dried for 48 h to eliminate water content and avoid aggregation of rGO. Finally, the negative (rGO) electrode typically composed of 75 wt% of rGO, 20 wt% of carbon black as conducting agent and 5 wt% of polyvinylidene fluoride (PVDF) as a mechanical binder in a small amount of N-Methyl-2-Pyrrolidone solvent to make a slurry. Then, a formed slurry is coated on SS substrate (2 cm × 2 cm) and dried at 70°C for 2 h.

5.2.A.3 Results and Discussion:

5.2.A.3.1 XRD Study:

The XRD patterns of graphene oxide (GO) and reduced graphene oxide (rGO) electrodes are shown in **Figure 5.1 (a, b)**. The intense characteristic peak at 11.08 corresponding to the (001) plane in the XRD of GO confirms successful oxidation of graphite flakes. Also, the characteristic diffraction peaks observed at 24.55 and 42.98° correspond to the (002) and (100) planes **[17]**. Moreover, the scattered and altered peak position at about 24.55° is distinguishable which confirms a reduction of GO material and formation of multi-layered rGO nanostructure **[18]**.

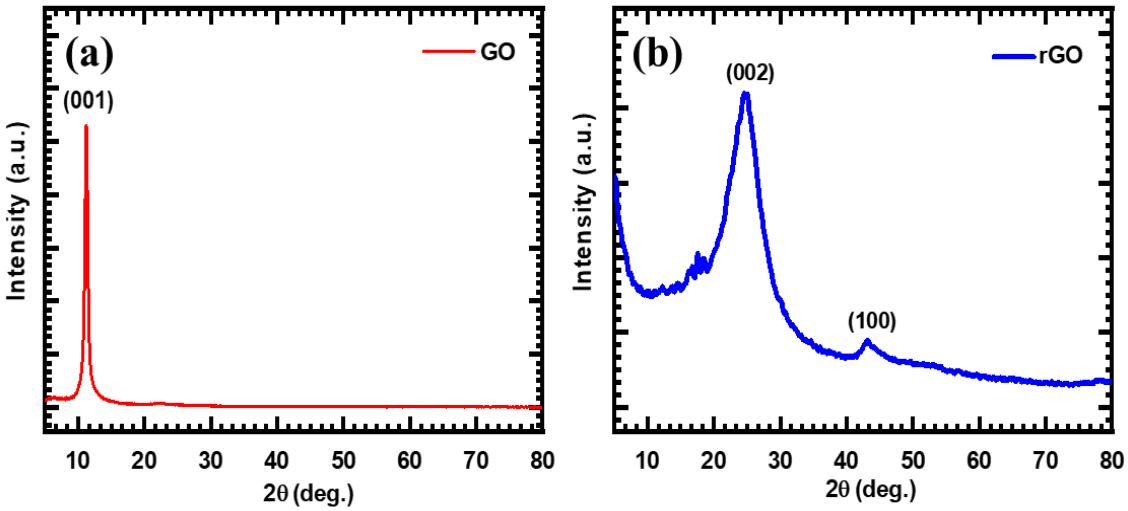

Figure 5.1: XRD patterns of (a) GO and (b) rGO electrodes.

5.2.A.3.2 Raman Study:

The Raman spectrum of GO and rGO is measured using the Raman spectroscopy in a range of 500-3200 cm^{-1}. Raman study is beneficial for understanding and measuring defects, identifying the number of graphene layers and orientation. The spectrum consists of three major peaks, D, G and 2D bands. The D band at 1350 cm^{-1} is assigned to the vibrations of the sp^3 disordered carbon atom and the G band at 1595 cm^{-1} corresponds to the sp^2 (C=C) hybridized

graphitic carbon atoms as shown in **Figure 5.2 (a, b) [19]**. Further, the 2D band at 2694 cm^{-1} is found to be a weak peak, which is another indication of the existence of disorder. Also, a peak at 2933 cm^{-1} (D+G) describes a disorder due to scattering of the combination **[20]**. The presence of a 2D band confirms the multilayer structure of GO and rGO material **[21]**. The D/G intensity ratio (I_D/I_G) of GO and rGO are 0.99 and 1.01, respectively. Interestingly, the I_D/I_G ratio is increased after reduction of GO that indicates some defects are introduced in the structure. Finally, this result confirms that GO is reduced successfully by hydrothermal method.

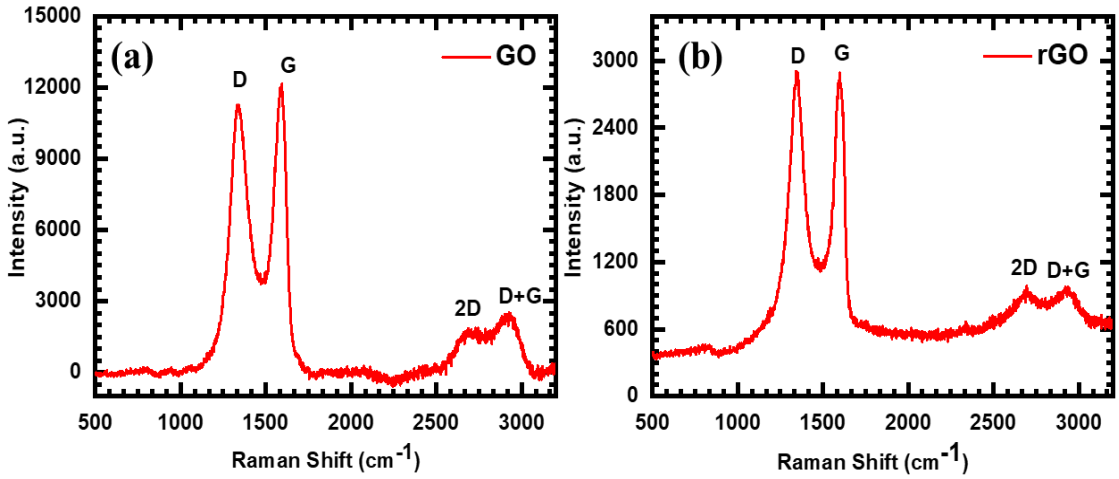

Figure 5.2: Raman spectra of (a) GO and (b) rGO electrodes.

5.2.A.3.3 BET study:

The N_2 adsorption-desorption isotherm of rGO is shown in **Figure 5.3 (a)**. Also, the corresponding BJH (Barrett-Joyner-Halenda) pore-size distribution plot is displayed in **Figure 5.3 (b)**. The occurrence of a hysteresis loop **(Figure 5.3 (a))** reveals the rGO has a porous structure, which is an absorption-desorption feature of the porous material. The rGO displays a high specific surface area of 237 $m^2\ g^{-1}$. Furthermore, the rGO material demonstrates a mesoporous distribution (average pore size) of 10.62 nm. The mesoporous structure of rGO can contribute in

reducing diffusion paths and low resistance pathways for ions, which can satisfy the demands of high value supercapacitor applications **[22, 23]**.

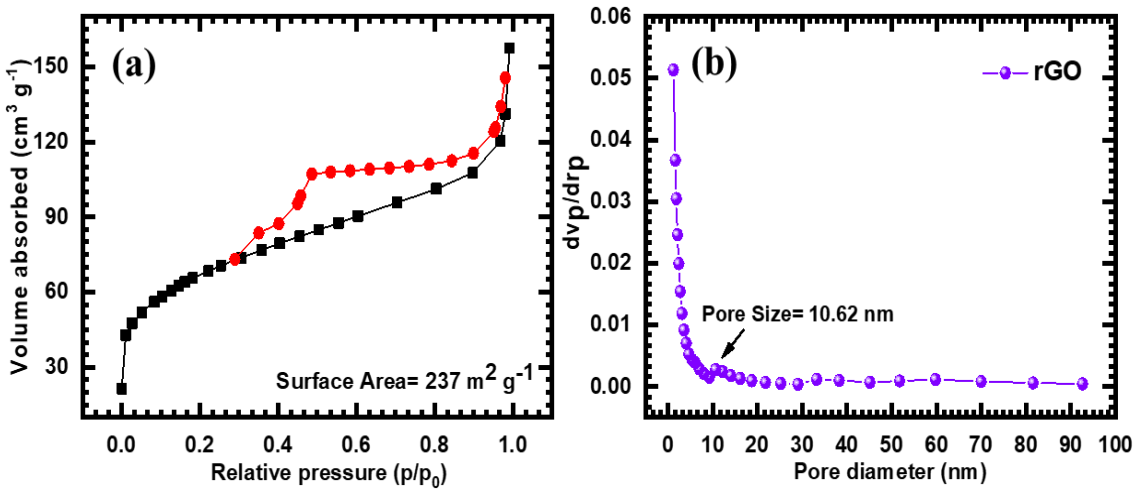

Figure 5.3: (a) N_2 adsorption-desorption isotherm and (b) BJH pore size distribution plot of rGO electrode.

5.2.A.3.4 FE-SEM Study:

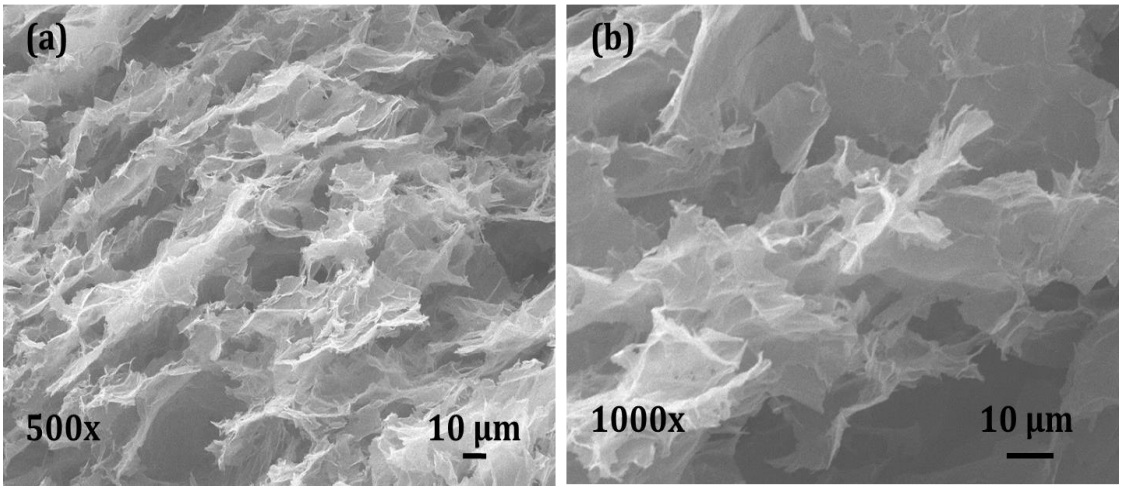

Figure 5.4: (a, b) FE-SEM micrographs of rGO electrode at different magnifications (500x and 1000x).

The morphology of rGO electrode at low (500x) and high (1000x) magnifications by field emission scanning electron microscopy (FE-SEM) is shown in **Figure 5.4 (a-b)**. A well-defined 3D porous structure and interconnected nanosheets are observed in **Figure 5.4 (a, b)**. The pore sizes of the network range

from several micrometers to sub-micrometers and the pore walls consist of thin layers of stacked graphene sheets can be seen from **Figure 5.4 (b)**. Partial overlapping or collapse of flexible graphene sheets is created by physical cross-linking sites in the rGO framework **[24]**.

5.2.A.4 Supercapacitive Performance Evaluation:

The electrochemical capacitive properties of rGO electrode tested by CV, GCD, stability and EIS techniques in 1 M KOH electrolyte using three-electrode cell configuration.

5.2.A.4.1 CV Study:

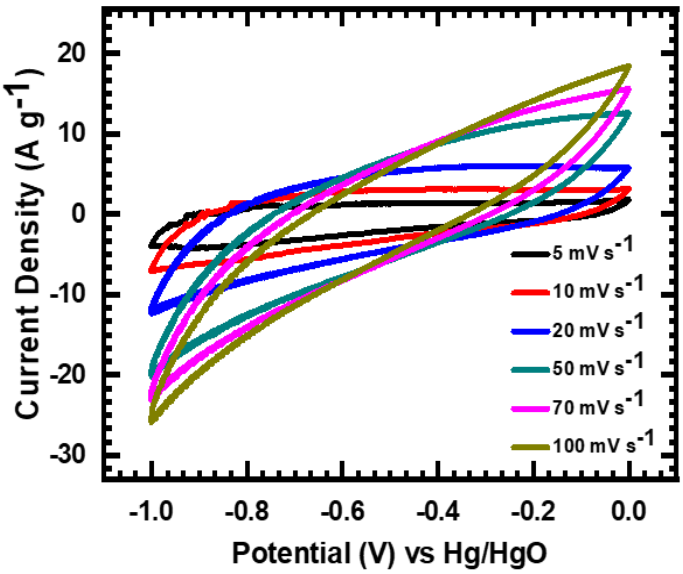

Figure 5.5: CV plots of rGO electrode at scan rates from 5-100 mV s^{-1}.

The CV plots of rGO (negative) electrode were studied within the potential range of 0.0 to -1.0 V vs Hg/HgO at various scan rates (5-100 mV s^{-1}) in 1 M KOH electrolyte **[Figure 5.5]**. The CV plots of rGO electrode display quasi-rectangular shape in KOH electrolyte. The current area under CV curve increases with increasing scan rate. In addition to verify performance, specific capacitance is determined using **Eqⁿ. (2.5)**. At 5 mV s^{-1} scan rate, the rGO electrode exhibits highest specific capacitance of 343 F g^{-1} as displayed in **Figure 5.6**. At a slow scan

rate, the specific capacitance value is higher because extra time is available for the electrochemical reaction at the interface of the electrode and electrolyte.

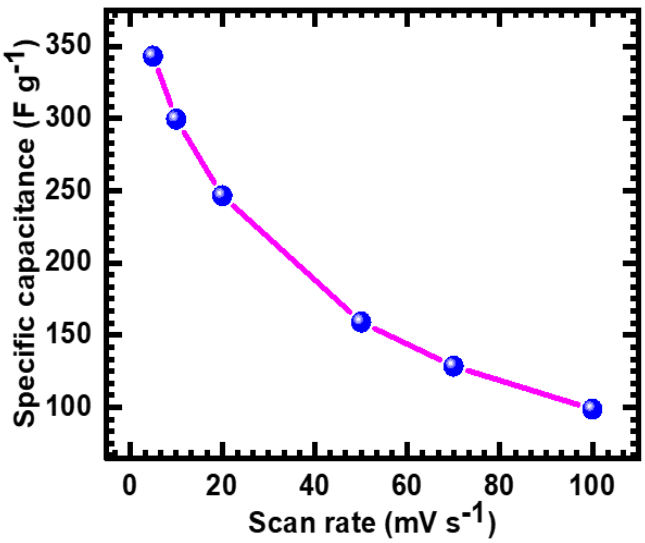

Figure 5.6: Specific capacitance of rGO electrode at scan rates from 5-100 mV s^{-1}.

5.2.A.4.2 GCD Study:

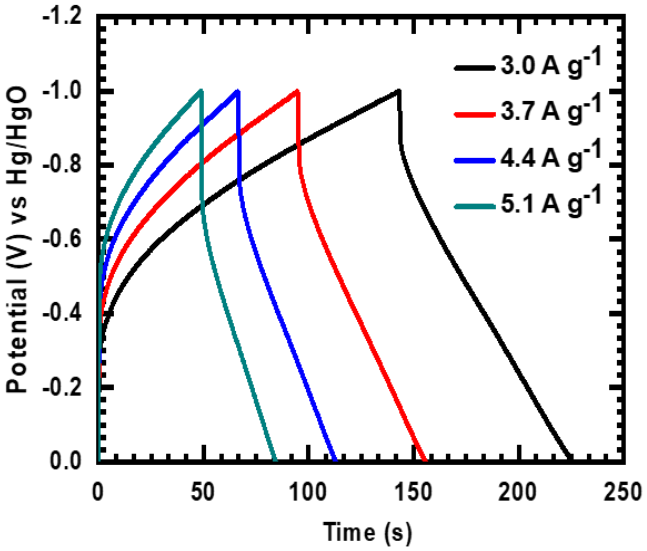

Figure 5.7: The GCD plots of rGO electrode at a different current densities (3.0 to 5.1 A g^{-1}).

The GCD curves of rGO thin film electrode measured at different current densities from 3.0 to 5.1 A g^{-1} in a potential window of 0.0 to -1.0 V/Hg/HgO are displayed in **Figure 5.7**. The little initial voltage drop at discharge of the electrode

indicates a lower intrinsic resistance (iR), superior conductivity and the ability for a fast charging-discharging **[25]**. The higher specific capacitance of rGO electrode is found to be 243 F g^{-1} at a current density of 3.0 A g^{-1} **[Figure 5.8]**. At a low charging current density, the charge-discharge process is slower. So, it provides more time for the electrochemical process (non-faradaic) between electrode-electrolyte. Therefore, the specific capacitance is higher at a lower current density (3.0 A g^{-1}).

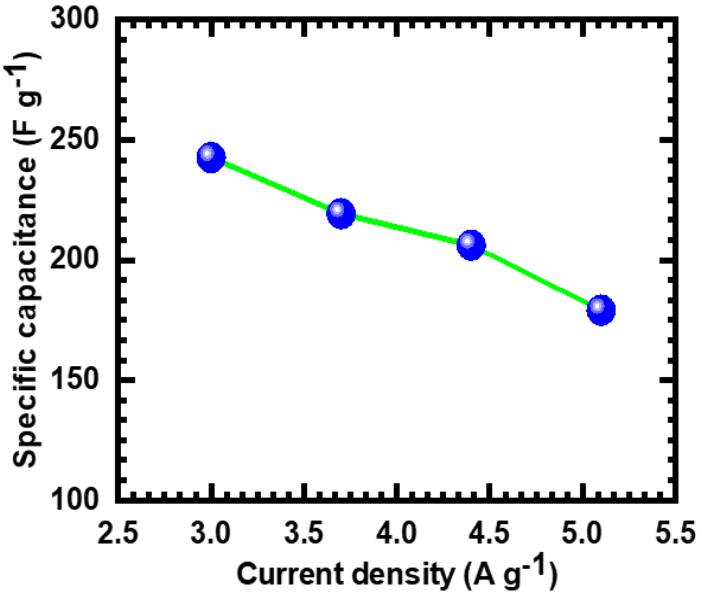

Figure 5.8: Specific capacitance of rGO electrode at 3.0-5.1 A g^{-1} current densities.

5.2.A.4.3 EIS Study:

The EIS study of rGO electrode was performed to monitor its electrochemical activity and conductivity **[Figure 5.9]**. Also, the fitted equivalent circuit is shown in an inset of **Figure 5.9**. This circuit displays solution resistance (R_s), charge transfer resistance (R_{ct}), constant phase element (CPE) and Warburg resistance (W). The EIS results show low R_s of 1.10 Ω and R_{ct} of 37.66 Ω for rGO electrode and a small value of total impedance indicates excellent electrical conductivity of electrode.

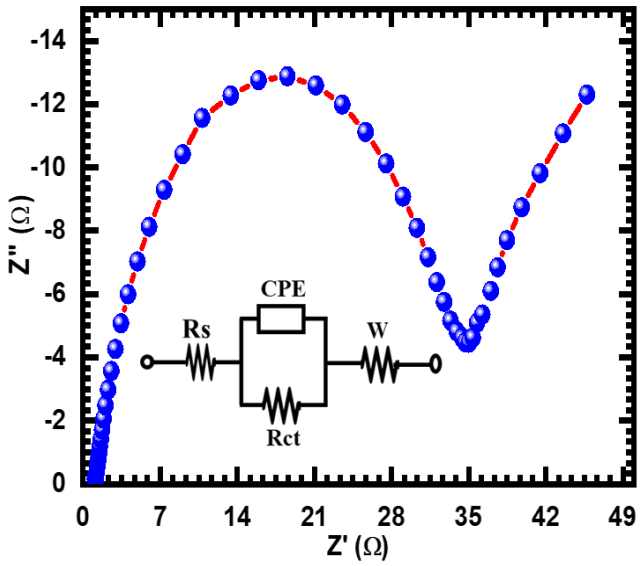

Figure 5.9: Nyquist plot of rGO electrode [Inset: equivalent circuit fitted with Nyquist plot].

5.2.A.4.4 Stability Study:

The cycling stability of rGO electrode investigated for 3000 cycles at a current density of 5.5 A g^{-1}. The rGO electrode exhibits superior capacitance retention of 82 % after 3000 cycles as shown in **Figure 5.10 (a)**. Also, **Figure 5.10 (b)** displays a little reduction in storing capacity of GCD after 1st, 1500th and 3000th cycle, which confirms the long-term stability of rGO electrode.

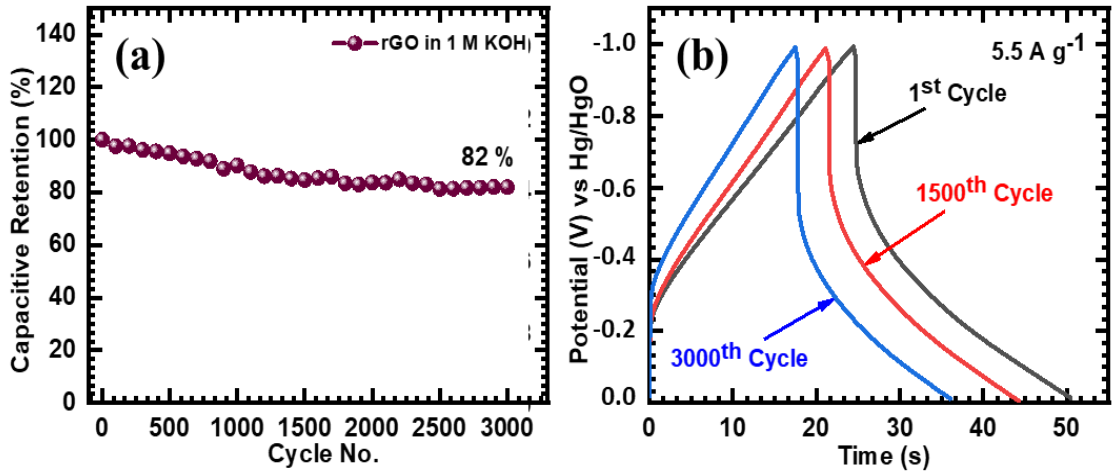

Figure 5.10: (a) GCD stability graph of rGO electrode for 3000 cycles and (b) 1st, 1500th and 3000th GCD cycle of rGO electrode.

5.2.A.5 Conclusions:

In summary, graphene oxide (GO) is successfully synthesized by the modified Hummer's method and further reduced (rGO) by hydrothermal method. The structural and morphological study of rGO was examined by different characterization techniques. The XRD study of GO confirms successful oxidation of graphite flakes and the reduction of graphene oxide into rGO. Nanosheets with a wrinkle structured morphology are obtained for rGO. The Raman study reveals an increase in defects at rGO material and confirms the production of qualitative rGO material. Also, the BET result reveals a high effective surface area (237 $m^2\ g^{-1}$) of rGO coming from the mesoporous three-dimensional structure of interconnected nanosheets. The rGO electrode shows excellent electrochemical performance in 1 M KOH electrolyte and exhibited maximum specific capacitance of 243 F g^{-1} at a current density of 3.0 A g^{-1}. The EIS results show low solution resistance (R_s- 1.10 Ω) and charge transfer resistance (R_{ct}- 37.66 Ω) of rGO electrode indicates excellent electrical conductivity. After 3000 cycles, 82 % of the capacitance is maintained which exhibits excellent cyclic stability. Attractive performance of rGO material makes it a promising candidate as a negative electrode (as an anode) for supercapacitors.

SECTION – B

Fabrication of Asymmetric Supercapacitor Devices

5.2.B.1 Introduction:

The selection of electrode material plays a significant role that can efficiently increase the potential window of device. Aqueous or solid-state gel electrolyte is sandwiched between two different charge storage materials in an asymmetric

configuration to achieve high energy densities while sustaining power density **[26-28]**. Typically, the working potential window of an asymmetric SCs device is defined by the electrolyte overpotential and the work function difference of the negative and positive electrodes **[29, 30]**. Further, a wider potential window increases the energy density of asymmetric devices and can be achieved by using different electrolytes (aqueous and solid-state). Nevertheless, the benefits of polymer gel electrolyte over liquid electrolyte are no internal shortening and electrolyte leakage **[31, 32]**.

5.2.B.2 Experimental details:

5.2.B.2.1 Electrode preparation:

Chapters 3 and **4** concluded that, the SILAR deposited Co-Mn Phosphate material exhibits high performance as compare to hydrothermally synthesized Co-Mn Phosphate electrode. Therefore, SILAR deposited Co-Mn Phosphate on the stainless steel substrate as a cathode (positive) electrode is used for asymmetric device fabrication. The preparative parameters given in **Chapter 4** are used for the preparation of large area (5 cm × 5 cm) Co-Mn Phosphate thin film (cathode electrode).

The anode (rGO) electrode was typically composed as discussed in **Section 5.2.A.2.2**. These cathode and anode electrodes are used for aqueous and solid-state device fabrication.

5.2.B.2.2 Preparation of PVA-KOH gel electrolyte:

Much effort has been made to improve the capacitance of asymmetric devices using PVA-KOH solid-state gel electrolyte and can be operated at high potential windows. Polymer gel electrolytes are neither liquid nor solid; they have both cohesive and diffusive properties **[33]**. The method for manufacturing PVA-based

gel electrolytes are addressed in earlier reported articles to build an all-solid-state asymmetric device **[34, 35]**. Furthermore, the choice of appropriate gel electrolyte is the most required criterion for the formation of asymmetric solid-state devices, as it offers low leakage due to less water content. The PVA-KOH gel has benefits like good flexibility, higher ionic conductivity which creates excellent contact with electrodes **[36, 37]**. The preparation of PVA-KOH gel was carried out in the following manner: firstly, 3 g of polyvinyl alcohol (PVA) was dissolved in 30 mL of water with heating (at 90°C) and continuous stirring up to a solution to become clear and transparent. Later, 1 M KOH solution (in 20 mL of DDW) was separately prepared and mixed in the above-mentioned transparent solution and continually stirred up to get a viscous appearance at ambient conditions. The transparent and viscous gel (PVA-KOH) is utilized as a separator and an electrolyte in solid-state device fabrication.

5.2.B.2.3 Fabrication of asymmetric aqueous device:

The important requirement in asymmetric aqueous device fabrication is that, both electrodes (cathode and anode) should have different potential windows. An asymmetric aqueous device fabricated using SILAR deposited Co-Mn Phosphate (S-CMP-4) and rGO as positive and negative electrodes, respectively in 1 M KOH electrolyte and tested with different electrochemical parameters.

5.2.B.2.4 Fabrication of asymmetric solid-state device:

To fabricate the asymmetric device, SILAR prepared Co-Mn Phosphate (S-CMP-4) and reduced graphene oxide (rGO) were used as positive and negative electrodes, respectively with PVA-KOH gel electrolyte as shown in **Scheme 5.1**. An asymmetric solid-state device was fabricated using a large area (5 × 5 cm^2) Co-Mn Phosphate and rGO electrodes. Moreover, those two electrodes were covered with

gel electrolyte to form a thin layer of electrolyte and then air-dried at ambient temperature to eliminate water content from the gel electrolyte. Next, the edges of the electrodes were sealed with insulating tape to prevent any shortening on the sides of electrodes. Then, both electrodes were combined together to form a solid-state device with gel electrolyte. The assembled solid-state asymmetric device is further packed with plastic tape. Finally, the fabricated device was pressed under 0.5 ton pressure for 5 h to increase the interfacial contact of gel electrolyte with active electrode materials and then the solid-state device was successfully obtained.

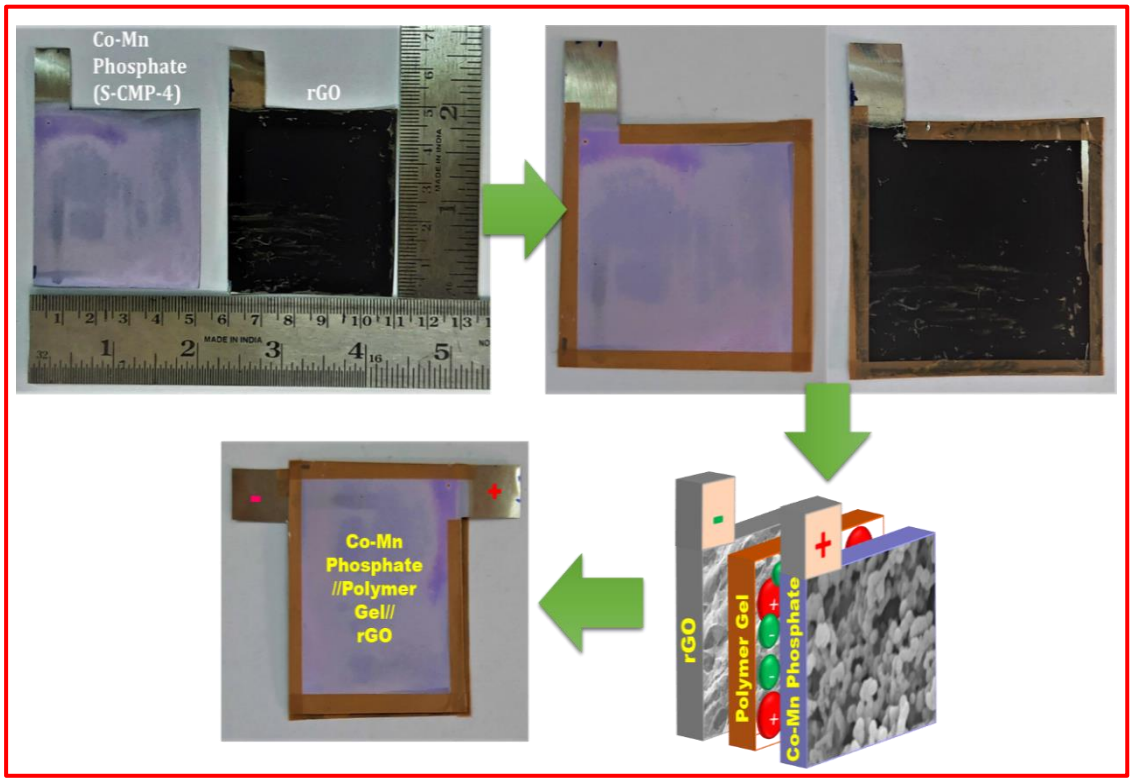

Scheme 5.1: Schematic diagram of solid-state device fabrication.

5.2.B.3 Conclusions:

In summary, a large area Co-Mn Phosphate thin film by SILAR method and rGO electrode by drop-casting method are prepared on SS substrate. Then, the asymmetric aqueous and solid-state supercapacitor devices are successfully

fabricated using Co-Mn Phosphate (S-CMP-4) as a positive electrode and rGO as a negative electrode. The 1 M KOH and PVA-KOH as aqueous and gel electrolyte, respectively are used to fabricate supercapacitor aqueous and solid-state devices.

SECTION – C

Electrochemical Performance Evaluation of Aqueous and Solid-State Devices (For S-CMP-4//rGO)

5.2.C.1 Introduction:

The electrochemical performance of an asymmetric aqueous device is measured by the two-electrode system using Co-Mn Phosphate (S-CMP-4) thin film as a cathode and rGO as an anode electrode. Also, to develop an asymmetric device, the primary requirement is that the electrode material must have different operating potential windows (positive and negative). Moreover, the initial significant task before constructing the asymmetric device is balancing the charges of both electrodes ($q^+ = q^-$) for receiving the highest electrochemical performance. Then, the mass loading of both electrodes was calculated according to the following formula: **[34]**

$$\frac{m_+}{m_-} = \frac{C_- \times \Delta V_-}{C_+ \times \Delta V_+} \quad (5.1)$$

where, m (+ or -), ΔV (+ or -), and C (+ or -) is the mass (mg), voltage window (V), and specific capacitance (F g^{-1}) of cathode and anode electrodes, respectively. The specific capacitance and operating potential windows for both electrodes (Co-Mn Phosphate and rGO electrodes) are different, so the charges were balanced by adjusting the mass loading of the electrode material. The optimal mass ratio between positive (0.684 mg cm^{-2}) and negative (1.168 mg cm^{-2}) electrode is found to be 0.58:1, in the present work.

5.2.C.2 Results and Discussion:

5.2.C.2.1 Electrochemical performance evaluation of S-CMP-4//KOH//rGO aqueous asymmetric device:

5.2.C.2.1.1 CV study:

To investigate the supercapacitor application of an aqueous device (S-CMP-4//KOH//rGO), the device is fabricated using the 1 M KOH electrolyte. The working potential window of S-CMP-4 (Co-Mn Phosphate) electrode from 0.0 to +0.65 V/Hg/HgO and the rGO electrode from 0.0 to -1.0 V/Hg/HgO. **Figure 5.11** shows the CV curves of S-CMP-4 and rGO electrodes operating at different potential windows in 1 M KOH electrolyte at a fixed 50 mV s^{-1} scan rate. The CV plots were recorded for S-CMP-4//KOH//rGO device in different potential windows (0.0-1.2 to 0.0-1.6 V) **(Figure 5.12 (a))**. Increase in the working potential window from 1.2 to 1.6 V, current response of the CV curve increases.

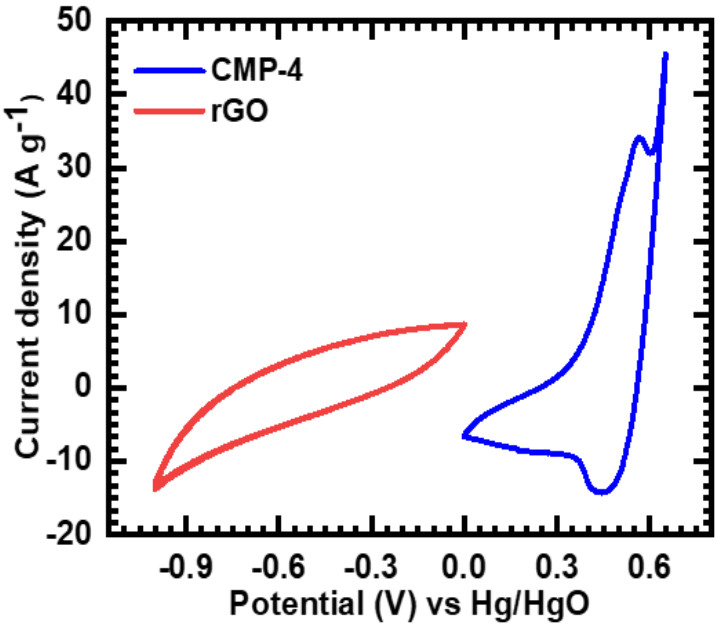

Figure 5.11: The CV plots of S-CMP-4 and rGO electrodes in 1 M KOH electrolyte.

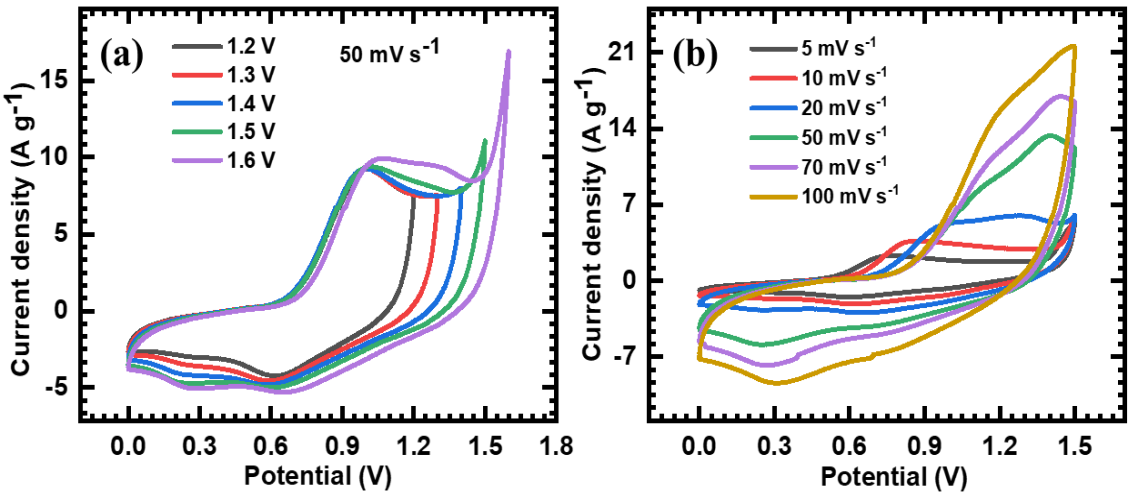

Figure 5.12: The CV plots of S-CMP-4//KOH//rGO asymmetric aqueous device (a) at different potential windows from +1.2 to +1.6 V and, (b) at different scan rates (5 to 100 mV s^{-1}).

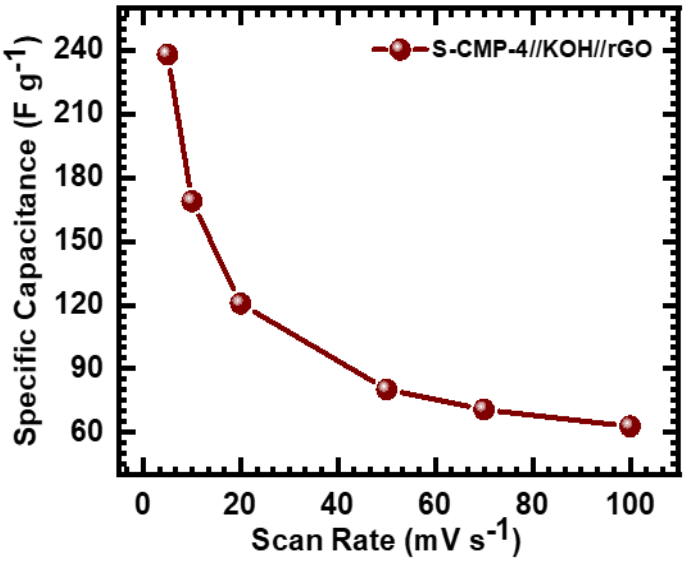

Figure 5.13: Specific capacitance of S-CMP-4//KOH//rGO device at different scan rates (5 to 100 mV s^{-1}).

Accordingly, the potential window of 0.0 to +1.5 V was selected for the S-CMP-4//KOH//rGO device. The assembled S-CMP-4//KOH//rGO asymmetric device exhibits quasi-rectangular CV curves at the potential window up to +1.5 V. **Figure 5.12 (b)** shows that the CV curves of the device were conducted at different scan rates of 5–100 mV s^{-1} within 0.0 to +1.5 V potential window. The device displays

CV curves with good rate capability at different scan rates **[38]**. Further, **Figure 5.13** shows a plot of specific capacitance vs different scan rates. It shows the highest specific capacitance achieved by S-CMP-4//KOH//rGO asymmetric aqueous device is 238 F g^{-1} at a 5 mV s^{-1} scan rate.

5.2.C.2.1.2 GCD study:

In this study, GCD graphs were recorded for S-CMP-4//KOH//rGO device in different potential windows (0.0-1.2 to 0.0-1.6 V) **(Figure 5.14 (a))**. An increase in working potential up to +1.6 V with an increased discharge time of the GCD curve was observed at a constant current density of 1.4 A g^{-1}. However, the GCD curve shows good performance (symmetric charge-discharge) within the potential window of 0.0 to +1.5 V, so it was selected for the S-CMP-4//KOH//rGO device.

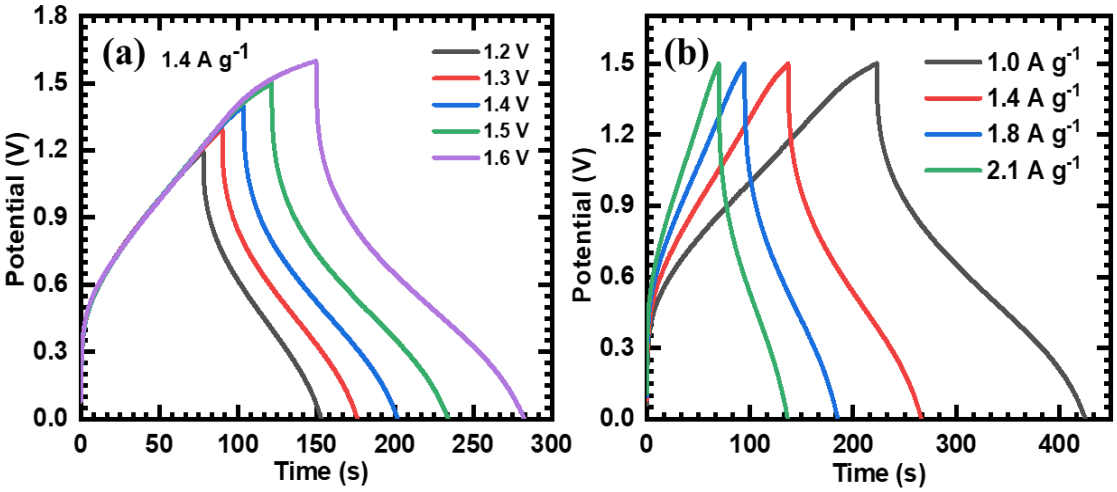

Figure 5.14: The GCD plots of S-CMP-4//KOH//rGO asymmetric aqueous device (a) at different operating potential windows from +1.2 to +1.6 V and, (b) at 1.0-2.1 A g^{-1} current densities.

Figure 5.14 (b) shows that, the GCD curve of the device at different current densities from 1.0-2.1 A g^{-1}. The discharge curve consists of two sections as a sudden potential drop and then a gradual potential decay. The first potential drop effect defining the internal resistance (iR) and after gradual potential decay

describes the capacitive properties of the electrodes. The values of specific capacitance with respect to current density are illustrated in **Figure 5.15**. The S-CMP-4//KOH//rGO asymmetric device exhibits excellent supercapacitive performance with values of 145 F g^{-1} at a current density of 1.0 A g^{-1}.

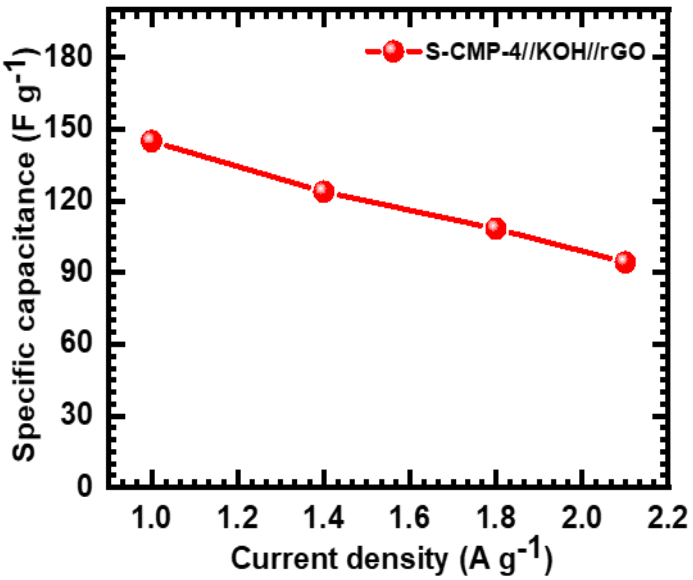

Figure 5.15: Specific capacitance of S-CMP-4//KOH//rGO device at different current densities.

5.2.C.2.1.3 EIS study:

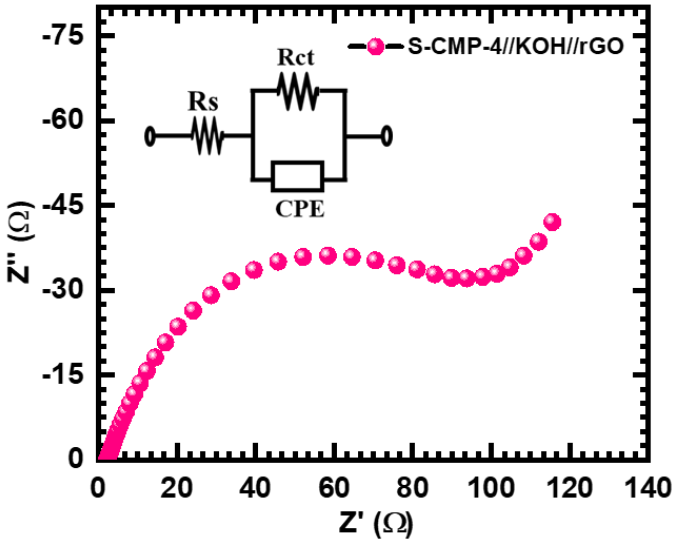

Figure 5.16: The Nyquist plot of S-CMP-4//KOH//rGO asymmetric aqueous device [Inset: fitted equivalent circuit].

Electrochemical impedance spectroscopy measurement of the aqueous asymmetric device was performed in order to understand the capacitive, electronic, and ionic resistive properties of the device. **Figure 5.16** shows a Nyquist plot of the S-CMP-4//KOH//rGO device with a fitted circuit. As depicted in figure 5.16, the intercept at real Z-axis is related to the solution resistance (R_s), and it is observed to be 2.1 Ω. Also, the charge transfer resistance (R_{ct}) is 119 Ω. The low R_s and R_{ct} values manifesting the good conductivity of the electrolyte and very low internal resistance of the electrode.

5.2.C.2.1.4 Ragone plot:

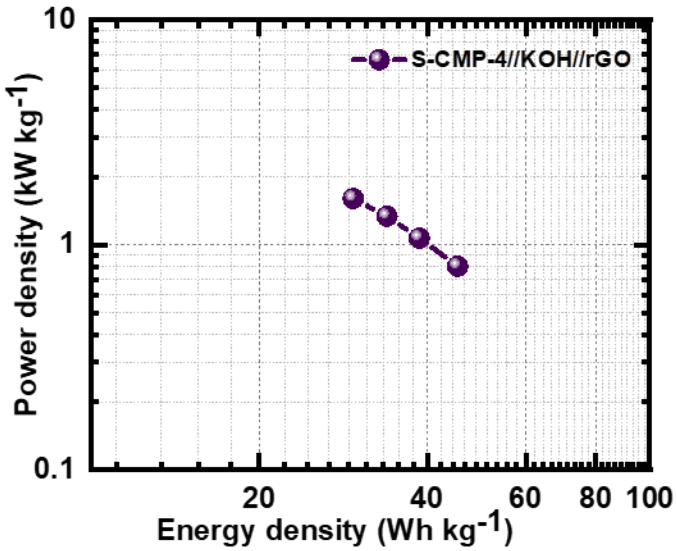

Figure 5.17: Ragone plot of S-CMP-4//KOH//rGO asymmetric aqueous device.

The power and energy density of the asymmetric device is shown in the Ragone plot **(Figure 5.17)**. The energy density of S-CMP-4//KOH//rGO asymmetric device reached 45.31 Wh kg^{-1} with a power density of 0.79 kW kg^{-1}. Moreover, the energy density remained 29.46 Wh kg^{-1} at a high power density of 1.60 kW kg^{-1}. The calculated power density depends on the current density and the low power density of the device with high energy density can be obtained with decreasing current density. In addition, the asymmetric device with two different

EDLC and pseudocapacitive material has improved the working potential window and the resulting energy as well as power density **[39]**.

5.2.C.2.1.5 Stability study:

The cyclic stability of the S-CMP-4//KOH//rGO asymmetric cell was studied by continuous 6000 GCD cycles at a current density of 3.0 A g^{-1} **(Figure 5.18)**. The excellent cyclic stability with a number of repeated cycles for an asymmetric cell was observed. After 6000 GCD cycles, about 91 % capacitance was retained. Moreover, the 1st, 3000th and 6000th GCD cycle displays a slight decrease in storing capacitance as shown in the inset of **Figure 5.18**. Superior cyclic stability confirms that, the excellent charge storage reaction of the supercapacitor device with a stable structure of electroactive materials on the substrate.

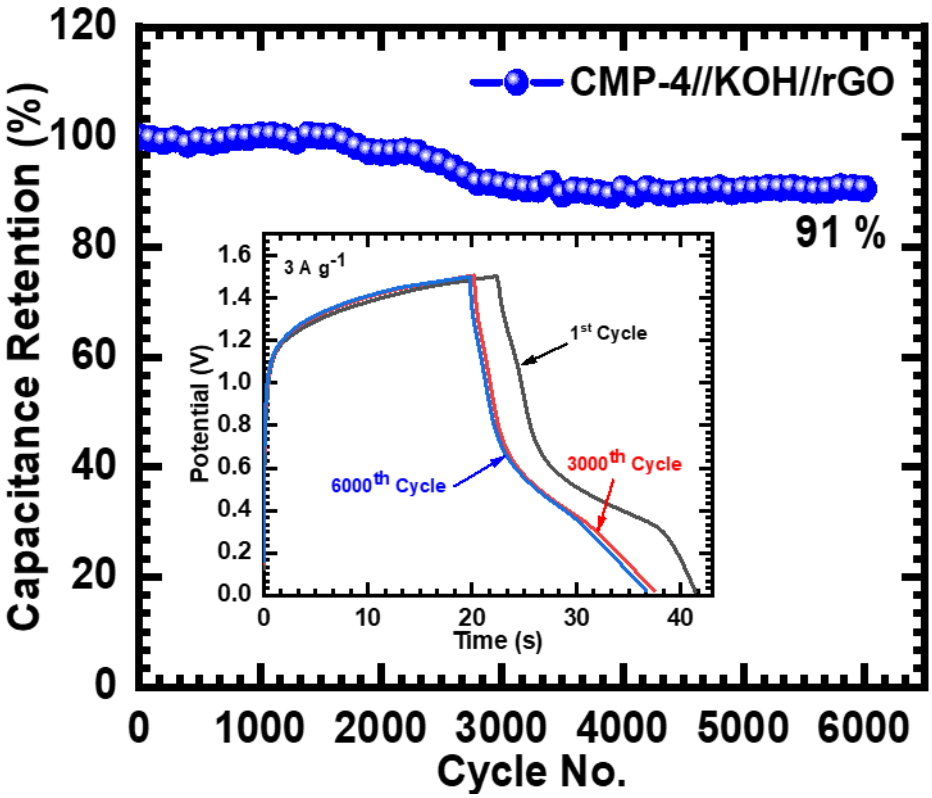

Figure 5.18: The plot of capacitance retention with cycle number for S-CMP-4//KOH//rGO asymmetric aqueous device (Inset: GCD cycles at 1st, 3000th, and 6000th cycle).

5.2.C.2.2 Electrochemical performance evaluation of S-CMP-4//PVA-KOH//rGO asymmetric solid-state device:

An all-solid-state asymmetric supercapacitor device is assembled as described in sub-section **5.2.B.2.4** of **Section B**. The electrochemical performance of an asymmetric solid-state device is measured (CV, GCD and EIS) by a two-electrode system. Also, PVA-KOH gel is used as an electrolyte as well as a separator.

5.2.C.2.2.1 CV study:

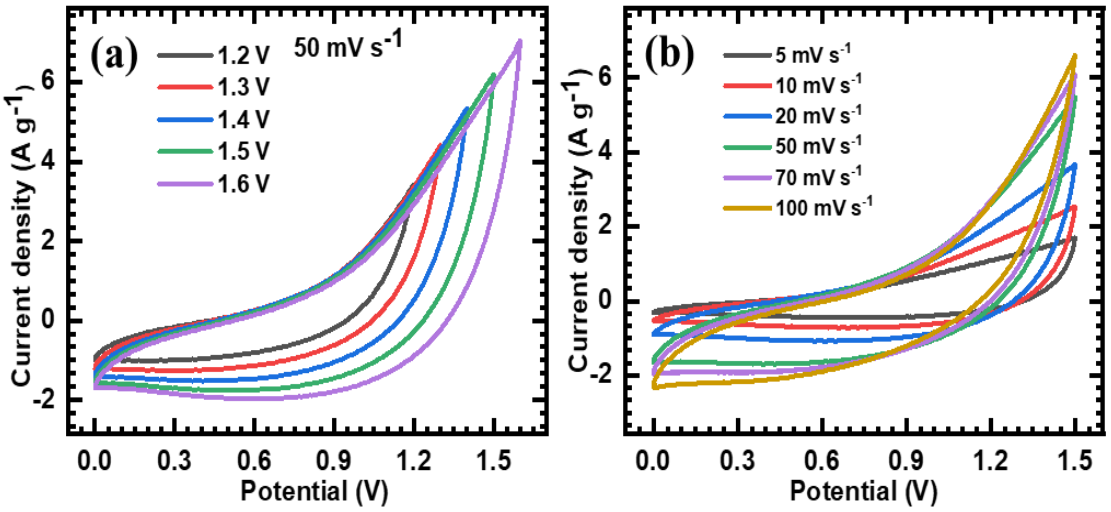

Figure 5.19: The CV plots of S-CMP-4//PVA-KOH//rGO asymmetric solid-state device (a) at different potential windows from +1.2 to +1.6 V and, (b) at different scan rates (5 to 100 mV s^{-1}).

Figure 5.19 (a) shows the CV curves of S-CMP-4//PVA-KOH//rGO asymmetric solid-state device at 50 mV s^{-1} fixed scan rate for different voltage varied from +1.2 to +1.6 V. The S-CMP-4//PVA-KOH//rGO asymmetric solid-state device can achieve the highest working potential window up to +1.5 V. Accordingly, the potential window of 0.0 to +1.5 V was chosen for S-CMP-4//PVA-KOH//rGO solid-state device and used for further electrochemical investigations. Then, **Figure 5.19 (b)** illustrates the CV curves of S-CMP-4//PVA-KOH//rGO asymmetric solid-state device at different scan rates (5 to 100 mV s^{-1}). The shapes of CV curves

are almost rectangular which indicates pseudocapacitive as well as EDLCs behavior of Co-Mn Phosphate and rGO electrode materials. All the CV curves maintain their shape irrespective of scan rate, indicating that the S-CMP-4//PVA-KOH//rGO asymmetric solid-state device exhibits excellent capacitive behaviour. Further, **Figure 5.20** shows the plot of specific capacitance with respect to the scan rate. The highest specific capacitance of 92 F g^{-1} is obtained for S-CMP-4//PVA-KOH//rGO asymmetric solid-state device at 5 mV s^{-1} scan rate.

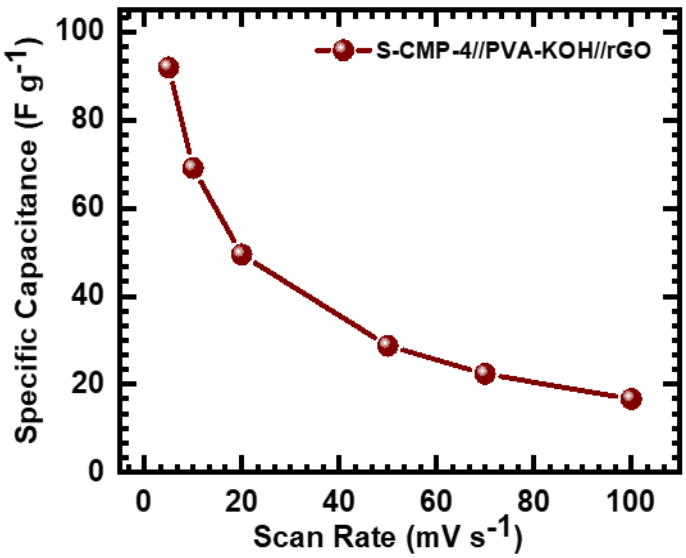

Figure 5.20: Specific capacitance of S-CMP-4//PVA-KOH//rGO device at different scan rates (5 to 100 mV s^{-1}).

5.2.C.2.2.2 GCD study:

The electrochemical performance of the asymmetric solid-state device is further investigated by the charge-discharge study. The GCD curves of S-CMP-4//PVA-KOH//rGO asymmetric solid-state device at different voltages (+1.2 to +1.6 V) are plotted in **Figure 5.21 (a)**. Up to potential of +1.5 V, the GCD curve shows better performance for S-CMP-4//PVA-KOH//rGO asymmetric solid-state device. The GCD curves of S-CMP-4//PVA-KOH//rGO asymmetric solid-state

device at different current densities from 1.0 to 2.1 A g^{-1} are shown in **Figure 5.21 (b)**.

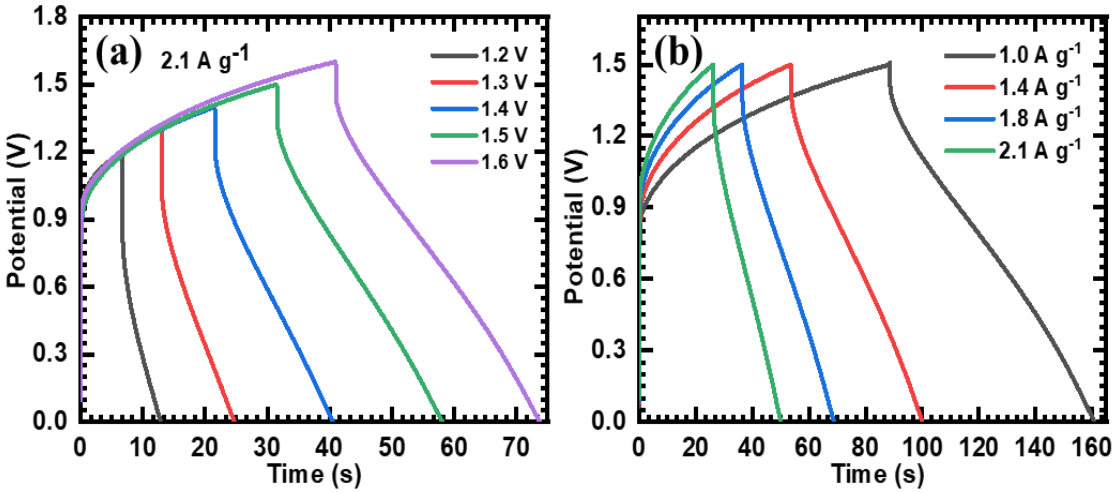

Figure 5.21: The GCD plots of S-CMP-4//PVA-KOH//rGO asymmetric solid-state device (a) at different operating potential windows up to +1.2 to +1.6 V and, (b) at different current densities from 1.0 to 2.1 A g^{-1}.

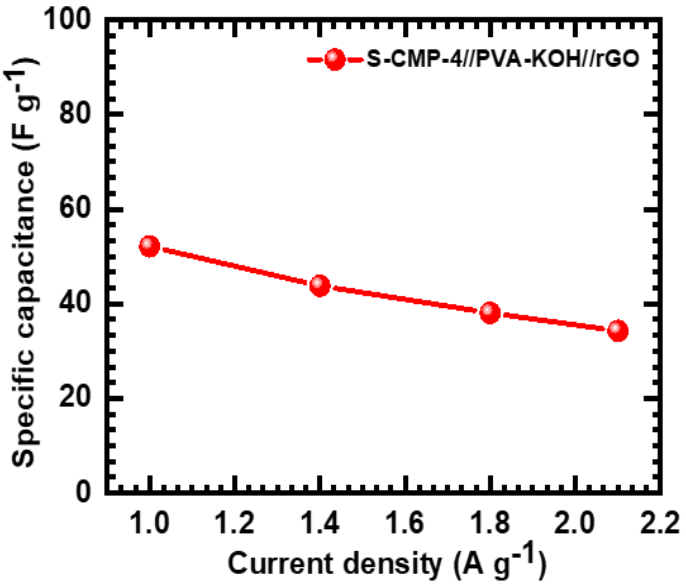

Figure 5.22: Specific capacitance of S-CMP-4//PVA-KOH//rGO device at different current densities (1.0 to 2.1 A g^{-1}).

Meanwhile, the non-linear GCD curves describe a good electrochemical capacitive behavior based on better reversible redox reactions. Further, the

specific capacitance is calculated from the charge-discharge study. The maximum specific capacitance of S-CMP-4//PVA-KOH//rGO asymmetric solid-state device is found to be 52 F g^{-1} at 1.0 A g^{-1} current density **(Figure 5.22)**.

5.2.C.2.2.3 EIS study:

The Nyquist plot for S-CMP-4//PVA-KOH//rGO asymmetric solid-state device was obtained using EIS analysis and shown in **Figure 5.23**. Inset of **Figure 5.23** shows the equivalent circuit diagram for the plotted Nyquist graph. The equivalent fitted circuit shows R_s, R_{ct}, CPE and W elements. The values of R_s observed to be 6.2 Ω and R_{ct} is 157 Ω for S-CMP-4//PVA-KOH//rGO asymmetric solid-state device. This result confirms that, the redox additive gel electrolyte provides low internal resistance.

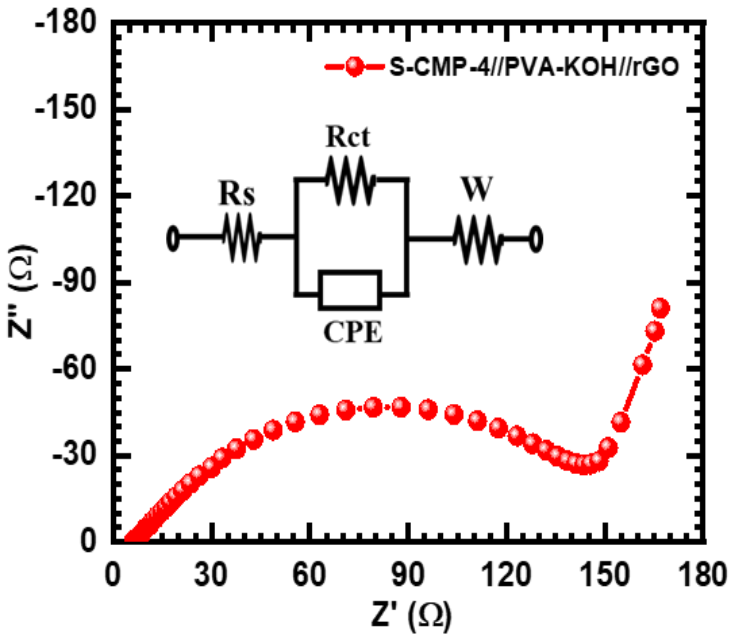

Figure 5.23: The Nyquist plot of S-CMP-4//PVA-KOH//rGO asymmetric solid-state device [Inset: fitted equivalent circuit].

5.2.C.2.2.4 Ragone plot:

The Ragone plot of S-CMP-4//PVA-KOH//rGO asymmetric solid-state device is shown in **Figure 5.24**. The highest energy density delivered by fabricated device

is 16.29 Wh kg^{-1} with a power density of 0.82 kW kg^{-1} and maintained 10.71 Wh kg^{-1} energy density at a maximum power density of 1.61 kW kg^{-1}. This result shows good rate capability and enhanced energy density for the solid-state device that can be understood from a broad working potential window and good specific capacitance.

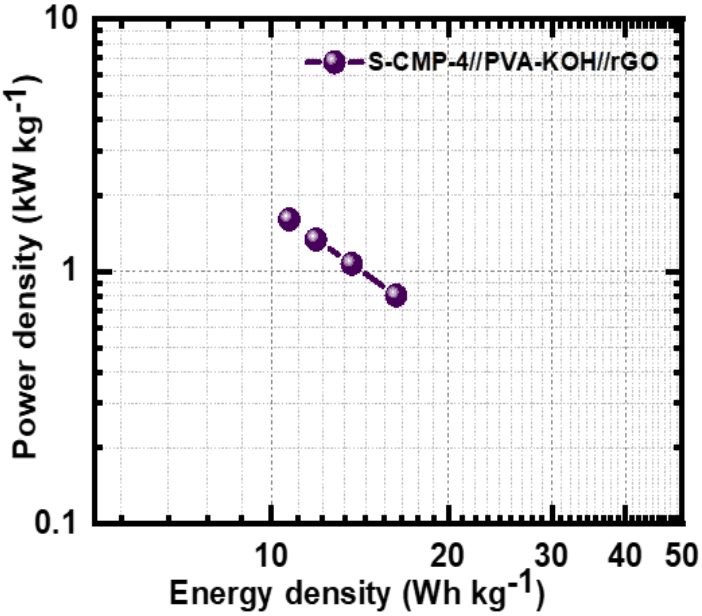

Figure 5.24: Ragone plot of S-CMP-4//PVA-KOH//rGO asymmetric solid-state device.

5.2.C.2.2.5 Stability study:

Electrochemical cyclic stability is an important factor that concludes the practicability of a device. The electrochemical cyclic stability of S-CMP-4//PVA-KOH//rGO asymmetric solid-state device is investigated by taking the GCD plots over 6000 cycles at a fixed current density of 2.8 A g^{-1} **(Figure 5.25)**. The S-CMP-4//PVA-KOH//rGO asymmetric solid-state device delivers 89 % capacitance retention over 6000 cycles. Inset of **Figure 5.25** presents the 1st, 3000th and 6000th GCD cycle and it exhibits a small decay in storing capacity. Thus, it highlights the long-term stability of S-CMP-4//PVA-KOH//rGO asymmetric solid-state device.

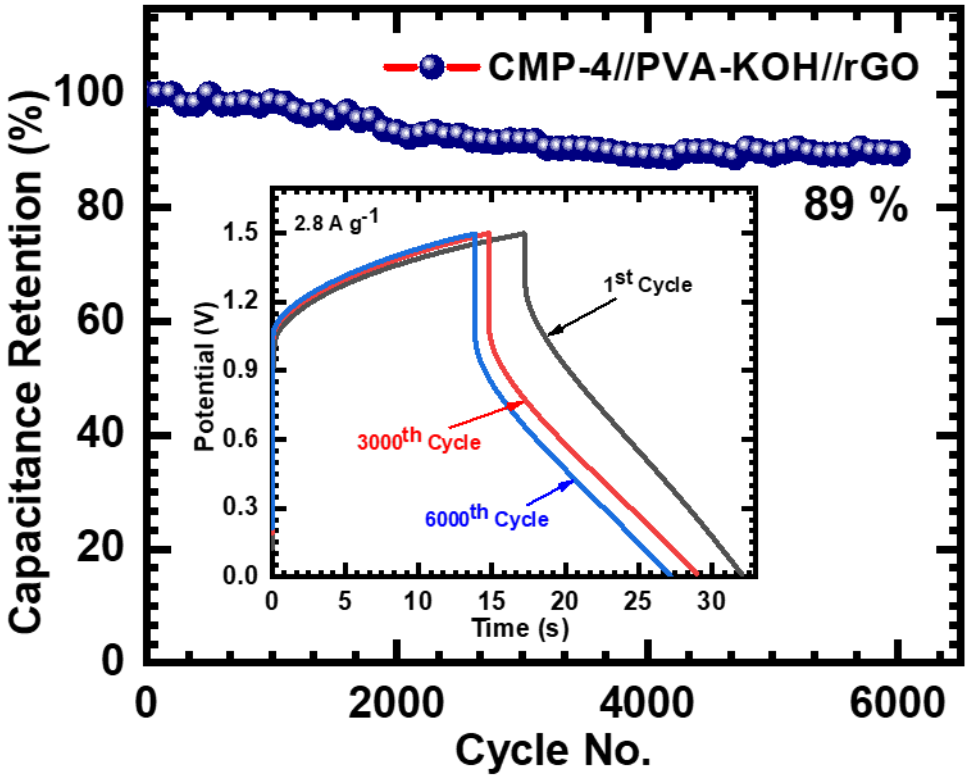

Figure 5.25: The plot of capacitance retention with cycle number for S-CMP-4//PVA-KOH//rGO asymmetric solid-state device (Inset: GCD cycles at 1st, 3000th and 6000th cycle).

5.2.C.2.2.6 Demonstration of S-CMP-4//PVA-KOH//rGO asymmetric solid-state device:

The practical applicability of S-CMP-4//PVA-KOH//rGO asymmetric solid-state device is experimented with by charging two serially connected devices for 30 s by employing a constant potential of +3.2 V and discharged over 201 red light-emitting diodes (LEDs) designed in different text. The text contains the words "DYPU" (D. Y. Patil University), "CDL" (Prof. Chandrakant D. Lokhande) and "GROUP" (Group). Prominently, the S-CMP-4//PVA-KOH//rGO asymmetric solid-state device easily lights up the LED panel up to 2 min **(Figure 5.26)**. Notably, the glowing intensity of LEDs suggesting the high power capacity, while the extended brightening time interval of LEDs suggesting the higher energy storing capacity of

the S-CMP-4//PVA-KOH//rGO asymmetric solid-state device. This demonstration clearly implies the high potential of the device as the most promising energy storage device in various portable electronic areas.

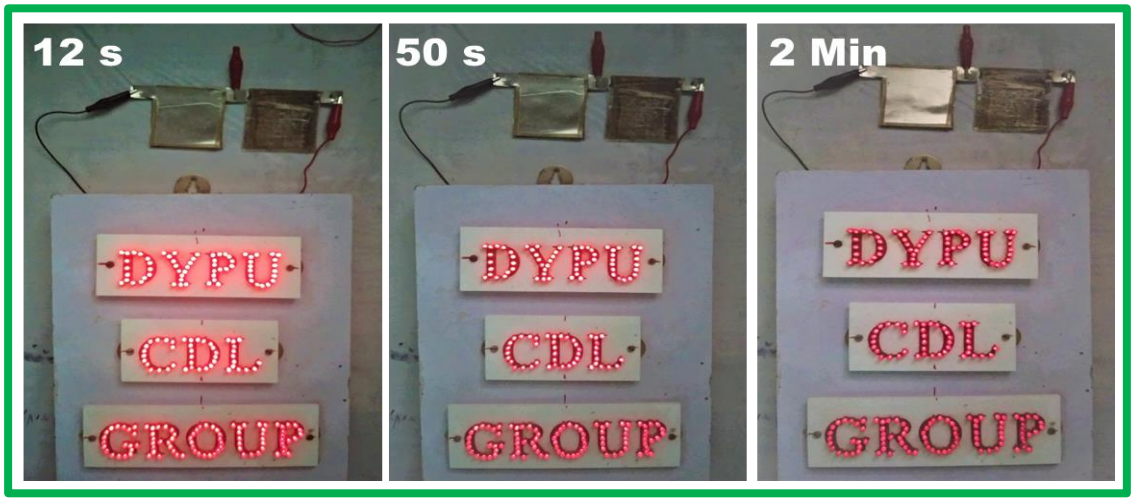

Figure 5.26: Digital photographs of device demonstration of S-CMP-4//PVA-KOH//rGO asymmetric solid-state device glowing panel of 201 red LEDs taken after 12 s, 50 s, and 2 min.

Table 5.1: Supercapacitive performance evaluation of S-CMP-4//rGO asymmetric device in an aqueous and solid-state electrolyte.

Sr. No.	Name of Device	Specific capacitance (F g^{-1}) at current density (1.0 A g^{-1})	Energy density (Wh kg^{-1})	Power density (kW kg^{-1})	Cycles No.	Stability (%)
1.	S-CMP-4//KOH //rGO	145	45.31	0.79	6000	91
2.	S-CMP-4//PVA-KOH//rGO	52	16.29	0.82	6000	89

5.2.C.3 Conclusions:

In summary, the supercapacitive performance of aqueous and solid-state devices are analyzed in this section. The asymmetric aqueous and solid-state devices exhibit excellent electrochemical capacitive performance with highest

specific capacitance of 145 and 52 F g^{-1}, respectively at 1 A g^{-1}. Moreover, the maximum energy density at a power density of asymmetric aqueous device achieved up to 45.31 Wh kg^{-1} at 0.79 kW kg^{-1} and 16.29 Wh kg^{-1} at 0.82 kW kg^{-1} for the solid-state device. In addition, S-CMP-4//rGO asymmetric aqueous device exhibits capacitance retention of 91 % and solid-state device displays 89 % over 6000 cycles, which confirms excellent cyclic stability of devices. Furthermore, for actual demonstration of an asymmetric solid-state device, 201 red LEDs are lightened up to 2 min using a series combination of two asymmetric solid-state devices. Conclusively, obtained outcomes confirm that the utilized theme of asymmetric supercapacitor device offers great promise in the field of energy storage devices.

5.3 References:

1) L. Deng, Y. Gu, Y. Gao, Z. Ma, G. Fan, J. Colloid Interf. Sci., 494, (2017), 355-362.
2) H. Zhang, H. Su, L. Zhang, B. Zhang, F. Chun, X. Chu, W. He, W. Yang, J. Power Sources, 331, (2016), 332-339.
3) B. K. Deka, A. Hazarika, O. B. Kwon, D. Y. Kim, Y. B. Park, H. W. Park, Chem. Eng., 325, (2017), 672-680.
4) N. Li, T. Lv, Y. Yao, H. Li, K. Liu, T. Chen, J. Mater. Chem. A, 5, (2017), 3267-3273.
5) Z. Tang, C. Jia, Z. Wan, Q. Zhou, X. Ye, Y. Zhu, RSC Adv., 6, (2016), 112307-112316.
6) L. L. Zhang, X. S. Zhao, Chem. Soc. Rev., 38, (2009), 2520-2531.
7) S. C. Lee, U. M. Patil, S. J. Kim, S. Ahn, S. W. Kang, S. C. Jun, RSC Adv., 6, (2016), 43844-43854.
8) D. P. Dubal, N. R. Chodankar, Z. C. Huertas, F. Wolfart, M. Vidotti, R. Holze, C. D. Lokhande, P. G. Romero, J. Power Sources, 308, (2016), 158-165.
9) F. Wang, S. Sun, Y. Xu, T. Wang, R. Yu, H. Li, Sci. Rep., 7, (2017), 1-11.
10) L. Liu, Z. Niu, J. Chen, Chem. Soc. Rev., 45, (2016), 4340-4363.
11) Q. Wang, J. Yan, Z. Fan, Energy Environ. Sci., 9, (2016), 729–762.
12) H. Ma, J. He, D. B. Xiong, J. Wu, Q. Li, V. Dravid, Y. Zhao, ACS Appl. Mater. Inter., 8, (2016), 1992–2000.
13) X. Chen, R. Paul, L. Dai, Natl. Sci. Rev., 4, (2017), 453–489.
14) W. S. Hummers, R. E. Offeman, J. Am. Chem. Soc., 80, (1958), 1339–1339.
15) D. C. Marcano, D. V. Kosynkin, J. M. Berlin, A. Sinitskii, Z. Sun, A. Slesarev, L. B. Alemany, W. Lu, J. M. Tour, ACS Nano, 4, (2010), 4806–4814.
16) J. Chen, Y. Li, L. Huang, C. Li, G. Shi, Carbon, 81, (2015), 826-834.
17) M. J. S. Mohamed, D. K. Bhat, AIMS Mater. Sci., 4, (2017), 158-171.
18) B. Ahmeda, A. K. Ojha, F. Hirsch, I. Fischer, D. Patrice, A. Materny, RSC Adv., 7, (2017), 13985-13996.

19) G. Bharath, S. Anwer, R. V. Mangalaraja, E. Alhseinat, F. Banat, N. Ponpandian, Sci. Rep., 8, (2018), 1-14.

20) F. Iskandar, O. B. Abdillah, E. Stavila, A. H. Aimon, New J. Chem., 42, (2018), 16362-16371.

21) M. S. Dresselhaus, A. Jorio, M. Hofmann, G. Dresselhaus, R. Saito, Nano Lett., 10, (2010), 751–758.

22) R. Li, L. Liu, F. Yang, Chem. Eng. J., 229, (2013), 460-468.

23) L. L. Zhang, X. Zhao, M. D. Stoller, Y. Zhu, H. Ji, S. Murali, Y. Wu, S. Perales, B. Clevenger, R. S. Ruoff, Nano Lett., 12, (2012), 1806–1812.

24) Y. Xu, K. Sheng, C. Li, G. Shi, ACS Nano, 4, (2010), 4324–4330.

25) D. P. Dubal, N. R. Chodankar, G. S. Gund, R. Holze, C. D. Lokhande, P. G. Romero, Energy Technol., 3, (2015), 168-176.

26) N. Choudhary, C. Li, J. Moore, N. Nagaiah, L. Zhai, Y. Jung, J. Thomas, Adv. Mater., 29, (2017), 1605336.

27) N. R. Chodankar, D. P. Dubal, G. S. Gund, C. D. Lokhande, Energy Technol., 3, (2015), 625-631.

28) G. Shen, S. H. Yu, Y. Xia, X. W. (David) Lou, J. Mater. Chem. A, 2, (2014), 10710-10711.

29) H. Gerischer, W. Ekardt, Appl. Phys. Lett., 43, (1983), 393-395.

30) J. Cheng, M. Sprik, Phys. Chem. Chem. Phys., 14, (2012), 11245-11267.

31) G. Ma, E. Feng, K. Sun, H. Peng, J. Li, Z. Lei, Electrochim. Acta, 135, (2014), 461-466.

32) A. M. Stephan, Eur. Polym., 42, (2006), 21–42.

33) G. Ju, M. A. Khan, H. Zheng, Z. An, M. Wu, H. Zhao, J. Xu, L. Zhang, S. Bilal, J. Zhang, Front. Mater. Sci., 13, (2019), 133–144.

34) P. K. Katkar, S. J. Marje, S. S. Pujari, S. A. Khalate, A. C. Lokhande, U. M. Patil, ACS Sustain. Chem. Eng., 7, (2019), 11205–11218.

35) V. J. Mane, D. B. Malavekar, S. B. Ubale, R. N. Bulakhe, Insik In, C. D. Lokhande, Electrochim. Acta, 335, (2020), 1-16.

36) A. M. Patil, A. C. Lokhande, N. R. Chodankar, P. A. Shinde, J. H. Kim, C. D. Lokhande, J. Ind. Eng. Chem., 46, (2017), 91-102.

37) P. K. Katkar, S. J. Marje, S. S. Pujari, S. A. Khalate, P. R. Deshmukh, U. M. Patil, Synth. Met., 267, (2020), 1-13.

38) X. Fan, H. Zhou, X. Guo, RSC Adv., 5, (2015), 45484-45491.

39) N. R. Chodankar, D. P. Dubal, Y. Kwon, D. H. Kim, NPG Asia Mater., 9, (2017), 1-10.

CHAPTER -6

SUMMARY AND CONCLUSIONS

Summary and conclusions:

Continuously growing demand for sustainable and renewable energy sources in smart electric power selling devices has led to comprehensive research into the development of eco-friendly and inexpensive energy storage devices. To date, three types of energy storage devices are available in the market such as batteries, capacitors and supercapacitors. However, battery has short cycle life, safety problems and low power which limits the applications in electronic devices that require high power. Out of these different energy storage devices, the supercapacitor is considered to be the most suitable and innovative choice for green energy storage devices due to its fast rechargeability, high energy and power density, long cycle life and safe operation. Therefore, supercapacitors are produced to fulfill the gap between conventional capacitors and batteries. Supercapacitors can be utilized in various electronic devices including hybrid electric vehicles, telecommunication, memory backup systems, flash cameras, etc.

Recently, different types of electrode materials have been studied for supercapacitor applications including carbon-based materials (CNTs, AC, graphene, etc.), conducting polymers (polyaniline, polypyrrole, etc.) and transition metal oxides/hydroxides/sulfides. Among different electrode materials, transition metal phosphates are the most promising electrode material for supercapacitors as they produce high reversible redox reactions and store higher energy as compared to the EDLCs. Nowadays, cobalt phosphate and manganese phosphate are frequently used as active electrode materials for supercapacitors because of their multiple oxidation states, cost-effectiveness, non-toxicity, good electrical conductivity and electrochemical stability. By combining such metal phosphates,

the performance of electrode can be increased. The synergistic effect of metal phosphates can enhance electrochemical capacitive performance.

The present research work is focused on the preparation of cobalt manganese phosphate thin films on SS substrate by binder-free, inexpensive and facile hydrothermal and SILAR methods. Furthermore, preparative parameters are optimized to get good quality and adherent thin films. The influence of cobalt and manganese concentrations on the structural, morphological and electrochemical performance of cobalt manganese phosphate thin films were investigated. By altering the concentrations of cobalt and manganese in both (hydrothermal and SILAR) methods, different nano/microstructured cobalt manganese phosphate thin films with enhanced electrochemical performance in terms of specific capacitance and energy density was achieved. In addition, the cobalt manganese phosphate electrodes with higher electrochemical performance are used to fabricate asymmetrically configured (Co-Mn Phosphate//rGO) aqueous and solid-state devices (PVA-KOH gel electrolyte). Also, a practical demonstration of 201 red LEDs illumination is carried out using an asymmetric (Co-Mn Phosphate//rGO) solid-state supercapacitor device. The present thesis work has been divided into six chapters.

Chapter 1 describes general introduction, energy demands of the future generation, different energy storage devices with various transition metal compound materials and a literature survey of different electrode materials for supercapacitor. Furthermore, it describes the progress in supercapacitors, the modern trend of research in supercapacitors and its classification. The potential of supercapacitors to meet the total energy demands of society is further explained in detail. Also, the fundamental and working mechanism of the supercapacitor has

been discussed in detail. The basic requirements for a supercapacitor using a wide variety of active electrode materials are described in detail. Moreover, it contains a comprehensive description of metal phosphate materials for supercapacitors. Furthermore, the literature review on cobalt phosphate, manganese phosphate, and cobalt manganese phosphate materials is summarized. Ultimately, the orientation and purpose of the dissertation are declared at the end of chapter 1.

Chapter 2 discusses the deposition methods of thin films and their classification, also the theoretical background of hydrothermal and SILAR methods and their advantages and the effect of preparation parameters for the production of thin films. Subsequently, the various thin film characterization techniques (structural, morphological and elemental analysis) with their theoretical background are described in this chapter, such as X-ray diffraction (XRD), Fourier transformation infrared spectroscopy (FTIR), X-ray photoelectron spectroscopy (XPS), field emission scanning electron microscopy (FE-SEM) and energy-dispersive X-ray spectroscopy (EDS). Finally, the theoretical background of electrochemical techniques used to assess the electrochemical capacitive performance of supercapacitor electrodes such as CV, GCD, and EIS has been also explained briefly.

Chapter 3 includes the synthesis, characterization and supercapacitive performance evaluation of hydrothermally prepared cobalt manganese phosphate thin films. This chapter is also distributed into two sections i.e. section 'A' and 'B'. **Section A** includes the preparation of cobalt manganese phosphate thin films on SS substrate at different concentrations of cobalt (Co) and manganese (Mn) using a simple binder-free hydrothermal method. Further, the influence of Co and Mn concentrations on the physico-chemical properties of cobalt manganese phosphate

thin films were studied. The successful preparation of cobalt manganese phosphate is confirmed from the XRD, FTIR, XPS, FE-SEM and EDS analysis. The XRD study discloses the obtained material is cobalt manganese phosphate with a monoclinic structure. Also, FTIR spectroscopy used to analyze the molecular bonds and confirms the formation of hydrous cobalt manganese phosphate material. Moreover, XPS analysis reveals the presence of Co, Mn, P and O elements in the prepared thin film. Further, the change in the nano/microstructures of cobalt manganese phosphate thin films as a consequence of the different amounts of cobalt and manganese is clearly seen in the FE-SEM images. The EDS study of cobalt manganese phosphate confirms the formation of good stoichiometric material with the nearly expected atomic percentage of Co and Mn used in experiments. **Section B** deals with the electrochemical performance evaluation of different nano/microstructured cobalt manganese phosphate thin films. Also, the effect of amount of Co and Mn on electrochemical properties of different cobalt manganese phosphate thin films is investigated. The three-electrode system consisting of cobalt manganese phosphate thin films as a working electrode, platinum plate as a counter electrode, Hg/HgO as a reference electrode, and 1 M KOH as an electrolyte is used to evaluate the electrochemical performance. The electrochemical measurements demonstrate that, the H-CMP-2 [$Co_{2.16}Mn_{0.84}(PO_4)_2$] electrode shows a high specific capacitance of 571 F g^{-1} at 2.2 A g^{-1} current density. Moreover, it displays excellent capacitance retention of 81 % after 4000 cycles. In addition, H-CMP-2 thin film exhibits small values of Rs (1.09 Ω) and Rct (7.73 Ω) as compared to other compositions. The enhancement in electrochemical performance is ascribed to strong adhesion among cobalt manganese phosphate and SS substrate with unique morphology, which provides more efficient pathways for easy

penetration of electrolyte into the interior of active material. Hence, the purpose behind making cobalt manganese phosphate thin film electrode to achieve high specific capacitance is fulfilled.

Chapter 4 consists of characterization, and supercapacitive performance evaluation of cobalt manganese phosphate thin films prepared by SILAR method. This chapter is distributed into two different sections viz. section 'A' and 'B'. **Section 'A'** deals with the preparation of cobalt manganese phosphate thin films directly on SS substrate by SILAR method and their structural, compositional, and morphological characterizations. Moreover, the optimization of parameters includes precursor concentration, precursor ratio, number of cycles, reaction and rinsing time. The structural evolution of cobalt manganese phosphate with increasing concentration of Co and Mn ions is analyzed from the XRD study. Also, the amorphous nature of cobalt manganese phosphate has been confirmed by the XRD. Furthermore, FT-IR analysis is used to determine the molecular bonding in prepared thin film electrodes and it indicates the formation of hydrous cobalt manganese phosphate. The XPS study reveals the presence of Co, Mn, P and O elements in the prepared samples. Further, the FE-SEM images for cobalt manganese phosphate electrodes confirm the formation of porous material consists of nanoparticles. According to the EDS study of cobalt manganese phosphate thin film, formation of a good stoichiometry with an almost expected composition of Co and Mn used in synthesis is achieved. Moreover, **Section B** deals with the evaluation of supercapacitive properties of nanostructured cobalt manganese phosphate thin films with effect of concentrations variation of Co:Mn. The best candidate of cobalt manganese phosphate (S-CMP-4) [$Co_{2.22}Mn_{0.78}(PO_4)_2$] thin film electrode illustrates the highest specific capacitance of 743 F g^{-1} at a

current density of 2.8 A g^{-1} with electrochemical stability up to 90.6 % after 4,000 GCD cycles in 1 M KOH electrolyte. The EIS study reveals small R_s (0.98 Ω) and R_{ct} (6.32 Ω) for cobalt manganese phosphate (S-CMP-4) thin film. Moreover, S-CMP-4 thin film was further employed during the fabrication of asymmetric devices.

Chapter 5 covers the fabrication and supercapacitive performance evaluation of asymmetric aqueous and solid-state devices. The SILAR synthesized cobalt manganese phosphate (S-CMP-4) [$Co_{2.22}Mn_{0.78}(PO_4)_2$] as a cathode and rGO as an anode was used to fabricate asymmetric aqueous and solid-state devices with aqueous (KOH) and polymer gel (PVA-KOH) electrolytes, respectively. This chapter is distributed into three sections (A, B and C). **Section A** describes the synthesis, structural and morphological characterization, and electrochemical performance evaluation of the rGO electrode. The rGO electrode is characterized using XRD, Raman, BET, and FE-SEM techniques. The XRD pattern confirms that, GO is reduced by hydrothermal method and forms reduced graphene oxide (rGO). Also, Raman spectra are beneficial for understanding and measuring defects, identifying the number of graphene layers and orientation, and the obtained D/G intensity ratio (I_D/I_G) of rGO is 1.01. In BET analysis, a high surface area of 237 m^2 g^{-1} with a mesoporous structure having a pore size of 10.62 nm is observed for rGO material. Further, the FE-SEM shows well-defined and interconnected 3D porous morphology with nanosheets of rGO. Also, the supercapacitive performance evaluation of rGO was studied in an electrochemical cell consists of three-electrodes with 1 M KOH electrolyte. It demonstrates maximum 243 F g^{-1} specific capacitance at a current density of 3.0 A g^{-1}. The EIS results show low solution resistance (R_s- 1.10 Ω) and charge transfer resistance (R_{ct}- 37.66 Ω) of rGO electrode. Furthermore, the rGO electrode displays superior capacitance retention

of 82 % over 3000 cycles. **Section B** gives detailed information about electrode preparation, PVA-KOH gel electrolyte preparation, and the aqueous and solid-state device fabrication process. **Section C** includes the supercapacitive performance evaluation of S-CMP-4 (SILAR deposited)//rGO asymmetric aqueous and solid-state devices. The asymmetric aqueous (S-CMP-4//KOH//rGO) and solid-state (S-CMP-4//PVA-KOH//rGO) supercapacitor devices are fabricated. The S-CMP-4//rGO asymmetric aqueous (145 F g^{-1} at 1.0 A g^{-1}) and solid-state (52 F g^{-1} at 1.0 A g^{-1}) device exhibited excellent electrochemical performance with highest specific capacitance. Moreover, the maximum energy and power density of asymmetric aqueous (45.31 Wh kg^{-1}, 0.79 kW kg^{-1}) and solid-state (16.29 Wh kg^{-1}, 0.82 kW kg^{-1}) device are obtained. In addition, S-CMP-4//rGO asymmetric aqueous (91 %) and solid-state (89 %) device exhibited excellent cyclic stability over 6000 cycles. Finally, for an actual demonstration of the asymmetric solid-state device, 201 red LEDs are lightened up to 2 min using a series combination of two solid-state devices.

Chapter 6 summarizes and concludes all the chapters. Evaluation of the electrochemical performance of all electrode materials is the basic entity of making supercapacitor devices. Therefore, FE-SEM images and supercapacitive performance results of best performed Co-Mn Phosphate thin film [$Co_xMn_{3-x}(PO_4)_2$] electrodes are shown in **Figure 6.1**. Also, the asymmetric aqueous and solid-state devices showed high electrochemical performance and good practical applicability (**Figure 6.2**). Moreover, the enhanced electrochemical performance of SILAR deposited Co-Mn Phosphate [$Co_{2.22}Mn_{0.78}(PO_4)_2$] thin film is clearly observed in **Figure 6.1**. This is due to the following aspects:

1) The Co-Mn Phosphate [$Co_{2.22}Mn_{0.78}(PO_4)_2$] nanoparticles structure provides effective accommodation for a large number of electrolyte ions.
2) Co-Mn Phosphate nanoparticles support fast and reversible faradaic reactions and decrease the ion diffusion length.
3) The Co-Mn Phosphate electrode holds good electrical conductivity, fast electron, and ion transport and better adhesion with the stainless steel substrate.
4) The synergistic effect of different concentrations of Co and Mn (0.75:0.25) in Co-Mn Phosphate thin film exhibits improved electrochemical capacitive performance.

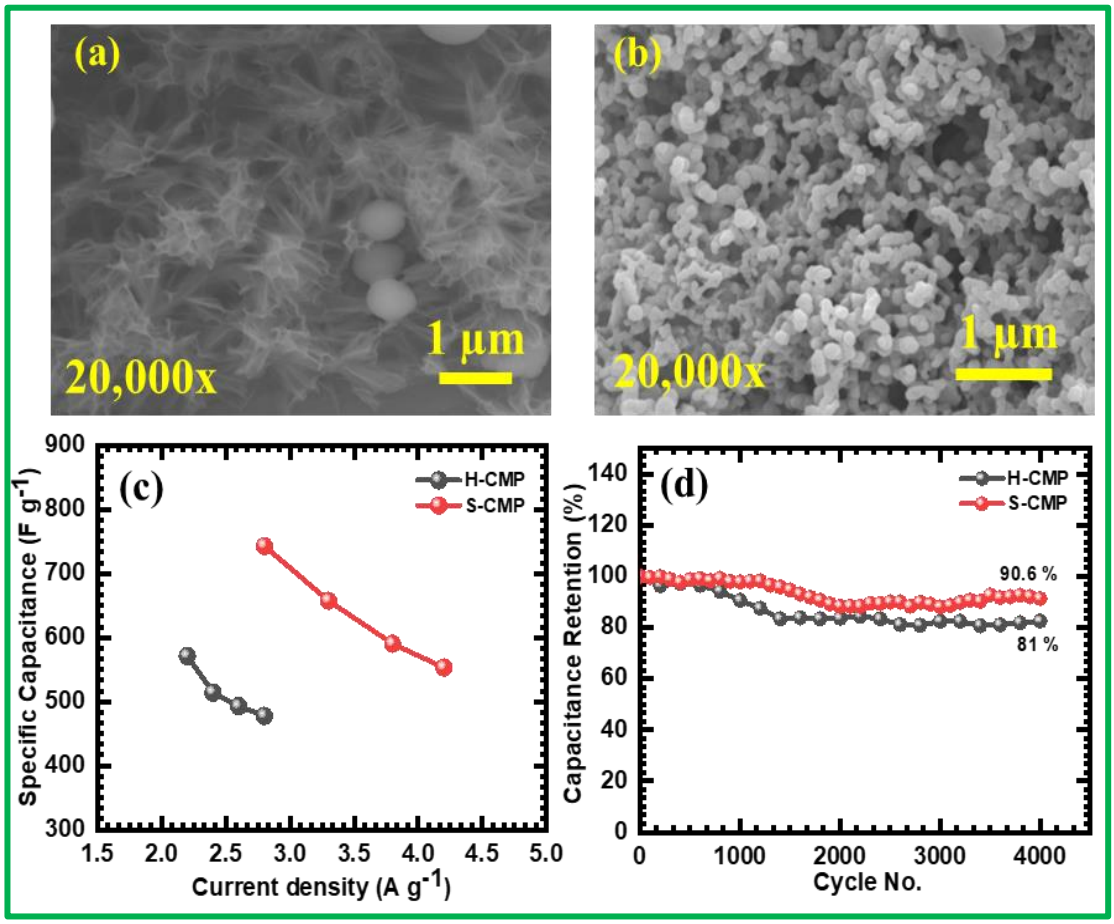

Figure 6.1: (a, b) FE-SEM images (20,000x), (c) plots of specific capacitance versus current density, and (d) cyclic stability of Co-Mn Phosphate electrodes prepared by hydrothermal and SILAR methods.

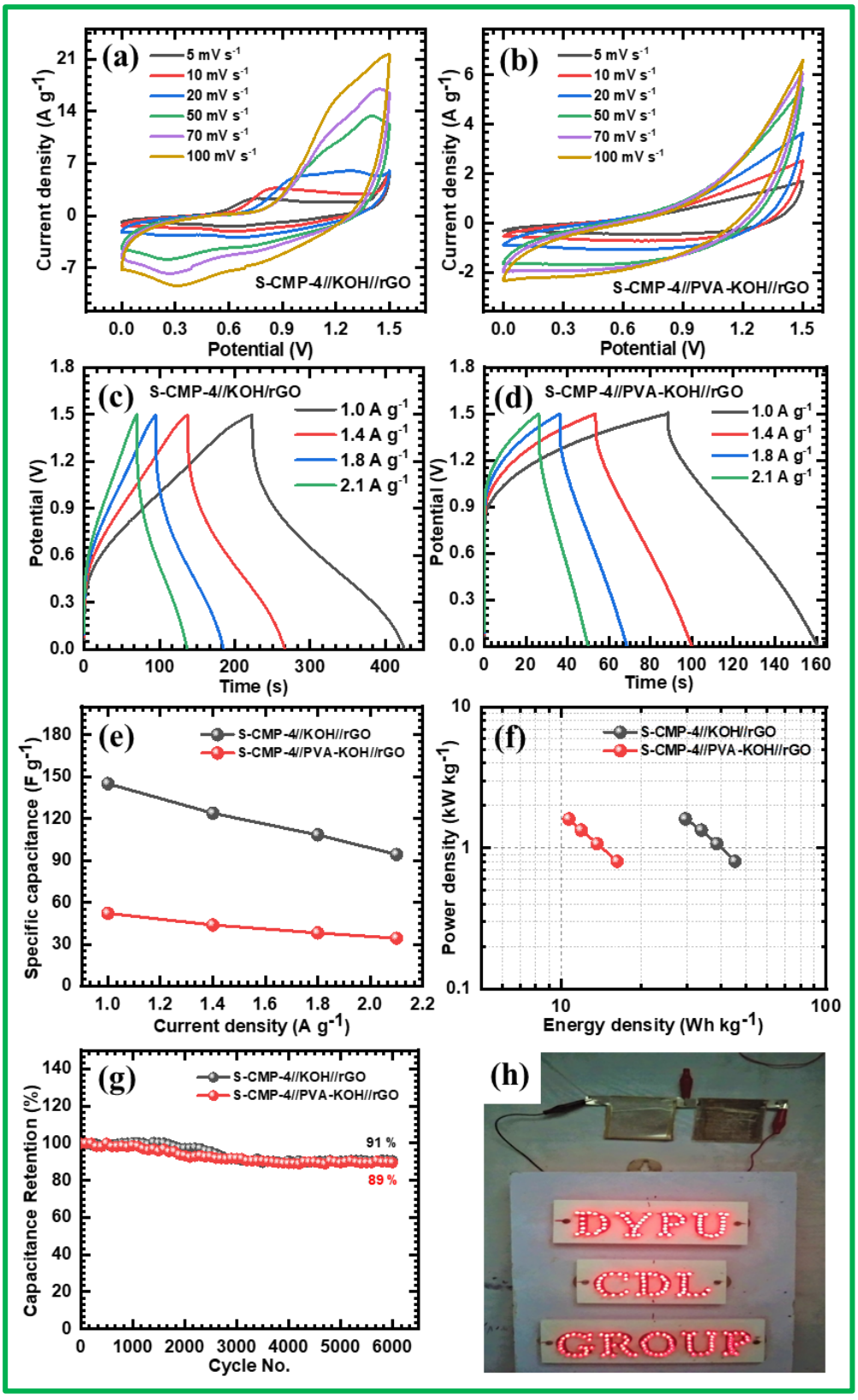

Figure 6.2: (a, b) CV curves, (c, d) GCD plots, (e) plot of specific capacitance vs current density, (f) plots of energy density vs power density, (g) cyclic stability of aqueous and solid-state devices and (h) solid-state device demonstration.